Analysis of pp → Data at Low Energy and its Implications

Mark Norman Oakden

Analysis of $\bar{p}p \to \pi\pi$ Data at Low Energy and its Implications

Mark Norman Oakden
Centre for Particle Theory
University of Durham

A thesis submitted to the University of Durham
for the Degree of Doctor of Philosophy
June 1994

Abstract

This thesis is a study of data on $\overline{p}p \rightarrow \pi^-\pi^+$ in the range $0.36 \leq P_{lab} \leq 1.55$ GeV/c taken by the PS172 experiment at CERN's LEAR facility. The aim is to elucidate the nature of mesonic states coupling both to baryon-antibaryon and meson-meson channels.

The PS172 data are compared with, and found to be consistent with, earlier data on the same channel, and, in a model independent way, the consistency of the PS172 results with BNL data on $\overline{p}p \rightarrow \pi^0\pi^0$ is also established.

The first amplitude analysis of $\overline{p}p \rightarrow \pi\pi$ to incorporate the PS172 data is performed and it is found that from the hundreds of possible amplitudes, only two are compatible with the BNL $\overline{p}p \rightarrow \pi^0\pi^0$ data and with threshold conditions. The latter may be applied in a far more rigorous way than has been previously possible since the PS172 momentum range extends so close to threshold.

Both of the solutions found exhibit resonances with spins 0–5 and the masses, widths and couplings of these states are deduced. The lowest spin resonances are found to have such large couplings to $\overline{N}N$ that they are unlikely to be simple $\overline{q}q$ states.

Acknowledgements

Firstly, I would like to thank my supervisor, Mike Pennington, for his guidance, advice and patience both during my time in Durham and in the months since I left.

I would also like to thank the staff and postgraduate students of the Centre for Particle Theory for numerous discussions and for helping to make my period of study in Durham so enjoyable. In particular I must thank both Matthew Reader and Andrew Morgan for putting up with being shot at point-blank range with rubber sucker darts and other such atrocities merely through the misfortune of having been allocated to share an office with me, and for doing so with such good humour.

I gratefully acknowledge the financial support of the UK SERC during my period of research.

Finally, I would like to thank my parents and my fiancée, Julia, for their support, encouragement and understanding.

Declaration

I declare that no material in this thesis has previously been submitted for a degree at this or any other university.

The research in this thesis has been carried out in collaboration with Dr. M.R. Pennington. Parts of this thesis have been summarised in the following papers

1. Amplitude analysis of $\overline{p}p \rightarrow \pi\pi$ at low energy, M.N. Oakden and M.R. Pennington, Durham University Centre for Particle Theory preprint DTP–93/60, To appear in Nucl. Phys. **A**.

2. Resonance Structures in PS172 Results on $\overline{p}p \rightarrow \pi\pi$, M.N. Oakden and M.R. Pennington, to appear in the Proceedings of the 2^{nd} Biennial Workshop on Nucleon-Antinucleon Physics, ITEP Moscow, Russia, 1993.

Contents

Chapter 1

Introduction

1.1 "Pre-Introduction"

Before putting forward what the aims of this Chapter are, it is perhaps appropriate to point out what it does not aim to do. Although the first part of the chapter is mainly historical in content, it is not, and cannot be, a comprehensive account of even the narrow section of physics history which it covers. Much will, of course, be omitted and much that is included will be covered in insufficient detail—to provide even a superficial history of all the physics relevent to this thesis would require a book many times longer than this thesis. A fuller account may be found, for example in [1]. This chapter, then, will be restricted to motivating the study of hadron spectroscopy, a subject which, in the minds of many of today's particle physicists, is seen as "a subject to be reminisced about by balding, greying, ageing old men" [2]. It is, indeed, odd that, in many particle theory groups one would find it more difficult to interest people, particularly new research students, in hadron spectroscopy—a study of the real world of particles—than to interest them in the mathematical complexity/elegance of theories which live in 26, 10 or 2 dimensions. One reason for this is undoubtedly the belief (almost certainly held more subconsciously than consciously) that with the advent of the theory of the strong interaction, QCD, everything about hadrons is, in principle,

determined by the Lagrangian $\mathcal{L}_{QCD}$ and hence hadron spectroscopy really is nothing more than collecting "stamps". The problem with this belief, of course, lies in the two words "in principle". To date, despite the best efforts of some of the most gifted particle theorists that there have ever been (R.P.Feynman is a notable example) the mechanism by which the fundamental objects appearing in the QCD Lagrangian, namely quarks and gluons, bind together to produce the real-world particles whose tracks can be seen in detectors is still not understood.

1.2 Historical Background

Before 1932, only three "elementary" particles were known. These were the electron, discovered by J.J. Thomson in his study of cathode rays; the photon, introduced by Einstein to explain the photoelectric effect; and the proton discovered by Rutherford. Furthermore, with the development and refinement of quantum mechanics, culminating in the electron theory of Dirac, the electron and photon were believed to be essentially understood and many believed that an understanding of the atomic nucleus, and hence all everyday matter could not lie too far ahead. Although the year 1932 saw the discovery of two new particles, the neutron and the positron, almost doubling the size of the spectrum of known particles, this did nothing to dispel that belief, since both particles fitted rather naturally into the scheme of things as it was understood at the time. It was realised that the neutron, discovered by Chadwick [3], was one of the two building blocks from which all atomic nuclei appeared to be made (the other being the proton), and the positron, found by Anderson [4], provided excellent confirmation of Dirac's ideas, being the anti-particle to the electron that his relativistic quantum mechanical equation required.

Further progress towards what must have appeared to be the end of particle physics was made in 1935 when Yukawa proposed a mechanism for the inter-nucleon force [5] based on the exchange of a new particle whose mass could be estimated from the uncertainty principle and the range of the nuclear force, estimated from measurements

of the deuteron binding energy. This particle Yukawa christened the mesotron since the estimate for its mass turned out to be intermediate between that of the electron and the nucleon, $m \sim 200m_e$ (although eventually, the name "meson" became prevalent). In 1937, it seemed that this hypothesis was correct as a particle was discovered [6] with a mass consistent with that of Yukawa's meson. "Unfortunately", during the next decade, it became clear that this particle could not be the nuclear force carrying particle of Yukawa's theory. Indeed, in 1947, Conversi *et al.* conducted an experiment which showed that its interactions with matter were much too weak for it to be the carrier of the strong force [7]—in fact, the particle's properties turned out to be alarmingly similar to those of the electron, apart from its greater mass, of course (this particle was named the μ-meson but is now known as the muon since it is not a meson in the modern sense of the word). Particle physics did not have to wait too long for Yukawa's particle to put in an appearance though since later in the same year a strongly interacting charged particle of appropriate mass was seen by Perkins [8], and also by Lattes *et al.* [9], who observed its decays into muons. So although Yukawa's ideas about the nature of the inter-nucleon force proved to be essentially correct, a puzzling extra particle, the muon, had appeared which confounded any hopes of completely understanding particle physics. To complicate matters further, in the same year, Rochester and Butler observed two events in which odd "V" shaped tracks appeared [10], now known to be due to decays of neutral "strange" particles, so called since they appeared to always be produced in association with other "strange" particles, i.e. never singly, but decayed quite happily into non-strange particles.

This was not the end of the proliferation in states either. During the 1950s and 1960s more particles appeared, and it soon became apparent that not all of these could be truly elementary. The particle spectrum could be broadly divided into two classes, those particles which take part in so-called strong interactions, known as hadrons, and particles such as electrons, positrons and muons which do not. By far the largest number of particles seen fell into the hadron category and it became clear that, in order to make any progress in understanding the nature of these, some orderly classification would

have to be found and hence the subject of hadron spectroscopy was born. One of the most notable pieces of order in the apparent chaos was the fact that hadrons appeared to occur in groups of almost exactly equal mass, the members of which differ in electric charge, for example, the proton and neutron have almost the same mass, and the three pions are also equal in mass to the level of a few MeV. This grouping of particles into (almost) degenerate multiplets could be understood in terms of isospin, which had been proposed by Heisenberg in 1932 to account for the degeneracy of the proton and neutron [11]. Since this thesis is a study of data on $\overline{p}p \rightarrow \pi\pi$, it is appropriate here to examine the application of isospin to the $\overline{p}p$ and $\pi\pi$ systems.

1.3 Isospin and $\overline{p}p \rightarrow \pi\pi$

By analogy to the hydrogen atom, where, owing to rotational invariance, states which differ only in the quantum number m are degenerate in energy, the degeneracy in mass of particles within the above mentioned groups is ascribed to an invariance group. This group is formally identical to spin and for this reason goes by the name isospin [12, 13]. The neutron and proton are thought of as belonging to an isospin doublet ($I = \frac{1}{2}$),

$$N = \begin{pmatrix} p \\ n \end{pmatrix}, \tag{1.1}$$

the proton being analogous to a spin up state, having third component of isospin, I_3, equal to $+\frac{1}{2}$ and the neutron having $I_3 = -\frac{1}{2}$. The strong force is considered to be invariant under $SU(2)$ transformations amongst these states, whilst the slight non-degeneracy between the proton and neutron masses is ascribed to a breaking of the $SU(2)$ invariance by electromagnetic interactions.

Representations of all isospins $0, \frac{1}{2}, 1, \ldots$ may be built up from combinations of the isospin $\frac{1}{2}$ fundamental representation. It is most natural, given the subject matter of this thesis, to examine here the combinations of nucleon and antinucleon. Before

embarking on this it is necessary to determine the appropriate form for the antinucleon spinor. A natural choice would be the complex conjugate spinor

$$N^* = \begin{pmatrix} p^* \\ n^* \end{pmatrix}, \tag{1.2}$$

since in field theory, where the nucleon fields are interpreted as operators, p destroying a proton and creating an antiproton, and similarly for n, the operator which destroys an antiproton and creates a proton will be p^*. There is, however, a more convenient choice, based on the fact that for $SU(2)$ the conjugate representation is equivalent to the fundamental representation. As it stands, the spinor N^* does not transform in the same way under $SU(2)$ rotations as does the fundamental representation spinor N. As has just been remarked, it is a peculiarity of $SU(2)$, that there exists a matrix Δ such that the spinor $\overline{N}$, defined as

$$\overline{N} = \Delta N^*, \tag{1.3}$$

transforms identically to N. It is more convenient to work with $\overline{N}$ than with N^* since the same Clebsch-Gordan coefficients, as are appropriate for decomposing systems of nucleons into representations with definite isospin, may be directly used for systems comprising both nucleons and antinucleons.

Consider the effect of an infinitesimal $SU(2)$ transformation on N,

$$N \to N' = \left(1 + \frac{i}{2}\underline{\delta} \cdot \underline{\sigma}\right), \tag{1.4}$$

where $\underline{\sigma}$ is a vector, the components of which are the Pauli spin matrices, i.e.,

$$\underline{\sigma} = (\sigma_1, \sigma_2, \sigma_3) \tag{1.5}$$

with

$$\sigma_1 = \begin{pmatrix} 0 & 1 \\ 1 & 0 \end{pmatrix} \quad \sigma_2 = \begin{pmatrix} 0 & -i \\ i & 0 \end{pmatrix} \quad \sigma_3 = \begin{pmatrix} 1 & 0 \\ 0 & -1 \end{pmatrix} \tag{1.6}$$

Taking the complex conjugate of Eq. (1.4) gives the transformation of N^* as

$$N^* \rightarrow N'^* = \left(1 - \frac{i}{2}\underline{\delta} \cdot \underline{\sigma}^*\right). \tag{1.7}$$

This transformation is equivalent to Eq. (1.4) if there is a matrix Δ such that

$$\left(1 + \frac{i}{2}\underline{\delta} \cdot \underline{\sigma}\right) = \Delta \left(1 - \frac{i}{2}\underline{\delta} \cdot \underline{\sigma}^*\right) \Delta^{-1} \tag{1.8}$$

i.e. if

$$\underline{\sigma} = -\Delta \underline{\sigma}^* \Delta^{-1}. \tag{1.9}$$

Multiplying on the right by Δ leads to the relations

$$\begin{aligned} \sigma_1\Delta + \Delta\sigma_1 &= 0 \\ \sigma_2\Delta - \Delta\sigma_2 &= 0 \\ \sigma_3\Delta + \Delta\sigma_3 &= 0 \end{aligned} \tag{1.10}$$

which are clearly satisfied by any matrix proportional to σ_2. The matrix $\Delta = i\sigma_2$ is a convenient choice, using which, the spinor $\overline{N}$, transforming identically to N, is

$$\overline{N} = \begin{pmatrix} n^* \\ -p^* \end{pmatrix}. \tag{1.11}$$

Nucleon-antinucleon states with definite isospin may then be constructed from the basis states $|p\rangle|\overline{n}\rangle$, $|n\rangle|\overline{n}\rangle$, $|p\rangle|\overline{p}\rangle$ and $|n\rangle|\overline{p}\rangle$. In this case one can easily construct them explicitly, using the Pauli matrices given above, although in more complicated systems it is much easier to make use of tabulated Clebsch-Gordon coefficients. The definite

isospin states of nucleon and anti-nucleon are

$$\begin{array}{cll} I_3 & I=1 & I=0 \\ \hline 1 & |p\rangle|\overline{n}\rangle & \\ 0 & \frac{1}{\sqrt{2}}(|n\rangle|\overline{n}\rangle - |p\rangle|\overline{p}\rangle) & -\frac{1}{\sqrt{2}}(|n\rangle|\overline{n}\rangle + |p\rangle|\overline{p}\rangle) \\ -1 & -|n\rangle|\overline{p}\rangle & \end{array} \tag{1.12}$$

(an overall minus sign is usually inserted in these states in order to make the sign in front of the isosinglet state positive). $\overline{p}p$ and $\overline{n}n$ states thus have contributions from both isospins $I = 1$ and $I = 0$.

Also of interest here is the isospin decomposition of combinations of two pions. Pions form an isotriplet,

$$\Pi = \begin{pmatrix} \pi^+ \\ \pi^0 \\ \pi^- \end{pmatrix}. \tag{1.13}$$

(In 1938, Kemmer extended Heisenberg's isospin ideas to include mesons [14] and found it necessary to introduce a neutral pion to complete the required isospin triplet, the π^0 was discovered in 1950 [15]). Two $I = 1$ states may combine to form states with isospins 0, 1, and 2. Again, the system is simple enough that it is not too tedious to calculate the decompositions explicitly[1] and these are:—

$$\begin{array}{cll} I_3 & I=1 & I=0 \\ \hline 1 & \frac{1}{\sqrt{2}}(|\pi^+\rangle|\pi^0\rangle - |\pi^0\rangle|\pi^+\rangle) & \\ 0 & \frac{1}{\sqrt{2}}(|\pi^+\rangle|\pi^-\rangle - |\pi^-\rangle|\pi^+\rangle) & \frac{1}{\sqrt{3}}(|\pi^+\rangle|\pi^-\rangle + |\pi^-\rangle|\pi^+\rangle - |\pi^0\rangle|\pi^0\rangle) \\ -1 & \frac{1}{\sqrt{2}}(|\pi^-\rangle|\pi^0\rangle - |\pi^0\rangle|\pi^-\rangle) & \end{array} \tag{1.14}$$

[1] An appropriate set of three dimensional Pauli matrices is

$$\sigma_1 = \frac{1}{\sqrt{2}}\begin{pmatrix} 0 & 1 & 0 \\ 1 & 0 & 1 \\ 0 & 1 & 0 \end{pmatrix} \quad \sigma_2 = \frac{1}{\sqrt{2}}\begin{pmatrix} 0 & -i & 0 \\ i & 0 & -i \\ 0 & i & 0 \end{pmatrix} \quad \sigma_3 = \begin{pmatrix} 1 & 0 & 0 \\ 0 & 0 & 0 \\ 0 & 0 & -1 \end{pmatrix}$$

and,

$$\begin{array}{cc} I_3 & I=2 \\ \hline 2 & |\pi^+\rangle|\pi^+\rangle \\ 1 & \frac{1}{\sqrt{2}}(|\pi^+\rangle|\pi^0\rangle + |\pi^0\rangle|\pi^+\rangle) \\ 0 & \frac{1}{\sqrt{6}}(|\pi^+\rangle|\pi^-\rangle + |\pi^-\rangle|\pi^+\rangle + 2|\pi^0\rangle|\pi^0\rangle) \\ -1 & \frac{1}{\sqrt{2}}(|\pi^-\rangle|\pi^0\rangle + |\pi^0\rangle|\pi^-\rangle) \\ -2 & |\pi^-\rangle|\pi^-\rangle \end{array} \tag{1.15}$$

The $\pi^+\pi^-$ states have contribution from all isospins 0, 1 and 2 whilst only even isospins contribute to the neutral pion system $\pi^0\pi^0$ (the isospin 2 component does not, however, play a role in $\overline{p}p \to \pi\pi$ since the strong interaction conserves isospin). It is easy to read off the relative weights of the isospin 1 and 0 amplitudes contributing to $\overline{p}p \to \pi^-\pi^+$, thus

$$T(\overline{p}p \to \pi^-\pi^+) = \frac{1}{2}T_{I=1} + \frac{1}{\sqrt{6}}T_{I=0}. \tag{1.16}$$

1.4 The Proliferation of Hadrons and the Eightfold Way

As time went on, more and more hadrons were found, and hadron spectroscopy was a "boom industry". Particles were classified according to their baryon number, strangeness (or hypercharge, Y, which is the sum of strangeness and baryon number $Y = S + B$), mass etc. Indeed, the strong interaction appeared to be invariant under the $SU(2)$ isospin group described earlier, and also under $U(1)$ hypercharge transformations. In 1961, Gell-Mann and Ne'eman made an important breakthrough in the classification of hadrons [16]. They noticed that the known hadrons could be fitted into representations of the group $SU(3)$ (which contains the product group $SU(2)_I \times U(1)_Y$ as a subgroup). In particular, the best known mesons and baryons fell into octet representations—Figs. 1.1 and 1.2 (hence the name "Eightfold Way").

Also, it was found that a decuplet representation could (almost) be filled by known spin-$\frac{3}{2}$ baryons, Fig. 1.3. One of the particles shown in Fig. 1.3 was, however, not known at the time. The Ω^- at the lower apex of Fig. 1.3, had not yet been discovered.

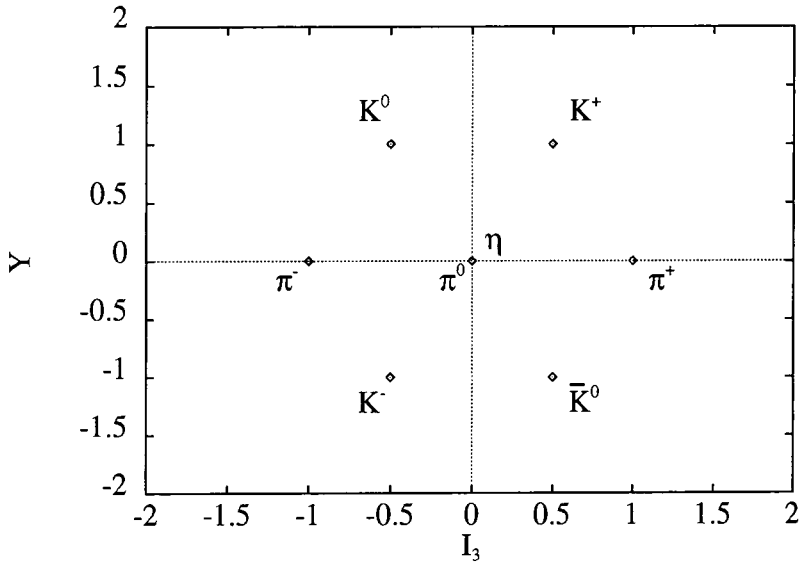

Figure 1.1: The lowest lying meson octet according to the Eightfold Way classification of Gell-Mann and Ne'eman.

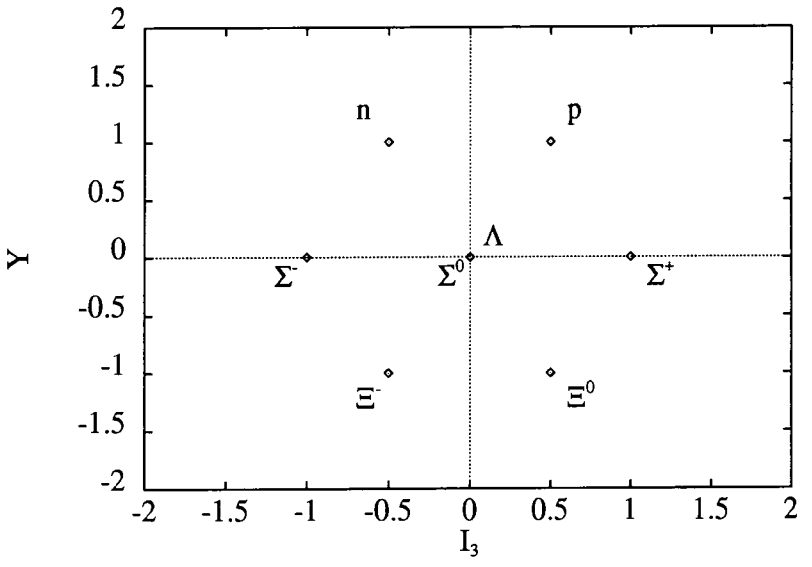

Figure 1.2: The lowest lying baryon octet according to the Eightfold Way classification of Gell-Mann and Ne'eman.

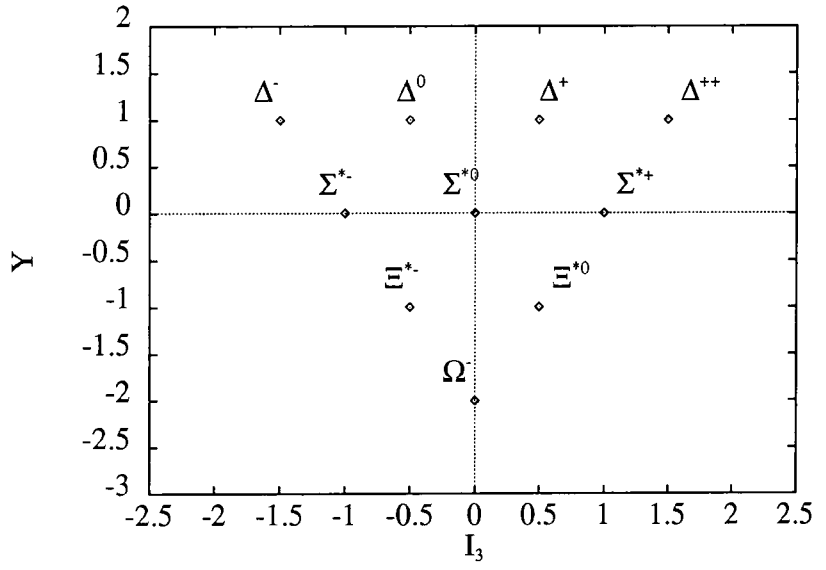

Figure 1.3: The lowest lying baryon decuplet according to the Eightfold Way classification of Gell-Mann and Ne'eman. The state Ω^- was not known at the time of Gell-Mann and Ne'eman's proposition.

The masses of particles within these $SU(3)$ multiplets vary quite strongly with Y so flavour $SU(3)$ symmetry is not exact. In fact the magnitude of the symmetry breaking may be parametrised in terms of the mass differences within the multiplets, and the mass of the Ω^- particle could be predicted by Gell-Mann and in 1963, the Ω^- was found with a mass and lifetime as expected [17].

However, in contrast to the case of $SU(2)$ isospin, where particles are found in the (doublet) fundamental representation (recall that all other isospin representations may be built up from combinations of the isospin-$\frac{1}{2}$ doublet), no particles were observed in the three dimensional fundamental representation of $SU(3)$, denoted **3**, or in the conjugate representation, $\overline{\mathbf{3}}$. In 1964, Gell-Mann and Zweig, working independently, came up with a model in which they postulated the existence of particles in the fundamental representation of $SU(3)$ [18]. Gell-Mann named these *quarks* and this name stuck. The three quarks in this model were named the up (u), down (d), and strange (s) quarks and, with the quantum number assignments of Table 1.1, could account for the

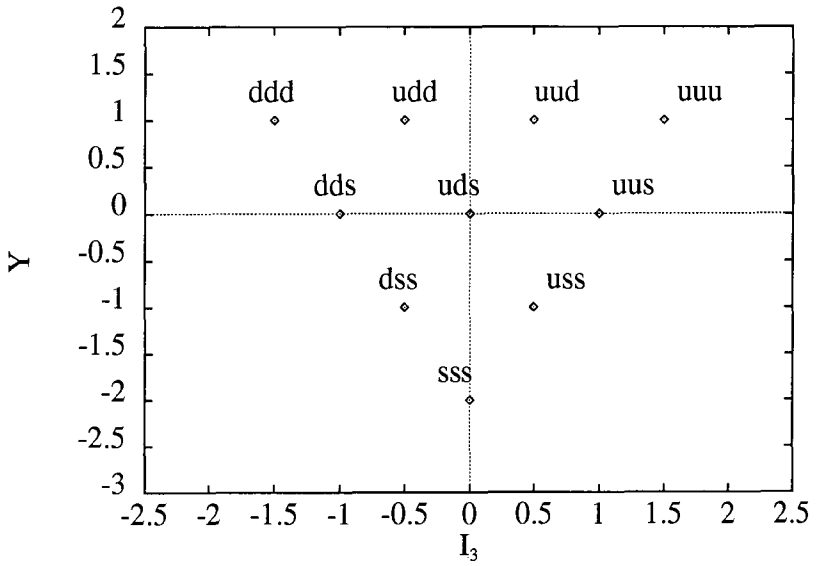

Figure 1.4: The quark composition of the hadrons in the lowest lying baryon decuplet. (See Fig. 1.3).

quantum numbers of the known hadrons, if baryons were composed of three quarks, $q_1q_2q_3$, (or antiquarks, $\overline{q_1q_2q_3}$) each and mesons made up of a quark and an antiquark,

Flavour	Q	I	I_3	S	B
up (u)	$+\frac{2}{3}$	$\frac{1}{2}$	$\frac{1}{2}$	0	$\frac{1}{3}$
down (d)	$-\frac{1}{3}$	$\frac{1}{2}$	$-\frac{1}{2}$	0	$\frac{1}{3}$
strange (s)	$-\frac{1}{3}$	0	0	-1	$\frac{1}{3}$

Table 1.1: The quantum numbers of the quarks proposed by Gell-Mann and Zweig to explain the spectrum of hadrons observed in 1964.

$\overline{q_1}q_2$ [19]. For example, the the particles comprising the baryon decuplet shown earlier in Fig. 1.3 have the quark compositions shown in Fig. 1.4.

1.5 Colo(u)red Quarks and New Types of Hadrons

The quark model, whilst "solving" the problem of the proliferation of hadrons by explaining them as composite systems, was quickly realised to pose a problem of its own. The Ω^- particle (as well as the other particles at the vertices of the baryon decuplet) is, in the quark model, composed of three quarks of the same flavour. In addition, since the Ω^- is the lowest mass particle with this flavour assignment, its spatial wave function will be symmetric under exchange of any pair of quarks (being the ground state of the sss system) and, all three quarks must have their spins aligned to produce the maximum projection states, $J_z = \pm\frac{3}{2}$, of the overall spin $\frac{3}{2}$ of the Ω^-. Hence, it would appear that the total wave function of the Ω^- must be symmetric under the exchange of identical quarks. At the time of the inception of the quark model, this was seen as a sign that either the quarks must obey strange statistics, given the name para-statistics (i.e. not the Fermi-Dirac statistics that one would expect spin-$\frac{1}{2}$ particles to obey), or the quark model must be fundamentally wrong. Greenberg, in 1964 [20], and Gell-Mann, in 1972 [21], proposed a third possible solution to this problem. They postulated that the quarks possessed a further degree of freedom, which Gell-Mann named colour[2], having three possible values. It is then easy to construct an antisymmetric wave function for the Ω^- simply by taking the colour part of the wave function to be proportional to ϵ_{ijk}, where the suffices i, j, and k range over the three colours R, G, and B. Furthermore, in terms of the new colour degree of freedom, those states which were postulated to be allowed within the naive quark model, namely $\overline{q}q$, qqq, and $\overline{qqq}$, are seen to have a common feature which states such as q and qq do not share. Each quark is considered to be in a triplet of colour, i.e. the up quark u is really a triplet of quarks, (u_R, u_G, u_B), fitting into the fundamental, three dimensional representation of $SU(3)$, $\mathbf{3}$. Similarly, the antiquarks are considered to be anti-triplets, in the conjugate representation $\overline{\mathbf{3}}$. (Note that this colour $SU(3)$ is distinct from the

[2] Actually he named it "color", a spelling which it is tempting to stick to since this would distinguish it from real colour which, as everybody knows, is spelt with a "u".

flavour $SU(3)$ of the Eightfold Way). The naive quark model allowed combinations of quarks and/or antiquarks all having the property that the decomposition of their colour structure always contains a colour singlet representation. For example, in the case of $\overline{q}q$, the colour decomposition of $\overline{\mathbf{3}} \otimes \mathbf{3}$ is[3]:—

$$\overline{\mathbf{3}} \otimes \mathbf{3} = \mathbf{8} \oplus \mathbf{1} \tag{1.17}$$

and that of the qqq state,

$$\mathbf{3} \otimes \mathbf{3} \otimes \mathbf{3} = \mathbf{10} \oplus \mathbf{8} \oplus \mathbf{8} \oplus \mathbf{1}. \tag{1.18}$$

In other words, it would appear that only states which are colourless (i.e.in a colour singlet) appear as observable hadrons, in the real world, and hence, for example, free quarks or pairs of quarks (known as diquarks) are naturally not seen—quarks are colour triplets whilst a pair of quarks can combine either into a $\mathbf{6}$ or a $\overline{\mathbf{3}}$ representation:

$$\mathbf{3} \otimes \mathbf{3} = \mathbf{6} \oplus \overline{\mathbf{3}}. \tag{1.19}$$

Of course, this is not a real explanation of quark confinement—it is merely a sort of "passing of the buck", quark confinement is "explained" if one *assumes* colour confinement.

Colour $SU(3)$ is believed to be an exact symmetry of nature, indeed, the currently favoured theory of the strong interaction, quantum chromodynamics (QCD) which was developed in the early 1970s [23], is a gauge theory based on $SU(3)$ colour invariance, modelled after the extremely successful theory of quantum electrodynamics. It is widely believed, but not yet proven, that QCD provides the mechanism for colour confinement. The problem with proving this is one of "technology". Virtually all calculations within field theory depend on the application of perturbative methods which

[3]The decomposition of such products of representations into their irreducible components may be calculated using Young tableaux, a description of which can be found in [22]

rely on the coupling in the theory being small. At very short distance scales (short relative to the sizes of hadrons that is) the QCD coupling is of order 0.1 and perturbative methods may be succesfully applied, the perturbative calculations of scaling violation in deep inelastic electron proton scattering are an example of this. As one goes towards energies corresponding to the sizes of hadrons, i.e. energies of the order 1 GeV , however, the QCD coupling becomes of order 1. No completely satisfactory way of calculating QCD in this regime has yet been developed.

If one does accept the dogma that only colour singlet states can be observable hadrons then this has interesting consequences for the spectrum of hadrons. Apart from the naive quark model states based on $\overline{q}q$, qqq and $\overline{qqq}$ configurations, a whole new range of possible states are allowed. Eq. 1.19 shows that diquarks can exist in a $\overline{\mathbf{3}}$ colour representation. Thus, a diquark may combine with an anti-diquark in exactly the same way as an antiquark may combine with a quark to form a colour singlet. The colourlessness of observed states, which is believed to be a consequence of QCD, leads then to the prediction of observable $\overline{qq}qq$ states. Indeed, it does not end here—one can build other colourless states out of more quarks and antiquarks e.g. $\overline{q}qqqq$; out of quarks, antiquarks and gluons e.g. $\overline{q}qg$ (so-called exotic states or meiktons); and even purely out of gluons e.g. gg or ggg (known as glueballs). Since none of these states lying outside the naive quark model are yet observed, hadron spectroscopy is definitely alive and kicking as a subject of study. The unequivocal discovery of any of them would be a powerful argument in favour of the belief that observable hadrons must be colourless and hence, assuming progress is made in showing that QCD leads to colour confinement, would provide evidence that QCD really does describe the strong interaction. There are two distinct approaches that are promising in the search for hadrons outside the naive quark model. Either one can try to identify such states by their properties, for example, the diquark-antidiquark states introduced above may have anomalously large couplings to baryon-antibaryon channels by virtue of the large overlap between the $\overline{qq}qq$ and $\overline{qqqqqq}$ wavefunctions; and other exotic states have quantum numbers which are not possible for naive quark model states, or one can use

a process of elimination, searching for and filling the boxes on the naive quark model scoresheet in the hope that states will be found for which there is no box left available to tick—the Sherlock Holmes approach to searching for states outside the naive quark model! Either way, it is clear that hadron spectroscopy is still an interesting subject. Even aside from the exciting prospect of searching for entirely new categories of states such as exotics and glueballs, there is the task of cataloguing all the quark model states (including the orbitally excited modes of these) which will surely be of use in fathoming the way in which QCD binds the quarks to form the observable hadrons, in much the same way as the careful cataloguing of the spectrum of hydrogen ultimately led to the development of quantum mechanics. Much effort is being put into attempts to calculate the consequences of QCD in the non-perturbative regime, for example via lattice gauge theoretical simulations [24] and via approximate solution of the field equations of QCD, the Schwinger-Dyson equations [25]. As and when these (or other) methods become sufficiently mature to predict hadronic masses, widths and other such properties it will be of paramount importance to have as much data, i.e. as many catalogued hadrons, with which to compare these predictions as possible.

Chapter 2

Model Independent Tests of the Data on $\overline{p}p \rightarrow \pi\pi$

2.1 Why study $\overline{p}p \rightarrow \pi\pi$?

When an antiproton, with some momentum P_{lab}, is incident on a target containing protons, annihilation can occur. As a consequence of the large masses of the proton and antiproton and hence the large amount of energy available in the centre of mass—even at small values of P_{lab}—such annihilations typically produce many hadrons in the final state. However, detailed analysis of such many body final states is extremely difficult (both theoretically and experimentally) and hence although these channels are becoming a valuable source of information about the strong interaction, their analysis is dogged by model dependent assumptions. Occasionally, though, just two particles are formed and by studying such 2→2 reactions it is hoped that knowledge may be gleaned about the details of the annihilation process. In particular, one may hope to learn more about states which couple to the $\overline{N}N$ system, a system of great theoretical interest since, as well as the large number of standard quark model states expected to couple to $\overline{N}N$, other bound states outside of the conventional quark model multiplets, for example, $\overline{q}\overline{q}qq$ are expected to have strong couplings to $\overline{N}N$. A heuristic argument

as to why such states would have this property may be easily given in terms of quark-line diagrams. In Fig. 2.1 the quark lines are shown for two possible ways in which the reaction $\overline{N}N \rightarrow \overline{N}N$ may take place. In Fig. 2.1(a), a pair of quarks and a pair of antiquarks from the N and $\overline{N}$ respectively annihilate leaving an intermediate state with $\overline{q}q$ quantum numbers. This intermediate state then combines with two quark–anti-

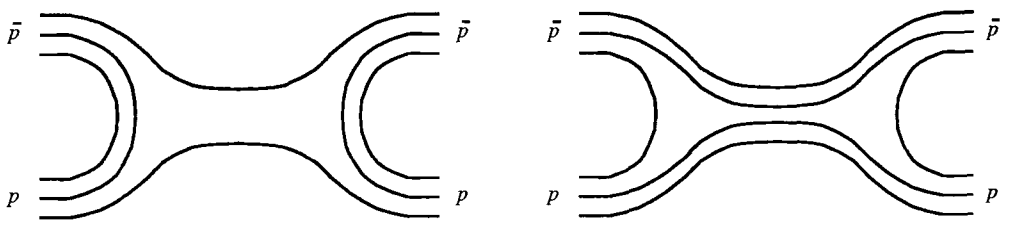

(a) (b)

Figure 2.1: Quark line diagrams for the reaction $\overline{N}N \rightarrow \overline{N}N$ showing contributions from (a) naive quark model $\overline{q}q$ intermediate states and (b) postulated $\overline{q}\overline{q}qq$ states.

quark pairs from the vacuum to produce the final state nucleon pair. In Fig. 2.1(b) a potentially more interesting scenario is depicted. A single quark and antiquark have annihilated, leaving as an intermediate state a $\overline{q}\overline{q}qq$ state. If such a state exists then it's coupling to $\overline{N}N$ could be expected to be higher than that for the simple quark model $\overline{q}q$ states since there is a much higher overlap between the four quark state and the $\overline{N}N$ system than between the $\overline{q}q$ state and the $\overline{N}N$ system as only a single $\overline{q}q$ annihilation is required to reach the four quark state. Indeed, naively, one would expect the rate for the reaction via the 4-quark state to be a factor of order $1/\alpha_s^2$ up on the rate for the reaction to go via a 2-quark state, all other things being equal. (Of course this is a hopelessly over-simplified view—the process being inherently non-perturbative makes such arguments in terms of the perturbative coupling α_s very dubious). These 2→2 reactions are amenable to more detailed analysis than is possible for more complicated final states, being characterised, at least in the case of spinless final state particles, by a single scattering angle in the centre of mass. At first sight, the ideal place to look

for evidence of states coupling to $\overline{N}N$ would be in the elastic and charge exchange channels, $\bar{p}p \rightarrow \bar{p}p$ and $\bar{p}p \rightarrow \bar{n}n$, channels on which large amounts of data have been taken. However, since the $\bar{p}p \rightarrow \bar{p}p$ and $\bar{p}p \rightarrow \bar{n}n$ involve spinning particles in the final state, a complete analysis of these channels would require the measurements of the polarisations of the final state particles as well as their angular distributions in order to determine the helicity amplitudes. Such measurements are not yet available and so an alternative channel in which to look for states coupling to $\overline{N}N$ must be found, preferably one with spinless particles in the final state. One such channel, amenable to amplitude analysis is $\bar{p}p \rightarrow \pi\pi$, the analysis of recent data on which is the subject of this thesis. That one would expect to see intermediate mesonic states in this channel is clear, the quark line diagram in Fig. 2.2(a) indicates one possible way in which such states may couple. In Fig. 2.2(b) a quark line diagram analogous to Fig. 2.1(b) is shown, indicating that, at least if their couplings to $\pi\pi$ are strong enough, it is possible that four-quark intermediate states may also be seen in this channel. A method, due

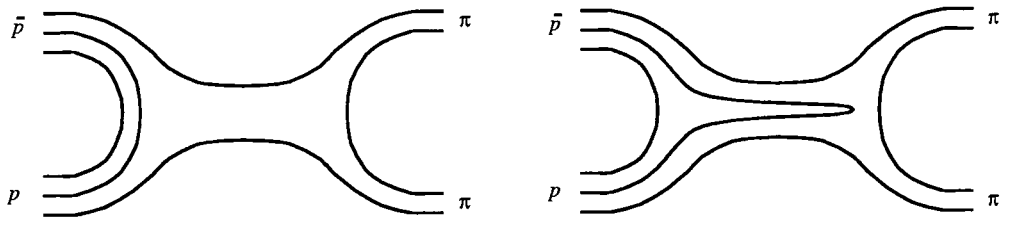

(a) (b)

Figure 2.2: Quark line diagrams for the reaction $\overline{N}N \rightarrow \pi\pi$ showing contributions from (a) naive quark model $\bar{q}q$ intermediate states and (b) postulated $\bar{q}\bar{q}qq$ states.

to Barrelet [26], for such a study and the results of its application to $\bar{p}p \rightarrow \pi\pi$ will be presented in the next chapter. (Other channels where amplitude analysis is potentially possible include $\bar{p}p \rightarrow \overline{K}K$ and $\bar{p}p \rightarrow \overline{\Lambda}\Lambda$. These channels will not be examined in detail here. The channel $\bar{p}p \rightarrow K^-K^+$ has also been measured recently by PS172 [27] but despite the kaons being spinless, the isospin composition of the final state

makes it necessary to measure eight observables in the four isospin related channels $\overline{p}p \rightarrow K^-K^+, \overline{p}p \rightarrow K_SK_S, \overline{p}p \rightarrow K_SK_L$ and $\overline{p}n \rightarrow K^-K^0$ before a complete analysis can be performed [28]. The reaction $\overline{p}p \rightarrow \overline{\Lambda}\Lambda$ has been measured by PS185 [29]. The final state, although containing spinning particles is "self-analysing" in the sense that the asymmetric decays of the Λ hyperons allow their polarisations to be deduced and hence sufficient measurements are possible for an amplitude analysis.)

Of all the hadronic two-body channels into which $\overline{p}p$ can annihilate, one in particular then stands out as especially worthy of close attention — the channel $\overline{p}p \rightarrow \pi\pi$, where the final state pair of pions may be charged $\pi^-\pi^+$, or neutral $\pi^0\pi^0$. This reaction is illustrated schematically in Fig. 2.3. The orbital angular momentum in the $\overline{p}p$ system is L while that in the $\pi\pi$ system is J. Parity conservation requires that, in this reaction, the $\overline{p}p$ annihilation takes place in a spin P-wave, thus $J = L \pm 1$. In Fig. 2.3 our

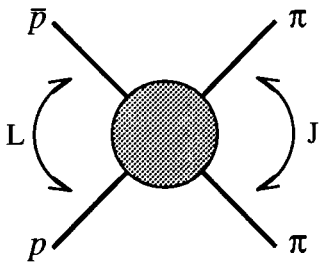

Figure 2.3: The reaction $\overline{p}p \rightarrow \pi\pi$.

ignorance of the way in which the proton and antiproton become a pair of pions, is indicated by depicting the process as a grey "blob". We can go a little further than this and identify some contributions to this "blob", e.g. in Fig. 2.4(a) a nucleon is exchanged in the t-channel. This contributes a pole in the amplitude for the process located at $t = m_N^2$. There will, of course, be a second pole at $u = m_N^2$ caused by the analogous exchange in the u-channel. In Fig. 2.4(b) the $\overline{p}p$ system has annihilated to form an unstable intermediate state, X, which then decays into a pair of pions. This will also contribute a pole in the amplitude, situated at $s = m_X^2 - im_X\Gamma_X$ where m_X

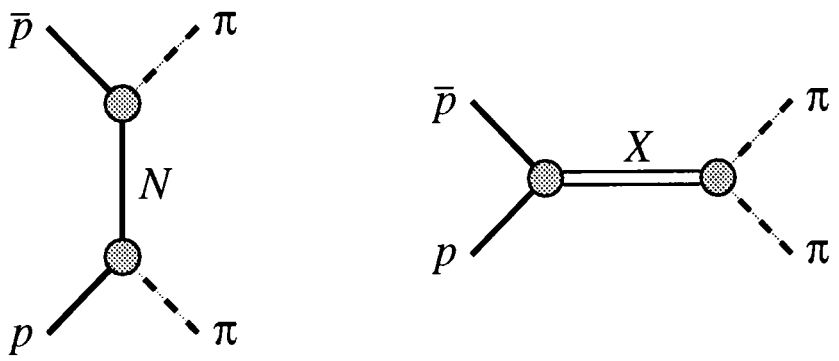

(a) (b)

Figure 2.4: Two contributions to the reaction $\bar{p}p \rightarrow \pi\pi$.

and Γ_X are the mass and width respectively of the state X. Both of these contributions will be examined in more detail later.

2.2 The Observables in $\bar{p}p \rightarrow \pi\pi$

In order to "define" the observables in the channel $\bar{p}p \rightarrow \pi\pi$, it is useful to consider an idealised experiment (Fig. 2.5). A beam of antiprotons of known energy is incident on a target of protons, which may be polarised either up or down (i.e. in or out of the plane of Fig. 2.5 respectively). The reaction is shown in the c.m. frame in Fig. 2.6 where θ the c.m. scattering angle is defined as the angle between the initial $\bar{p}$ direction and the final π^- direction. Note that in the absence of any polarisation of the nucleons, the π^- is equally likely to emerge, at a given angle θ to the $\bar{p}$-direction, either to the left or right of the beam direction (indicated by L and R in Fig. 2.6). Considering first the charged channel, the differential cross section, $d\sigma^c/d\Omega$ is, given perfect detectors, just proportional to the number of π^- seen at a given angle, $N(\theta)$, which will be equal to $N(-\theta)$. If the target proton is polarised, however, this symmetry is no longer necessarily true, and the numbers of π^-'s emerging to the left and right of the beam direction at an angle θ (i.e. at θ and $-\theta$) may be different, so that in general, using the

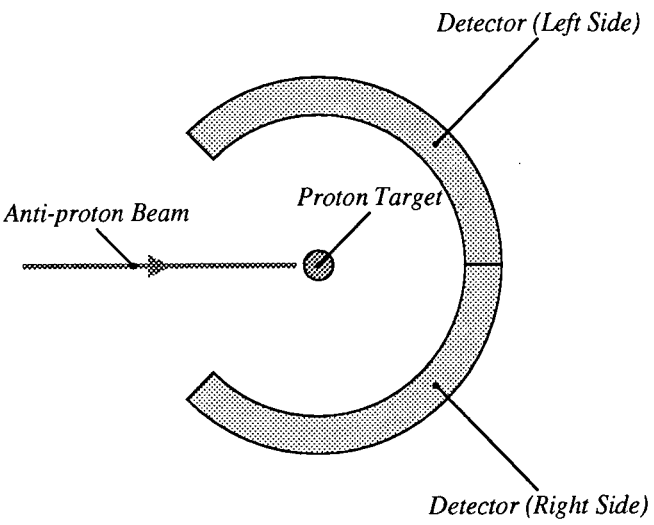

Figure 2.5: An idealised $\overline{p}p \rightarrow \pi\pi$ experimental setup. The proton target is polarisable in the up and down directions (i.e. in or out of the plane of the figure).

subscripts L and R to indicate the left and right sides of the detector, $N_L(\theta) \neq N_R(\theta)$. A measure of this difference is provided by the asymmetry parameter P ($\equiv A_{0n}$), which, following common usage, will be referred to here as the polarisation. This is defined (for a perfect detector) as

$$\begin{aligned} P_c &= \frac{N_L^{\Uparrow}(\theta) - N_R^{\Uparrow}(\theta)}{N_L^{\Uparrow}(\theta) + N_R^{\Uparrow}(\theta)} \\ &= \frac{N_R^{\Downarrow}(\theta) - N_L^{\Downarrow}(\theta)}{N_R^{\Downarrow}(\theta) + N_L^{\Downarrow}(\theta)}, \end{aligned} \tag{2.1}$$

where the arrow indicates the direction of the target proton spin and the second equality follows from considering the apparatus rotated through 180° around the beam axis. In actual fact these relations are *not* used to determine the experimental value of P_c. This is because the use of the Eq. (2.1) for P_c requires the comparison of measurements taken in different halves of the detector, which in a real experiment will have differing

acceptances. Much better is to use

$$\begin{aligned} P_c &= \frac{N_L^{\Uparrow}(\theta) - N_L^{\Downarrow}(\theta)}{N_L^{\Uparrow}(\theta) + N_L^{\Downarrow}(\theta)} \\ &= \frac{N_R^{\Downarrow}(\theta) - N_R^{\Uparrow}(\theta)}{N_R^{\Downarrow}(\theta) + N_R^{\Uparrow}(\theta)}, \end{aligned} \tag{2.2}$$

where only measurements taken in the same half of the detector are compared.

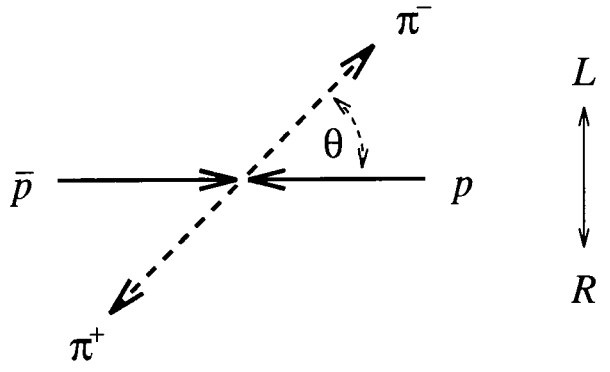

Figure 2.6: The process $\bar{p}p \rightarrow \pi^-\pi^+$ in the centre of mass frame.

These observables may be written as Legendre series :—

$$\frac{d\sigma^c}{d\Omega} = \sum_{i=0}^{2N} a_i P_i(z) \tag{2.3}$$

$$P_c \frac{d\sigma^c}{d\Omega} = \sum_{i=1}^{2N} b_i P_i^1(z) \tag{2.4}$$

where the order $2N$ at which the series may be truncated increases with increasing P_{lab}, from 0 at threshold where the reaction must be isotropic to ~ 10 at $P_{lab} \simeq 2.0$ GeV/c . Above this energy even higher moments will become appreciably non-zero. The $P_i(z)$ ($z = \cos\theta$) are the Legendre polynomials and the $P_i^1(z)$ are the associated Legendre functions with $m = 1$ satisfying $P_i^1(z) = \sqrt{1-z^2}P_i'(z)$ where the $\sqrt{1-z^2}(= \sin\theta)$

ensures that the series representation of $P_c d\sigma^c/d\Omega$ vanishes at $z = \pm 1$.

The neutral channel observables are defined similarly but the presence of identical particles in the final state leads to the observables being symmetric in $\cos(\theta)$. Hence in the Legendre series, only even terms contribute i.e.

$$\frac{d\sigma^n}{d\Omega} = \sum_{i=0}^{N'} c_{2i} P_{2i}(z) \tag{2.5}$$

where the series for $P_n d\sigma^n/d\Omega$ is omitted since the neutral channel polarised cross-sections are not measured.

In place of the observables $d\sigma/d\Omega$ and P, it is useful to consider two combinations of these, the transversity cross sections $(1 \pm P)d\sigma/d\Omega$. These are then given as the squared modulae of the transversity amplitudes, $T^{\pm}_{c,n}$ thus:—

$$(1 \pm P_{c,n}(z)) \frac{d\sigma^{c,n}(z)}{d\Omega} = \left| T^{\pm}_{c,n}(z) \right|^2 , \tag{2.6}$$

where the transversity amplitudes are related to the more familiar helicity flip and non-flip amplitudes, $F_{+\pm}$, by

$$T^{\pm} = \frac{1}{\sqrt{2}} (F_{++} \pm i F_{+-}) . \tag{2.7}$$

Assuming exact isospin invariance implies that the neutral channel amplitude, T_n, may be expressed simply in terms of T_c. The isospin decomposition of the channel is:

$$\begin{aligned} T^{\pm}_c(z) &= \frac{1}{\sqrt{6}} T^{\pm}_0(z) + \frac{1}{2} T^{\pm}_1(z) \\ T^{\pm}_n(z) &= \frac{1}{\sqrt{6}} T^{\pm}_0(z) \end{aligned} \tag{2.8}$$

where the isospin 0 and 1 amplitudes $T^{\pm}_0(z)$ and $T^{\pm}_1(z)$ have the following symmetries

under $z \mapsto -z$:

$$\begin{aligned} T_0^{\pm}(-z) &= T_0^{\mp}(z) \\ T_1^{\pm}(-z) &= -T_1^{\mp}(z) \end{aligned} \tag{2.9}$$

This implies the simple relation

$$T_n^{\pm}(z) = \frac{1}{2}\left[T_c^{\pm}(z) + T_c^{\mp}(-z)\right], \tag{2.10}$$

between the neutral and charged channel amplitudes.

2.3 The Data

The channels $\pi^-\pi^+$ and $\pi^0\pi^0$ have been measured by several collaborations in the region $P_{lab} \leq 2.5$ GeV/c [30, 31, 32, 33, 27]. A summary of available data on angular distributions for $\overline{p}p \to \pi\pi$ is given in Fig. 2.7 showing the values of lab. momentum P_{lab} at which the different experimental collaborations have taken data. The PS172 data have by far the largest statistiics and hence form the basis for the analysis of which this thesis is an account. Before using the PS172 data in conjunction with older datasets on $\overline{p}p \to \pi^-\pi^+$ and $\overline{p}p \to \pi^0\pi^0$, it is essential to check that they are in fact compatible. In the next section, a model-independent test of the compatibility of PS172 results with those taken on the neutral channel will be derived and applied. In this section the older charged channel data are, where possible, directly compared with the PS172 measurements in order to check their compatibility. Turning first to the charged channel differential cross-section, data on which have been taken by Tanimori *et al.* [33] and Eisenhandler *et al.* [30]. In Figs. 2.8–2.10 the Tanimori *et al.* [33] results on the folded differential cross section $d\sigma_c(z)/d\Omega + d\sigma_c(-z)/d\Omega$ are compared with the PS172 results, appropriately folded, taken at nearby values of P_{lab}. The agreement between these data is, on the whole quite good, especially considering

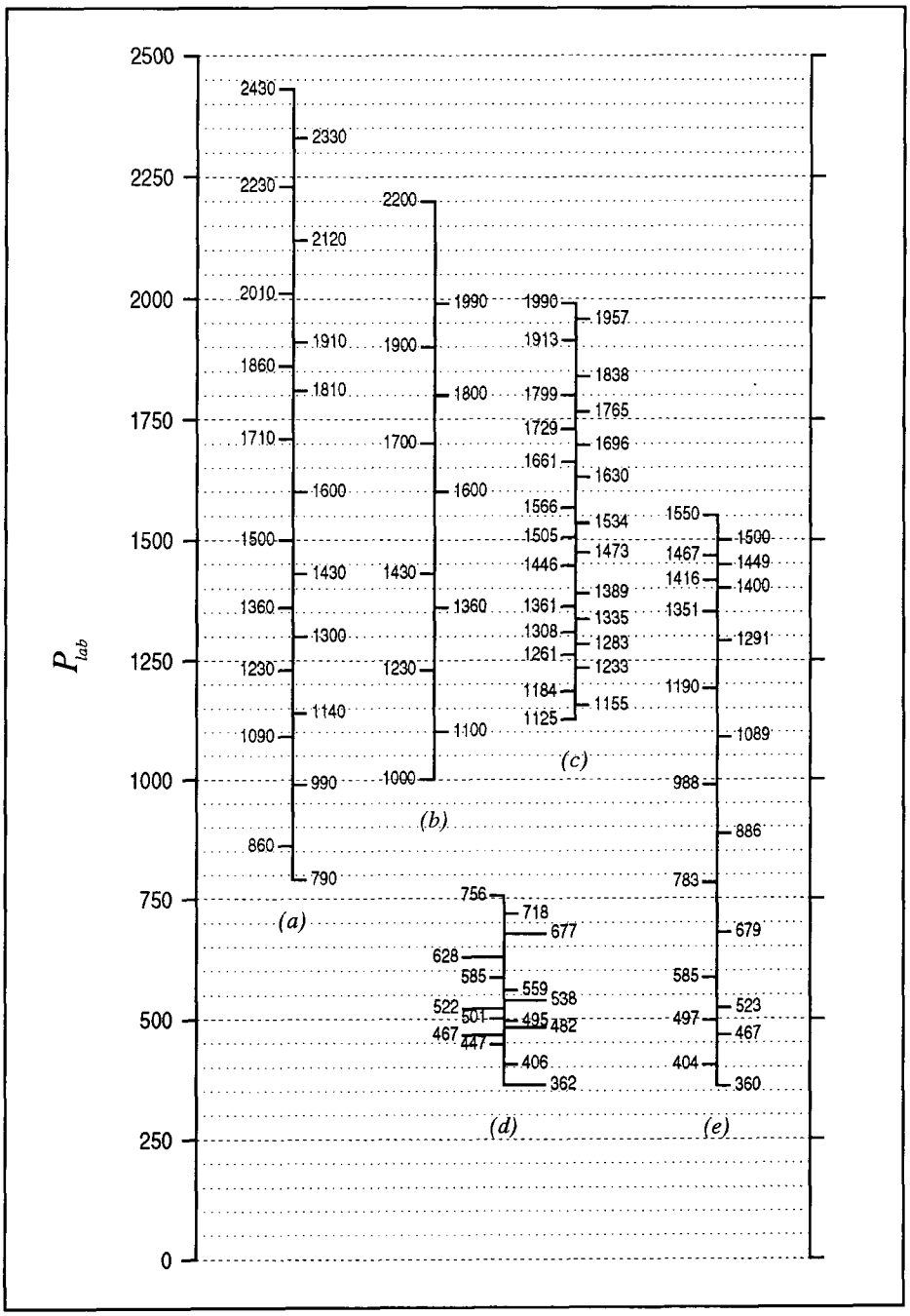

	Channel	Observable(s)	Reference
(a)	$\pi^-\pi^+$	$d\sigma^c/d\Omega$	Eisenhandler *et al.* [30]
(b)	$\pi^-\pi^+$	P_c (, $d\sigma^c/d\Omega$)	Carter *et al.* [31]
(c)	$\pi^0\pi^0$	$d\sigma^n/d\Omega$	Dulude *et al.* [32]
(d)	$\pi^-\pi^+$	$d\sigma^c(z)/d\Omega + d\sigma^c(-z)/d\Omega$	Tanimori *et al.* [33]
(e)	$\pi^-\pi^+$	P_c, $d\sigma^c/d\Omega$	Hasan *et al.* [27]

Figure 2.7: Summary of available data on $\overline{p}p \rightarrow \pi\pi$.

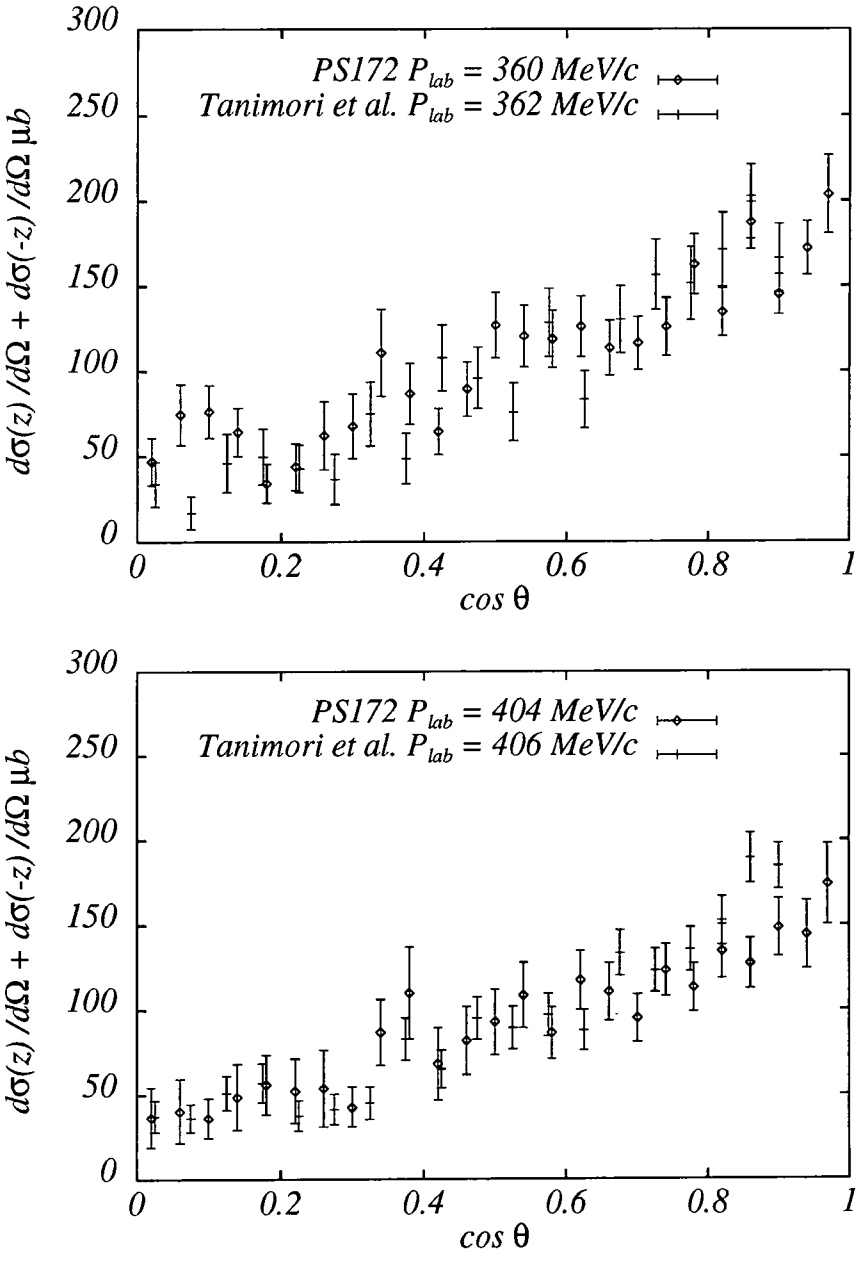

Figure 2.8: A comparison of folded $d\sigma^c/d\Omega$ derived from the measurements of PS172 [27] and Tanimori *et al.* measurements taken at nearby energies.

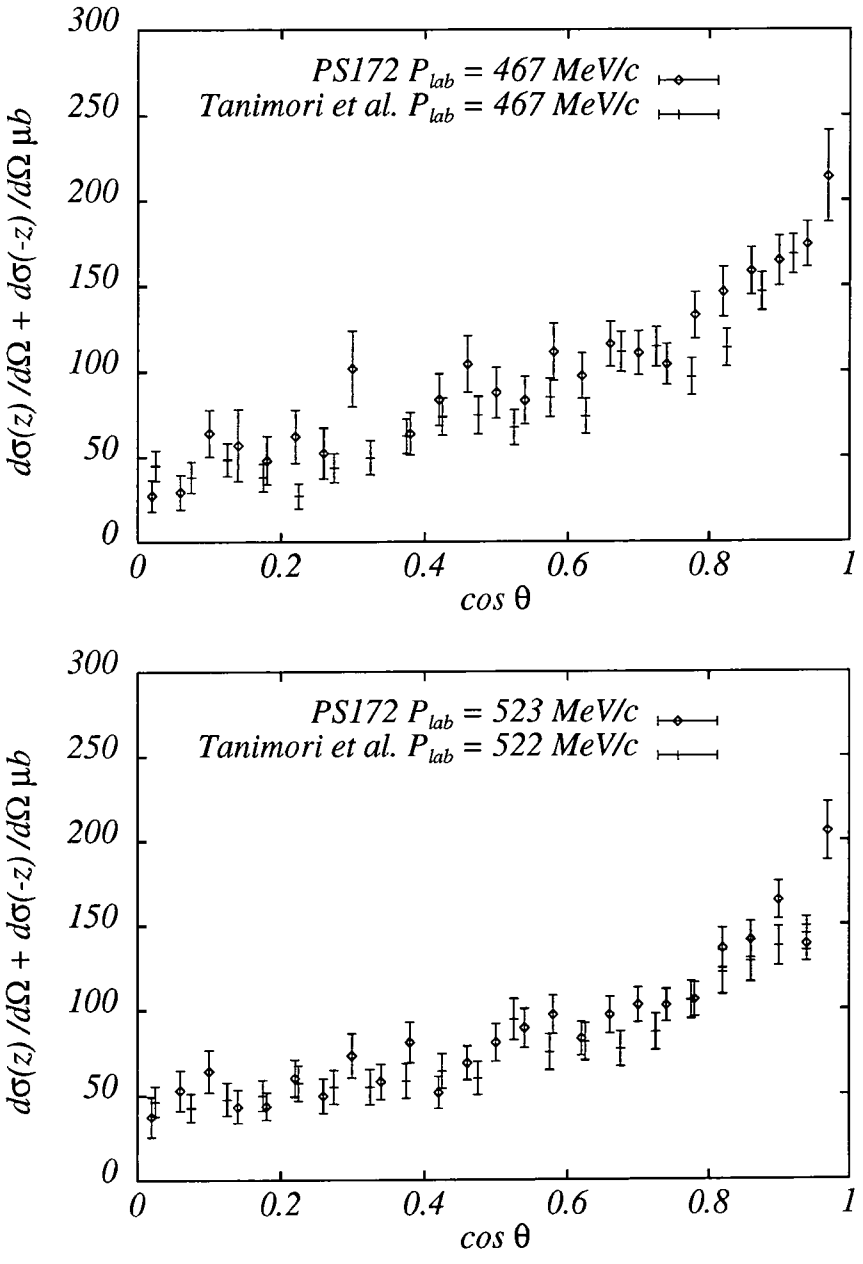

Figure 2.9: A comparison of folded $d\sigma^c/d\Omega$ derived from the measurements of PS172 [27] and Tanimori *et al.* measurements taken at nearby energies.

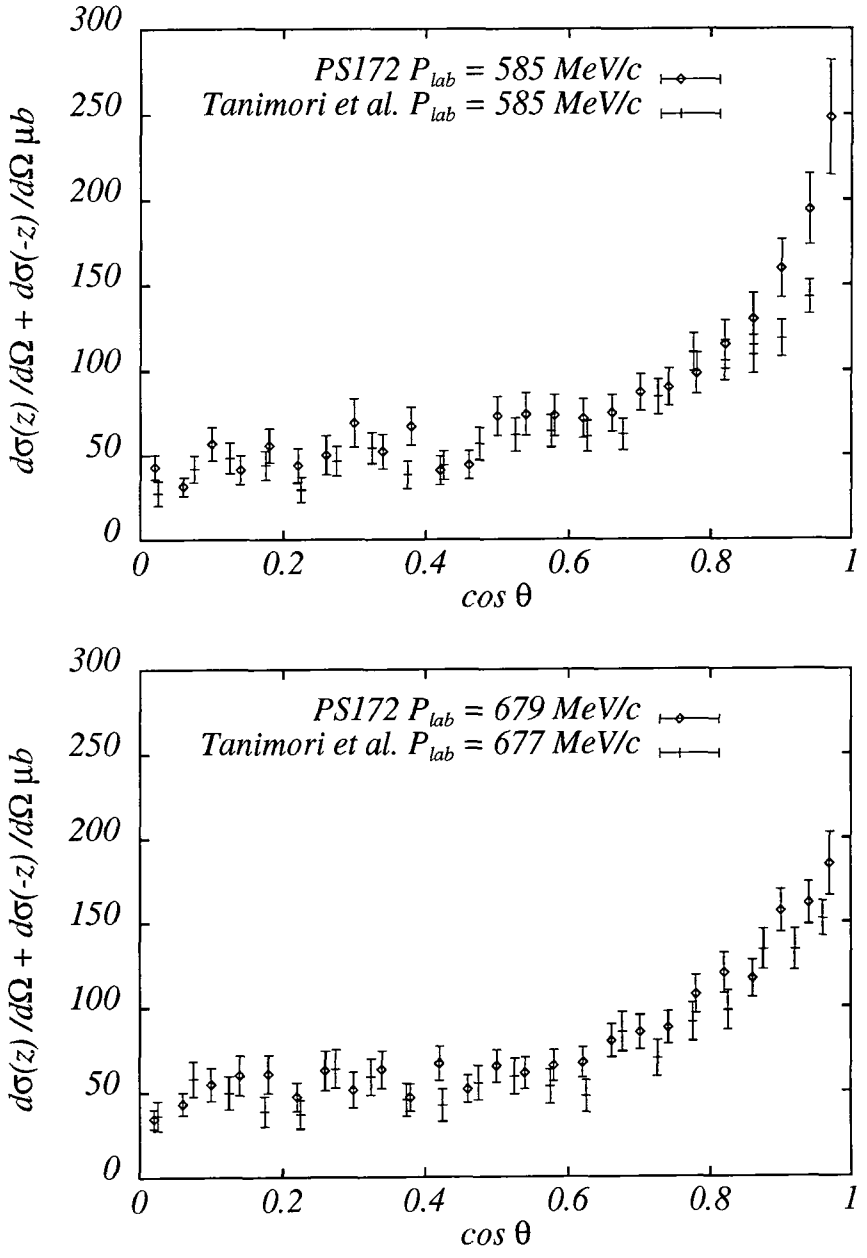

Figure 2.10: A comparison of folded $d\sigma^c/d\Omega$ derived from the measurements of PS172 [27] and Tanimori *et al.* measurements taken at nearby energies.

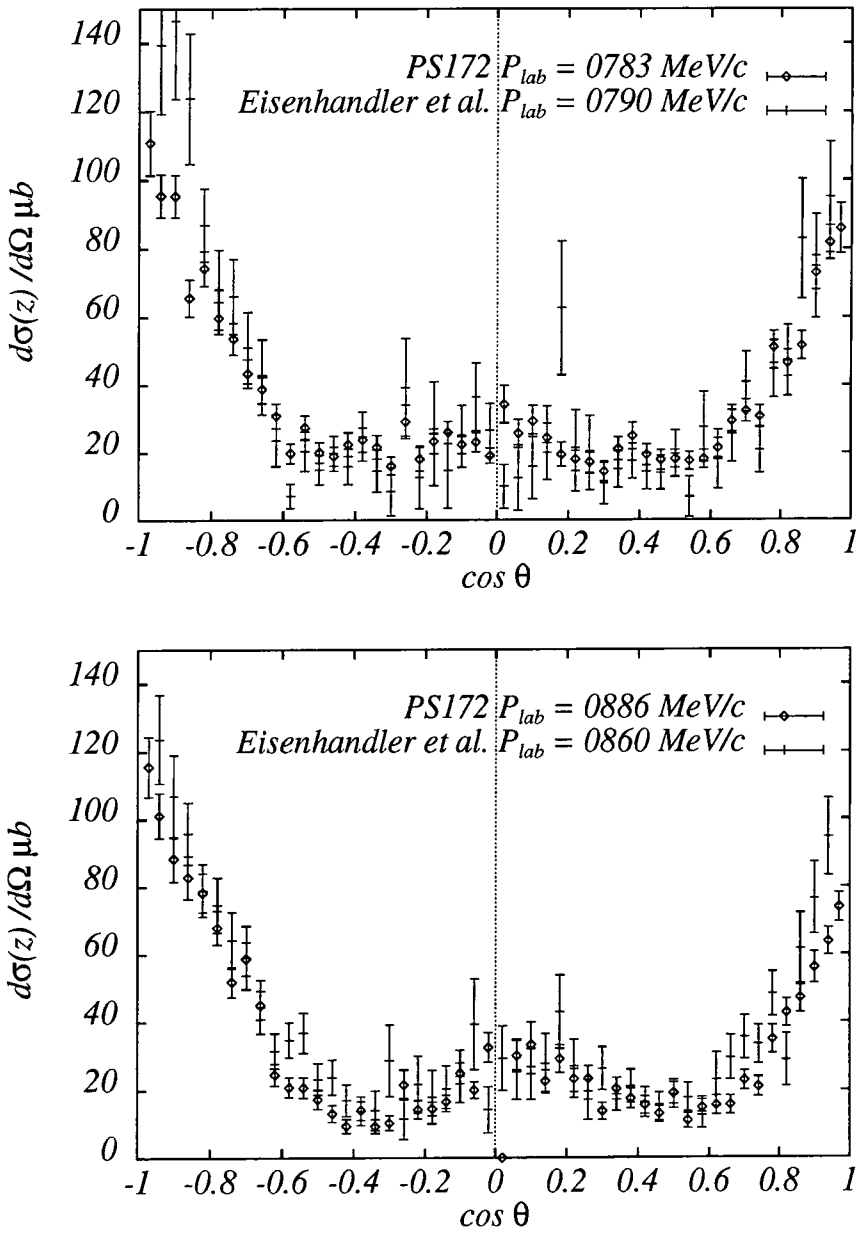

Figure 2.11: A comparison of $d\sigma^c/d\Omega$ data taken by PS172 and Eisenhandler at nearby energies

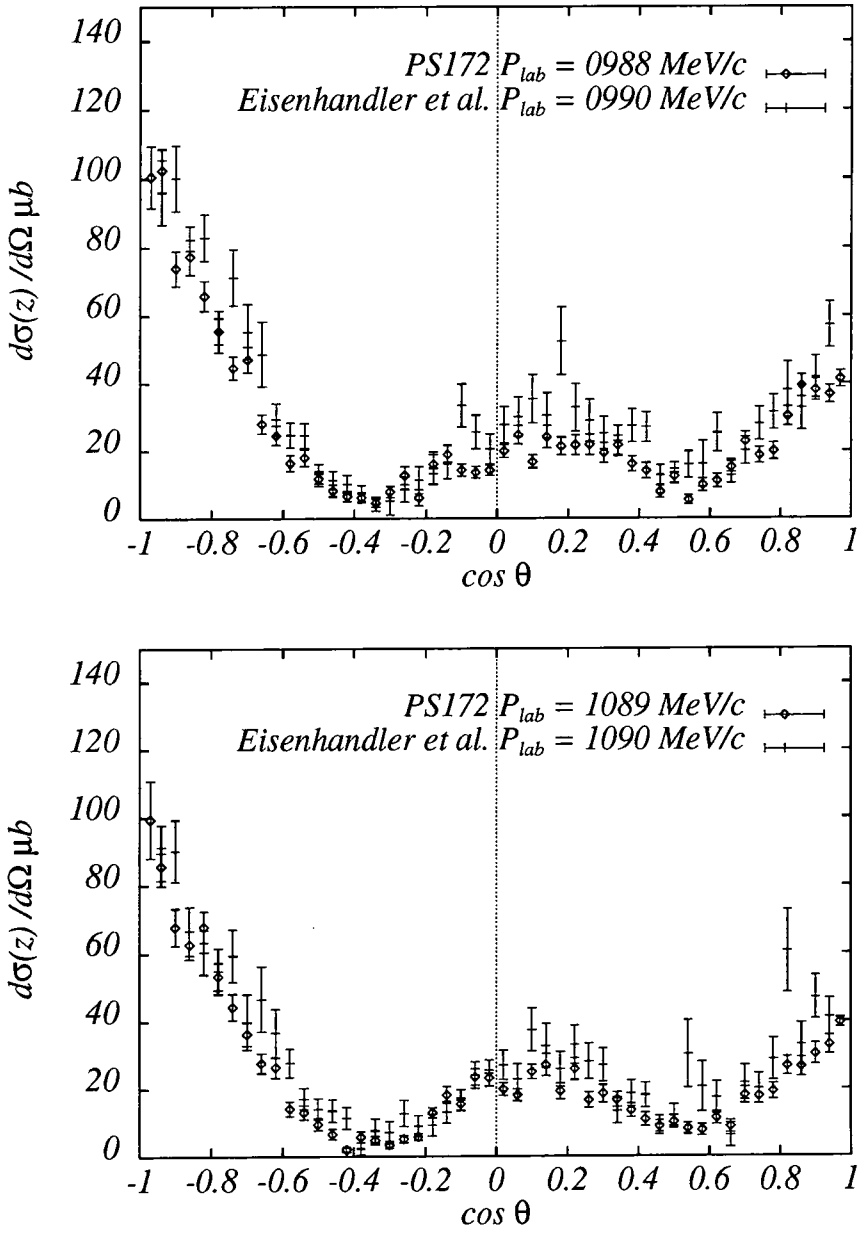

Figure 2.12: A comparison of PS172 and Eisenhandler at nearby energies

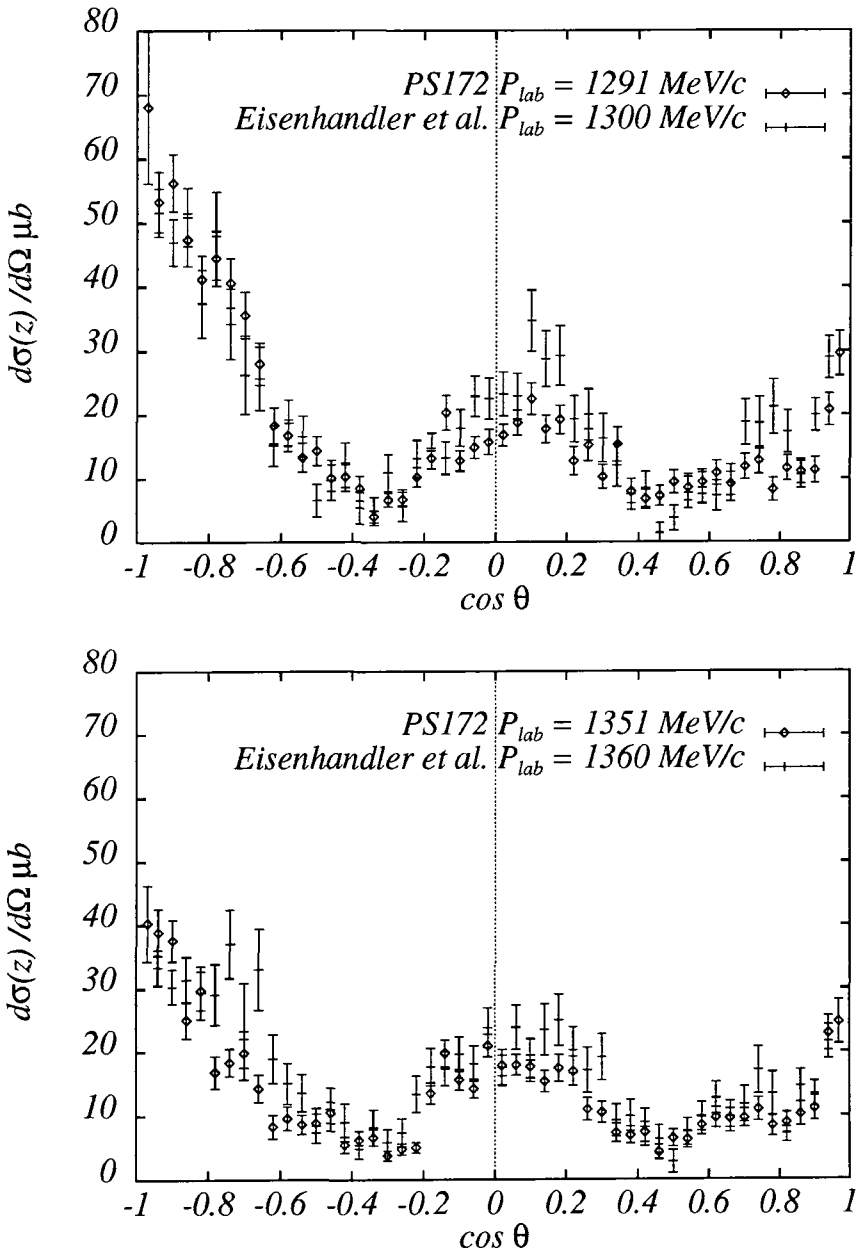

Figure 2.13: A comparison of $d\sigma^c/d\Omega$ data taken by PS172 and Eisenhandler at nearby energies

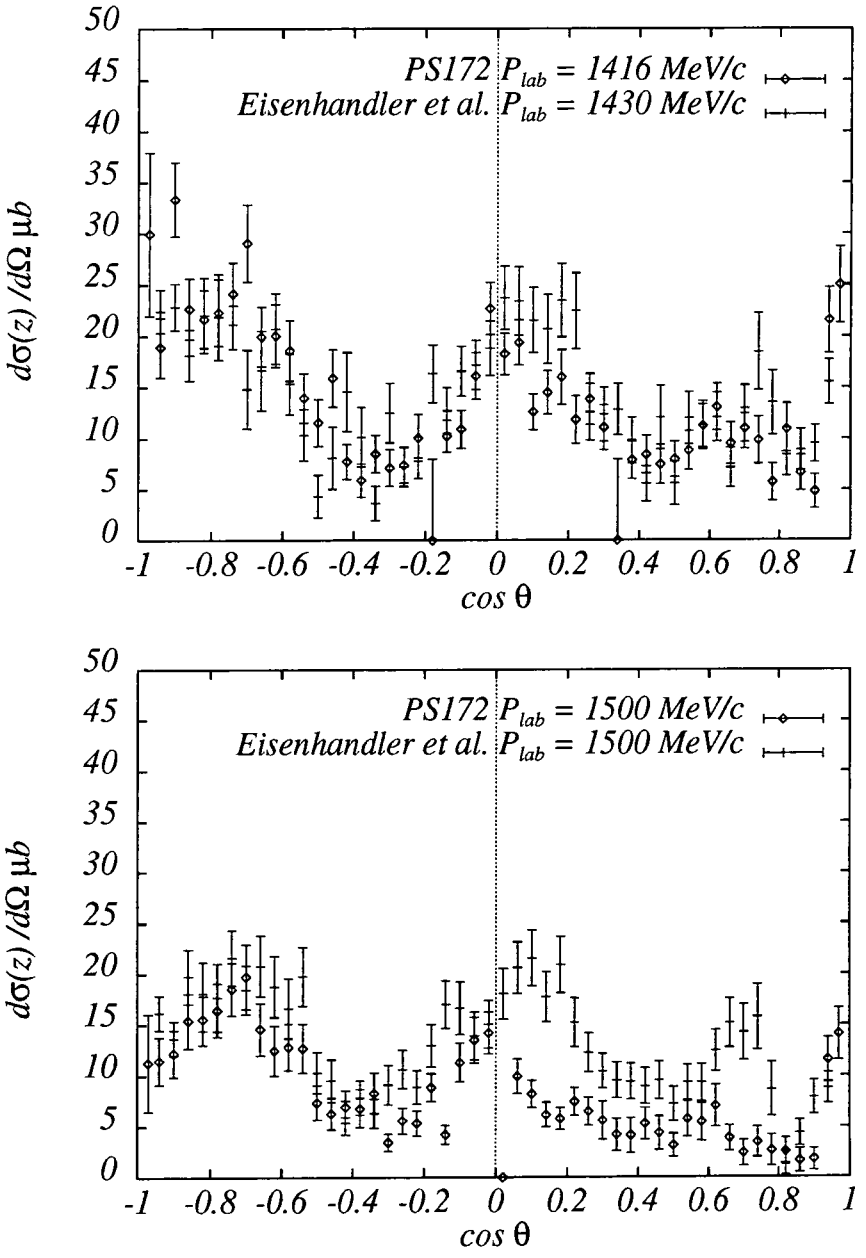

Figure 2.14: A comparison of $d\sigma^c/d\Omega$ data taken by PS172 and Eisenhandler at nearby energies

that the two data-sets have been taken at slightly different values of P_{lab}. The possible exception to this being the region near to $\cos\theta = 1$ at $P_{lab} = 0.585$ GeV/c where the PS172 data points are noticably higher than the corresponding Tanimori *et al.* points. It is, however, hard to evaluate this since the two sets of data are taken on differing $\cos\theta$ grids making it impossible to form a measure such as χ^2 which could be used to quantify their compatibility.

In Figs. 2.11–2.14 the Eisenhandler *et al.* [30] data on $d\sigma^c/d\Omega$ are compared with the results from PS172 [27] at nearby values of P_{lab}. Again the agreement is on the whole good, except perhaps for $P_{lab} = 1.500$ GeV/c where the PS172 points are consistently above the Eisenhandler *et al.* results by more than would be expected given the errors on the data. These datasets *are* taken on the same $\cos\theta$ grid (with the exception of two extra $\cos\theta$ points at ± 0.97 in the PS172 dataset which do not appear in the Eisenhandler *et al.* measurements). This allows the differences between the datasets to be quantified and indeed, the *by eye* comparison is borne out by the values of the χ^2 per degree of freedom between the two datasets which is defined as

$$\chi^2_{dof} = \frac{1}{N_{\rm dof}} \sum_i \frac{(d\sigma^{\rm Eis}(z_i)/d\Omega - d\sigma^{\rm PS172}(z_i)/d\Omega)^2}{\Delta(d\sigma^{\rm Eis}(z_i)/d\Omega)^2 + \Delta(d\sigma^{\rm PS172}(z_i)/d\Omega)^2} \tag{2.11}$$

where the sum runs over all points which have common values of $z(=\cos\theta)$ in both datasets, $\Delta(X)$ denotes the error on X and $N_{\rm dof}$ is the number of degrees of freedom (taken here to be the number of terms in the sum). The χ^2_{dof} between the PS172 and Eisenhandler *et al.* measurements in Figs. 2.11–2.14 are given in Table 2.1, the value of $\chi^2 = 5.28$ at $P_{lab} = 1.500$ GeV/c being considerably higher than the χ^2 values at other P_{lab} points despite the two datasets being taken at precisely the *same* value of P_{lab} there, as opposed to merely "nearby" values at all the other P_{lab}'s compared.

There are also measurements of P_c taken prior to PS172 by Carter *et al.* [31]. Again there are a convenient set of nearby values of P_{lab} at which the data-sets may be compared although, like the folded $d\sigma^c/d\Omega$ data of Tanimori *et al.* , the Carter *et al.* data is taken on a different $\cos\theta$ grid to the PS172 data, preventing their numerical

P_{lab}^{PS172} (MeV/c)	P_{lab}^{Eis} (MeV/c)	χ^2_{dof}
783	790	1.42
886	860	1.70
988	990	2.47
1089	1090	2.01
1291	1300	1.96
1351	1360	1.85
1416	1430	1.90
1500	1500	5.28

Table 2.1: χ^2 per degree of freedom between datasets on $d\sigma^c/d\Omega$ due to PS172 [27] and Eisenhandler *et al.* [30].

comparison in terms of χ^2. Again agreement is good although the Carter *et al.* data have considerably larger errors than the corresponding PS172 data. The polarisation measurements are compared at two representative energies in Fig. 2.15

2.4 Constraints on $\overline{p}p \longrightarrow \pi^0\pi^0$ From PS172 Measurements of $\overline{p}p \longrightarrow \pi^-\pi^+$

As a consequence of Eqs. (2.8), (2.9) and (2.10), it is possible to construct bounds on the neutral channel observables given only those for the charged channel [34]. These are most easily derived by introducing the new variable $\omega = e^{i\theta}$, with the physical values of ω being those with $|\omega| = 1$. Then, $T^+(z)$ and $T^-(z)$ are the boundary values of a single analytic function $T(\omega)$ with $T^+(z)$ being $T(e^{-i\theta})$ and $T^-(z)$ being $T(e^{i\theta})$, $\theta \in [0, 2\pi]$ (see Fig. 2.16). In terms of $T(\omega)$ Eq. (2.10) becomes

$$T_n(\omega) = \frac{1}{2}\left[T_c(\omega) + T_c(-\omega)\right], \tag{2.12}$$

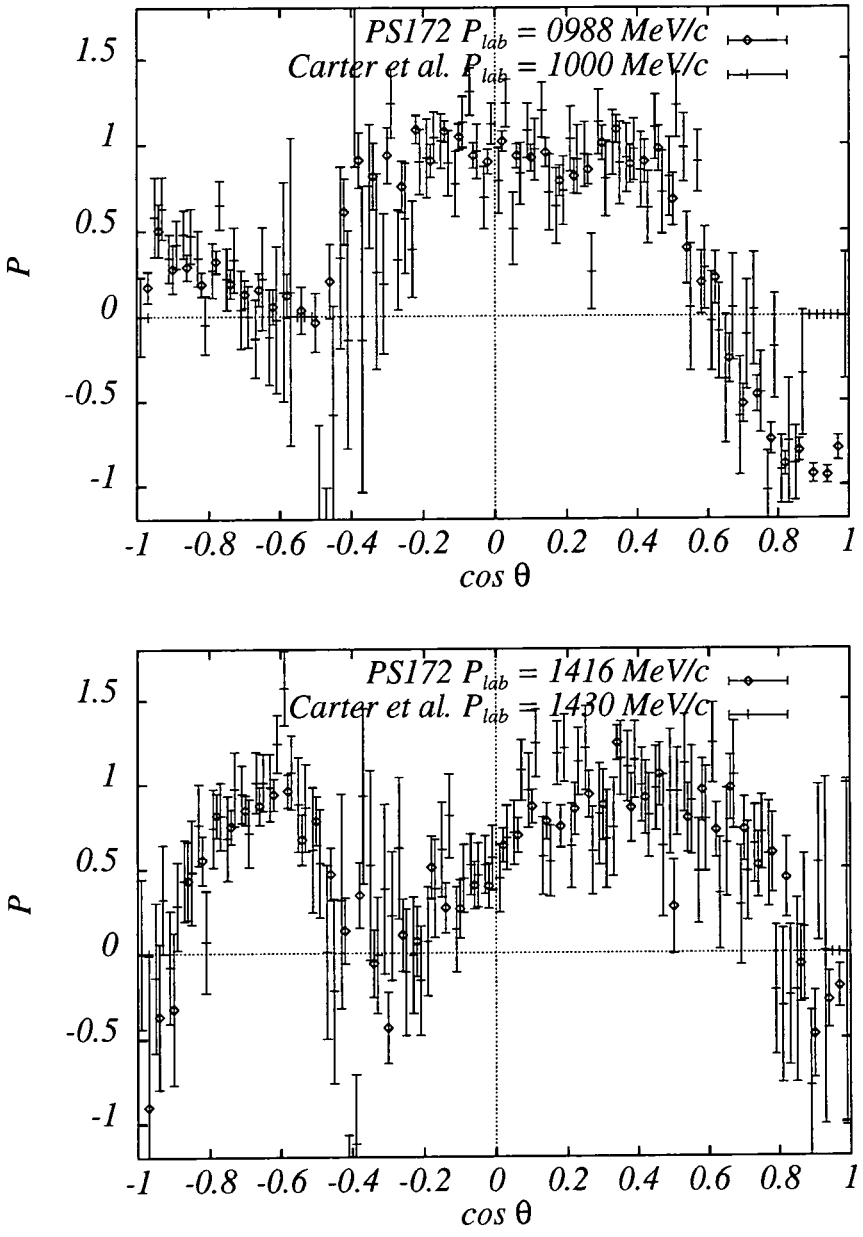

Figure 2.15: A comparison of measurements of P_c taken by Carter *et al.* [31] and PS172 [27] at nearby values of P_{lab}.

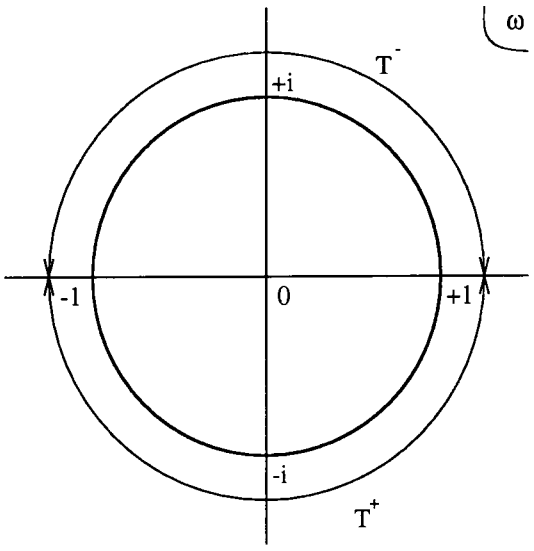

Figure 2.16: The complex ω-plane showing the unit circle, and regions of definition of definition of T^+ and T^- on the unit circle.

and hence,

$$|T_n(\omega)|^2 = \frac{1}{4}\left[|T_c(\omega)|^2 + |T_c(-\omega)|^2 + 2\Re\{T_c(\omega)T_c^*(-\omega)\}\right], \tag{2.13}$$

where $\Re\{A\}$ denotes the real part of A. Now, although the interference term $2\Re\{T_c(\omega)$ $T_c^*(-\omega)\}$, cannot be determined from the charged channel data alone, we may place bounds on it as a consequence of the Schwarz inequality,

$$-|T_c(\omega)|\,|T_c^*(-\omega)| \leq \Re\{T_c(\omega)T_c^*(-\omega)\} \leq |T_c(\omega)|\,|T_c^*(-\omega)| \tag{2.14}$$

So, Eq. (2.13) along with Eq. (2.14) imply that

$$|T_n(\omega)|^2 \leq \frac{1}{4}\left[|T_c(\omega)|^2 + |T_c(-\omega)|^2\right] + \frac{1}{2}|T_c(\omega)|\,|T_c(-\omega)| \tag{2.15}$$

and,

$$|T_n(\omega)|^2 \geq \frac{1}{4}\left[|T_c(\omega)|^2 + |T_c(-\omega)|^2\right] - \frac{1}{2}|T_c(\omega)|\,|T_c(-\omega)| \tag{2.16}$$

Where the right hand sides of Eqs. (2.15) and (2.16) involve only the charged channel observables. These constraints on $(1 \pm P_n)d\sigma^n/d\Omega$ imply separate constraints on $d\sigma^n/d\Omega$ and $P_n d\sigma^n/d\Omega$, thus

$$\begin{aligned}\frac{d\sigma^n(z)}{d\Omega} \leq \frac{1}{4}\Bigg[&\frac{d\sigma^c(z)}{d\Omega} + \frac{d\sigma^c(-z)}{d\Omega} \\ &+\sqrt{(1+P_c(z))\frac{d\sigma^c(z)}{d\Omega}}\sqrt{(1-P_c(-z))\frac{d\sigma^c(-z)}{d\Omega}} \\ &+\sqrt{(1-P_c(z))\frac{d\sigma^c(z)}{d\Omega}}\sqrt{(1+P_c(-z))\frac{d\sigma^c(-z)}{d\Omega}}\Bigg],\end{aligned} \tag{2.17}$$

$$\begin{aligned}\frac{d\sigma^n(z)}{d\Omega} \geq \frac{1}{4}\Bigg[&\frac{d\sigma^c(z)}{d\Omega} + \frac{d\sigma^c(-z)}{d\Omega} \\ &-\sqrt{(1+P_c(z))\frac{d\sigma^c(z)}{d\Omega}}\sqrt{(1-P_c(-z))\frac{d\sigma^c(-z)}{d\Omega}} \\ &-\sqrt{(1-P_c(z))\frac{d\sigma^c(z)}{d\Omega}}\sqrt{(1+P_c(z))\frac{d\sigma^c(-z)}{d\Omega}}\Bigg],\end{aligned} \tag{2.18}$$

$$\begin{aligned}P_n(z)\frac{d\sigma^n(z)}{d\Omega} \leq \frac{1}{4}\Bigg[&P_c(z)\frac{d\sigma^c(z)}{d\Omega} + P_c(-z)\frac{d\sigma^c(-z)}{d\Omega} \\ &+\sqrt{(1+P_c(z))\frac{d\sigma^c(z)}{d\Omega}}\sqrt{(1-P_c(-z))\frac{d\sigma^c(-z)}{d\Omega}} \\ &-\sqrt{(1-P_c(z))\frac{d\sigma^c(z)}{d\Omega}}\sqrt{(1+P_c(-z))\frac{d\sigma^c(-z)}{d\Omega}}\Bigg]\end{aligned} \tag{2.19}$$

and,

$$P_n(z)\frac{d\sigma^n(z)}{d\Omega} \geq \frac{1}{4}\left[P_c(z)\frac{d\sigma^c(z)}{d\Omega} + P_c(-z)\frac{d\sigma^c(-z)}{d\Omega}\right.$$

$$-\sqrt{(1+P_c(z))\frac{d\sigma^c(z)}{d\Omega}}\sqrt{(1-P_c(-z))\frac{d\sigma^c(-z)}{d\Omega}}$$
$$+\sqrt{(1-P_c(z))\frac{d\sigma^c(z)}{d\Omega}}\sqrt{(1+P_c(-z))\frac{d\sigma^c(-z)}{d\Omega}}\Bigg], \quad (2.20)$$

which may be compared with measurements taken. In fact, only the first two relationships, Eqs. (2.17) and, (2.18) are useful since, as was noted earlier, the polarised cross-section in the neutral channel is not measured.

Of course, direct comparison of the PS172 and Dulude *et al.* datasets using Eqs. (2.17) and (2.18) is not possible since they are not taken at identical values of P_{lab}, so in order to ascertain their consistency one could either compare the bounds with the neutral cross-section at nearby values of P_{lab} (the approach taken earlier when comparing datasets on $\overline{p}p \rightarrow \pi^-\pi^+$), or interpolate one of the datasets to values of P_{lab} at which measurements were taken in the other dataset and then compare. Since, eventually, the aim is to perform a fit simultaneously to both datasets, it is most convenient to choose the latter option. Also, as there are three observables to fit to, two of which already exist at identical values of P_{lab} ($d\sigma^c/d\Omega$ and P_c are both measured by PS172 at common momenta) it seems most sensible to interpolate the $d\sigma^n/d\Omega$ data of Dulude *et al.* to those values of P_{lab} at which PS172 have measured $d\sigma^c/d\Omega$ and P_c. This is achieved in practice by interpolating the neutral channel Legendre moments $\{c_i\}$ and reconstructing $d\sigma^n/d\Omega$ from these. For this purpose, the interpolated moments used by (A.D.) Martin and Pennington in their amplitude analysis [34] of the Eisenhandler *et al.* data on $\overline{p}p \rightarrow \pi^-\pi^+$ have been used, re-interpolated to the PS172 lab. momenta. In Figs. 2.17–2.21 these interpolated $\overline{p}p \rightarrow \pi^0\pi^0$ cross-sections are compared with the bounds of Eqs. (2.17) and (2.18). It is seen that these bounds, though not very tight, do at least constrain the position of the deep dip in the neutral cross section to be around $\cos\theta \simeq 0.5$, the position at which it is observed in the data. Indeed, the data are seen to fall within the bounds within errors throughout the P_{lab} range, except perhaps for the region near $\cos\theta \simeq 0.5$ at $P_{lab} = 1.089$ GeV (Fig. 2.17) where the

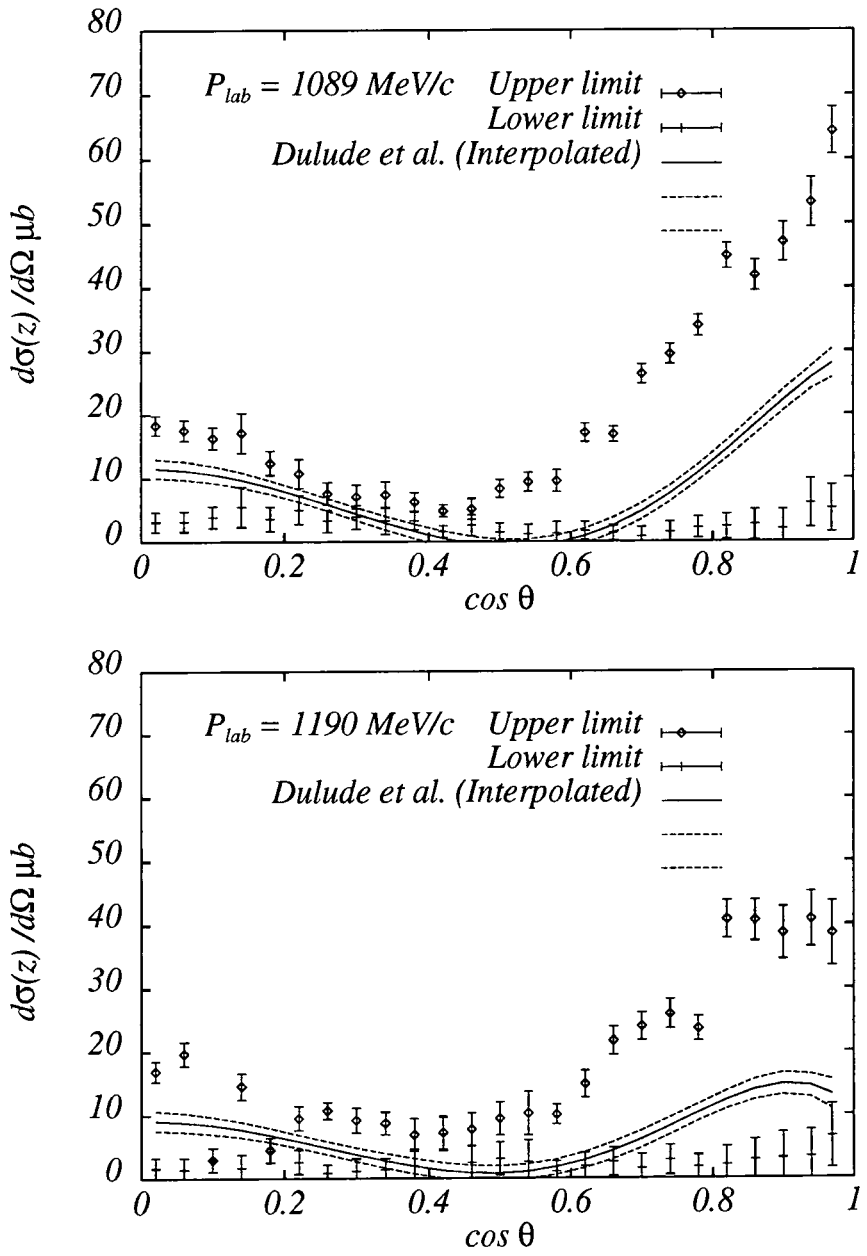

Figure 2.17: Bounds on $d\sigma^n/d\Omega$ derived from PS172 data on $d\sigma^c/d\Omega$ compared with the measurements of Dulude *et al.* .

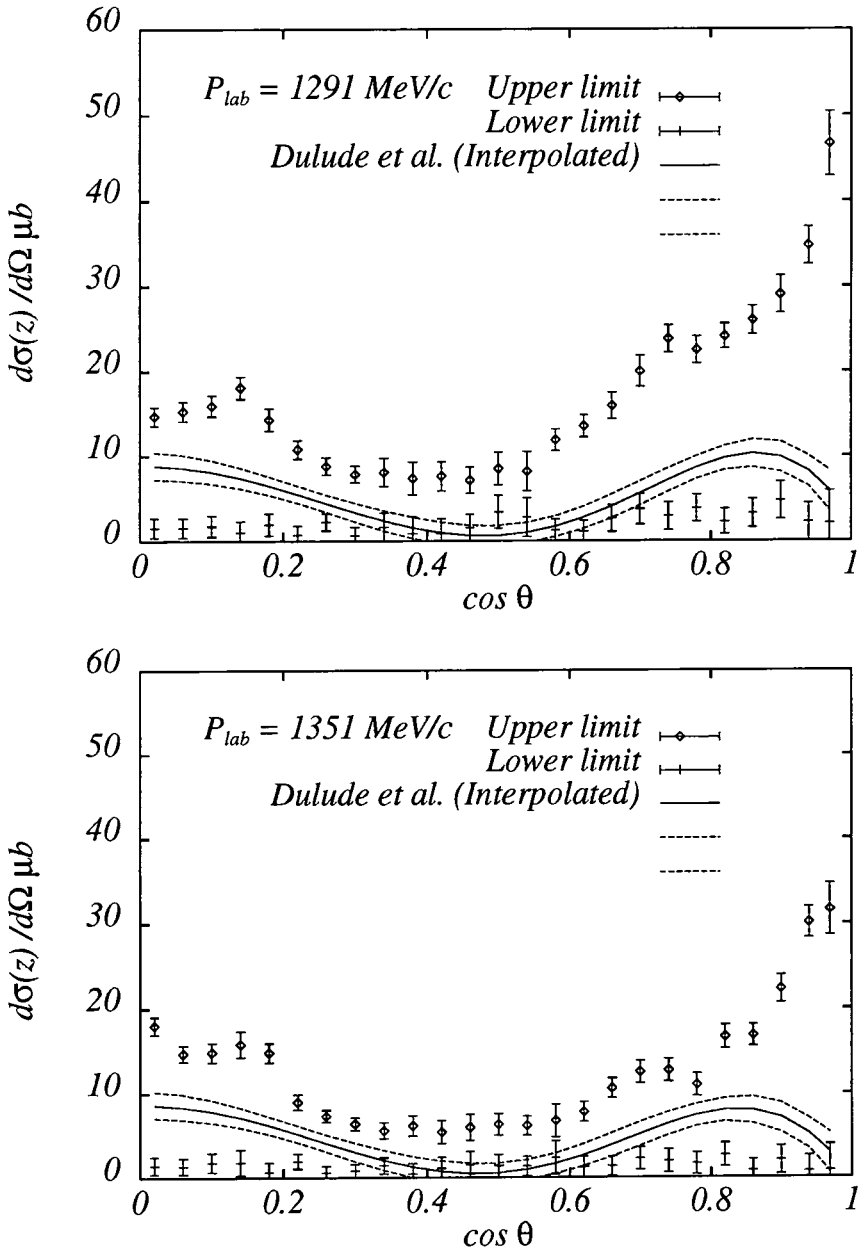

Figure 2.18: Bounds on $d\sigma^n/d\Omega$ derived from PS172 data on $d\sigma^c/d\Omega$ compared with the measurements of Dulude *et al.* .

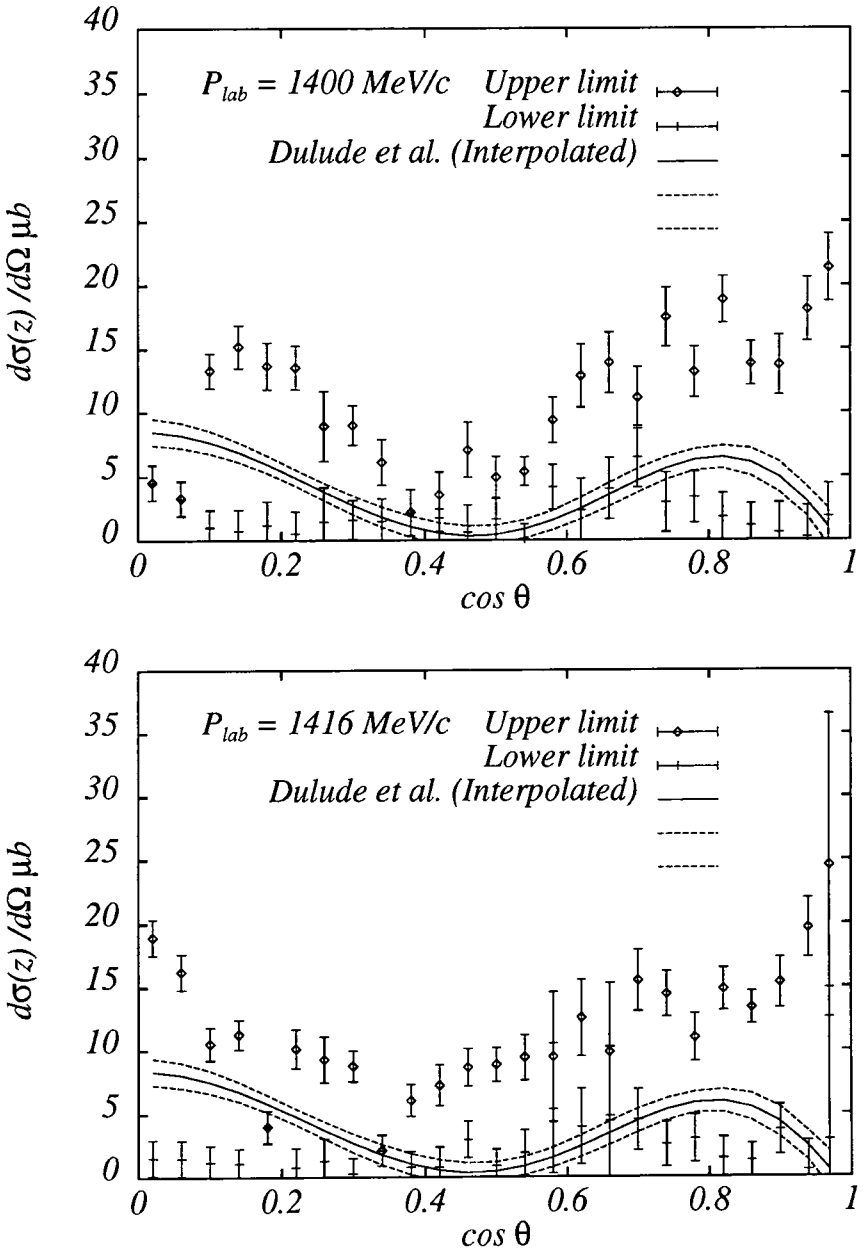

Figure 2.19: Bounds on $d\sigma^n/d\Omega$ derived from PS172 data on $d\sigma^c/d\Omega$ compared with the measurements of Dulude *et al.* .

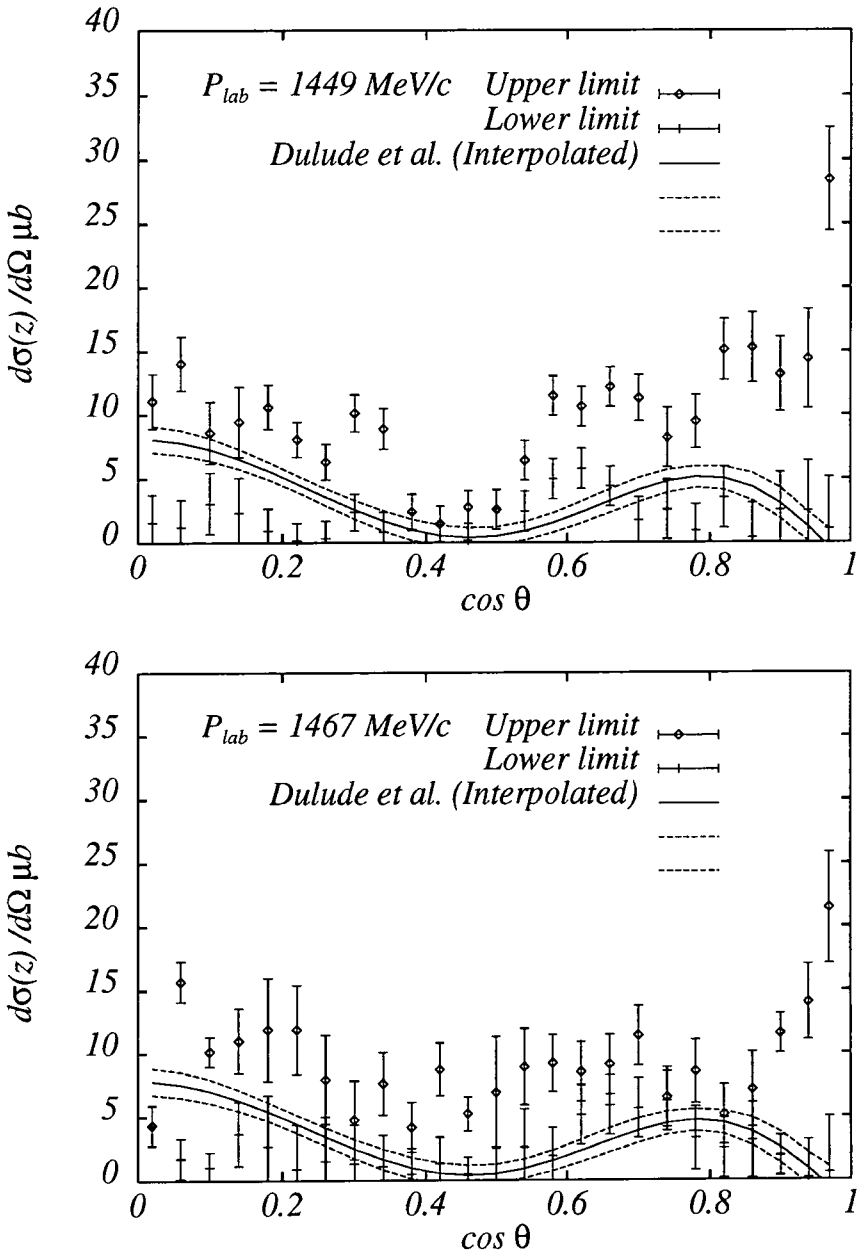

Figure 2.20: Bounds on $d\sigma^n/d\Omega$ derived from PS172 data on $d\sigma^c/d\Omega$ compared with the measurements of Dulude *et al.* .

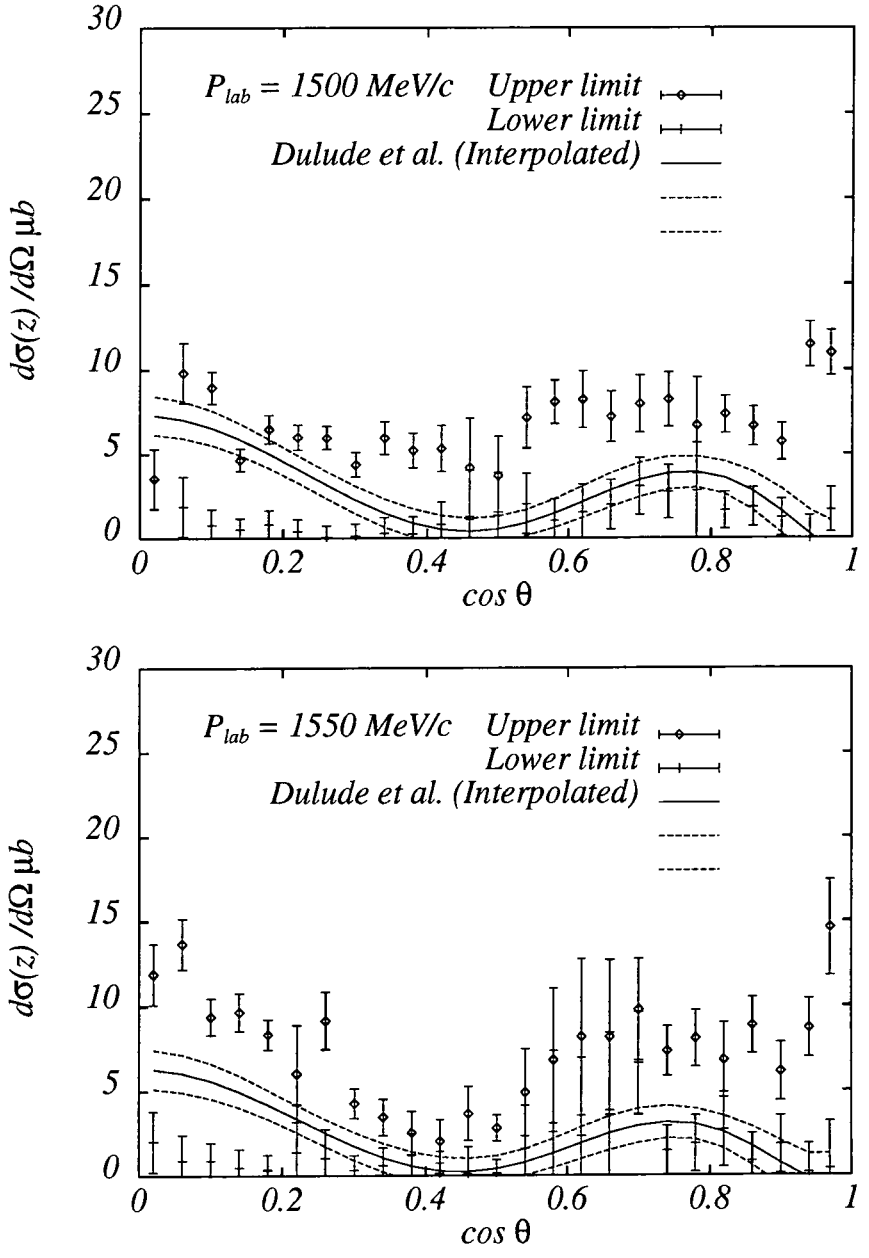

Figure 2.21: Bounds on $d\sigma^n/d\Omega$ derived from PS172 data on $d\sigma^c/d\Omega$ compared with the measurements of Dulude *et al.* .

extrapolation procedure has caused the cross section to become unphysically negative.

In summary, the PS172 data are seen to be in good agreement with earlier measurements of the same observables, with the possible exception of $d\sigma^c/d\Omega$ at $P_{lab} = 1.500$ GeV where the χ^2 between the Eisenhandler *et al.* and PS172 seems anomalously high. Furthermore, the interpolated Dulude *et al.* data satisfy constraints derived from the PS172 measurements. The simultaneous fitting of the PS172 and Dulude *et al.* data-sets may then be done with the confidence that the data-sets are, at least, mutually compatible and largely in agreement with older measurements.

Chapter 3

The Barrelet Formalism and its application to $\overline{p}p \rightarrow \pi\pi$

3.1 Resonances $\not\Leftrightarrow$ Bumps

In chapters 1 and 2 the importance of hadron spectroscopy and the promise of the channel $\overline{p}p \rightarrow \pi\pi$ were stressed. However, in order to find any resonant states which may couple in this channel, it is not sufficient to merely search for bumps in the integrated cross-section. Indeed one would be rather disappointed by such a search since the cross-section in this channel is relatively featureless. However, as the title of this section asserts, the existance of a resonance does not necessarily imply the existance of a bump in the integrated cross-section and vice versa. Of course, almost everybody is familiar with the simplest case of a Breit-Wigner resonant amplitude (with no background)

$$T_{BW} \sim \frac{m\Gamma}{m^2 - s - im\Gamma} \tag{3.1}$$

which describes an anticlockwise arc in the Argand plane as s increases (Fig. 3.1(a)). In this case, the resonance does indeed lead to a bump appearing in the cross-section as illustrated in Fig. 3.1(b). This behaviour, although perhaps that which most would associate with a resonance is not, in fact, at all typical. The counter-clockwise loop

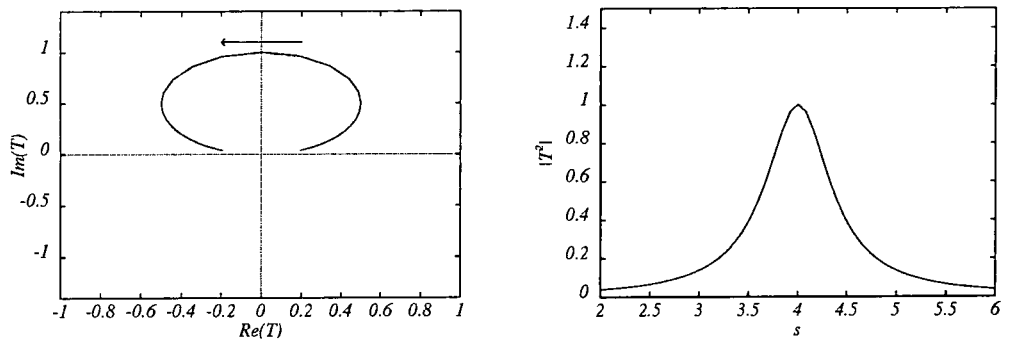

(a) (b)

Figure 3.1: A simple Breit-Wigner resonant amplitude. (a) The amplitude in the Argand plane, the arrow indicates the direction of increasing s around the loop. (b) The modulus squared of the amplitude. In both (a) and (b) the units are arbitrary.

is characteristic of a resonant state, but in most cases of interest it is accompanied by some (often non-resonant) background in the amplitude

$$T \sim \frac{m\Gamma}{m^2 - s - im\Gamma} + T_{\text{bg}}. \tag{3.2}$$

In Fig. 3.2 this is illustrated. The same resonant loop as appears in Fig. 3.1(a) is again present but this time superposed with a non-resonant background (here assumed constant). This leads to a radically different behaviour in the cross-section (Fig. 3.2(b))—the bump has now become a dip! Of course, this is an extreme case but does serve to illustrate the point. A resonance may produce, in the cross-section, a bump; two or more bumps; a shoulder; a dip or something else altogether depending on the nature of the background. In actual physical cases, the situation will, in general be complicated further by the fact that the background may also be energy dependent, and may even be resonant itself. Also, many overlapping resonances may, even when added incoherently and in the absence of other backgrounds, conceivably combine to produce a smooth looking integrated cross section—shown schematically in Fig. 3.3. In order to identify

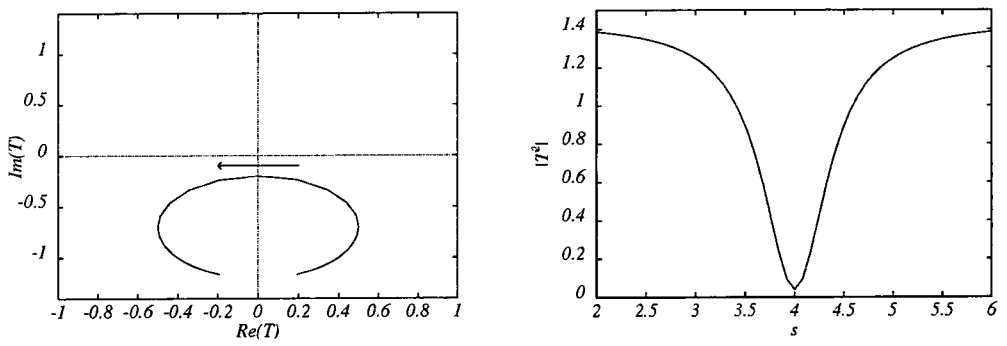

(a) (b)

Figure 3.2: A simple Breit-Wigner resonant amplitude with a constant non-resonant background equal to $-1.2i$. (a) The amplitude in the Argand plane, the arrow indicates the direction of increasing s around the loop. (b) The modulus squared of the amplitude. In both (a) and (b) the units are arbitrary.

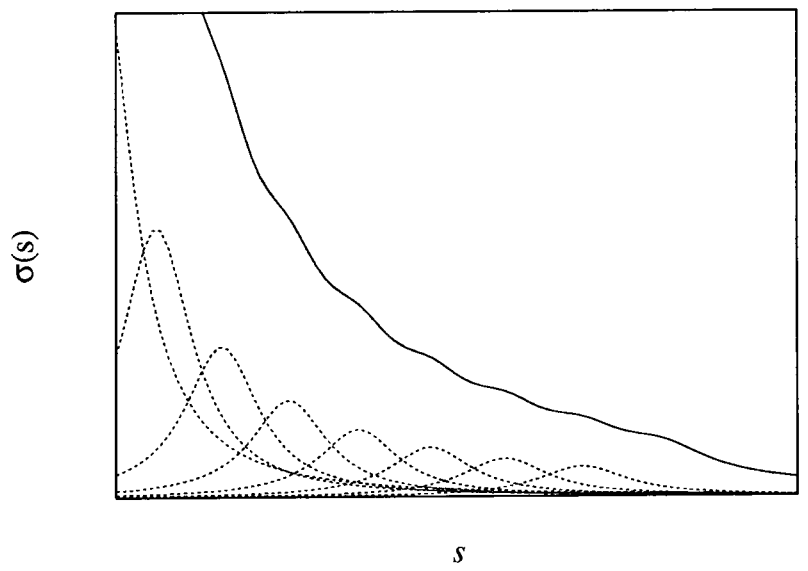

Figure 3.3: Many resonances (dotted lines) combining to produce a seemingly featureless integrated cross-section.

such resonances, it is necessary to be able to separate out components with different quantum numbers. In this chapter, a method, due to Barrelet [26], which allows such a separation is described and applied to the channel $\overline{p}p \rightarrow \pi\pi$. The Barrelet formalism allows the amplitude to be determined and makes its decomposition into partial wave ampitudes particularly simple (this separation will be the subject of the next chapter).

3.2 Barrelet Zeros

As is apparent from Figs. (2.11)–(2.14), the differential cross-section for $\overline{p}p \rightarrow \pi\pi$ has a great deal of angular structure in the P_{lab} region which has been probed by PS172. In Chapter 2 it was found useful to introduce a variable $\omega = e^{i\theta}$ in place of $z = \cos\theta$ when working with the transversity amplitudes for $\overline{p}p \rightarrow \pi\pi$. In terms of this variable, the dips in the transversity cross-sections, $(1 \pm P)d\sigma/d\Omega$, have particularly simple interpretations. The transversity cross sections may be simply expanded as Legendre series in terms of the moments of $d\sigma/d\Omega$ and $Pd\sigma/d\Omega$ (Eqs. (2.3) and (2.4)) thus:

$$(1 \pm P)\frac{d\sigma}{d\Omega} \;=\; |T^{\pm}(z)|^2 = \sum_{i=0}^{2N} a_i P_i(z) \pm \sum_{i=1}^{2N} b_i P_i^1(z). \tag{3.3}$$

Now, since $\cos\theta = z = (\omega + \omega^*)/2$ and hence $\sin\theta = (\omega - \omega^*)/2i$ with $\omega^* = \omega^{-1}$ for physical ω (i.e. ω such that $|\omega| = 1$), the RHS of Eq. (3.3) is a polynomial in ω with powers of ω running from ω^{-2N} up to ω^{2N}. This polynomial will have $4N$ complex roots but since the RHS of Eq. (3.3) is real only half of these, $\omega_i (i = 1, 2N)$, will be independent. Writing Eq. (3.3) in terms of a product over these gives

$$|T(s,\omega)|^2 = |C(s)|^2 \prod_{i=1}^{2N} \frac{(\omega - \omega_i(s))(1/\omega - \omega_i^*(s))}{(1 - \omega_i(s))(1 - \omega_i^*(s))} \tag{3.4}$$

where the factors in the denominator normalise $|C|^2$ to be the forward cross-section. $|T(\omega)|^2$ is displayed in Fig. 3.4 along with the positions of the $\{\omega_i\}$. The circle $|\omega| = 1$, $|T|^2 = 0$ is indicated with a dashed line. The zero positions are shown as open points,

raised to the $|T|^2 = 0$ level. Examining the figure, the role of the zeros in producing

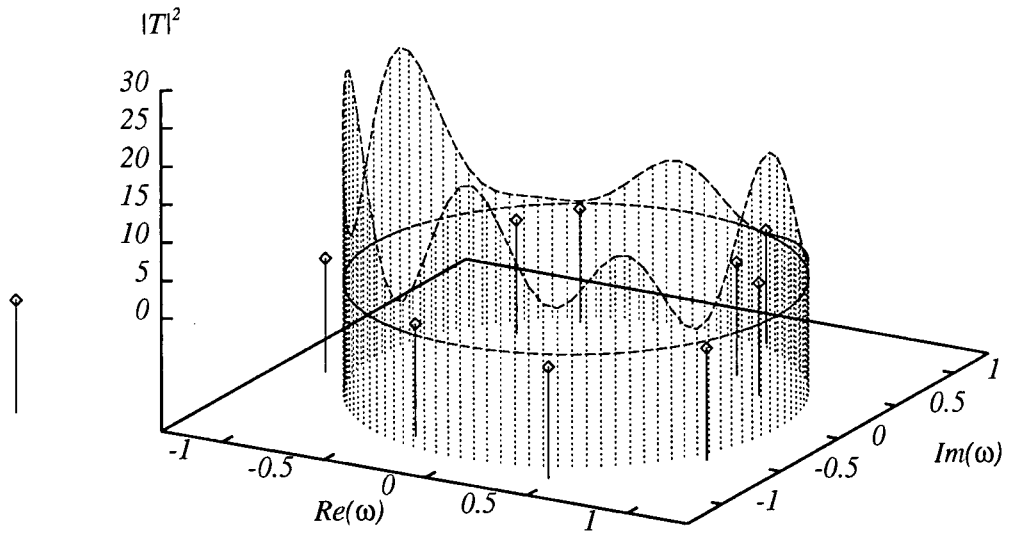

Figure 3.4: $|T(\omega)|^2$ plotted as a function of ω. The points (on stalks) show the positions of the zeros in the ω-plane.

dips in the transversity cross sections becomes apparent. Looking first at the near-most half of the ω-plane in Fig. 3.4, there are four distinct dips in $|T|^2$ caused by the four nearby zeros. On the rear-most half of the unit circle there are two major dips, each caused by the influence of more than one zero—two in the case of the dip around $\omega \simeq (-1+i)/\sqrt{2}$ and three in the case of the wide dip around $\omega \simeq (1+i)/\sqrt{2}$. The one remaining zero, appearing to the left of the vertical axis in Fig. 3.4 is distant from the physical region and hence does not contribute a dip, but instead provides a smooth background to the dips caused by the nearby zeros.

In Chapter 2, it was noted that the exchange of a nucleon in the t- or u-channel leads to poles in the amplitude for $\overline{p}p \to \pi\pi$ situated at $t = m_N^2$ and $u = m_N^2$. These poles will provide a natural criterion by which it may be decided whether a Barrelet zero is to be considered distant from the physical region. A zero further from the unit

circle than the nucleon exchange pole should not be interpreted as an actual zero of the amplitude, but rather as a convenient parameter with which to represent the data. The positions of these poles in the ω-plane may be deduced easily. With the choice of

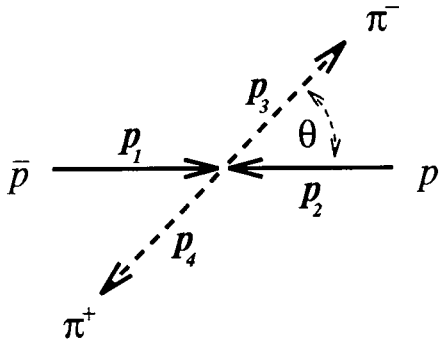

$$p_1 = (E, 0, 0, p)$$

$$p_2 = (E, 0, 0, -p)$$

$$p_3 = (E, 0, k\sin\theta, k\cos\theta)$$

$$p_4 = (E, 0, -k\sin\theta, -k\cos\theta)$$

Figure 3.5: The momenta in $\overline{p}p \rightarrow \pi\pi$.

momenta shown in Fig. 3.5,

$$t = -k^2\sin^2\theta - (p - k\cos\theta)^2 = -k^2 - p^2 + 2kpcos\theta \tag{3.5}$$

with a similar expression for u:

$$u = -k^2 - p^2 - 2kpcos\theta. \tag{3.6}$$

The nucleon poles will then appear at $\cos\theta$ such that

$$m_N^2 = -E^2 + m_\pi^2 - E^2 + m_N^2 \pm 2\sqrt{E^2 - m_\pi^2}\sqrt{E^2 - m_N^2}\cos\theta \tag{3.7}$$

where the upper and lower signs refer to t and u respectively. Now, since $s = 4E^2$, $\cos\theta$ must satisfy

$$-\frac{s}{2} + m_\pi^2 \pm \frac{1}{2}\sqrt{s - 4m_\pi^2}\sqrt{s - 4m_N^2}\cos\theta = 0 \tag{3.8}$$

i.e.

$$\cos\theta = \pm \frac{s - 2m_\pi^2}{\sqrt{s - 4m_\pi^2}\sqrt{s - 4m_N^2}}. \tag{3.9}$$

The poles are then at values of $\cos\theta$ which are real and greater than 1. This implies

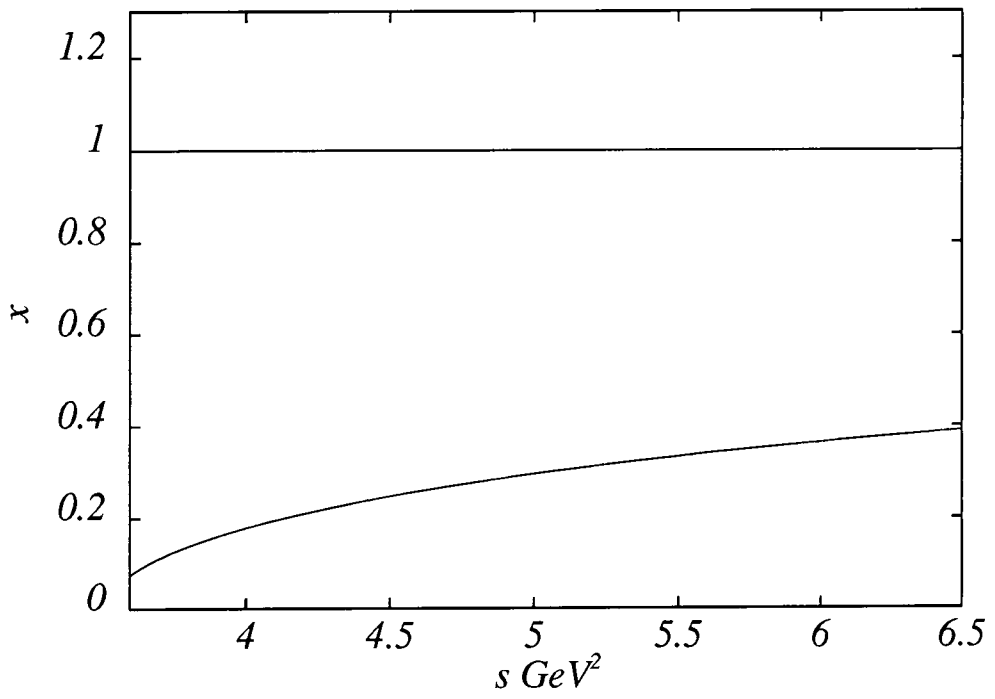

Figure 3.6: Distance x along the real axis of the t- and u-channel nucleon poles. The horizontal line at $x = 1$ corresponds to the physical region $|\omega| = 1$.

that in the ω-plane the poles will lie along the positive and negative real axes. The distance x from the origin of the poles inside the circle along the real axis are shown in Fig. 3.6, the line $x = 1$ would correspond to the poles reaching the unit circle at $\omega = \pm 1$. The t- and u-channel poles are situated at $\pm x$ and $\pm 1/x$. In the PS172 momentum range (corresponding to the region $3.6 \leq s \leq 5.2$ GeV ^{2}) the nucleon poles are around $\omega \simeq \pm 0.25, \pm 4$.

Examining Eq. (3.4) it is clear that it is possible to separate the RHS to give an

expression for $T(\omega)$ thus :—

$$T(\omega) = |C(s)|e^{i\phi(s,w)} \prod_{i=1}^{2N} \frac{\omega - \omega_i(s)}{1 - \omega_i(s)} \tag{3.10}$$

But this separation is far from unique. The RHS of Eq. (3.4) is a product over $2N$ factors of the form XX^*. Thus, any or all of the $2N$ factors in Eq. (3.10) may be substituted by its complex conjugate without affecting the values of the observable transversity cross-sections $(1 \pm P_c)d\sigma^c/d\Omega = |T(\omega = e^{\mp i\theta})|^2$ at all. This swapping of factors between the amplitude and its complex conjugate is easily shown to be equivalent to transforming roots ω_i to their reflections in the unit circle $|\omega = 1|$ i.e. $\omega_i \mapsto 1/\omega_i^*$. Indeed, as far as the charged channel data are concerned, the side of the unit circle on which the zeros lie is irrelevant. This is the source of a discrete ambiguity, referred to as the Barrelet ambiguity, inherent in the application of this method to $\overline{p}p \to \pi^-\pi^+$. A second source of ambiguity, referred to as the continuum ambiguity, is the overall phase of the amplitude, $\phi(s,\omega)$ in Eq. (3.10), which is undetermined by the data. Now, since the transversity cross-sections (Eq. (3.3)) are sums over partial waves up to order $2N$, it is reasonable to expect that the amplitude is a sum over waves up to order N. This is not, however, rigorous. The assumption that there is no collusion between higher waves has been tacitly applied. The ω-dependence of the phase function $\phi(s,\omega)$ takes on a simple form if the assumption that partial waves of order $> N$ make absolutely no contribution to the amplitude. In this case the phase function becomes $\phi(s)/\omega^m$ where m is an integer determined by the particular interpretation of the phrase "of order $> N$". This cut-off criterion is, as it stands, ambiguous since there are two distinct angular momenta associated with the reaction $\overline{p}p \to \pi\pi$: J, the orbital angular momentum of the $\pi\pi$ system and L, the orbital angular momentum associated with the $\overline{p}p$ system. It is possible to choose a basis in which one expands the amplitude in terms of partial wave amplitudes which have definite values of both J and L. It is then, *a priori*, unclear whether one should include only amplitudes with $J \leq N$ or those with $L \leq N$, choices which imply values for m of N and $N+1$ respectively. Previous

analyses of the channel $\overline{p}p \rightarrow \pi\pi$ have been performed using both J- and L-truncation schemes in the region $P_{lab} \geq 1$ GeV/c [35, 36, 34] and it is by no means clear which scheme is the more appropriate in that P_{lab} region. The J-truncation scheme can be argued to be a simpler representation of the data [36] while the L-truncation scheme may be motivated by appeal to angular momentum barrier arguments since waves are suppressed by factors of $(s-4m_N^2)^{L/2}$ as the threshold at $s = 4m_N^2$ is approached [34]. These threshold supression arguments have been criticised on the grounds that there are many examples of cases where an ordering in magnitude of waves in violation of the angular momentum suppression implied ordering quickly establishes itself as energy increases away from threshold. While this objection can certainly be raised in the region $P_{lab} \geq 1$ GeV/c , the data taken by PS172 approach very close to the $\overline{p}p$ threshold and it is most likely that the partial waves, at least in the main, will retain some imprint of the angular momentum suppression implied ordering. Hence, in this analysis of the PS172 results, the L-truncation scheme has been adopted and hence the amplitude is taken to be

$$T(\omega) = |C(s)|\frac{e^{i\phi(s)}}{\omega^{N+1}}\prod_{i=1}^{2N}\frac{(\omega-\omega_i(s))}{(1-\omega_i(s))}. \tag{3.11}$$

The remaining phase function $\phi(s)$ is, for the moment, ignored i.e. $\phi(s)$ is assumed to be 0. This assumption will be relaxed in Chapter 4 when the partial waves will be examined.

3.3 Fitting to $\overline{p}p \rightarrow \pi^-\pi^+$

As a first stage in the fitting, the Barrelet ambiguity is ignored, and a fit is performed to the charged channel data only with the phase of the amplitude chosen as detailed in

the previous section, i.e. using the expression

$$T(\omega) = \frac{|C(s)|}{\omega^m} \prod_{i=1}^{N} \frac{(\omega - \omega_i(s))}{(1 - \omega_i(s))} \tag{3.12}$$

for the amplitude. A minimum χ^2 method is employed, using the CERN MINUIT subroutines [37]. For the purposes of this fit, all zeros are confined to the inside of the unit circle. Since the charged channel data do not discriminate between the inside and outside positions of the zeros, zeros that start inside the circle might be expected to stay there throughout the minimisation since there can be no lowering of the χ^2 merely by crossing the circle. Indeed, if one considers the minimisation process as a simple gradient descent then the zeros will have no tendency to cross the circle since the derivative of the χ^2 in the radial direction must be equal to zero at the physical region. In practice, however, the finite step size employed by MINUIT (particularly at the start of the minimisation when the χ^2 is far from its minimum) leads to the possibility of zeros "jumping" out of the unit circle during minimisation. For the purposes of the preliminary fit, any zero crossing the circle is transformed back into the inside of it. This also avoids having to deal with numerical problems caused when a zero approaches infinity. The Barrelet ambiguity will be addressed later in this chapter when the threshold conditions and the data on $\overline{p}p \to \pi^0\pi^0$ are taken into account.

Using the zero positions, $\{\omega_i\}$, (transformed to the inside of the unit circle) and the overall scale $|C(s)|$ in Eq. (3.12) as parameters, a fit is performed to the charged channel differential cross-section and polarisation simultaneously. This is repeated for each of the PS172 momenta. There are two main drawbacks to this procedure. Firstly, as Fig. 3.7 shows, there is far more angular structure in the differential cross-section at higher energies than at lower energies—the data at $P_{lab} = 1.550$ GeV/c , for example, are far more "dippy" than those at 1.089 GeV/c which are in turn "dippier" than those at 0.360 GeV/c . As was seen earlier, in the Barrelet formalism, dips in the transversity cross-sections (and hence dips in $d\sigma/d\Omega$ and points where $|P| \simeq 1$) are caused by Barrelet zeros approaching the unit circle. Since more zeros are near to the unit circle

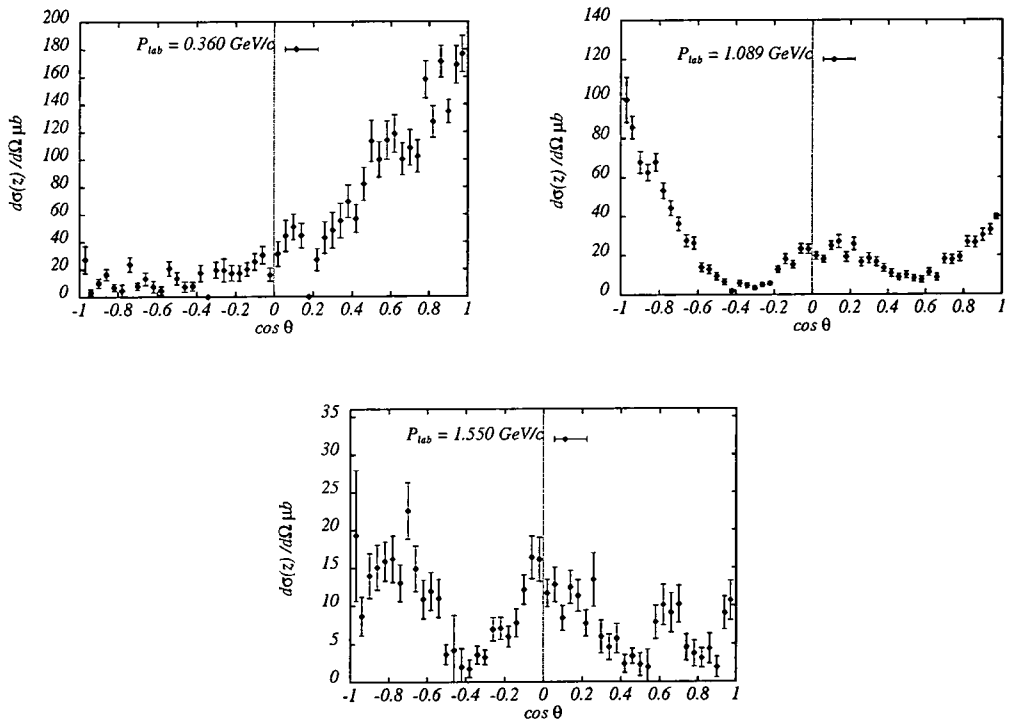

Figure 3.7: The differential cross-section for $\overline{p}p \rightarrow \pi^-\pi^+$ at three representative PS172 momenta [27].

at higher energies (more dips in the cross-sections) it is most convenient to fit using a decreasing number of zeros as P_{lab} decreases. This corresponds to putting higher partial waves exactly to zero as the threshold at $s = 4m_N^2$ is approached. This approach "builds in" the expected suppression of higher angular momentum amplitudes as the laboratory momentum goes to zero. Secondly, minimising completely separately at each energy can lead to problems with the expected continuity of the zero trajectories. Trajectories which are continuous may appear discontinous owing to zeros re-ordering themselves during minimisation, since the connectivity of the zeros is not constrained from one energy to the next. The most reasonable and objective way to choose the connections between the zeros from each energy to the next in order to ensure continuous zero trajectories is to re-order the zeros such that the total distance between zeros at one energy and those at the next is a minimum i.e. if the zeros at one energy are $\{\omega_i\}$ and those at the next are $\{\eta_i\}$ then the best guess at the correct connections is the re-ordering of the η_i's such that the quantity

$$\Delta = \sum_i |\omega_i - \eta_i| \tag{3.13}$$

is a minimum. Of course, even this method has a certain amount of ambiguity since one may raise the terms in the sum on the RHS of Eq. (3.13) to an arbitrary power and still have a positive definite quantity. Even ignoring this ambiguity, the task is computationally quite expensive since it requires a search through 10! different orderings of the η_i. This number may be reduced somewhat if a subset of the zeros are known not to move very far from one energy to the next, in which case their connections should be trivially known. Configurations of the η_i which do not connect these zeros in this way may then be omitted from the search, reducing the number of configurations to be checked to $(10 - n)!$ where n is the number of zeros whose connectivity is obvious. While this certainly does help, it is limited by how many connections are obvious at each energy. In addition, these "obvious" connections have to be input by hand which limits the usefulness of the method to those cases where only a few minimisations are

to be performed over not too many energies. However, given data taken at P_{lab} values on a fine enough grid, one may expect that none of the zeros would move very far in going from one momentum to the next, making the connections between zeros at adjacent momenta easy to determine. Indeed, the hope would be that the minimisation procedure would not swap over any zeros since this would involve moving them very much further than the distance to the minimum, if the starting positions of the zeros for minimising at one energy are taken to be the positions obtained by fitting at an adjacent energy. The PS172 data, however, are not on a sufficiently fine P_{lab} grid to ensure this but an alternative procedure for ensuring smooth connections from one momenta to the next is suggested by these considerations. After fitting at one momenta p_1, form the quantity

$$\tilde{\chi}^2(\alpha) = (1-\alpha)\chi^2(p_1) + \alpha\chi^2(p_2), \tag{3.14}$$

where $\chi^2(p_i)$ is the χ^2 between the cross-sections given by the current fit parameters and the data at the momentum p_i. The number α may be varied between 0 and 1 in steps. Minimising using $\alpha = 0$ would then be equivalent just to re-minimising at p_1, starting the parameters from their values at the minimum of χ^2 at p_1 i.e. a trivial minimisation! While minimising with $\alpha = 1$ would be the procedure described above of minimising at one energy starting the parameters from their values at an adjacent energy. By minimising in N steps with $\alpha = \alpha_1, \ldots \alpha_N$, with $\alpha_i \in (0, 1]$, starting the parameters for each succesive minimisation from the final values of the previous minimisation, it is hoped that the zeros will not move far during any one minimisation. Indeed, by taking sufficiently many steps (increasing N), the distance that any zero moves between minimisations may be reduced at will. This process of minimising in many small steps reduces the possibility of any unintentional re-ordering of the zeros between PS172 momenta. This is gained at the cost of performing $(N-1)$ extra minimisations, but this does not, as might be naively expected, increase the computing time by a factor of N. This is because although there are N times more minimisations to be performed, in each minimisation the parameters start off much closer to the desired minimum and

hence less iterations are required for each minimisation to converge. The intermediate points in $\{\omega_i\}$ and the scale param $|C(s)|$ corresponding to values of α other than 0 and 1 are, of course, unphysical, merely serving to aid in the smooth connection of the Barrelet zeros. The resulting Barrelet zero trajectories are shown in Figs. 3.8 and 3.9 where the regions $0.360 \leq P_{lab} \leq 0.988$ GeV/c and $0.988 \leq P_{lab} \leq 1.550$ GeV/c

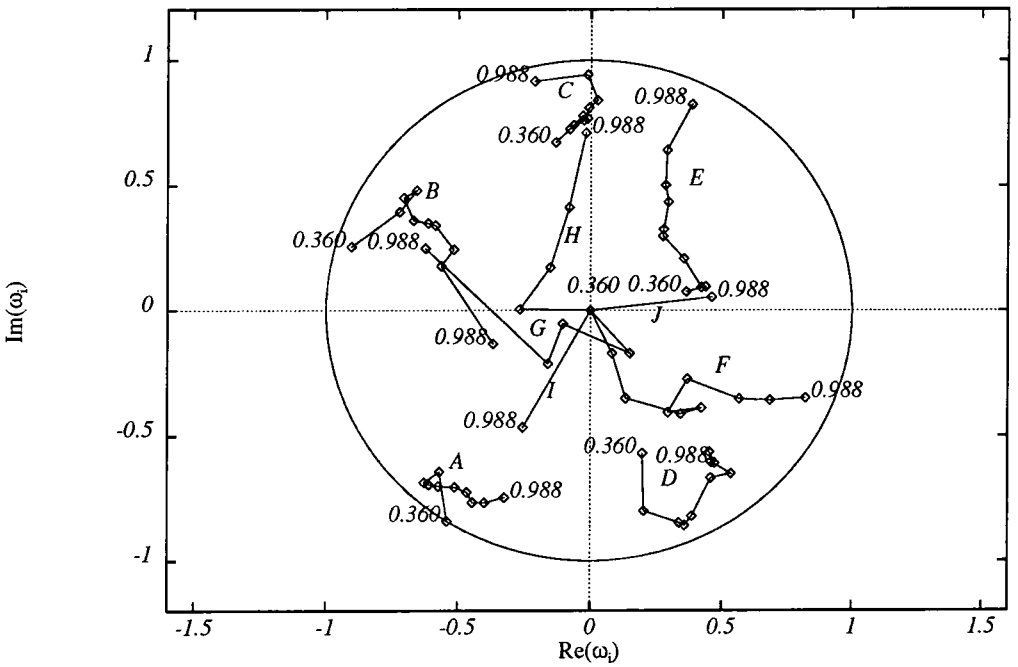

Figure 3.8: Positions of the Barrelet zeros obtained fitting to the charged channel data of PS172

are shown on separate plots for clarity. There are some general features worthy of note. Firstly, there are a number of zeros, labelled A–D in Figs. 3.8 and 3.9 which remain near to the unit circle for all or most of the P_{lab} range. These are responsible for the persistant deep dips in the transversity cross-sections (recall Fig. 3.4). Secondly, a varying number of zeros are used throughout the energy range. The experimentally observed non-vanishing of the a_{10} moment of the charged channel cross section at energies towards the top of the PS172 energy range is evidence that at least 10 Barrelet

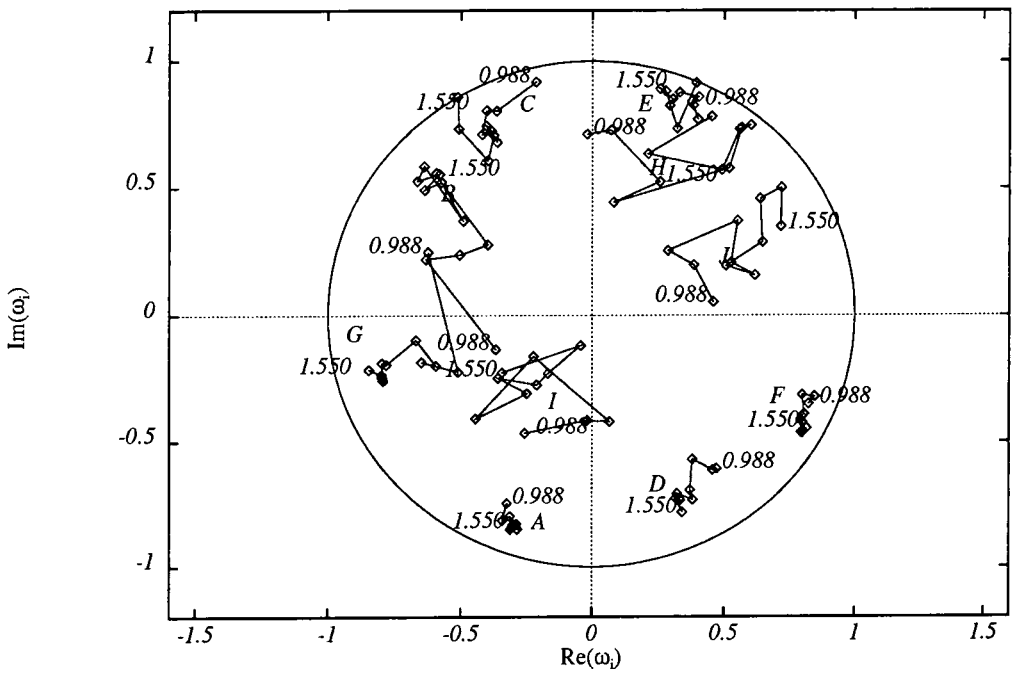

Figure 3.9: Positions of the Barrelet zeros obtained fitting to the charged channel data of PS172

zeros are required to describe the data there. This moment (and a_9) become smaller as P_{lab} decreases until, at around $\sim$ 1 GeV/c, the cross-section is adequately described in terms of 8 zeros. The zeros furthest from the physical region at this energy, labelled I and J being the pair which disappear. As the lab momentum decreases still further, more zeros move away from the unit circle and approach the origin in the ω-plane (recall that the zeros have been confined to the inside of the circle) and at around $\sim$ 0.6GeV/c, two zeros, labelled as G and H make it to the origin. This pairing of zeros $\{I, J\}$ and $\{G, H\}$ coupled with threshold considerations will aid in the resolution of the Barrelet ambiguity described earlier.

3.4 Resolving the Barrelet ambiguity

3.4.1 Threshold Behaviour of the Zero Trajectories

As zeros appear, they must do so in pairs, one arriving from the origin and its partner from infinity in the ω-plane. That this is so may be seen as follows. Consider an amplitude T, with no zeros,

$$T \sim b \tag{3.15}$$

where b is a constant. (In the L-truncation scheme there will be an additional overall factor of $1/\omega$ in T which is unimportant in the present discussion). As the next partial wave appears, T will receive independent contributions proportional to the Legendre functions P_1 and P_1^1, i.e. contributions proportional to ω and $1/\omega$.

$$T \to T_{\text{new}} \sim \frac{\delta b}{\omega} + b + \epsilon b \omega \tag{3.16}$$

where δ and ϵ are infinitesimal quantities. Thus,

$$\begin{aligned} T_{\text{new}} &\sim b\left(\frac{\delta}{\omega} + 1 + \epsilon\omega\right) \\ &= b\left(\frac{1}{\omega} + \epsilon\right)(\omega + \delta) + O(\delta\epsilon), \end{aligned} \tag{3.17}$$

i.e. when the new partial wave is just appearing and terms of order $\delta\epsilon$ may be neglected, T acquires two new zeros,

$$\omega_1 = -\delta, \qquad \omega_2 = -\frac{1}{\epsilon}, \tag{3.18}$$

where it is manifest that ω_1 appears from the origin and ω_2 appears from infinity. Hence, although it is not *a priori* known on which side any given zero is, it is at least known that the zeros which disappear must be on opposite sides of the circle (unless, of course, they have had time to move away from the origin/infinity and actually cross

the unit circle at some energy). This reduces the possible *in/out* configurations of these four zeros from $2^4 = 16$ to just $2^2 = 4$, so reducing the total number of Barrelet related amplitudes which need to be considered by a factor of 4. This still leaves 256 equally acceptable candidiates for the amplitude for $\overline{p}p \rightarrow \pi\pi$ to be chosen between.

3.4.2 The $\overline{p}p \rightarrow \pi^0\pi^0$ Data

It is in choosing between the 256 configurations of the zeros still allowed by the threshold considerations of the previous Section that the third observable, $d\sigma^n/d\Omega$ is used in the analysis. Whilst the charged channel observables do not know on which side of the circle the zeros lie the neutral channel observables do. As a consequence of Eq. (2.12), the different *in/out* configurations of the zeros lead to different predictions for the neutral channel observables. This is illustrated in Figs. 3.10 and 3.11 where the

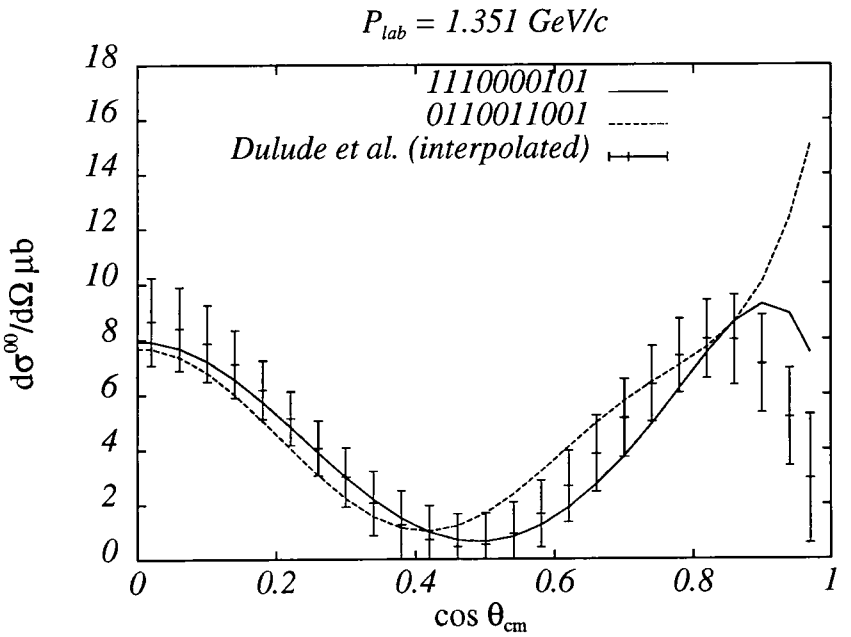

Figure 3.10: Comparison of the predictions for $d\sigma^n/d\Omega$ of two different configurations.

predictions for $d\sigma^n/d\Omega$ of the zeros positions of Fig. 3.9 at 1.351 GeV/c are compared

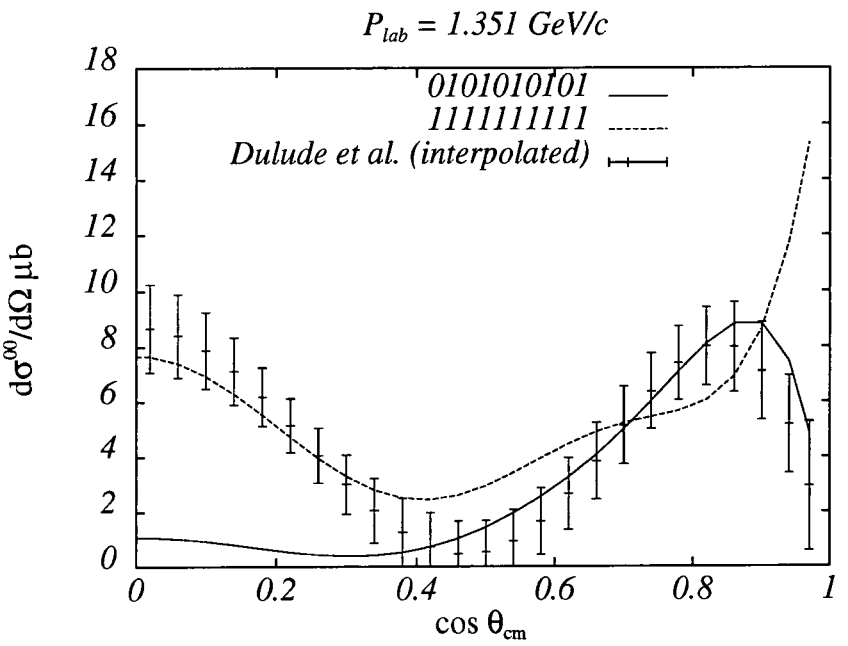

Figure 3.11: Comparison of the predictions for $d\sigma^n/d\Omega$ of two different configurations.

with the data for four different configurations in order to illustrate the power of both the threshold considerations discussed in the last section and the neutral channel data to select the *in/out* configuration. The configurations have been labelled with a string of 1's and 0's, with 1 (0) indicating that the corresponding zero lies inside (outside) the unit circle with the zeros in the order $ABCDEFGHIJ$. In Fig. 3.10 two configurations which have acceptable threshold behaviour (i.e. which have zero I on the opposite side of the circle to zero J and similarly for zeros G and H) are shown. Both fit the data reasonably well, although the configuration 0110011001 fares worse near $\cos\theta = 1$ (this configuration actually fits the better of the two at most other momenta). In Fig. 3.11 the predictions in the configurations 1111111111 and 0101010101 are shown. the former while agreeing not too badly with the data, has unacceptable threshold behaviour since all the threshold paired zeros (indeed *all* the zeros) lie inside the circle while the latter configuration has acceptable threshold behaviour but misses the data

completely for $\cos\theta < 0.5$. The predictions for the $\pi^0\pi^0$ cross section given by the zero positions obtained by fitting to the $\overline{p}p \to \pi^-\pi^+$ PS172 data may then be compared to the interpolated Dulude *et al.* data with the zeros ranging through all of the possible (i.e. threshold allowed) *in/out* configurations. However, before attempting this, it should be noted that there is one transformation of the zero positions which leaves the neutral channel observables unchanged. This transformation is known as the Minami transformation and is achieved by simultaneously transforming *all* of the zeros to their reflections in the unit circle, i.e. $\{\omega_i\} \mapsto \{1/\omega_i^*\}$. That this transformation does indeed leave the neutral channel observables unchanged may be seen as follows. Combining Eqs. (2.12) and (3.12), an expression for the neutral channel amplitude in terms of the ω_i's may be obtained:—

$$T^n(\omega) = |C| \left[\frac{1}{\omega^m} \prod_{i=1}^{N} \frac{\omega - \omega_i}{1 - \omega_i} + \frac{(-1)^{m+N}}{\omega^m} \prod_{i=1}^{N} \frac{\omega + \omega_i}{1 - \omega_i} \right]. \tag{3.19}$$

Then, taking the modulus squared gives,

$$\begin{aligned} |T^n(\omega)|^2 = \; & |C|^2 \left[\prod_{i=1}^{N} \frac{(\omega - \omega_i)(1/\omega - \omega_i^*)}{(1 - \omega_i)(1 - \omega_i^*)} \right. \\ & + (-1)^{N+m} \prod_{i=1}^{N} \frac{(\omega - \omega_i)(1/\omega + \omega_i^*)}{(1 - \omega_i)(1 - \omega_i^*)} \\ & + (-1)^{N+m} \prod_{i=1}^{N} \frac{(1/\omega + \omega_i^*)(\omega + \omega_i)}{(1 - \omega_i^*)(1 - \omega_i)} \\ & \left. + (-1)^{2(N+m)} \prod_{i=1}^{N} \frac{(\omega + \omega_i)(1/\omega + \omega_i^*)}{(1 - \omega_i)(1 - \omega_i^*)} \right], \end{aligned} \tag{3.20}$$

which, upon extracting a factor of $1/\omega^N$ and rearranging slightly, becomes

$$\begin{aligned} |T^n(\omega)|^2 = \; & |C|^2 \frac{1}{\omega^N} \left[\prod_{i=1}^{N} \frac{(\omega - \omega_i)(\omega - 1/\omega_i^*)}{(1 - \omega_i)(1 - 1/\omega_i^*)} \right. \\ & \left. + (-1)^{N+m}(-1)^N \prod_{i=1}^{N} \frac{(\omega - \omega_i)(\omega + 1/\omega_i^*)}{(1 - \omega_i)(1 - 1/\omega_i^*)} \right. \end{aligned}$$

$$+ \quad (-1)^{N+m} \prod_{i=1}^{N} \frac{(\omega - 1/\omega_i^*)(\omega + \omega_i)}{(1 - 1/\omega_i^*)(1 - \omega_i)}$$

$$+ \quad (-1)^{N} \prod_{i=1}^{N} \frac{(\omega + \omega_i)(\omega + 1/\omega_i^*)}{(1 - \omega_i)(1 - 1/\omega_i^*)} \Bigg]. \qquad (3.21)$$

Examining Eq. (3.21) term by term, it is clear that the first and fourth terms will remain unchanged when any zero is transformed to its reflection in the physical region, since each of the factors in the product is manifestly symmetric in $\omega_i \leftrightarrow 1/\omega_i^*$. In fact, this had to be the case since the first and fourth terms are nothing more than the charged channel transversity cross-sections $|T^c(\omega)|^2$ and $|T^c(-\omega)|^2$ which, as has already been noted, are insensitive to the in/out placement of the zeros. This symmetry under $\omega_i \leftrightarrow 1/\omega_i^*$ is not, however, present in the second and third terms in Eq. (3.21). Indeed, transforming any one zero $\omega_i \rightarrow 1/\omega_i^*$ will in general change these two interference terms. Transforming all the zeros at once, although it will still change these terms, does so in a special way. Provided N is even (which is the physically reasonable case) the second and third terms in Eq. (3.21) will transform into each other when the Minami transformation, $\{\omega_i\} \mapsto \{1/\omega_i^*\}$, is applied, even though this would not happen if just some subset of the zeros were so transformed. Therefore, it is only necessary to check 128 of the 256 *in/out* configurations allowed by the threshold considerations against the neutral channel data, the other 128 just being Minami transforms of these and hence predicting the same $\overline{p}p \rightarrow \pi^0\pi^0$ cross-sections. The χ^2 values for these comparisons may then be used to determine which are the likely configurations. Since the zero trajectories are expected to be continuous in energy, the χ^2 is evaluated using a given configuration throughout the energy range (as opposed to allowing the configuration to vary from energy to energy which would lead to discontinuous trajectories with zeros hopping in and out of the circle). Table 3.1 shows the χ^2 per degree of freedom, averaged over the 10 PS172 P_{lab} values at which the interpolated Dulude *et al.* data exists, for the best 10 configurations, where the configurations have been denoted by a binary number whose bits represent whether a particular zero is in (1) or out (0) of the unit circle. Simultaneous fits to both channels are then attempted in the favoured in/out

configurations. Note that the "best" configurations in Table 3.1 are not necessarily going to be the best configurations after fitting to both channels has been performed.

Configuration	χ^2/N_{dof}
0110011001	3.05
1110000101	3.08
0110111001	3.12
1010101001	3.18
0110101001	3.24
0010001001	3.28
1110111001	3.34
1010001001	3.37
0110001001	3.38
1010011001	3.65

Table 3.1: χ^2 per degree of freedom between the predictions for the neutral channel cross-section given by the fits to the charged channel data only and the interpolated neutral channel data. The χ^2 is averaged over the ten PS172 momenta which overlap the region of availability of data on $\overline{p}p \rightarrow \pi^0\pi^0$.

In fact, it turns out that the majority of the threshold allowed configurations, including most in Table 3.1, fail to produce fits which converge satisfactorily. Typically, the zeros re-arrange themselves within the circle in order to change their effective *in/out* configuration. In addition, zeros may try to cross the circle although because of the choice of parametrisation the best they can do is to butt up against it. These changes in the effective in/out configuration tend to lead to violations of the threshold behaviour described above. An example is given in Fig. 3.12 where the data on both channels have been refitted using the in/out configuration 0110011001, the configuration which appeared best on the basis of the comparisons with the neutral channel data using the fits to the charged channel only (see Table 3.1). The zeros labelled H and J have swapped over during the minimisation and since these are on differing sides of the circle, this leads to a change in the effective configuration. The zeros labelled B, G and I are also indistinct, again swapping around. Also, the zero labelled E has attempted to cross the circle at all but one of the P_{lab} values in this range. This behaviour is

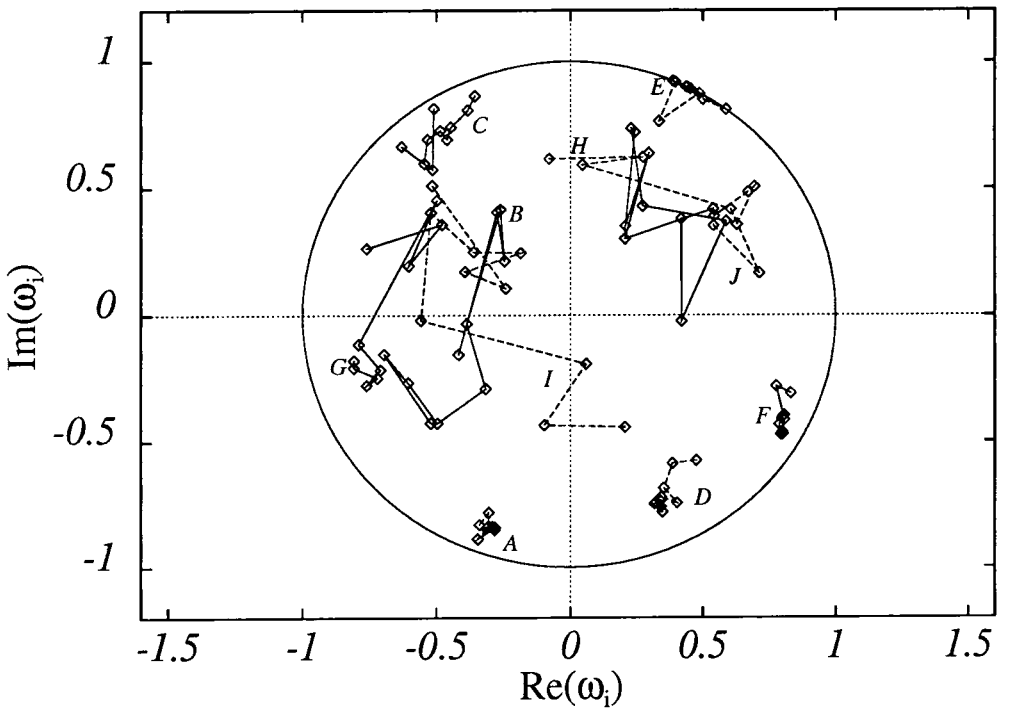

Figure 3.12: Zero positions obtained fitting to $\overline{p}p \to \pi^-\pi^+$ and $\overline{p}p \to \pi^0\pi^0$ using the configuration 0110011001. The zeros connected with solid (dotted) lines lie inside (outside) the unit circle.

indicative of the fact that the configuration 0110011001 does not produce a good *simultaneous* fit to the charged and neutral channels at many energies. This is typical of the behaviour of fits in the configurations of Table 3.1. The problem being that, in order to produce satisfactory fits to the $\overline{p}p \rightarrow \pi^0\pi^0$ cross-section in a given configuration, the zeros must move slightly from their positions given by fitting to the data on $\overline{p}p \rightarrow \pi^-\pi^+$ alone. If this slight change in the zero positions is compatible with still fitting the charged channel cross-sections then a well-behaved minimisation will result. If, however, the perturbations to the zero positions required to fit the neutral channel cross-section in a given *in/out* configuration are incompatible with the charged channel fitting, the above described rearrangement of the zeros will occur in order to change to an effective configuration for which the perturbations are compatible.

One of the configurations in Table 3.1 does produce a well behaved fit. This is the configuration 1110000101 which appears second in Table 3.1. Indeed, this configuration would have achieved the lowest χ^2 of all the threshold allowed configurations if the comparison at 1.089 GeV/c were omitted from the average. All configurations appear to have higher χ^2 at this momentum, perhaps due to the extrapolated cross section becoming unphysically slightly negative at around $\cos\theta = 0.5$, as was mentioned in Chapter 2. The zero positions obtained are shown in Fig. 3.13. Comparing with Fig. 3.9 it is apparent that the zero trajectories do not have to move far to accomodate the $\overline{p}p \rightarrow \pi^0\pi^0$ data, confirming the conclusion of Chapter 2 that the data on the two channels are compatible.

The charged channel cross section and polarisation measurements of PS172 are shown along with the fits in Figs. 3.14–3.33. In Figs. 3.14–3.23 the curve shown on each plot is the fit to the PS172 data in the P_{lab} region $0.360 \leq P_{lab} \leq 0.988$ GeV/c . In Figs. 3.24–3.33 the curve shown is the fit to both the charged and neutral channels simultaneously (using the Barrelet zero positions displayed in Fig. 3.13).

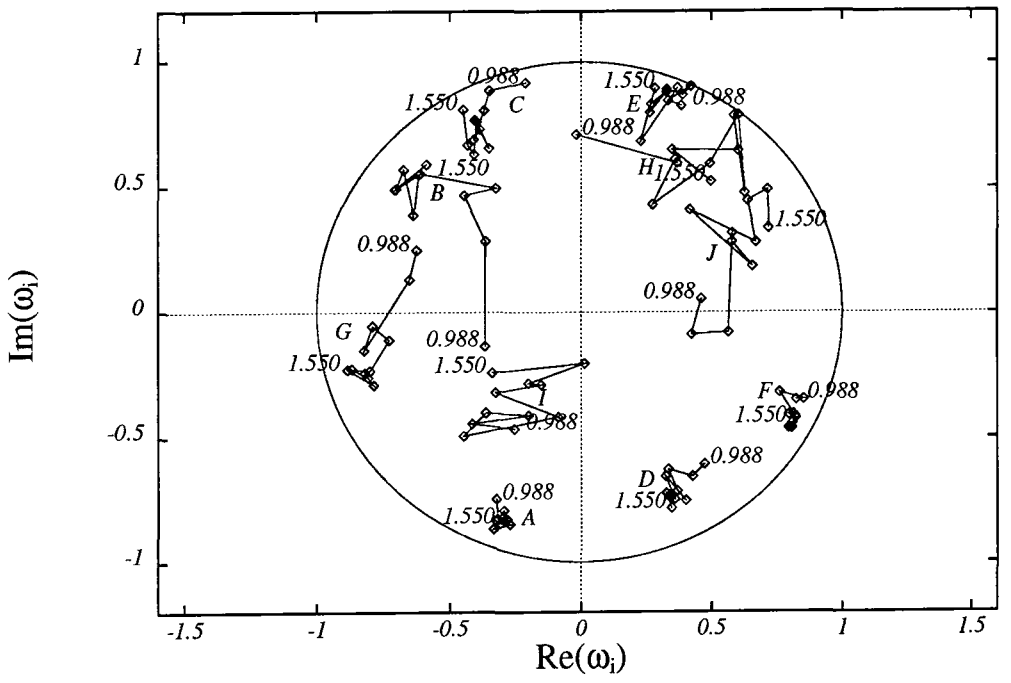

Figure 3.13: Positions of the Barrelet zeros obtained fitting to PS172 data on $\overline{p}p \rightarrow \pi^-\pi^+$ simultaneously with the Dulude *et al.* data on $\overline{p}p \rightarrow \pi^0\pi^0$ using the *in/out* configuration 1110000101.

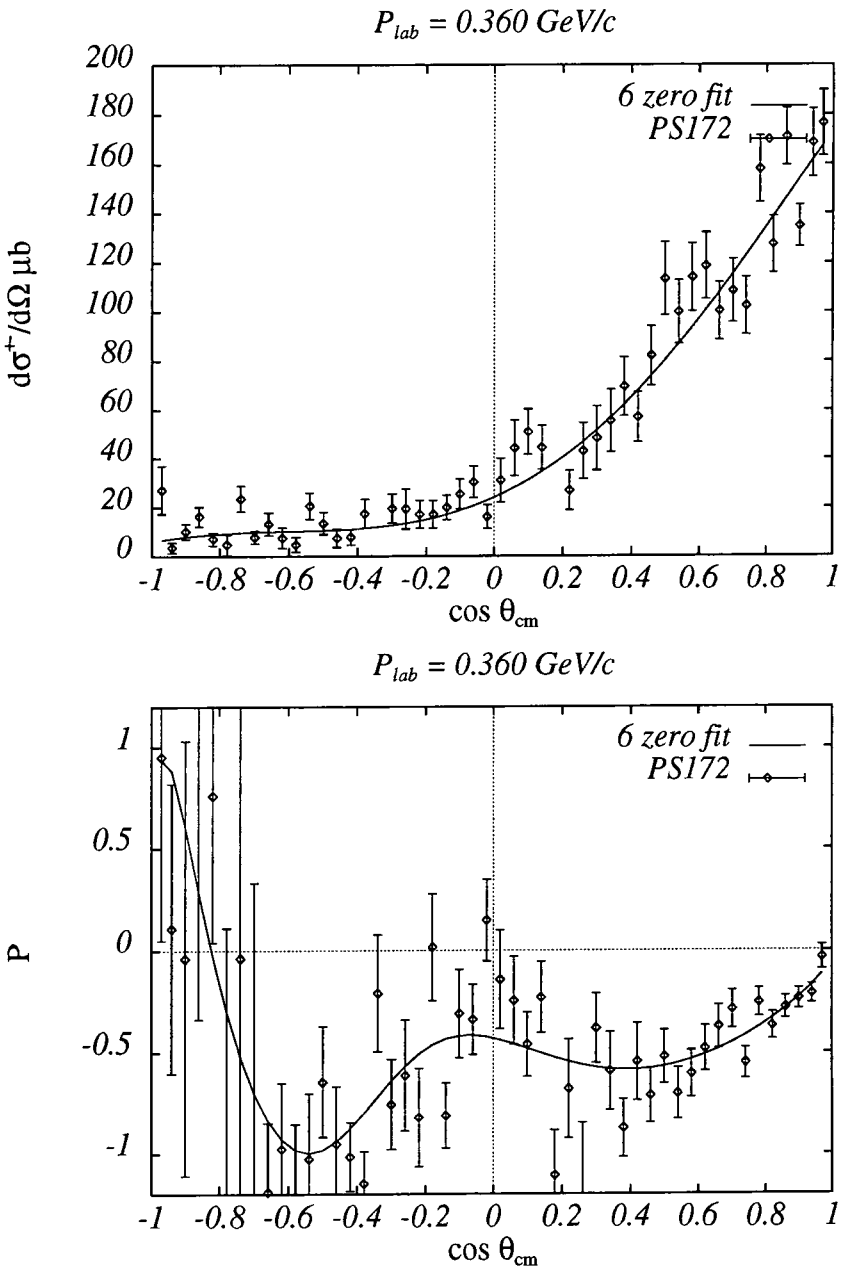

Figure 3.14: Fits to the PS172 measurements of $d\sigma^c/d\Omega$ and P^c at 0.360 GeV/c .

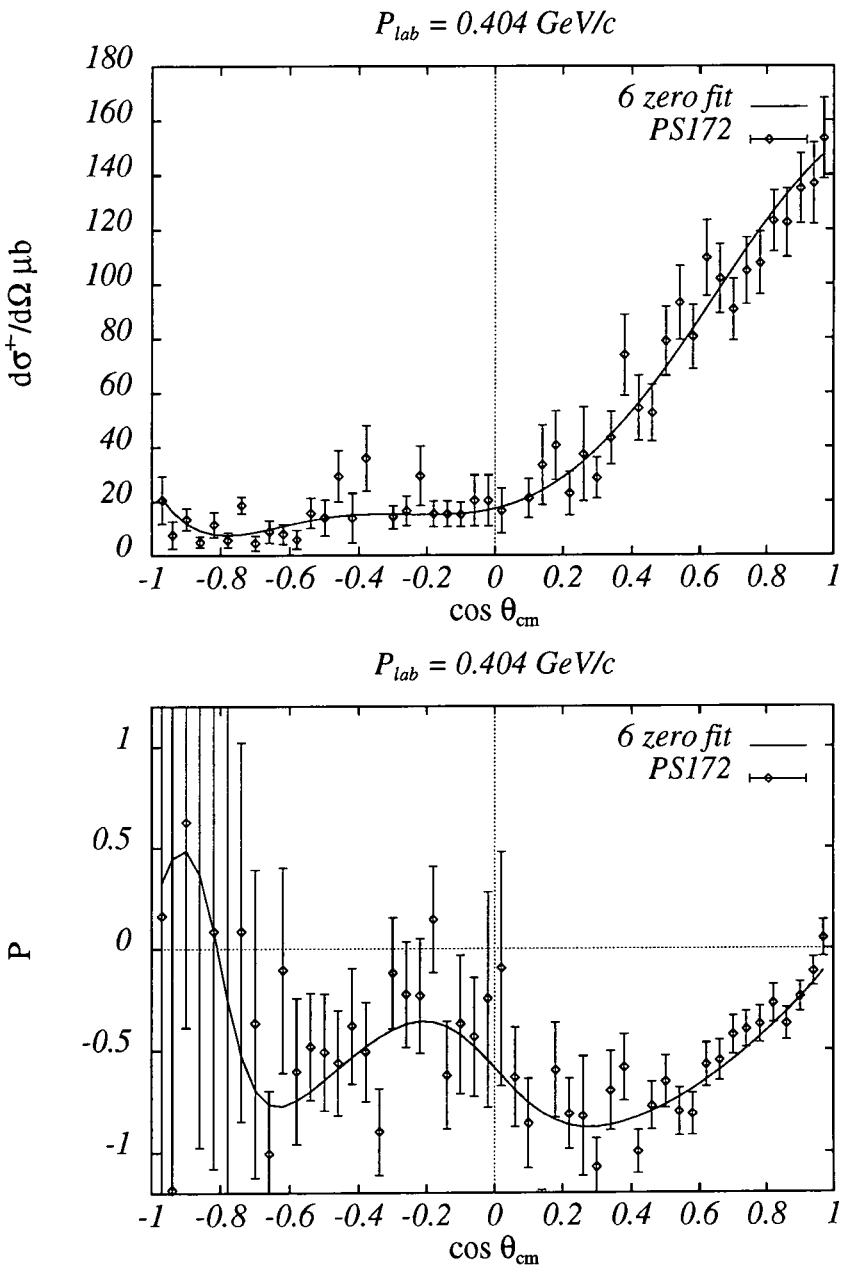

Figure 3.15: Fits to the PS172 measurements of $d\sigma^c/d\Omega$ and P^c at 0.404 GeV/c .

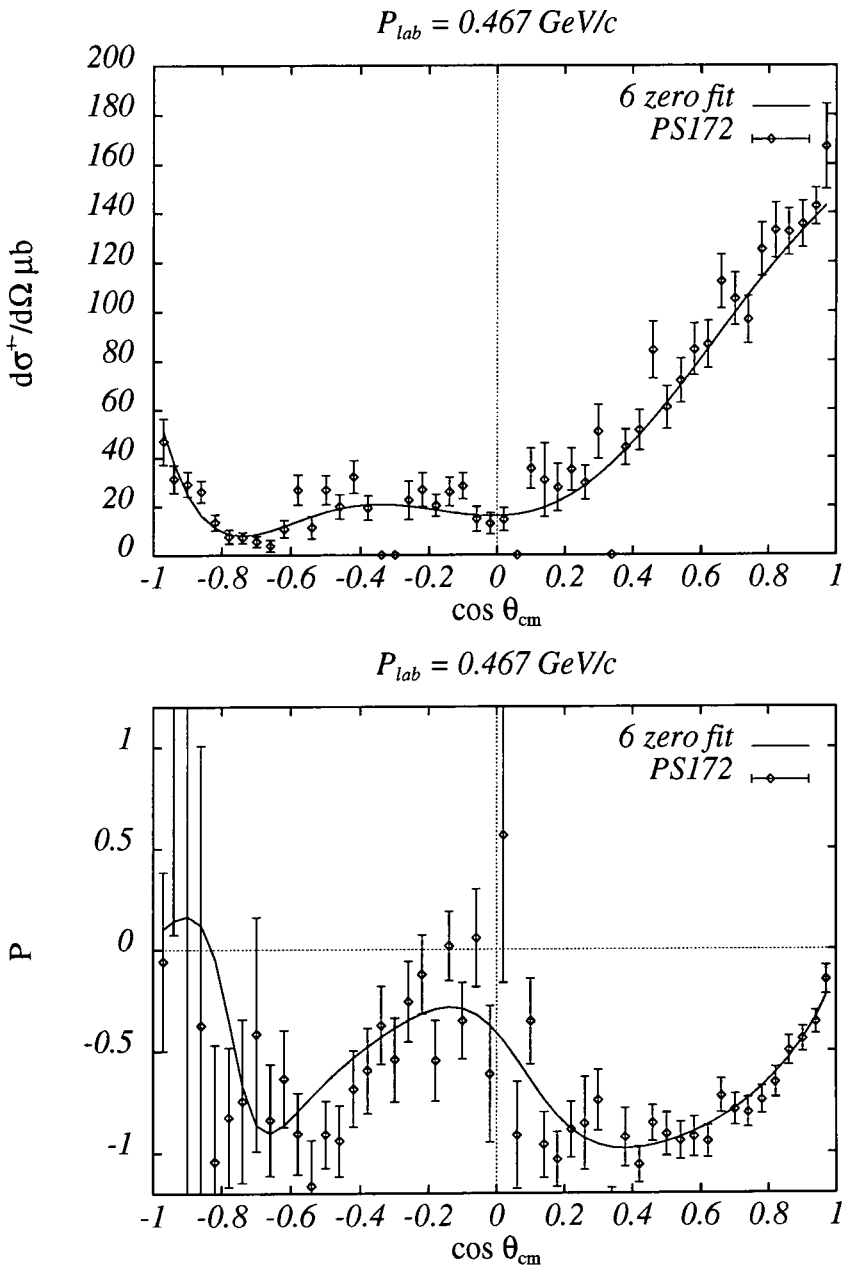

Figure 3.16: Fits to the PS172 measurements of $d\sigma^c/d\Omega$ and P^c at 0.467 GeV/c .

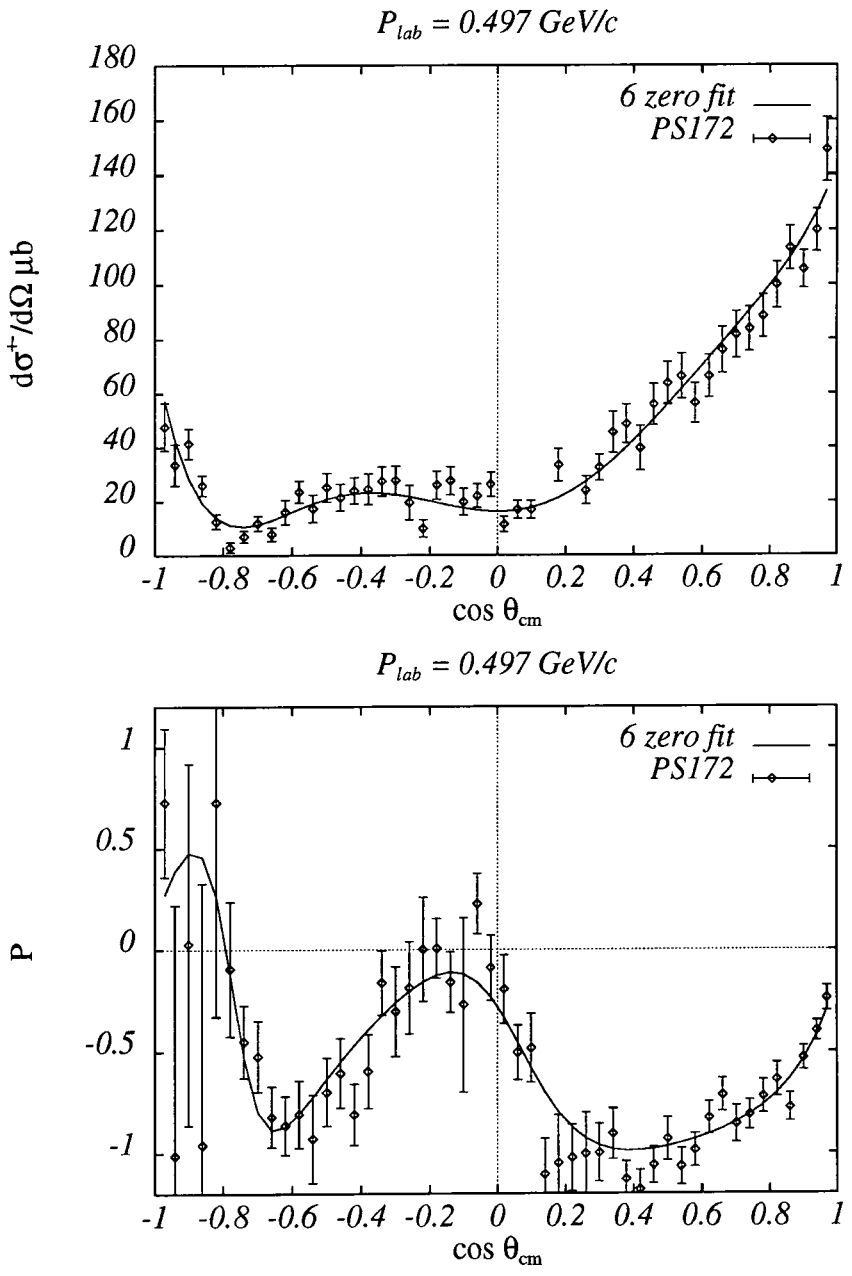

Figure 3.17: Fits to the PS172 measurements of $d\sigma^c/d\Omega$ and P^c at 0.497 GeV/c .

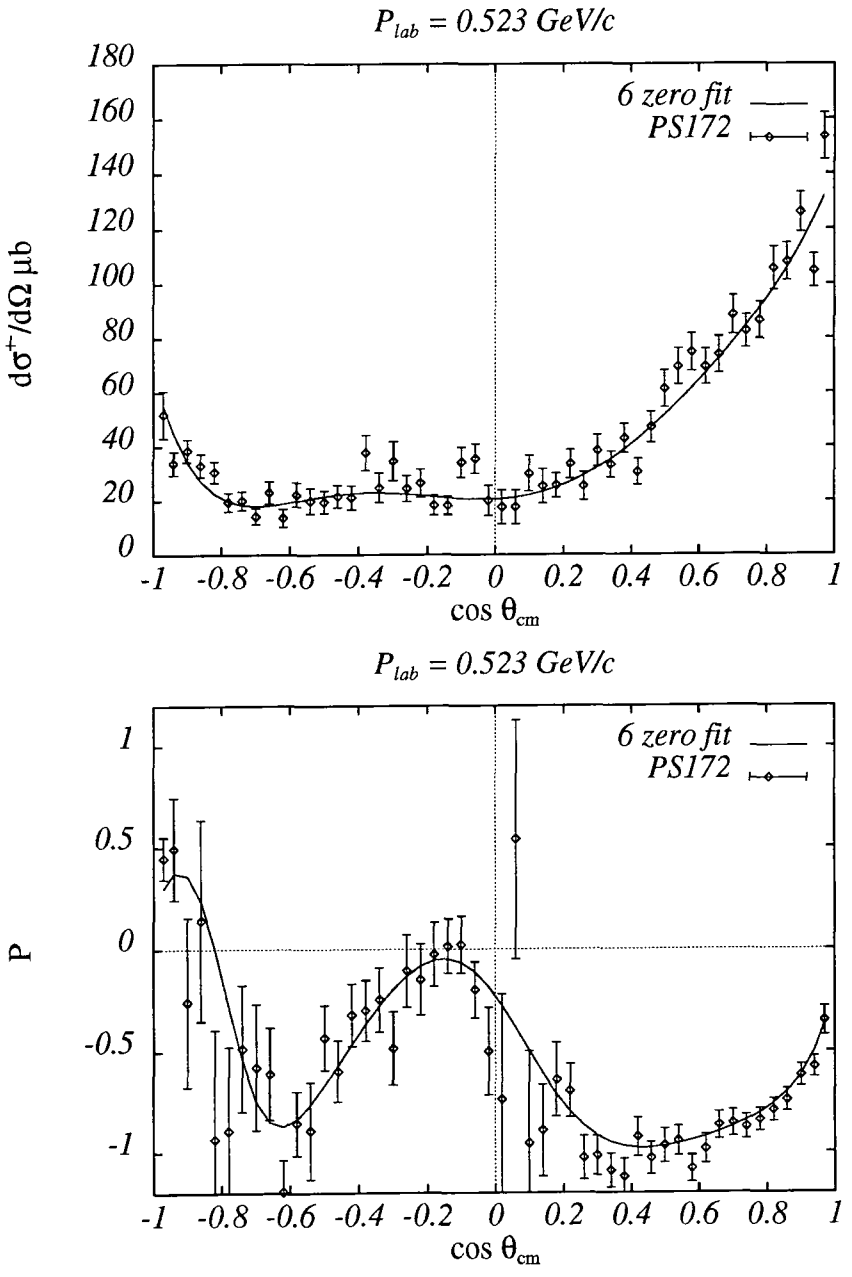

Figure 3.18: Fits to the PS172 measurements of $d\sigma^c/d\Omega$ and P^c at 0.523 GeV/c .

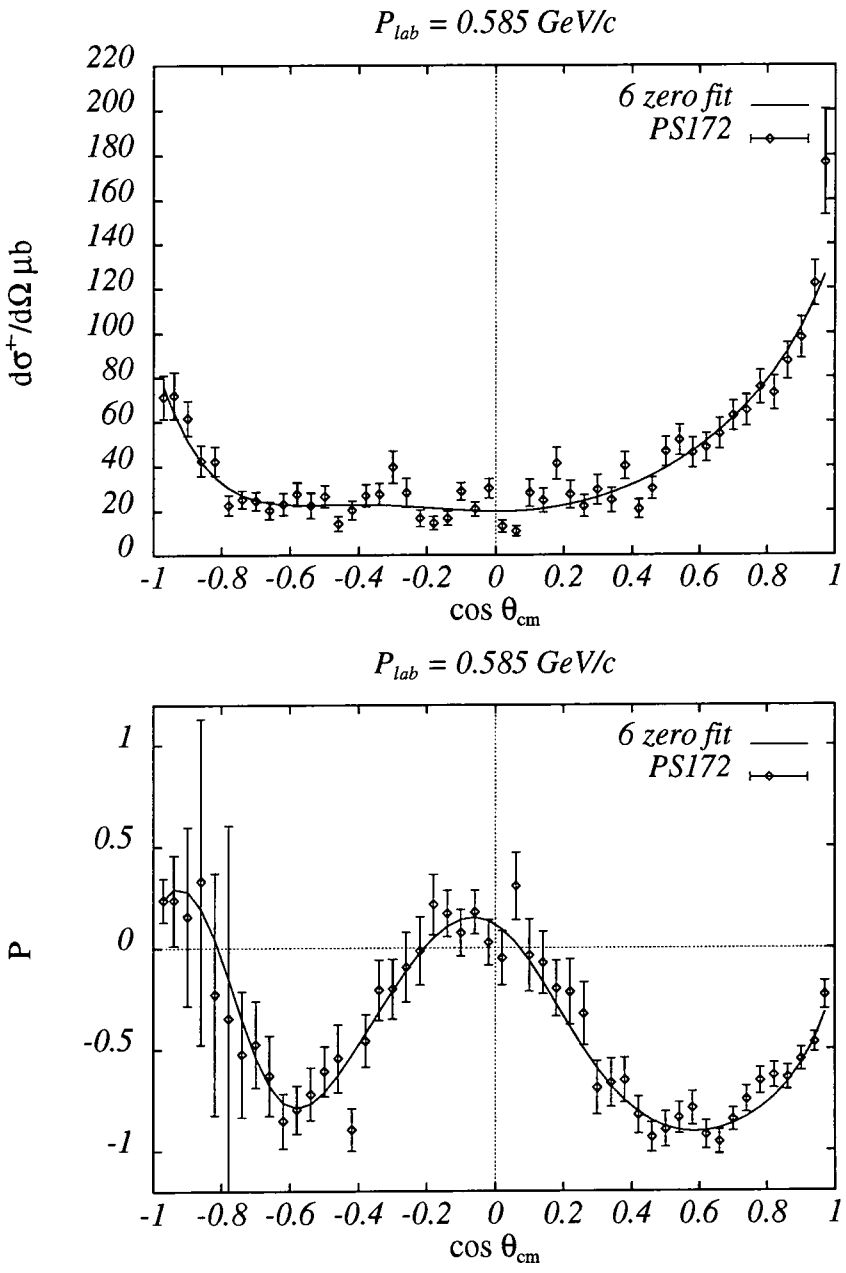

Figure 3.19: Fits to the PS172 measurements of $d\sigma^c/d\Omega$ and P^c at 0.585 GeV/c .

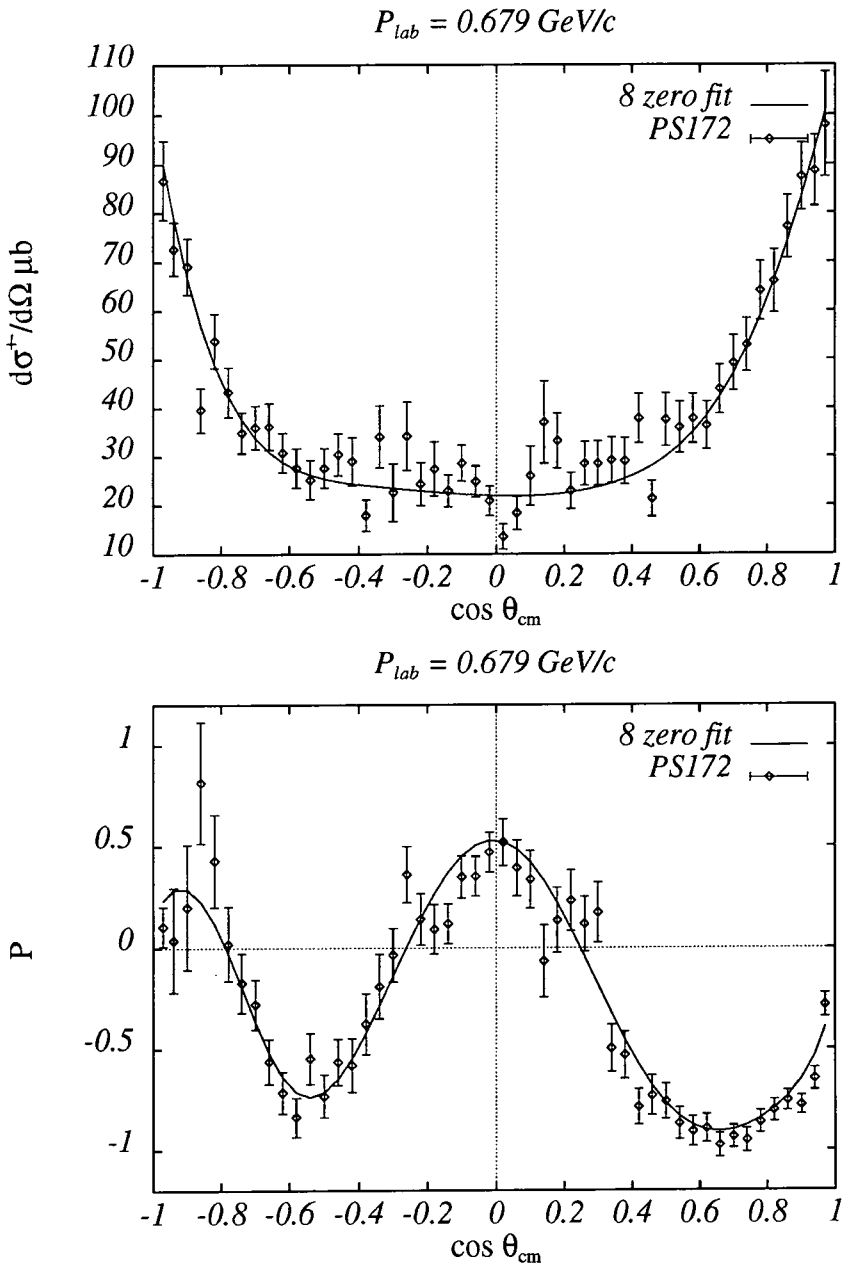

Figure 3.20: Fits to the PS172 measurements of $d\sigma^c/d\Omega$ and P^c at 0.679 GeV/c .

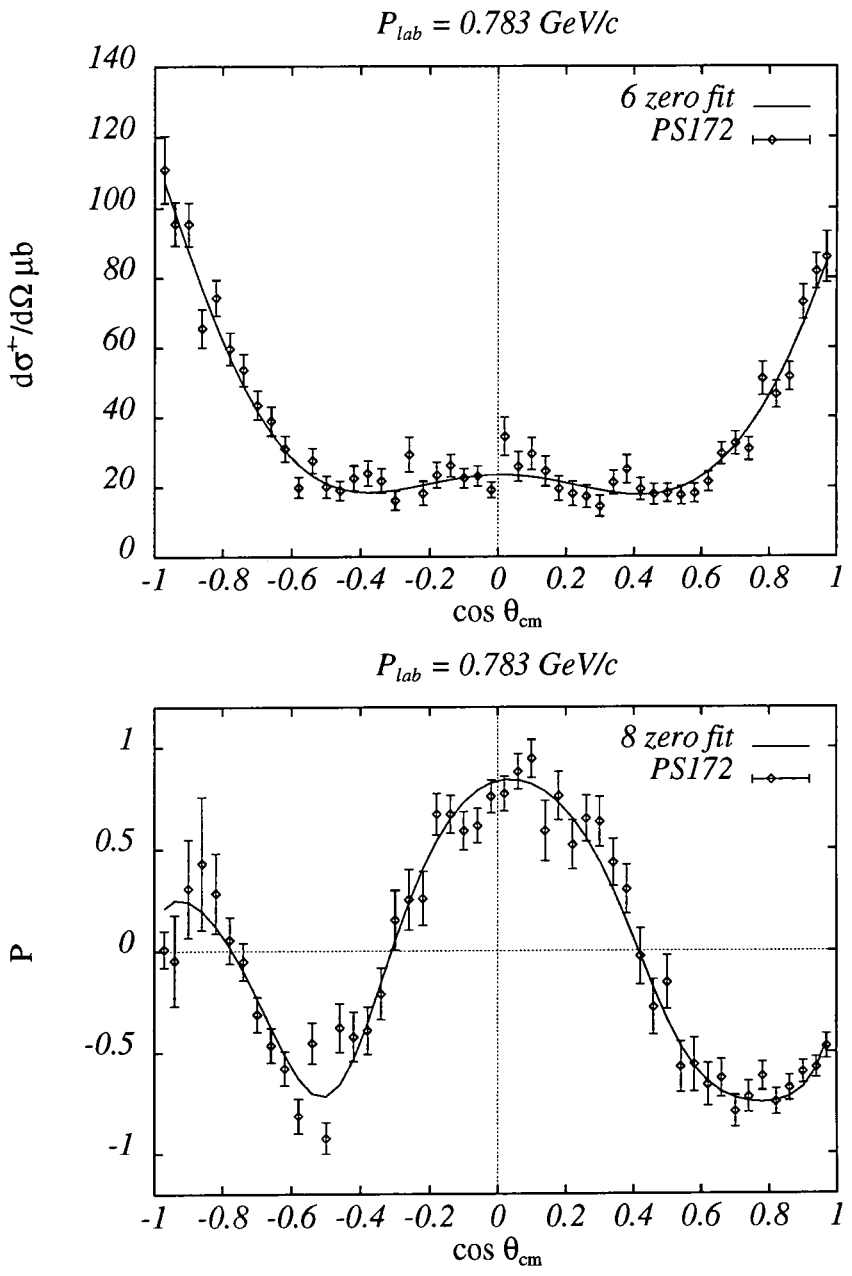

Figure 3.21: Fits to the PS172 measurements of $d\sigma^c/d\Omega$ and P^c at 0.783 GeV/c .

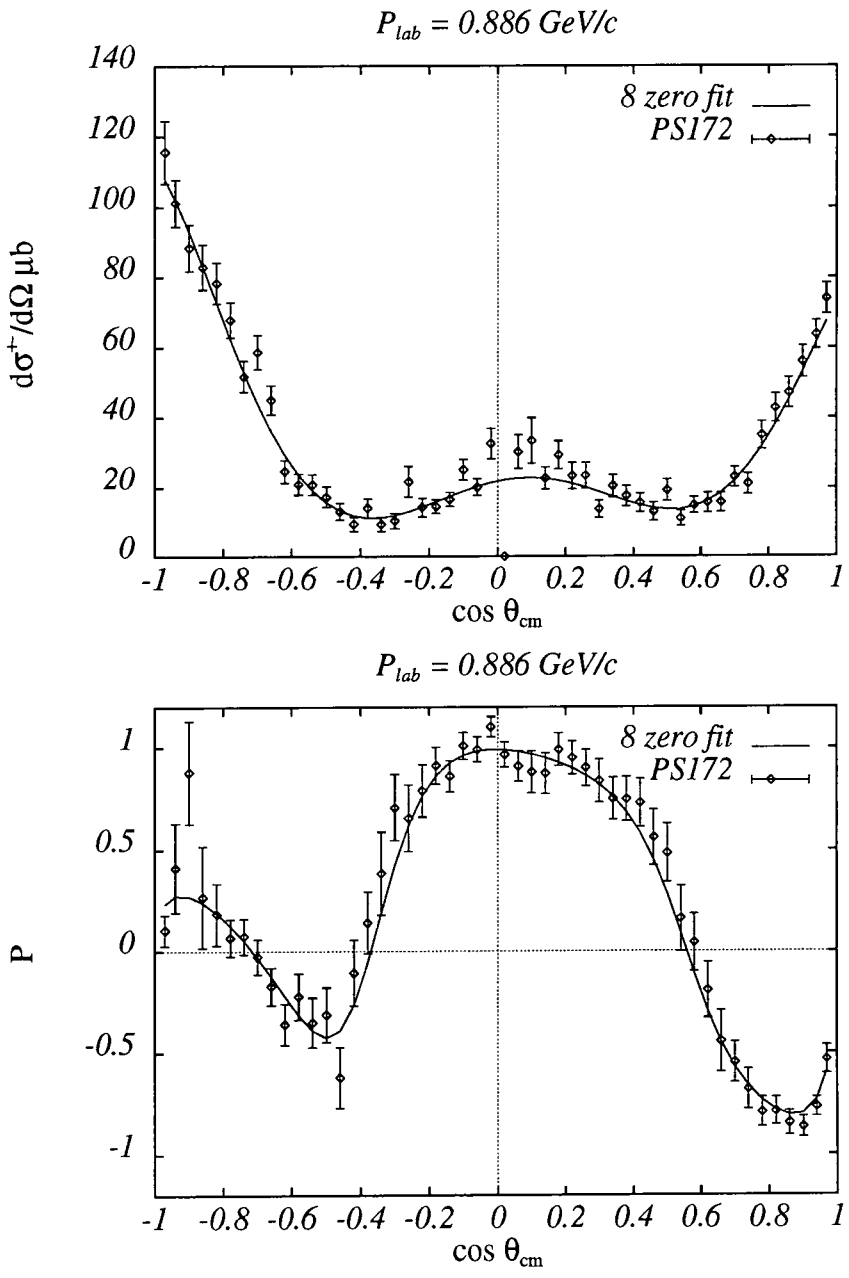

Figure 3.22: Fits to the PS172 measurements of $d\sigma^c/d\Omega$ and P^c at 0.886 GeV/c .

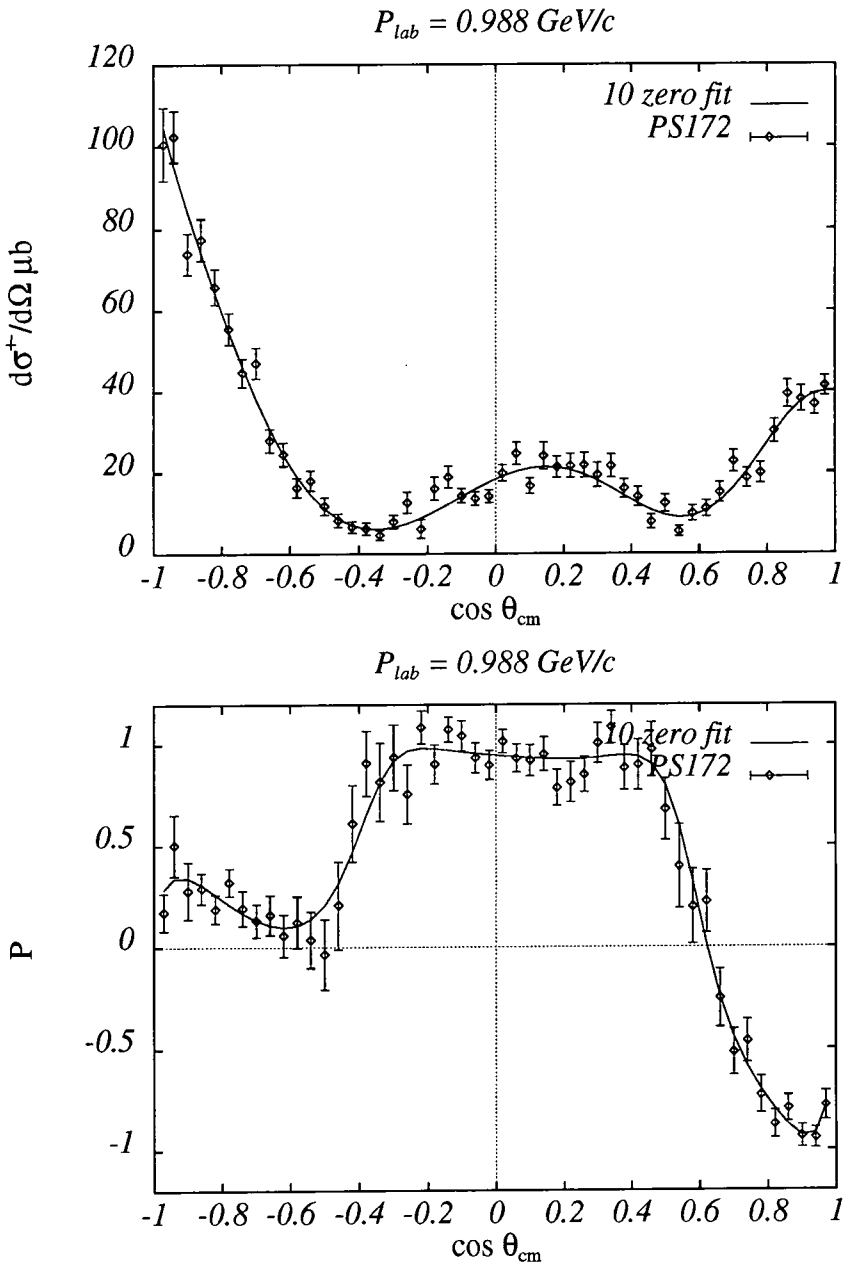

Figure 3.23: Fits to the PS172 measurements of $d\sigma^c/d\Omega$ and P^c at 0.988 GeV/c .

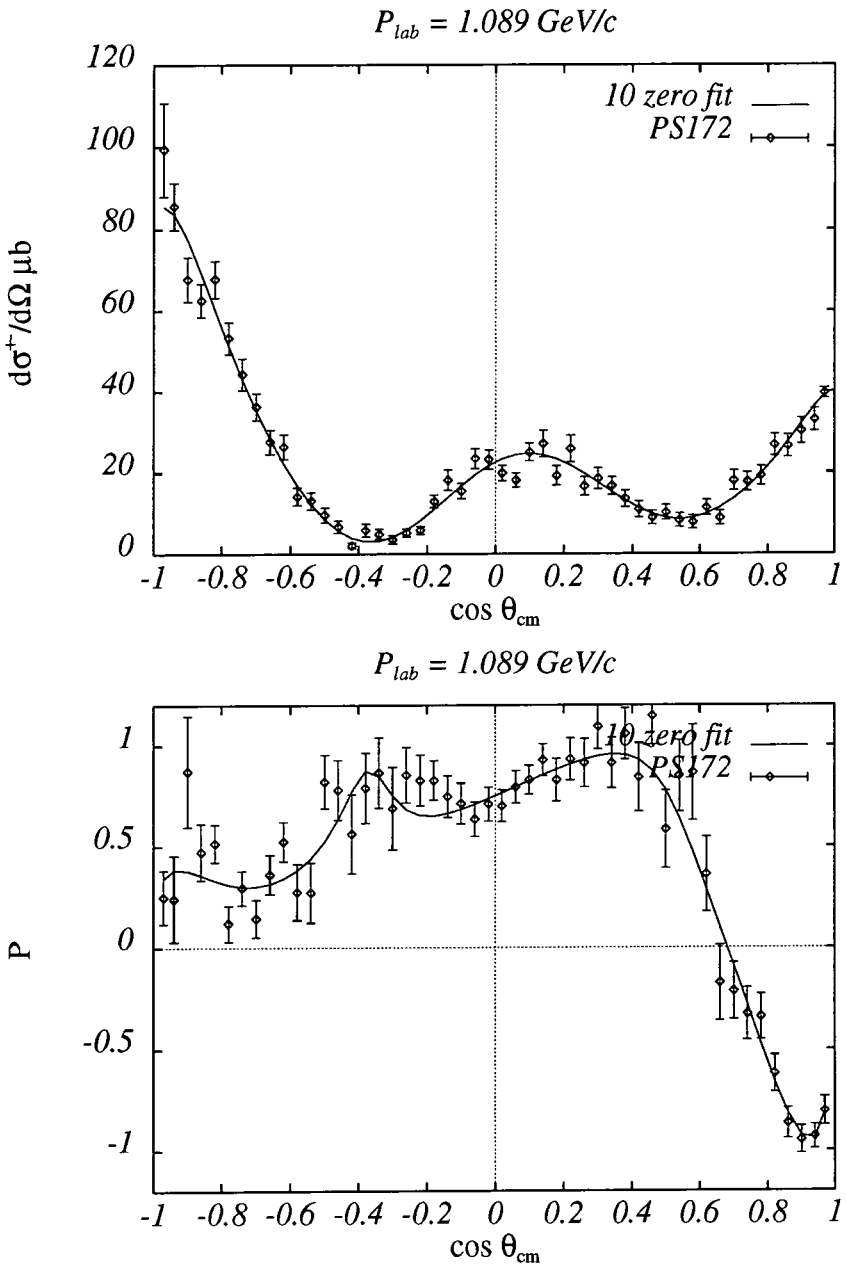

Figure 3.24: Fits to the PS172 measurements of $d\sigma^c/d\Omega$ and P^c at 1.089 GeV/c .

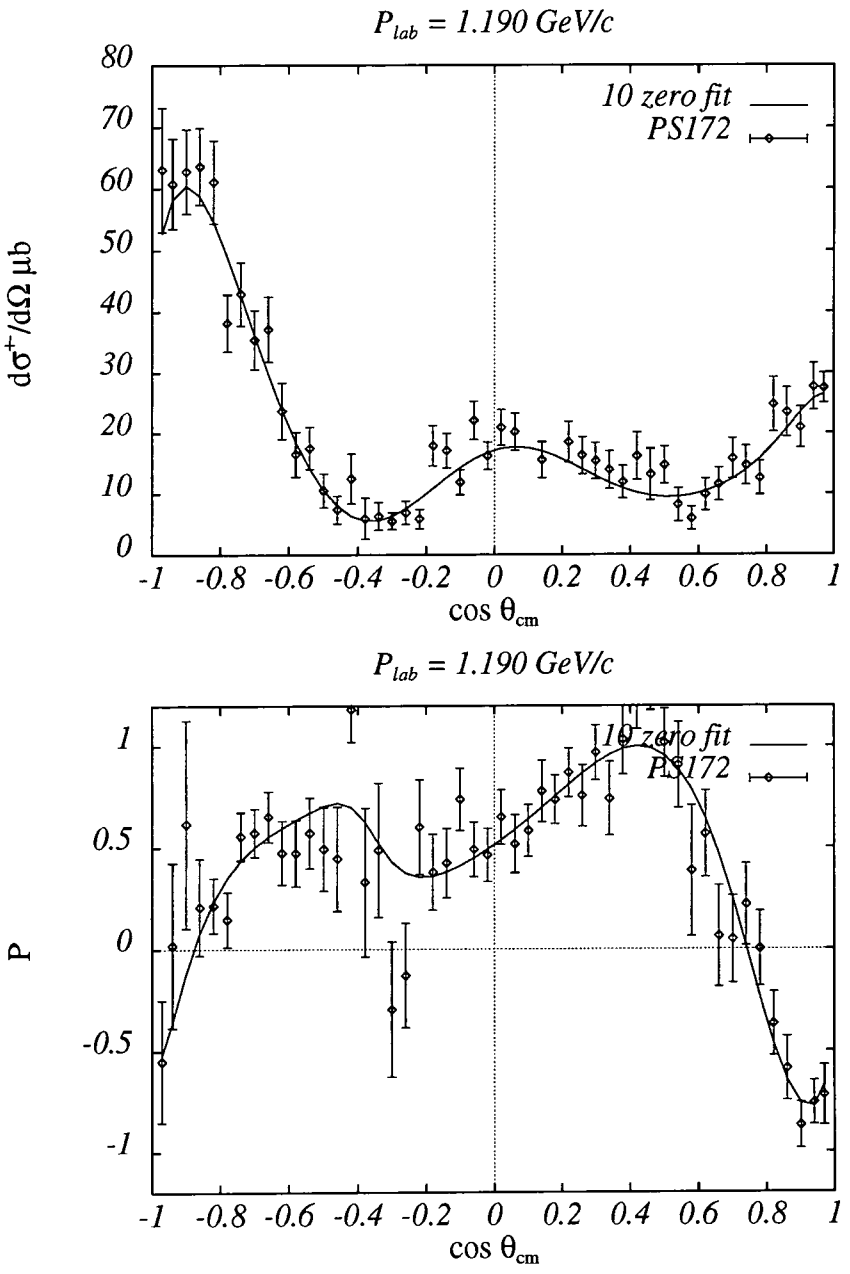

Figure 3.25: Fits to the PS172 measurements of $d\sigma^c/d\Omega$ and P^c at 1.190 GeV/c .

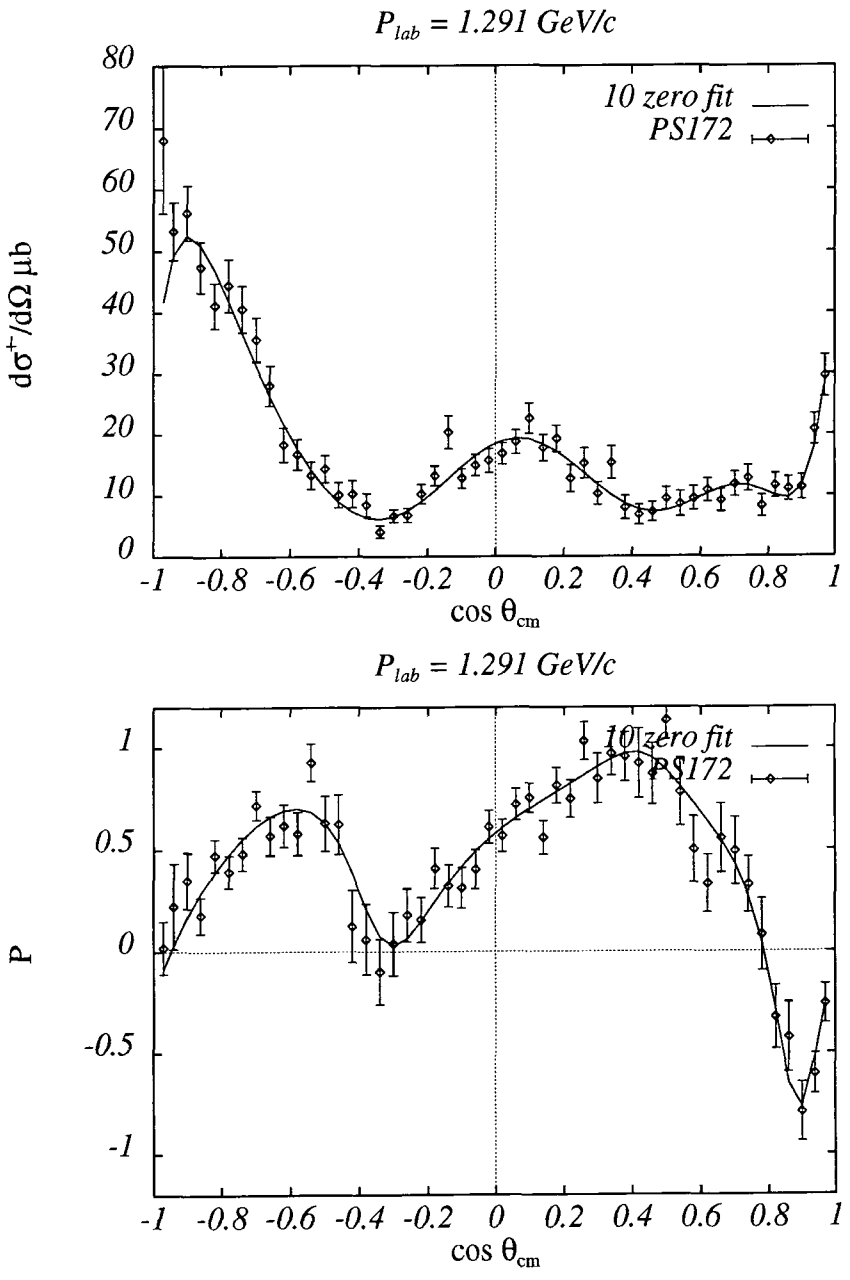

Figure 3.26: Fits to the PS172 measurements of $d\sigma^c/d\Omega$ and P^c at 1.291 GeV/c .

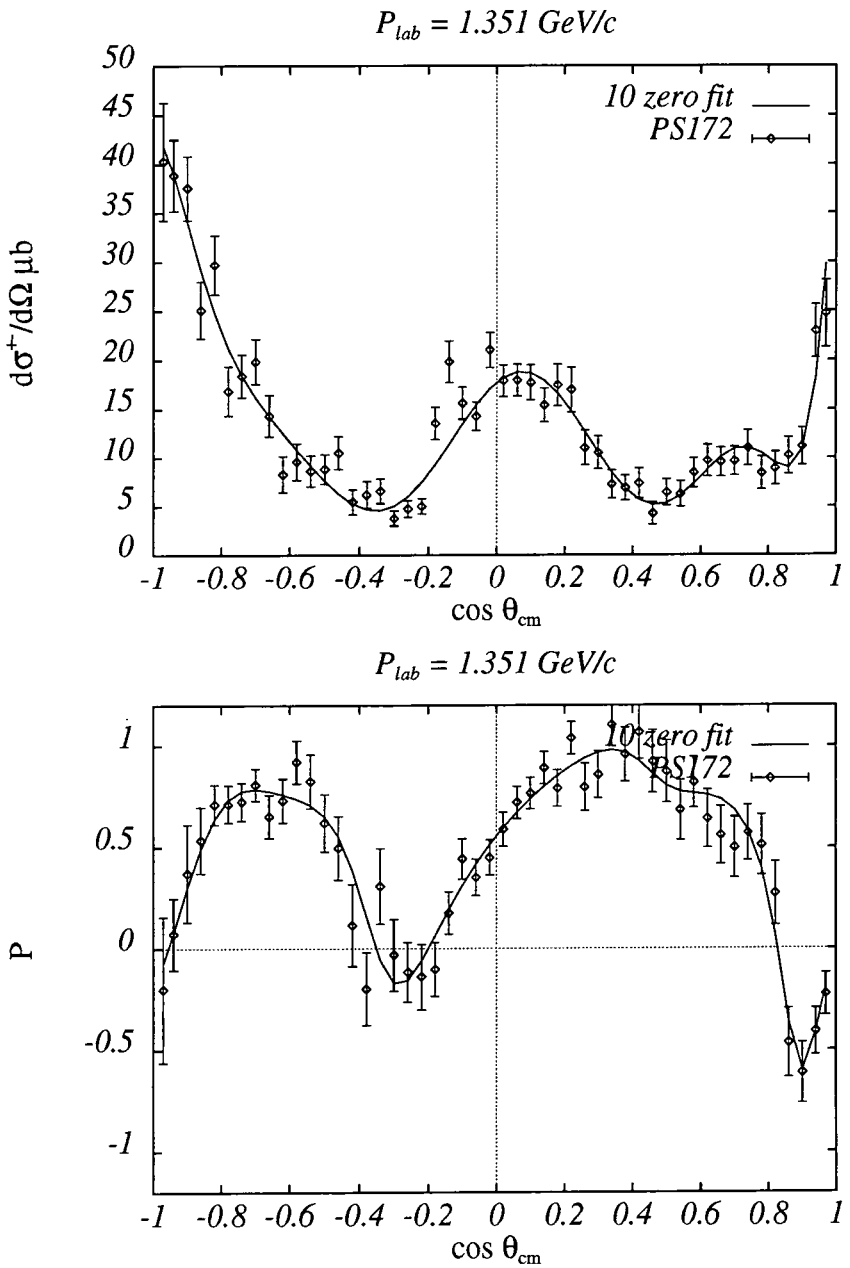

Figure 3.27: Fits to the PS172 measurements of $d\sigma^c/d\Omega$ and P^c at 1.351 GeV/c .

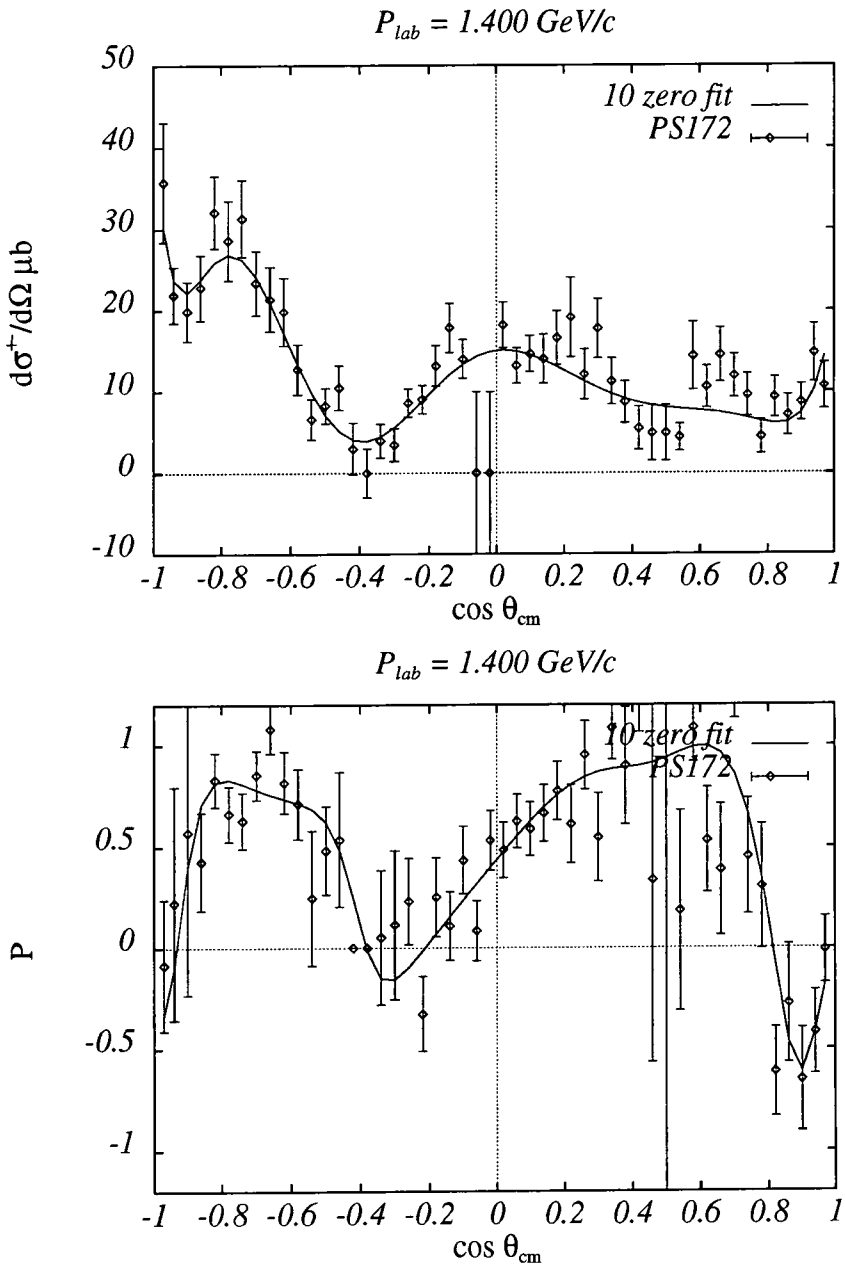

Figure 3.28: Fits to the PS172 measurements of $d\sigma^c/d\Omega$ and P^c at 1.400 GeV/c .

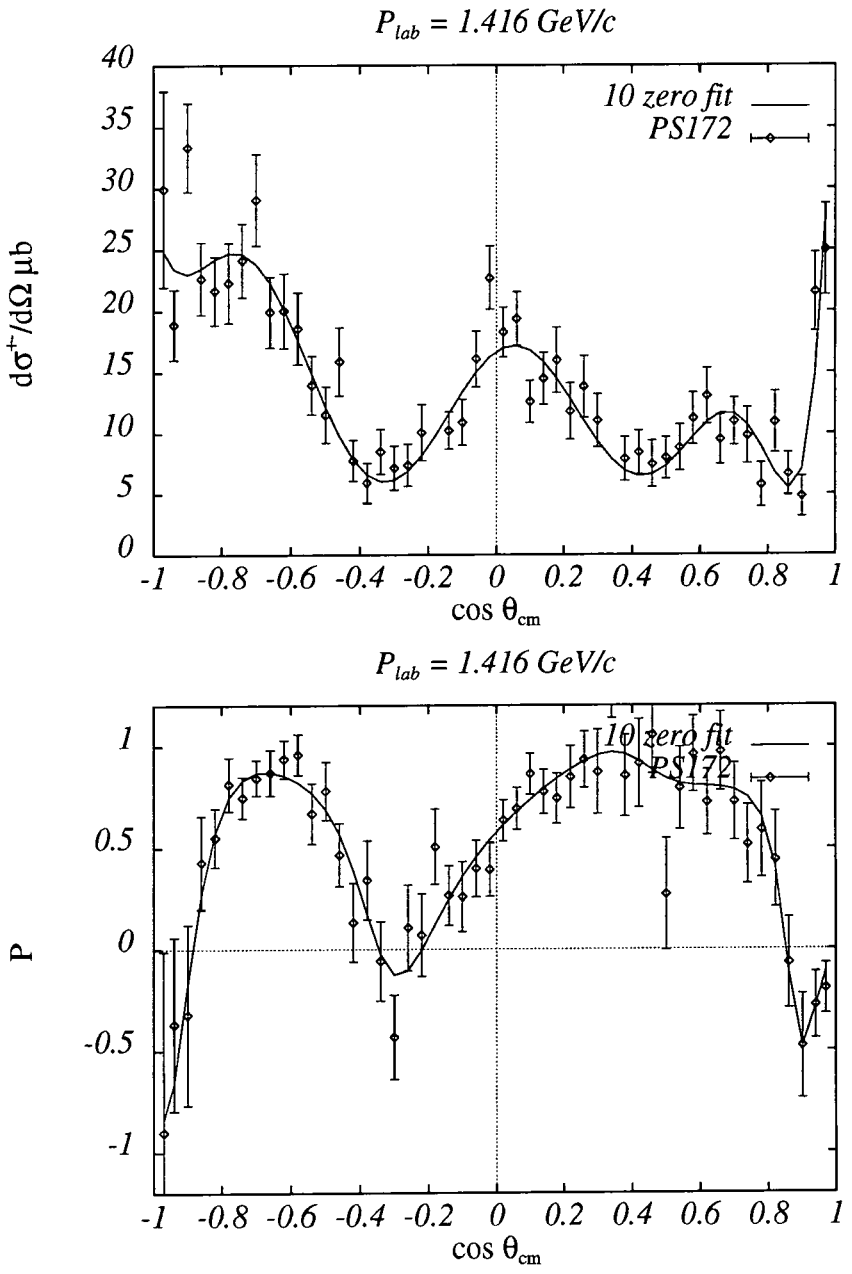

Figure 3.29: Fits to the PS172 measurements of $d\sigma^c/d\Omega$ and P^c at 1.416 GeV/c .

Figs. 3.34–3.38 show the corresponding neutral channel fits. The solid curve indicates the fit to both channels simultaneously, while the dashed curve shows the "prediction" for the neutral channel cross-section implied by the zero positions of Fig. 3.9 taking them to be in the configuration 1110000101. A marked improvement is seen, especially considering the small movements of the Barrelet zeros required to produce this.

Of course, although this procedure has resulted, at least up to the Minami ambiguity, in just one zero configuration (Table 3.2), and hence just one solution for the amplitude,

Threshold pairing							⌒		⌒	
Zero	A	B	C	D	E	F	G	H	I	J
In/out	1	1	1	0	0	0	0	1	0	1

Table 3.2: Zero configuration **I**. A 1(0) indicates a zero is inside(outside) the unit circle.

this configuration only applies to the region $P_lab > 1$ GeV/c where the neutral channel data are available. How to extend this knowledge down below 1 GeV/c has not yet been discussed. The natural approach would be to assume that this configuration is "frozen in", i.e. that the zeros remain in this *in/out* configuration as the lab momentum decreases and the threshold is approached. Indeed, this has already been tacitly assumed for the threshold paired zeros $\{G, H\}$ and $\{I, J\}$ in that the threshold condition that they disappear on opposite sides of the unit circle has been applied to their *in/out* configuration in the region $P_{lab} > 1$ GeV/c even though the momenta at which they disappear are somewhat less than 1 GeV/c . This freezing in of the configuration must, however, be applied with caution. Here, naively applying the configuration of Table 3.2 throughout the PS172 energy range does indeed lead to an acceptable solution but this is not the whole story. There is another possible (indeed perhaps more likely!) solution which could be missed if the above freezing in were applied without care. This second solution arises from the fact that the zero labelled E in Figs. 3.8 and 3.13 approaches *extremely* close to the unit circle at around $P_{lab} = 1$ GeV/c . This means that although

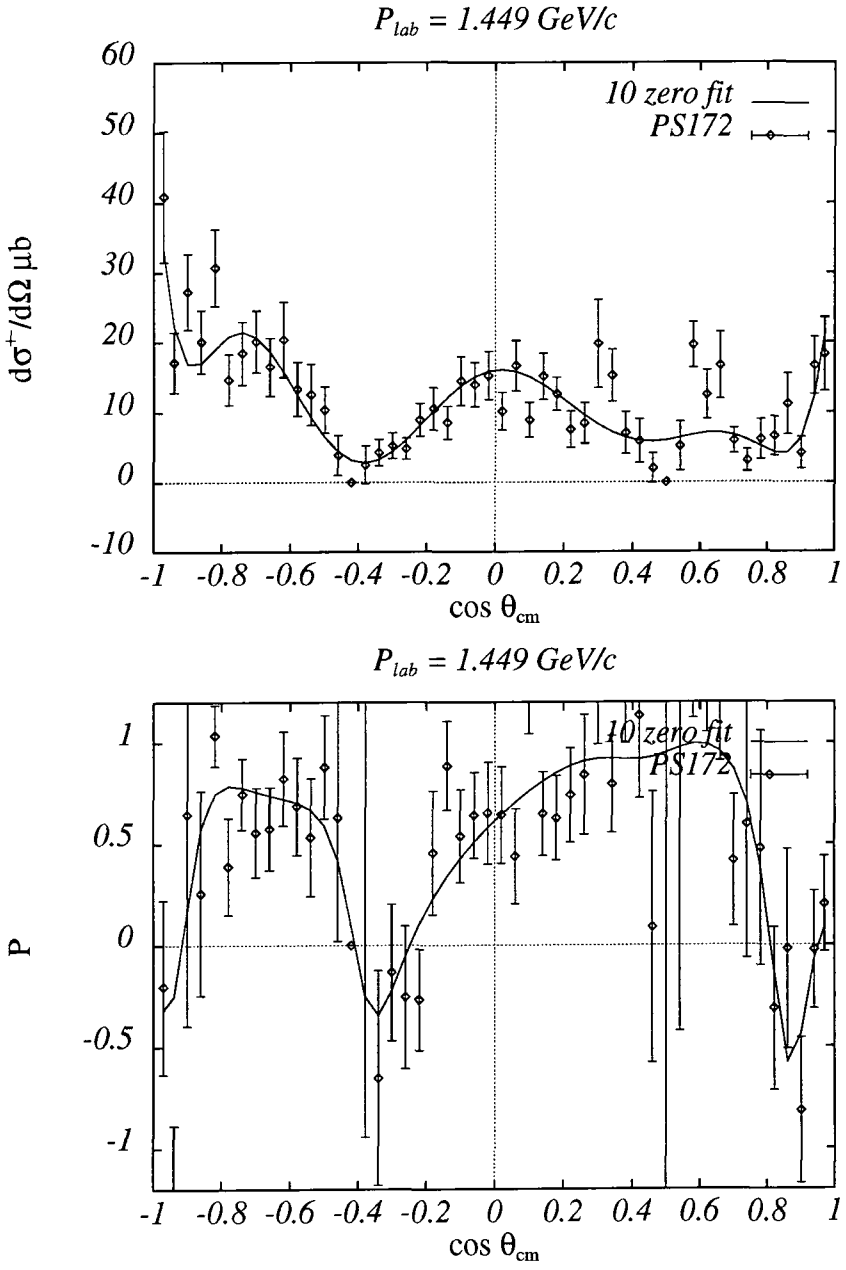

Figure 3.30: Fits to the PS172 measurements of $d\sigma^c/d\Omega$ and P^c at 1.449 GeV/c .

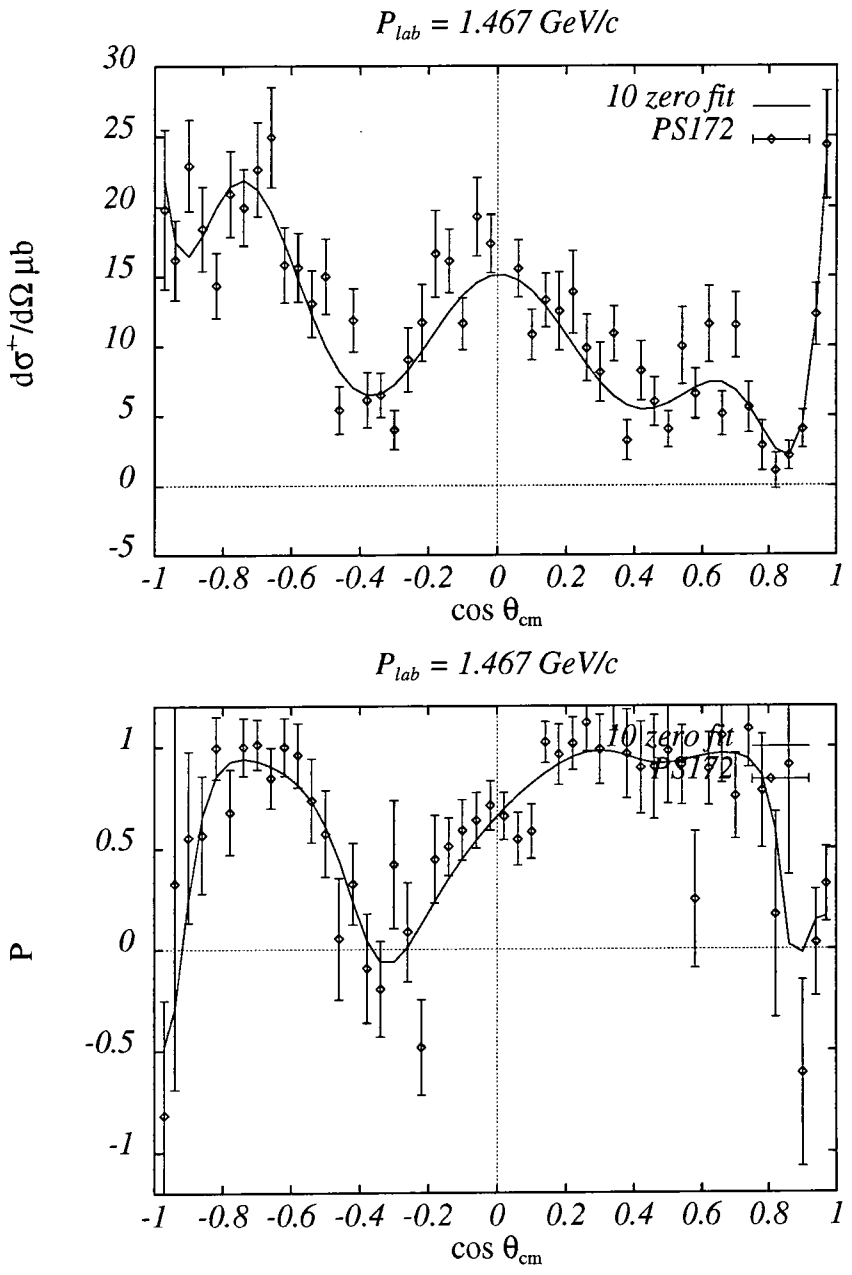

Figure 3.31: Fits to the PS172 measurements of $d\sigma^c/d\Omega$ and P^c at 1.467 GeV/c .

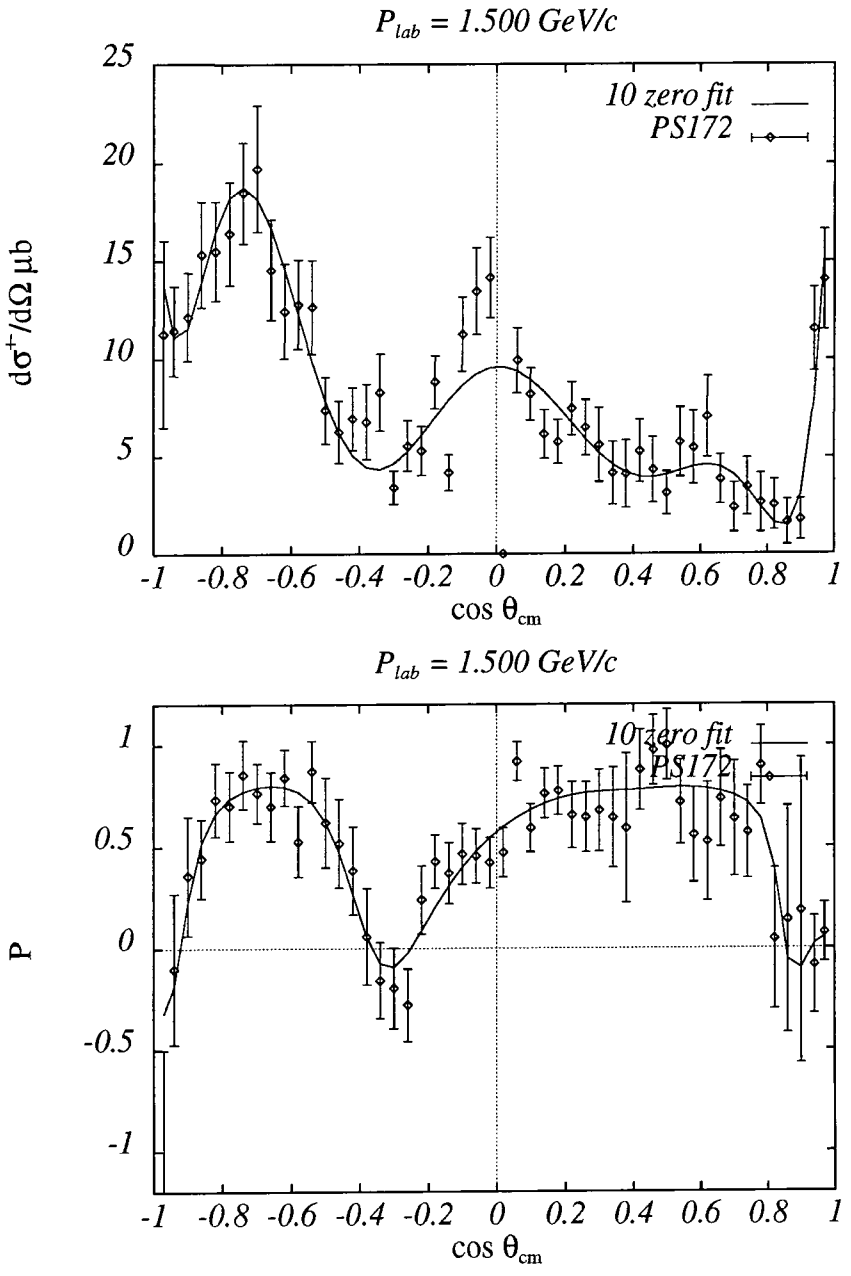

Figure 3.32: Fits to the PS172 measurements of $d\sigma^c/d\Omega$ and P^c at 1.500 GeV/c .

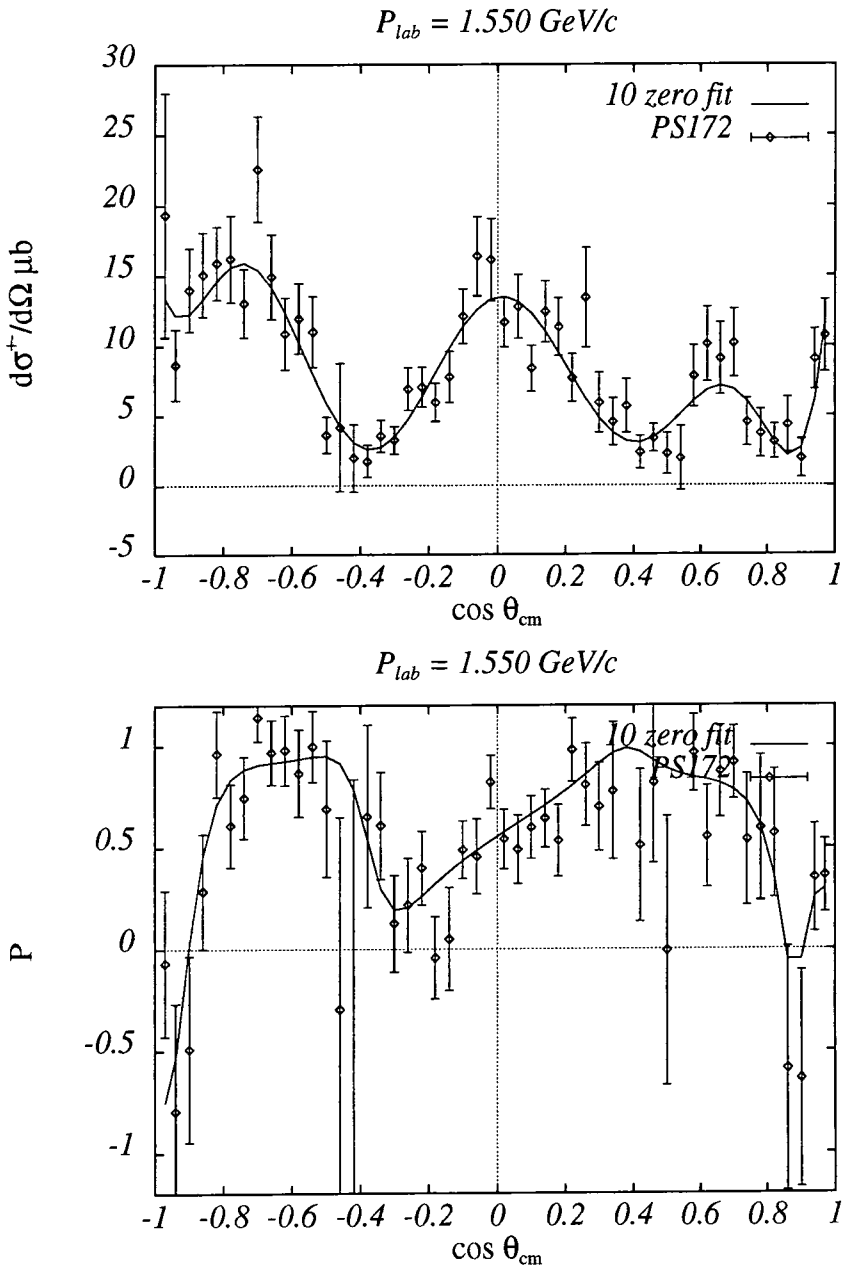

Figure 3.33: Fits to the PS172 measurements of $d\sigma^c/d\Omega$ and P^c at 1.550 GeV/c .

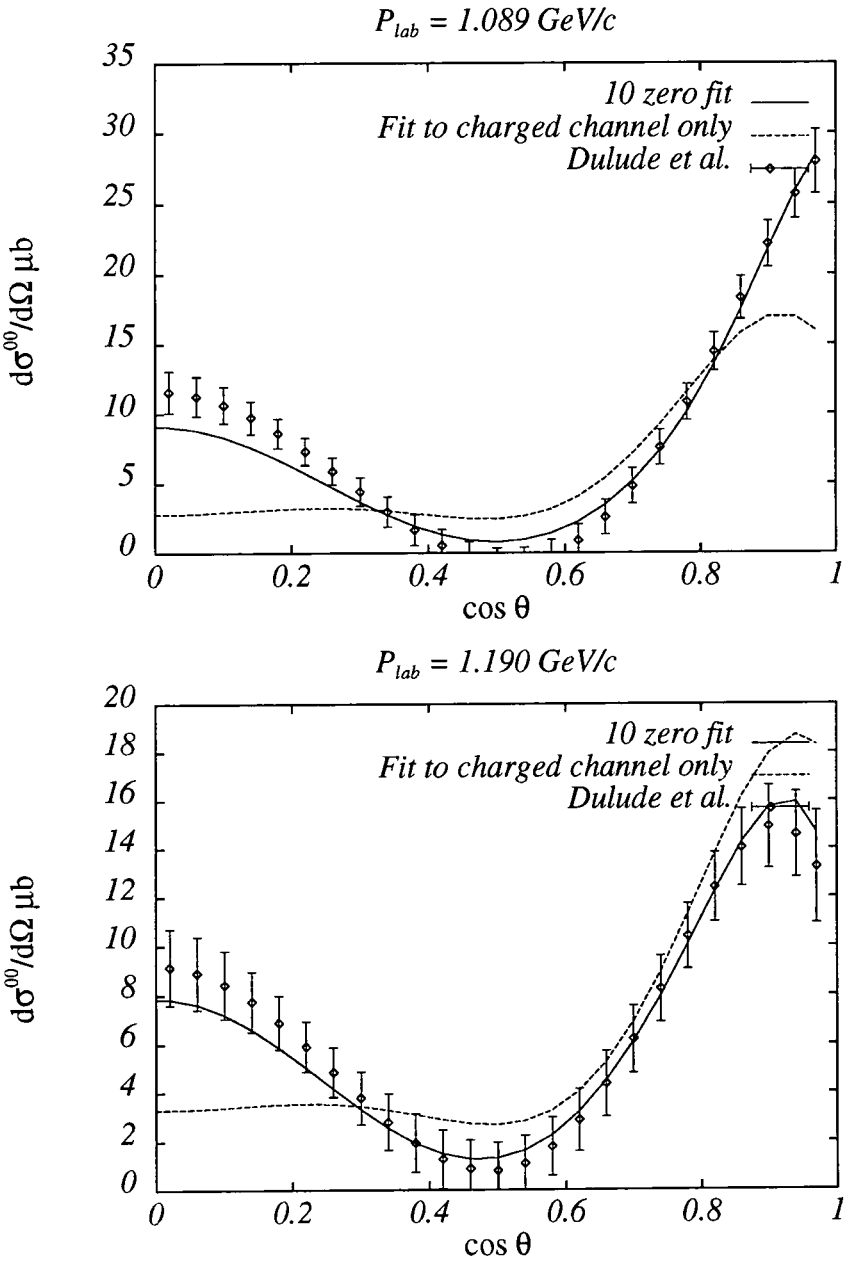

Figure 3.34: Fits to the Dulude *et al.* measurements of $d\sigma^n/d\Omega$ at 1.089 and 1.190 GeV/c (solid curves) compared with predictions from fits to the charged channel observables only (dashed curves).

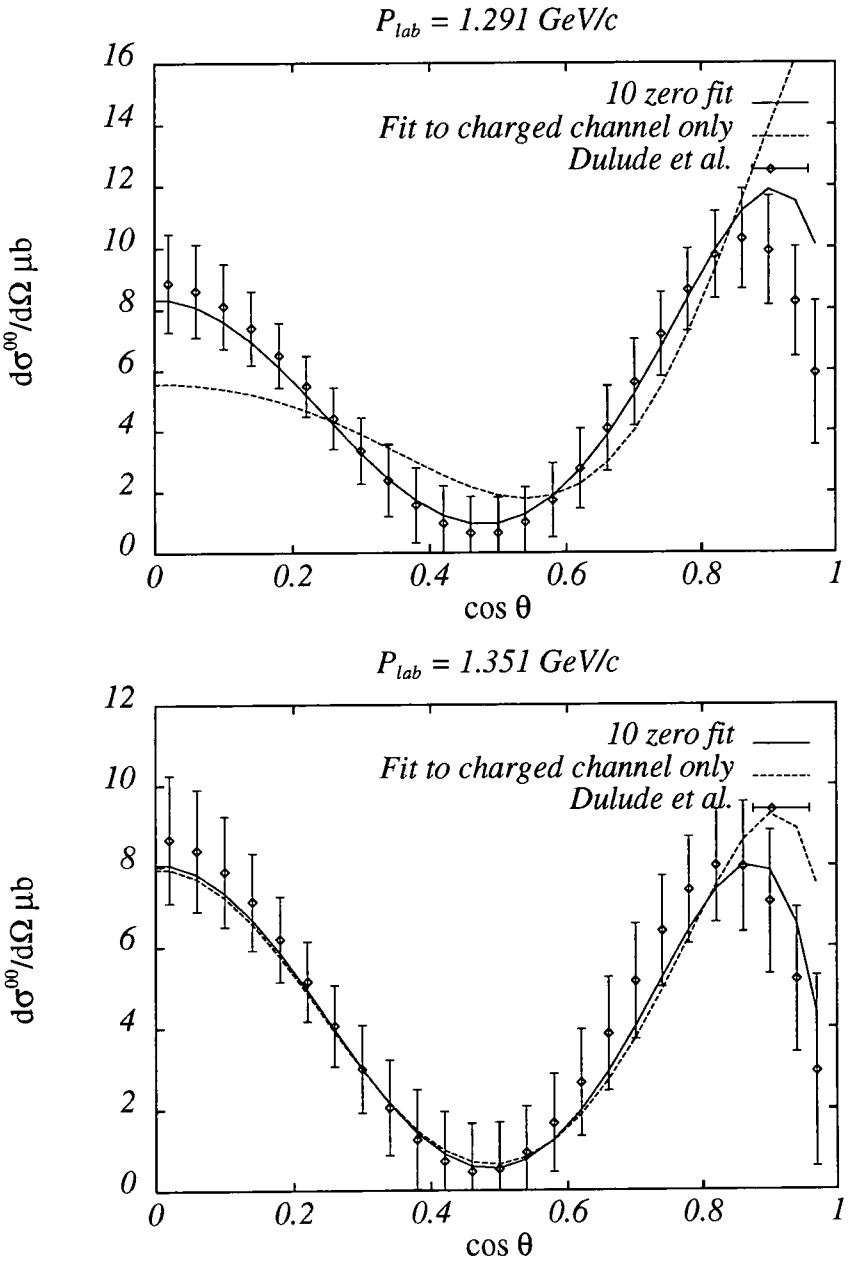

Figure 3.35: Fits to the Dulude *et al.* measurements of $d\sigma^n/d\Omega$ at 1.291 and 1.351 GeV/c (solid curves) compared with predictions from fits to the charged channel observables only (dashed curves).

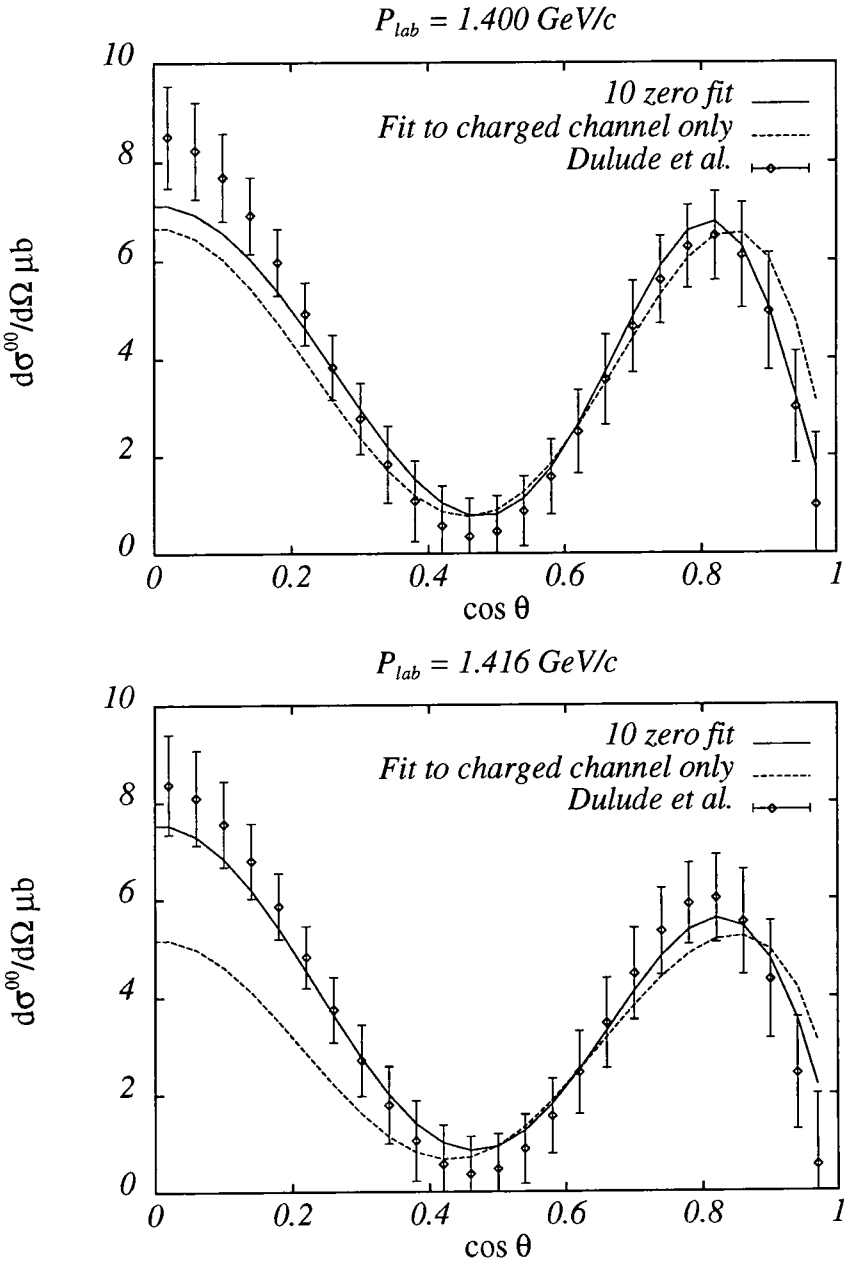

Figure 3.36: Fits to the Dulude *et al.* measurements of $d\sigma^n/d\Omega$ at 1.400 and 1.416 GeV/c (solid curves) compared with predictions from fits to the charged channel observables only (dashed curves).

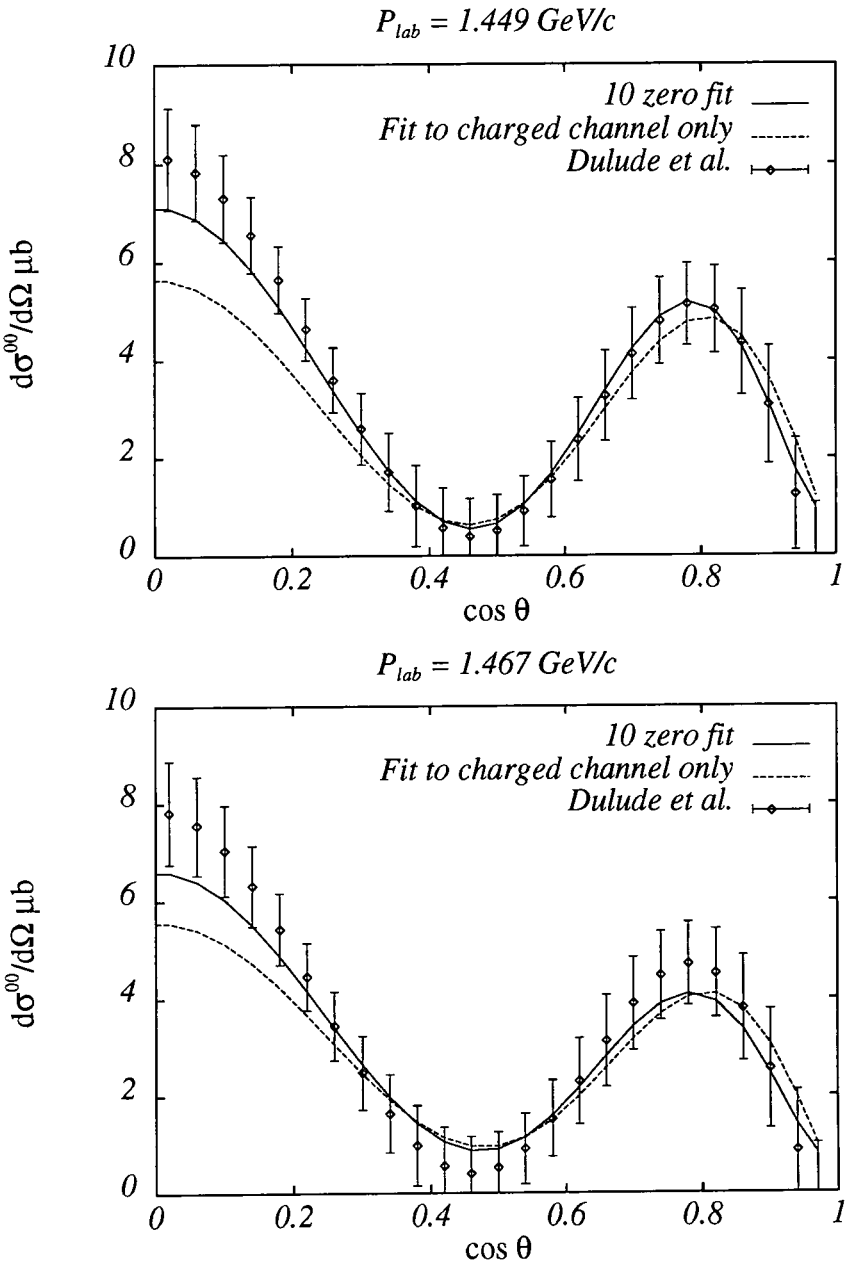

Figure 3.37: Fits to the Dulude *et al.* measurements of $d\sigma^n/d\Omega$ at 1.449 and 1.467 GeV/c (solid curves) compared with predictions from fits to the charged channel observables only (dashed curves).

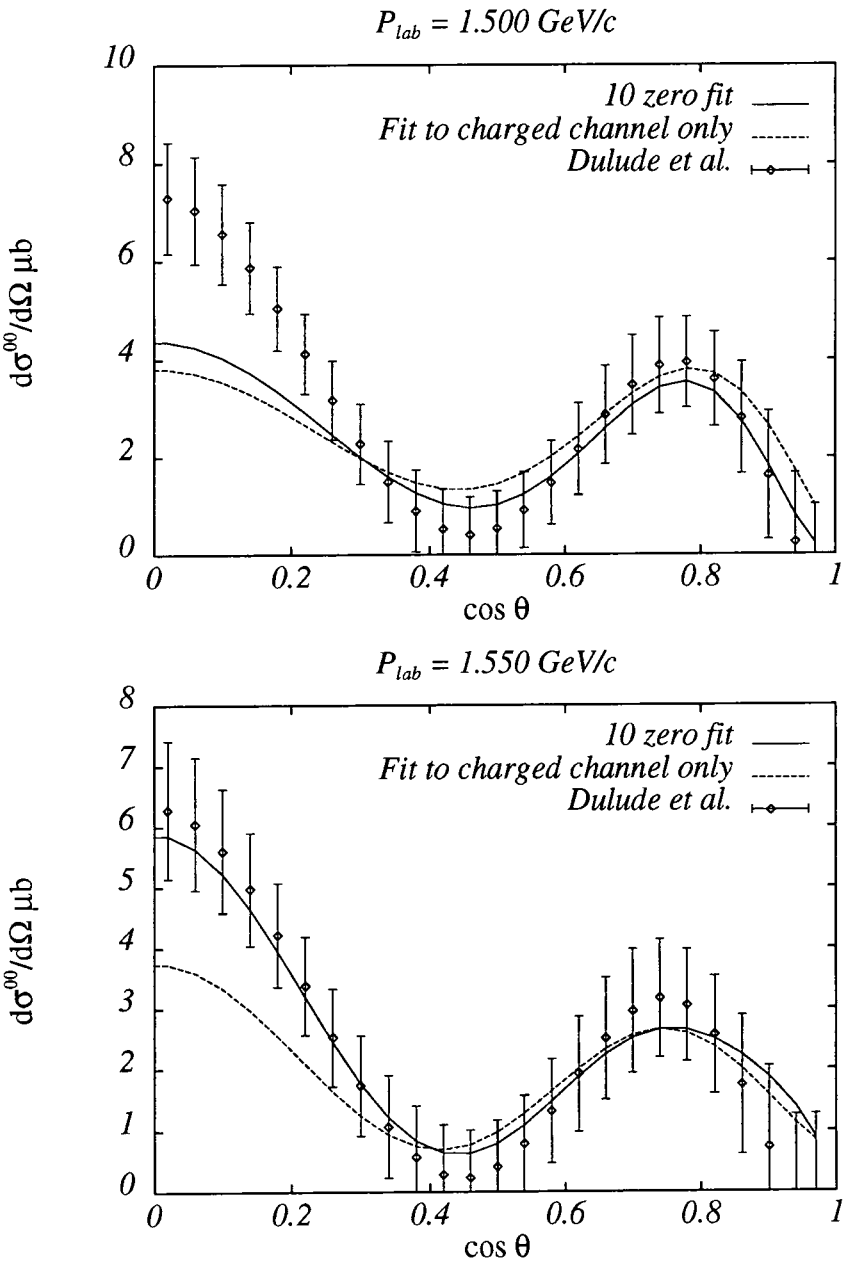

Figure 3.38: Fits to the Dulude *et al.* measurements of $d\sigma^n/d\Omega$ at 1.500 and 1.550 GeV/c (solid curves) compared with predictions from fits to the charged channel observables only (dashed curves).

the *in/out* configuration is determined above 1 GeV/c , this zero may cross the circle around this energy, leading to a different configuration (Table 3.3) in the region below 1 GeV/c . This is perhaps desirable since the zero E appears, in Fig. 3.8 to be heading

Threshold pairing					⌒		⌒		⌒	
Zero	A	B	C	D	E	F	G	H	I	J
In/out	1	1	1	0	1	0	0	1	0	1

Table 3.3: Zero configuration **II**. A 1(0) indicates a zero is inside(outside) the unit circle.

for the origin as the lab. momentum approaches 0.36 GeV/c , making it possible that it is threshold paired with the zero F. This would not be possible if the configuration favoured in the region above 1 GeV/c were just frozen in since then these zeros would be on the same side of the circle, although the pairing of these zeros is not definite and so this does not allow us to discount the solution obtained by merely freezing in the configuration of Table 3.2. There are, then, two solutions (along with their Minami transforms) which must be considered. One solution, hereafter referred to as solution $\mathcal{A}$, which has the zeros of Figs. 3.8 and 3.13 in the configuration of Table 3.2 throughout the PS172 P_{lab} range, and another solution solution $\mathcal{B}$ which has the same zero positions with the same *in/out* configuration in the region $P_{lab} > 1$ GeV/c but with the zero E crossing the circle at or around $P_{lab} = 0.988$ GeV/c leading to the configuration of Table 3.3 for $P_{lab} < 1$ GeV/c . These two solutions will have differing predictions for the $\overline{p}p \rightarrow \pi^0\pi^0$ observables and hence could be distinguished between given data on $d\sigma^n/d\Omega$ in this region. The predictions for $d\sigma^n/d\Omega$ of the two solutions are shown in Fig. 3.39 at two representative P_{lab} values and indeed do show a measurable difference.

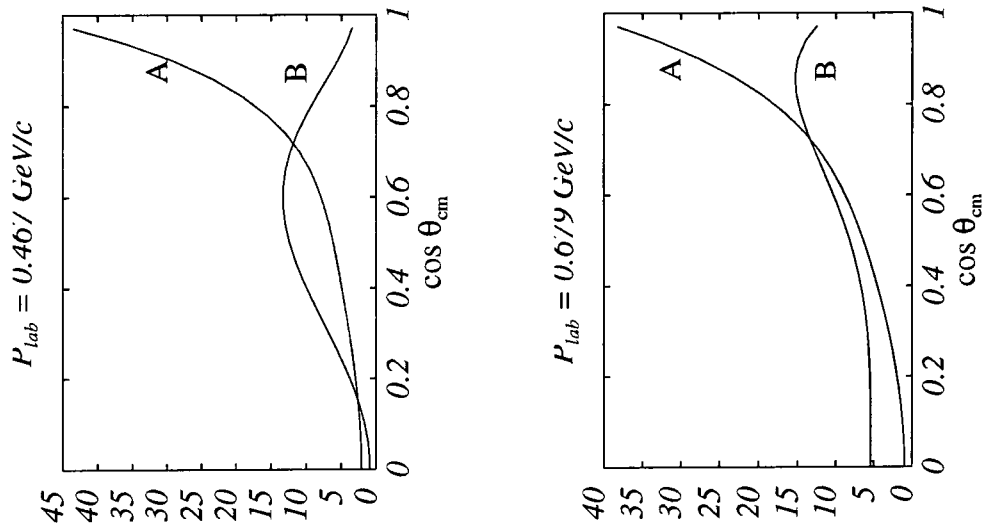

Figure 3.39: Predictions for $d\sigma^n/d\Omega$ at 0.467 and 0.679 GeV/c of solutions $\mathcal{A}$ and $\mathcal{B}$.

3.5 Postscript: The Older Data Revisited

It is now possible to check, at least indirectly, the consistency of the PS172 measurements with the older data of Tanimori *et al.* and Carter *et al.* which was impossible to do directly in Chapter 2 owing to the differing $\cos\theta$ grids utilised by the different experiments. The above presented fits to PS172 are compared to the Tanimori *et al.* data in Table 3.4. The first χ^2 column is the χ^2 between the PS172 fit (folded) and the data. In the second column, a further minimisation has been performed, allowing the overall normalisation parameter, $|C|$, to vary in order to better fit the Tanimori *et al.* data whilst holding all the zero positions constant. In general, very little change in the normalisation is required, evidencing the compatibility between the datasets which the "by eye" comparisons of Chapter 2 suggested although the figures at $P_{lab} = 0.585$ GeV are an exception, the unrefitted χ^2 being much higher than the refitted one here, as may have been expected in the light of the discrepancy between the data-sets at this mo-

$P_{\text{lab}}^{\text{Tan}}$	$P_{\text{lab}}^{\text{PS172}}$	χ^2_{Unmin}	χ^2_{Min}
0.360	0.360	1.83	1.83
0.406	0.404	1.84	1.39
0.467	0.467	1.45	1.15
0.495	0.497	0.71	0.44
0.522	0.523	0.84	0.59
0.585	0.585	2.60	0.92
0.679	0.679	1.79	1.01

Table 3.4: Comparison of Tanimori *et al.* data on the folded differential cross-section with folded fits to the PS172 measurements.

mentum noted in Chapter 2. The Carter *et al.* data on the polarisation is compared

$P_{\text{lab}}^{\text{Car}}$	$P_{\text{lab}}^{\text{PS172}}$	χ^2_{dof}
1.000	0.988	1.70
1.100	1.089	1.55
1.230	1.190	2.30
1.360	1.351	1.65
1.430	1.416	1.51

Table 3.5: Comparison of Carter *et al.* data on the polarisation with fits to the PS172 measurements.

with the PS172 fits in Table 3.5 where again the χ^2_{dof} values show that the datasets are compatible.

Chapter 4

The Partial Wave Content of the Amplitudes

In Chapter 3, arguments were presented to emphasise the unfortunate fact that resonances do not necessarily produce clear signals in the shape of (no pun intended) bumps in the integrated cross-section. It was suggested that the ideal way to uncover resonant states would be to determine the amplitude and decompose it into its separate spin components i.e. its partial waves and the amplitude was determined up to a four-fold discrete ambiguity (the solutions $\mathcal{A}$ and $\mathcal{B}$ and their Minami transforms) and a continuous ambiguity in that the overall phase of the amplitude, $\phi(s)$ in Eq. 3.11, was not considered since it is not directly determined by the data. In this Chapter, the separation of these amplitudes into partial waves will be discussed and this will lead naturally to a treatment of both the continuum ambiguity and the Minami ambiguity.

4.1 Partial Waves in the Barrelet Formalism

In order to derive the relation between the Barrelet zeros, $\{\omega_i\}$, and the (L-truncation scheme) partial waves, it is most convenient to work in terms of the Helicity amplitudes

introduced in Chapter 2, $F_{+\pm}$. These may be decomposed thus:–

$$\begin{aligned} F_{++}(z) &= \frac{1}{p}\sum_{J=0}^{N}(2J+1)f_J^{++}P_J(z) \\ F_{+-}(z) &= \frac{1}{p}\sum_{J=1}^{N}\frac{(2J+1)}{\sqrt{J(J+1)}}f_J^{+-}P_J^1(z), \end{aligned} \tag{4.1}$$

where the $f_J^{+\pm}$ are the flip and non-flip partial wave amplitudes and p is the centre of mass momentum of the proton (or the antiproton). Recalling the relation between $T^{\pm}$ and the helicity amplitudes leads to the decomposition

$$T^{\pm}(z) = \frac{1}{p\sqrt{2}}\left[\sum_{J=0}^{N} n_J P_J(z) \pm i\sum_{J=1}^{N} f_J P_J^1(z)\right] \tag{4.2}$$

where the J-dependent conventional factors in Eq. (4.1) have been absorbed into the amplitudes n_J and f_J. In terms of the variable ω this becomes

$$T(\omega) = \frac{1}{p\sqrt{2}}\left[\sum_{J=0}^{N} n_J P_J\left(\frac{1}{2}(\omega+1/\omega)\right) + i\sum_{J=1}^{N} f_J P_J^1\left(\frac{1}{2}(\omega+1/\omega)\right)\right]. \tag{4.3}$$

The polynomial on the right hand side of Eq. (4.3) may be re-written in a different basis, the monomials ω^n, the coefficients of these being easy to determine in terms of the Barrelet zeros $\{\omega_i\}$ and the overall normalisation parameter $|C(s)|$. Thus

$$T(\omega) = \sum_{i=0}^{2N} c_i \omega^{i-m} \tag{4.4}$$

where in the L-truncation scheme $m = N+1$ and the c_i may be determined by examination of Eq. (3.3). Turning first to the ten zero case, the c_i are

$$\begin{aligned} c_0 &= D\prod_{i=1}^{10}\omega_i \\ c_1 &= -D\sum_{j=1}^{10}\prod_{i\neq j}\omega_i \end{aligned}$$

$$
\begin{aligned}
c_2 &= D\sum_{k=1}^{9}\sum_{j=k+1}^{10}\prod_{i\neq j,k}\omega_i \\
&\vdots \\
c_8 &= D\sum_{j=1}^{9}\sum_{i=j+1}^{10}\omega_j\omega_i \\
c_9 &= -D\sum_{i=1}^{10}\omega_i \\
c_{10} &= D
\end{aligned}
\tag{4.5}
$$

where D is given by

$$
D = \sqrt{2}\,p|C(s)|e^{i\phi(s)}\prod_{i=1}^{10}\frac{1}{1-\omega_i}. \tag{4.6}
$$

Thus by equating coefficients of ω^n in Eqs (4.3) and (4.4), a set of linear relations between the $\{n_J, f_J\}$ and the $\{c_i\}$ are found which may be solved to give the following formulae for the n's and f's:

$$
\begin{aligned}
n_0 &= -\frac{1}{35}c_0 - \frac{1}{15}(c_2+c_{10}) - \frac{1}{3}(c_4+c_8) + c_6 \\
n_1 &= -\frac{1}{7}c_1 - \frac{3}{5}(c_3+c_9) + c_5 + c_7 \\
n_2 &= -\frac{4}{21}c_0 - \frac{16}{21}(c_2+c_{10}) + \frac{4}{3}(c_4+c_8) \\
n_3 &= -\frac{8}{9}c_1 + \frac{8}{5}(c_3+c_9) \\
n_4 &= -\frac{384}{385}c_0 + \frac{64}{35}(c_2+c_{10}) \\
n_5 &= \frac{128}{63}c_1 \\
n_6 &= \frac{512}{231}c_0 \\
f_1 &= -\frac{1}{35}c_1 - \frac{1}{5}(c_3-c_9) + c_5 - c_7
\end{aligned}
$$

$$
\begin{aligned}
f_2 &= -\frac{2}{63}c_0 - \frac{4}{21}(c_2 - c_{10}) + \frac{2}{3}(c_4 - c_8) \\
f_3 &= -\frac{8}{45}c_1 + \frac{8}{15}(c_3 - c_9) \\
f_4 &= -\frac{64}{385}c_0 + \frac{16}{35}(c_2 - c_{10}) \\
f_5 &= \frac{128}{315}c_1 \\
f_6 &= \frac{256}{693}c_0.
\end{aligned} \tag{4.7}
$$

The corresponding formulae in the case of eight and six zeros may be determined from these once the behaviour of the c_i's as zeros disappear is known. Recall from Chapter 3 that the zeros must disappear pairwise as the threshold is approached, one to the origin and one to infinity in the ω-plane. For definiteness, consider the two limits, $\omega_9 \to \infty$ and $\omega_{10} \to 0$. It is convenient to re-label the c_i and D, adding a superscript to indicate the number of zeros, thus the above described c_i become $c_i^{(10)}$, and $D^{(n)} = \sqrt{2}\,p|C(s)|e^{i\phi(s)}\prod_{i=1}^{n} 1/(1-\omega_i)$. Examining first the limit $\omega_{10} \to 0$, one should first note that $D^{(10)}$ simply becomes $D^{(9)}$, since $\lim_{\omega_{10}\to 0} 1/(1-\omega_{10}) = 1$. It is also apparent that the coefficient $c_0^{(10)}$, which is proportional to the product over all the Barellet zeros, will vanish as this limit is taken. Now, turning to $c_1^{(10)}$,

$$
c_1^{(10)} = -D^{(10)}\left(\omega_1\omega_2\omega_3\omega_4\omega_5\omega_6\omega_7\omega_8\omega_9 + \omega_{10}\,(\text{products over 8 zeros})\right) \tag{4.8}
$$

and hence,

$$
\lim_{\omega_{10}\to 0} c_1^{(10)} = -D^{(9)}\,\omega_1\omega_2\omega_3\omega_4\omega_5\omega_6\omega_7\omega_8\omega_9. \tag{4.9}
$$

Examining the limit $\omega_9 \to \infty$ it is clear that the factor of $1/(1-\omega_9)$ in $D^{(9)}$ will kill all terms in the c_i which do not contain a factor of ω_9 in the numerator. The effect of this limit on the remaining terms will be determined by $\lim_{\omega_9\to\infty} \omega_9/(1-\omega_9)$ which is

simple to evaluate:—

$$\lim_{\omega_9\to\infty}\frac{\omega_9}{1-\omega_9}=\lim_{\omega_9\to\infty}\frac{1}{1/\omega_9-1}=-1. \tag{4.10}$$

the coefficient $c_1^{(10)}$ then becomes, after both limits are taken,

$$\lim_{\omega_9\to\infty}\lim_{\omega_{10}\to 0}c_1^{(10)}=D^{(8)}\omega_1\omega_2\omega_3\omega_4\omega_5\omega_6\omega_7\omega_8\equiv c_0^{(8)}. \tag{4.11}$$

$c_{10}^{(10)}$ is nothing more than $D^{(10)}$ and hence

$$\lim_{\omega_9\to\infty}\lim_{\omega_{10}\to 0}c_{10}^{(10)}=\lim_{\omega_9\to\infty}D^{(9)}=0. \tag{4.12}$$

Also,

$$\lim_{\omega_9\to\infty}\lim_{\omega_{10}\to 0}c_9^{(10)}=\lim_{\omega_9\to\infty}-D^{(9)}\sum_{i=1}^{9}\omega_i=\lim_{\omega_9\to\infty}-D^{(9)}\omega_9=D^{(8)}\equiv c_8^{(8)} \tag{4.13}$$

and indeed, it is true that for each $c_i^{(10)}$ with $1\le i\le 9$ the limits are simply:

$$\lim_{\omega_9\to\infty}\lim_{\omega_{10}\to 0}c_i^{(10)}=c_{i-1}^{(8)}, \tag{4.14}$$

with an analogous treatment of the limits $\omega_7\to\infty$ and $\omega_8\to 0$ leading to the corresponding formulae for the eight zeros $\to$ six zero transition,

$$\begin{aligned}
\lim_{\omega_7\to\infty}\lim_{\omega_8\to 0}c_0^{(8)} &= 0\\
\lim_{\omega_7\to\infty}\lim_{\omega_8\to 0}c_8^{(8)} &= 0\\
\lim_{\omega_7\to\infty}\lim_{\omega_8\to 0}c_i^{(8)} &= c_{i-1}^{(6)}, \qquad i=1,\ldots,7.
\end{aligned} \tag{4.15}$$

The formulae for the non-flip and flip partial waves, n_j and f_J, Eq. (4.7), although derived for the ten zero case may be directly applied to the eight and six zero cases by merely substituting $c_0=c_{10}=0$, $c_i=c_{i-1}^{(8)}, i=1,\ldots,9$ and $c_0=c_{10}=c_1=c_9=0$,

$c_i = c_{i-2}^{(6)}$ respectively. The results of this procedure are given in Appendix A.

It seems, however, more natural, in the light of the L-truncation scheme adopted, to determine the partial waves in a basis in which waves of definite L are separated. The L-S coupling scheme provides such a basis, where the partial wave amplitudes have definite values of L, S, and J, although, as was mentioned in Chapter 2, S is constrained by parity conservation to take the value 1 and hence, $L = J \pm 1$. These L-S basis amplitudes will be denoted here by f_L^J (or spectroscopically J_L) and are given in terms of the n_J and f_J helicity basis amplitudes as:—

$$\begin{aligned} f_{J-1}^J &= \frac{1}{2J+1}\sqrt{\frac{2J}{2J+1}}[(J+1)f_J + n_J] \\ f_{J+1}^J &= \frac{1}{2J+1}\sqrt{\frac{2J+2}{2J+1}}[Jf_J - n_J] \end{aligned} \tag{4.16}$$

where, in the L-truncation scheme, only waves with $L \leq N$ are considered. Specifically, the highest J, highest L wave in the L-truncation scheme will be f_N^{N+1}, which would not be present if J-truncation were employed, whilst the wave with highest L and J in the J-truncation scheme would be f_{N+1}^N which is not present in the L-truncated expansion adopted in this thesis.

The contributions to the cross-section of the L-S scheme amplitudes are $\pi(2J+1)|f_{J\pm}^J|^2$ and are shown in Figs. 4.1–4.3 for solution $\mathcal{A}$ and in Figs. 4.4–4.6 for solution $\mathcal{B}$. The corresponding Minami transformed solutions will be considered in Section 4.2.

Amplitudes with equal L have been shown on the same plot and are labelled J_L. The errors are constructed by separately allowing the real and imaginary parts of the (helicity) amplitudes to vary and comparing the resulting cross-sections with the data. This will, of course, only give a rough guide to the size of the expected errors since no account has been taken of the full correlation matrix in their construction.

In the upper part of the energy region, above $\sqrt{s} = 2.1$ GeV , both solutions are identical, having the same zero positions in the same configuration there. Both show a large structure in the 2_1 wave at around $\sqrt{s} = 2.15$ GeV , which is suggestive of

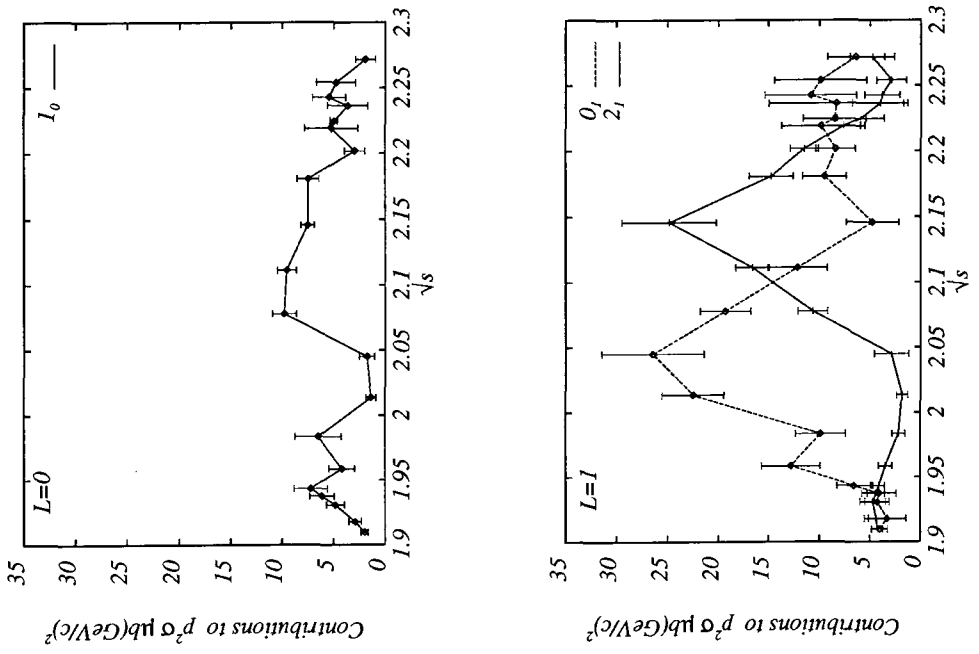

Figure 4.1: Contributions to $p^2\sigma(s)$ of the $L = 0$ and $L = 1$ partial waves of solution $\mathcal{A}$

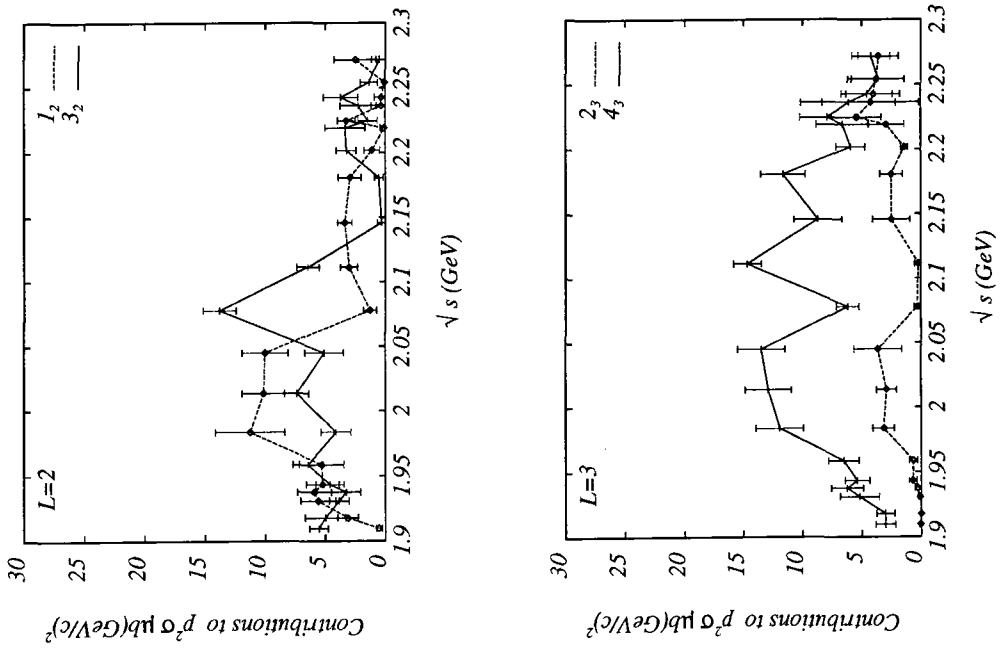

Figure 4.2: Contributions to $p^2\sigma(s)$ of the $L = 2$ and $L = 3$ partial waves of solution $\mathcal{A}$

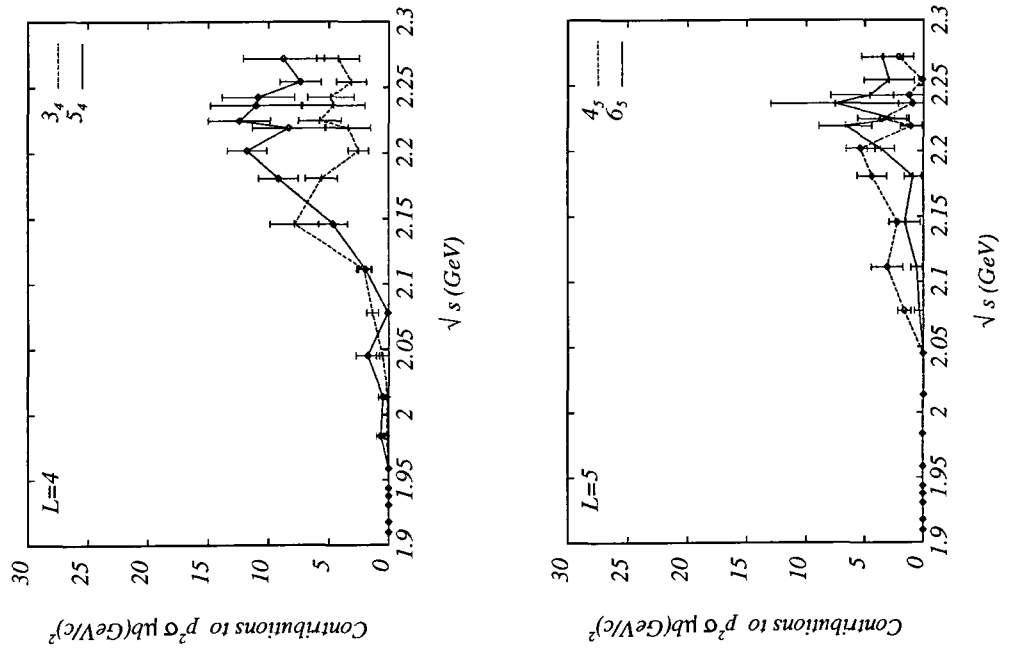

Figure 4.3: Contributions to $p^2\sigma(s)$ of the $L = 4$ and $L = 5$ partial waves of solution $\mathcal{A}$

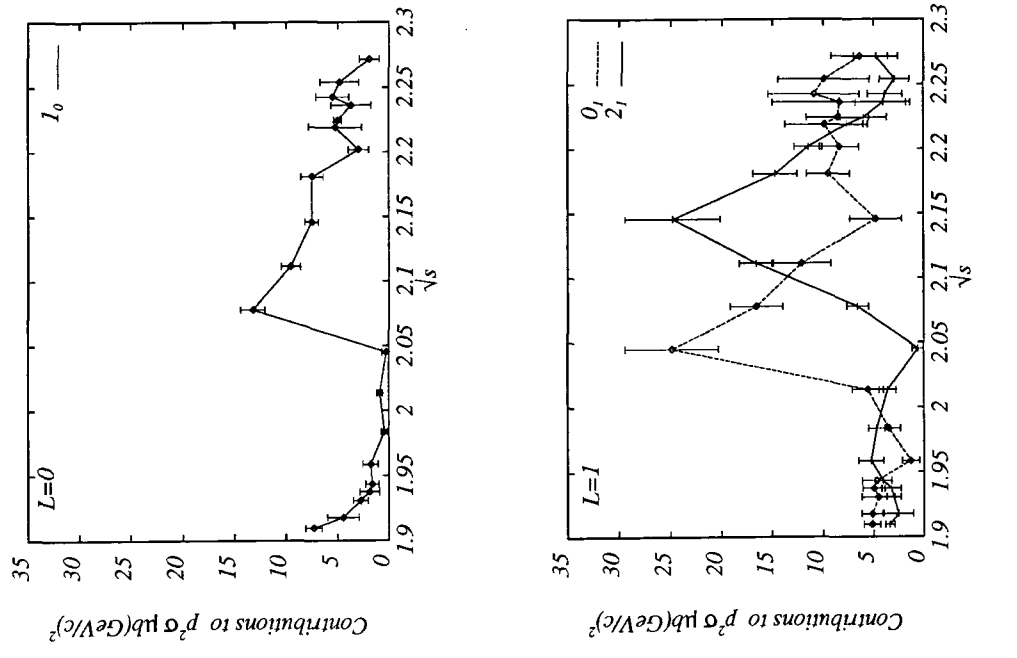

Figure 4.4: Contributions to $p^2\sigma(s)$ of the $L = 0$ and $L = 1$ partial waves of solution $\mathcal{B}$

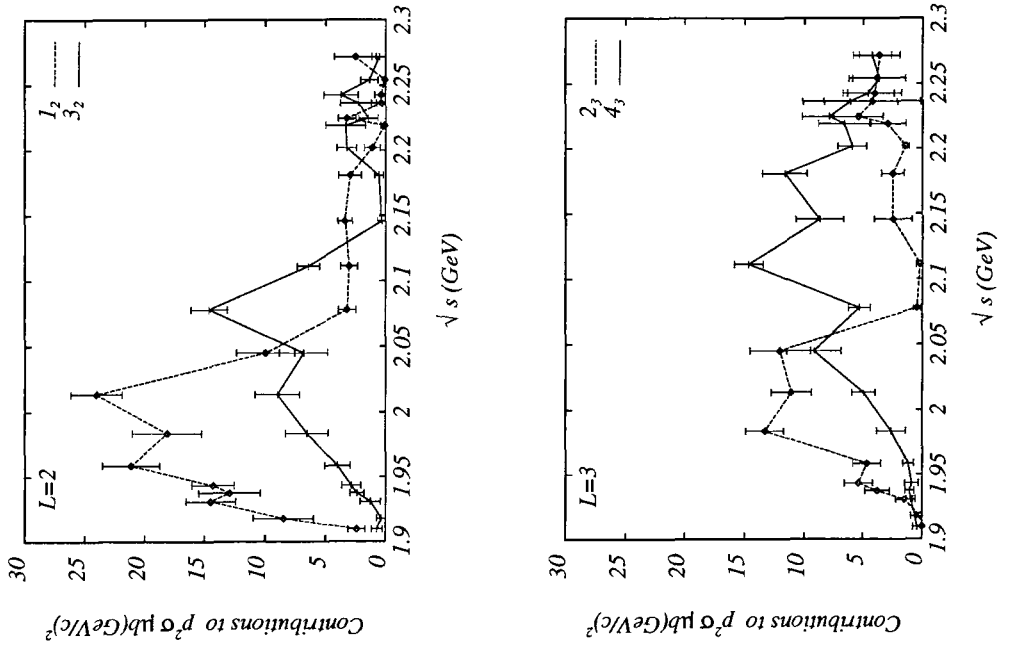

Figure 4.5: Contributions to $p^2\sigma(s)$ of the $L = 2$ and $L = 3$ partial waves of solution $\mathcal{B}$

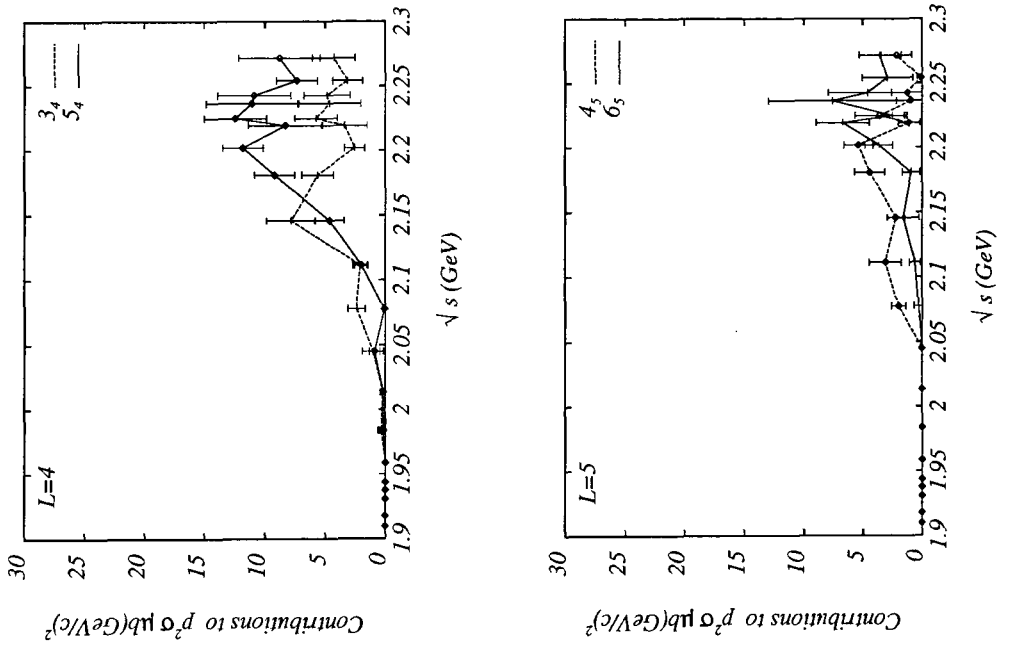

Figure 4.6: Contributions to $p^2\sigma(s)$ of the $L = 4$ and $L = 5$ partial waves of solution $\mathcal{B}$

resonant behaviour. Below $\sqrt{s} = 2.1$ GeV , the solutions differ considerably in their details, while still having some features in common. Both solutions seem to have structure in the 0_1 wave, it being considerably narrower in solution $\mathcal{B}$ than in solution $\mathcal{A}$. The higher L waves are in the main more suppressed in solution $\mathcal{B}$ as $\sqrt{s}$ approaches the threshold at $\sqrt{s} = 2m_N \simeq 1.88$ GeV as may have been expected considering the extra threshold pair of zeros which this solution has. A notable exception to this being the $L = 2\ 1_2$ wave, which is much more pronounced in solution $\mathcal{B}$ (Fig. 4.5) than in solution $\mathcal{A}$ (Fig. 4.2). It would, of course, in the light of the arguments presented in Section 3.1, be premature to interpret any bumps in Figs. 4.1–4.6 as resonances, but they may serve as a guide in making a plausible choice of the arbitrary overall phase of the amplitudes.

In order to make progress with the identification of any resonant states coupling in $\overline{p}p \to \pi\pi$, it is useful to make a simple, physically motivated guess as to the overall phase $\phi(s)$. An obvious first choice would be to take $\phi(s)$ to be such that the apparently structured waves 0_1 and 2_1 have phase varaitions commensurate with the masses and widths that one would estimate from Figs. 4.1 and 4.4, assuming that they were indeed resonant. One important danger which must be kept in mind when choosing the overall phase is that, clearly, if one simply chose the *overall* phase of one partial wave amplitude so that it had a sufficiently fast anticlockwise trajectory in the Argand plane as $\sqrt{s}$ increased, then, since the *relative* phases of all the partial wave amplitudes are fixed, this would cause *all* of the other partial waves to be dragged around anticlockwise too. There would then be a danger of ascribing resonant behaviour to amplitudes in which no such behaviour is present. Therefore great care must be taken both in the choice of $\phi(s)$ and it must be checked that the other waves are not being dragged anticlockwise by artificially fast phase variation in the wave whose phase is being fixed. A useful guide to the resonance content exists in the shape of the phase *differences* between the partial waves. These are determined in the Barrelet analysis and may be used to check that suspected resonant states are in fact resonant since if a wave is undergoing a Breit-Wigner type resonant looping, its phase variation should show up in the phase

differences between it and other waves which are not looping at the same energy. This cannot, however, be naively applied since, as with bumps in the integrated cross-section, the situation is clouded considerably when the resonant loops are superimposed on background amplitudes.

4.1.1 The Solution $\mathcal{A}$ Partial Waves in the Argand Plane

Examining first solution $\mathcal{A}$, Fig. 4.1 shows that the two dominant waves, the 0_1 and 2_1 will, if resonant, have masses and widths approximately given by $m_{01} = 2.05$, $\Gamma_{01} = 0.13$, $m_{21} = 2.15$, and $\Gamma_{21} = 0.13$ GeV . The partial wave amplitudes for this solution are shown in the Argand plane in Figs. 4.7–4.21. The overall phase has been chosen so that the 0_1 wave has the phase of a Breit-Wigner amplitude with parameters m_{01}, Γ_{01} given above, in the energy region $\sqrt{s} < 2.1$ GeV whilst the phase has been chosen in the region $\sqrt{s} > 2.1$ such that the 2_1 wave has Breit-Wigner phase variation with the values for m_{21} and Γ_{21} given above and with a starting phase chosen to ensure continuity of the partial waves at 2.1 GeV where the phase fixing switches from the 0_1 wave to the the 2_1 wave. The resulting amplitudes may now be examined to determine whether this phase choice is sensible, and if so, to judge which amplitudes, if any, exhibit resonant behaviour.

Proceeding, then, in order of increasing L, there is a hint of a loop in the $L = 0$ 1_0 wave (Fig. 4.7) at around $\sqrt{s} = 2.08$ GeV although it is perhaps a little too unclear to be interpreted as a resonance. If this were resonant, however, since the loop appears to be superimposed on a background amplitude of around $-0.025 - 0.02i$, this wave would in fact provide an example of the situation described in Section 3.1 where a dip in the integrated cross-section (here the dip in Fig. 4.1 around $\sqrt{s} = 2.05$ GeV which corresponds to the two points near the origin in Fig. 4.7) is caused by destructive inteference between a resonant loop and the background. Examination of the phase differences to try to determine whether this wave is actually resonant are, however, inconclusive, there being no discernible drop in $\phi_1^0 - \phi_0^1$, Fig. 4.8, at the appropriate

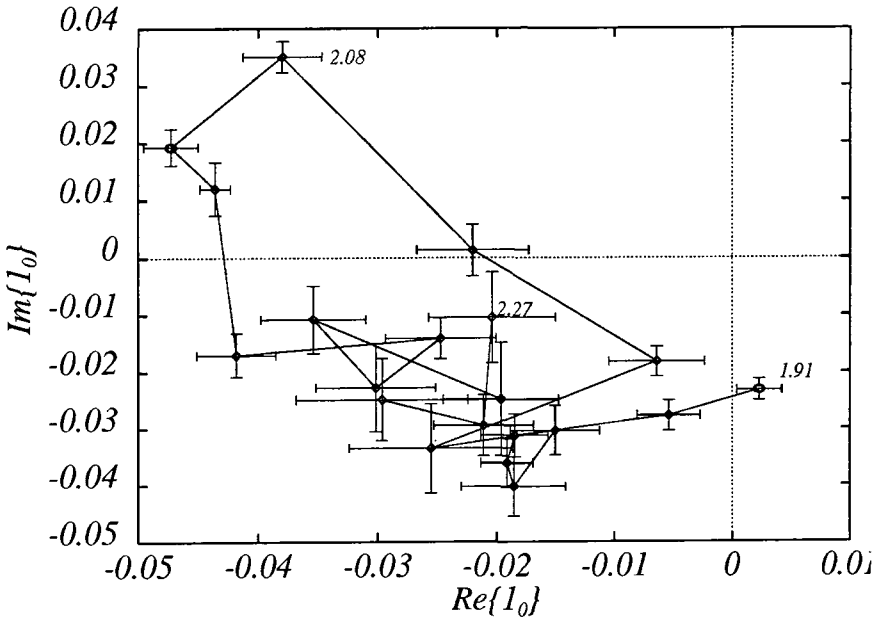

Figure 4.7: The solution $\mathcal{A}$ $J_L = 1_0$ amplitude in the Argand plane.

energy although it could just be that it is hidden by the rise in $\phi_1^0 - \phi_0^1$ which is indicative of the 0_1 state being resonant as assumed. Other phase differences are equally unhelpful although there are slight signals around $\sqrt{s} = 2.08$ in some of them, e.g. in $\phi_3^2 - \phi_0^1$ (Fig. 4.9) there is a slight drop at 2.08 GeV which could be interpreted as being due to ϕ_0^1 rising.

Moving on to consider the $L = 1$ amplitudes 0_1 and 2_1 pictured in Figs 4.10 and 4.11, it becomes apparent that choosing the overall phase as described above, is in fact a reasonable choice. Ignoring for the moment the impressive looking loops (since the overall phase has been chosen precisely so that these waves appear as Breit-Wigner type loops) and considering each amplitude in the energy region where the phase has been determined by the assumed structure *in the other amplitude*, it is notable that, in the 0_1 wave, above $\sqrt{s} = 2.1$ GeV . where the Breit-Wigner phase of the 2_1 wave has been imposed, the 0_1 wave is approximately constant. If the assumed structure in the 2_1 wave were not actually resonant, one would expect that the 0_1 wave would

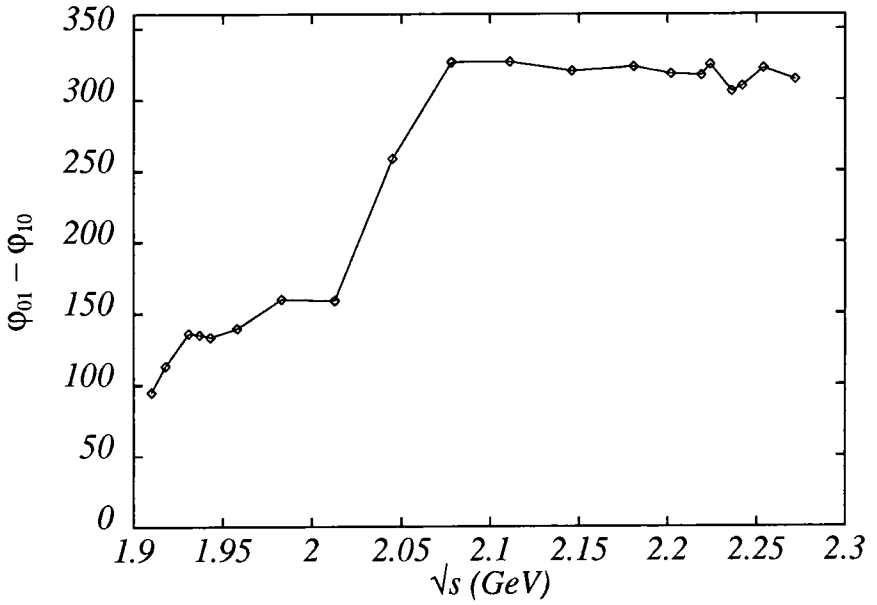

Figure 4.8: The phase difference between the 0_1 and 1_0 partial waves in solution $\mathcal{A}$.

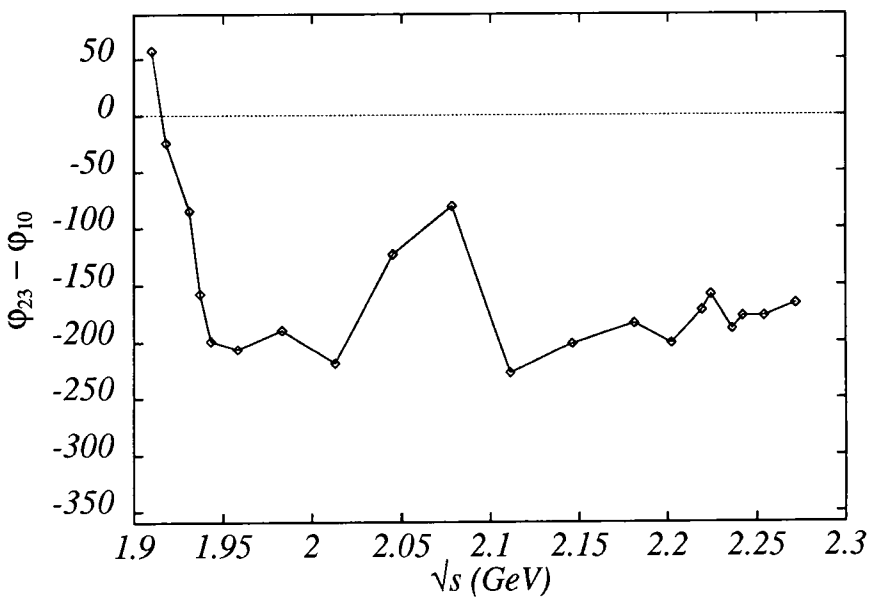

Figure 4.9: The phase difference between the 2_3 and 1_0 partial waves in solution $\mathcal{A}$.

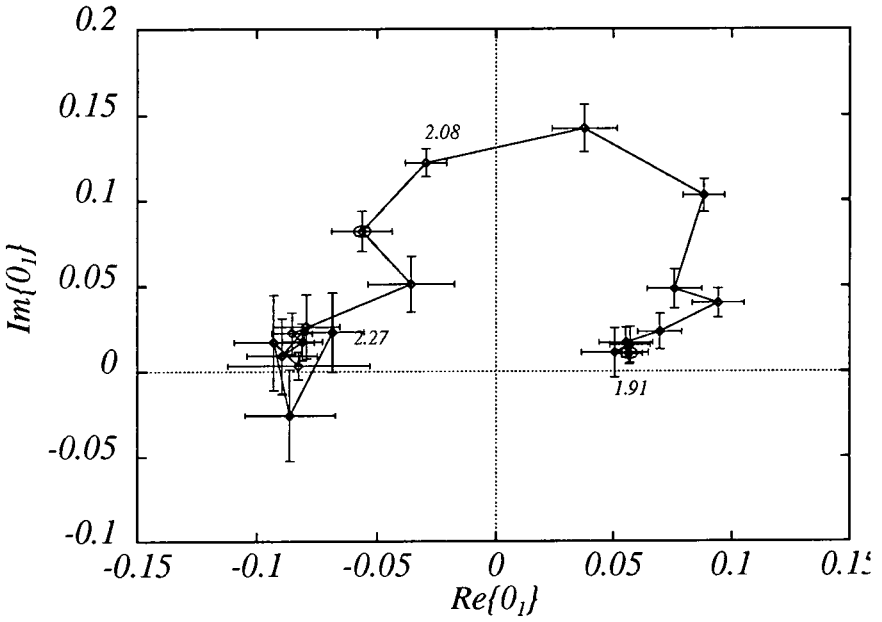

Figure 4.10: The solution $\mathcal{A}$ $J_L = 0_1$ amplitude in the Argand plane.

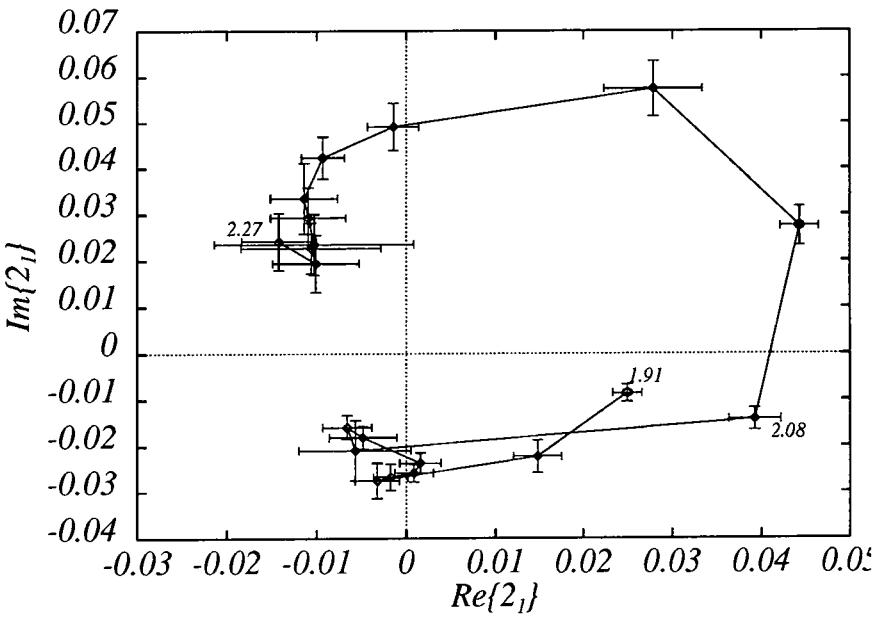

Figure 4.11: The solution $\mathcal{A}$ $J_L = 2_1$ amplitude in the Argand plane.

proceed anticlockwise above 2.1 GeV . This indicates that the relative phase of the two $L = 1$ amplitudes is compatible with there being a resonance in the 2_1 wave with parameters approximately as given above. Similarly, if the structure in the 0_1 which has been assigned resonant phase variation below 2.1 GeV (the large loop in Fig. 4.10) was actually non-resonant one would expect that, in this energy region, the 2_1 wave would have been pulled anticlockwise around the origin. In fact, it progresses slowly clockwise, and although, of course, changing the estimate of the 0_1 width could conceivably slow this, the width would have to be far less than Fig. 4.1 would indicate in order to convert this to an anticlockwise motion. Already then, it appears that the phase choice adopted here is, in fact, reasonable although it could be refined further since at present no account is taken of any backgrounds which may be present in the 0_1 and 2_1 waves. While Figs. 4.10 and 4.11 indicate that these backgrounds are small, they will have an effect on the optimum phase choice, particularly in the case of the 2_1 which appears to have the larger background of the two. The states assumed to be present in the 0_1 and 2_1 also show up in the relative phases between the 0_1 and 2_1 amplitudes and other waves. In Fig. 4.12 the relative phase $\phi_1^0 - \phi_1^2$ between the two $L = 1$ waves in solution $\mathcal{A}$ is shown. This phase difference does indeed rise below 2.05 GeV and fall above 2.05 GeV as would be expected if the assumed resonant states were, in fact, resonant.

Turning next to the $L = 2$ amplitudes, the 1_2 wave, shown in Fig. 4.13 shows no obvious structure, although it is possible that there are two small loops, one at around $\sqrt{s} = 2.1$ GeV and the other at a lower energy $\sqrt{s} \simeq 2.0$ GeV although the errors are too large to draw any firm conclusions. The 3_2 wave, however, does show a discernible loop, centred at about $\sqrt{s} = 2.08$ GeV with very fast phase variation, indicating quite a small width. This phase variation also shows up in the phase differences between waves, for example in $\phi_2^1 - \phi_2^3$ (Fig. 4.15) there is a distinct drop around $\sqrt{s} = 2.08$ GeV . The 3_2 loop appears also to have quite a small background and hence does show up as a peak in Fig. 4.2.

The $L = 3$ amplitudes are shown in Figs. 4.16 (2_3) and 4.17 (4_3). It is difficult

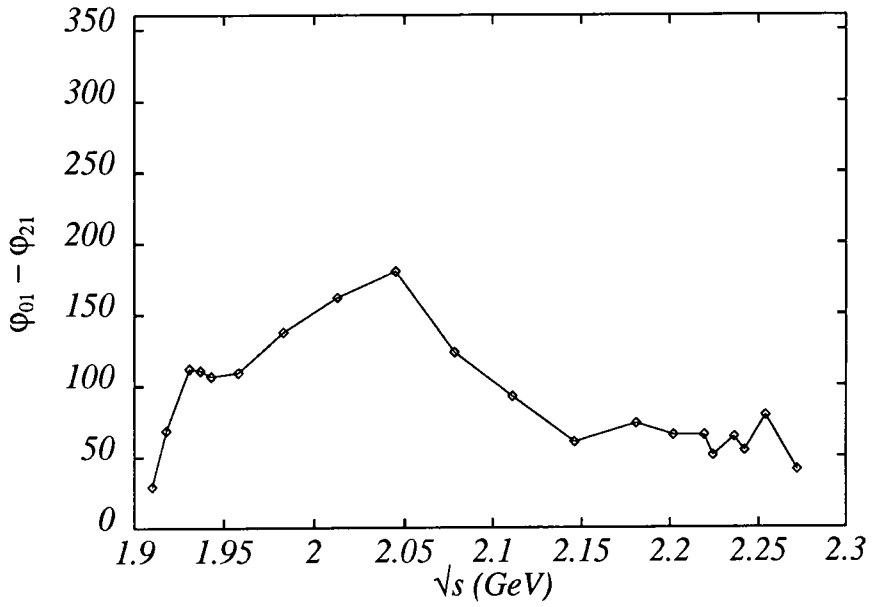

Figure 4.12: The phase difference between the 0_1 and 2_1 partial waves in solution $\mathcal{A}$.

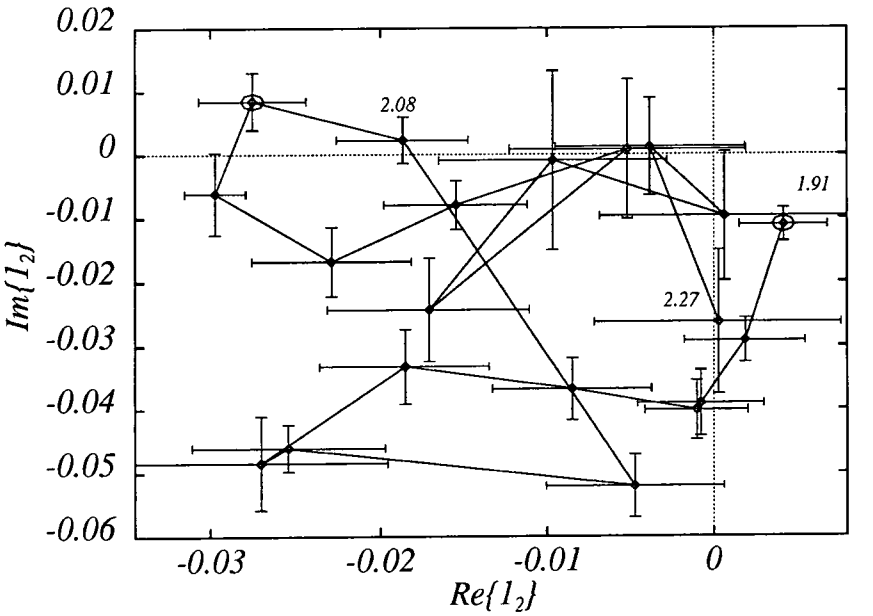

Figure 4.13: The solution $\mathcal{A}$ $J_L = 1_2$ amplitude in the Argand plane.

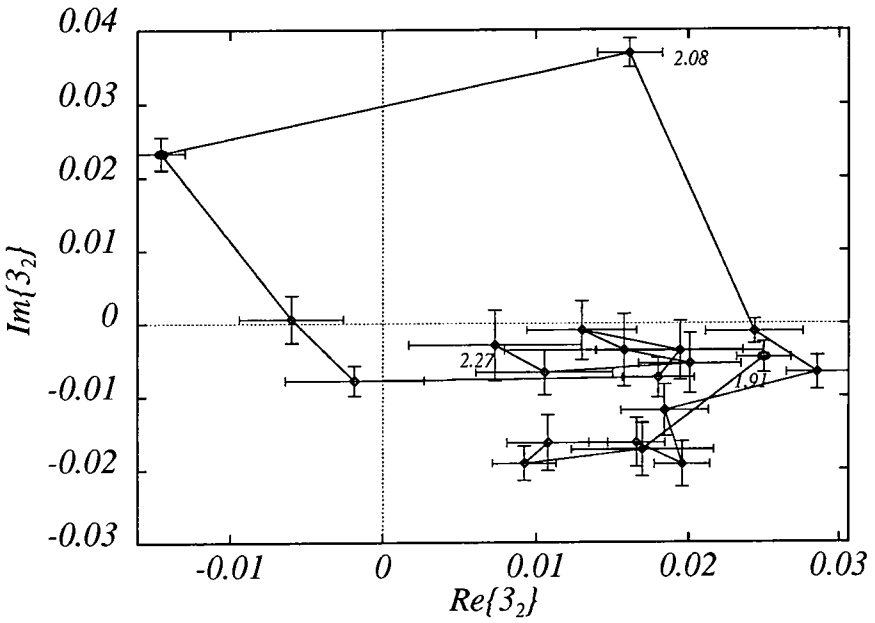

Figure 4.14: The solution $\mathcal{A}$ $J_L = 3_2$ amplitude in the Argand plane.

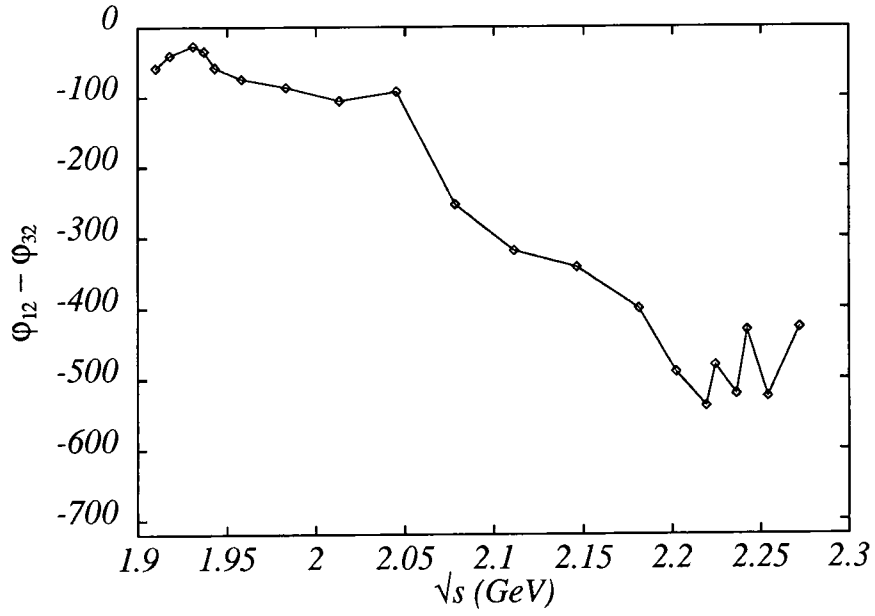

Figure 4.15: The phase difference between the 1_2 and 3_2 partial waves in solution $\mathcal{A}$.

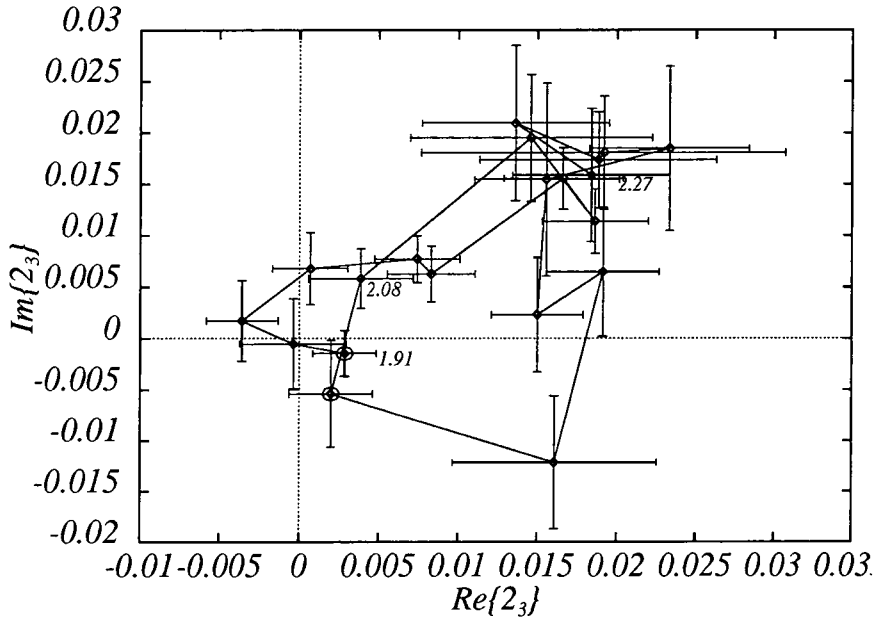

Figure 4.16: The solution $\mathcal{A}$ $J_L = 2_3$ amplitude in the Argand plane.

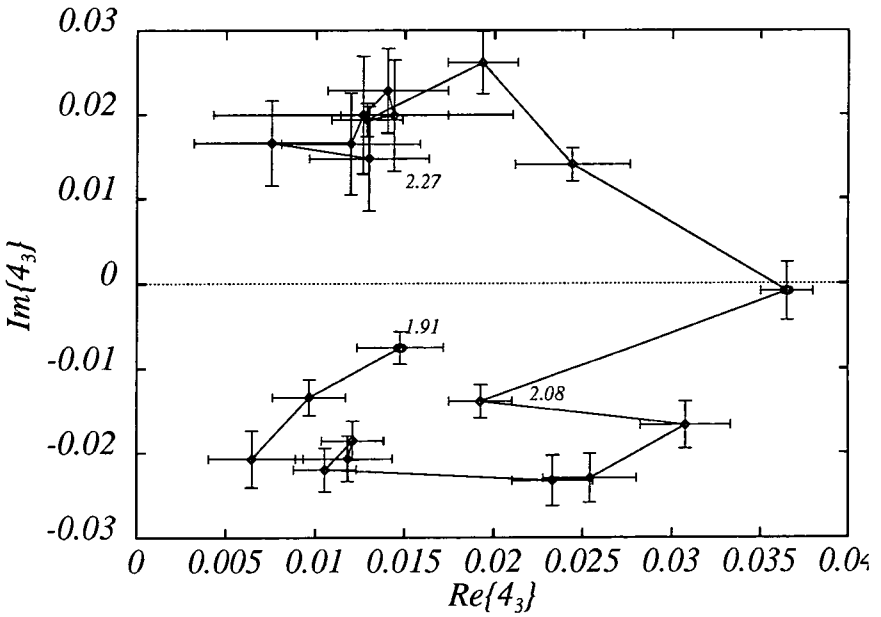

Figure 4.17: The solution $\mathcal{A}$ $J_L = 4_3$ amplitude in the Argand plane.

to pick out any structure in the 2_3 wave, the errors being too large to allow any sure interpretation of the hint of a loop which appears towards the upper end of the PS172 energy region. The 4_3 wave has far less erratic behaviour, there being a possible loop starting near the bottom of the energy range and finishing around 2.08 GeV . This is possibly a signal for the $f_4(2050)$ superimposed on a background which is roughly constant and approximately equal to the value of the 4_3 amplitude at $\sqrt{s} = 1.91$ GeV but again, this interpretation is far from clear, for example the 4_3 could also be interpreted as a much wider structure, looping anticlockwise for almost all of the energy range, with the point at $\sqrt{s} = 2.08$ GeV being a statistical "blip".

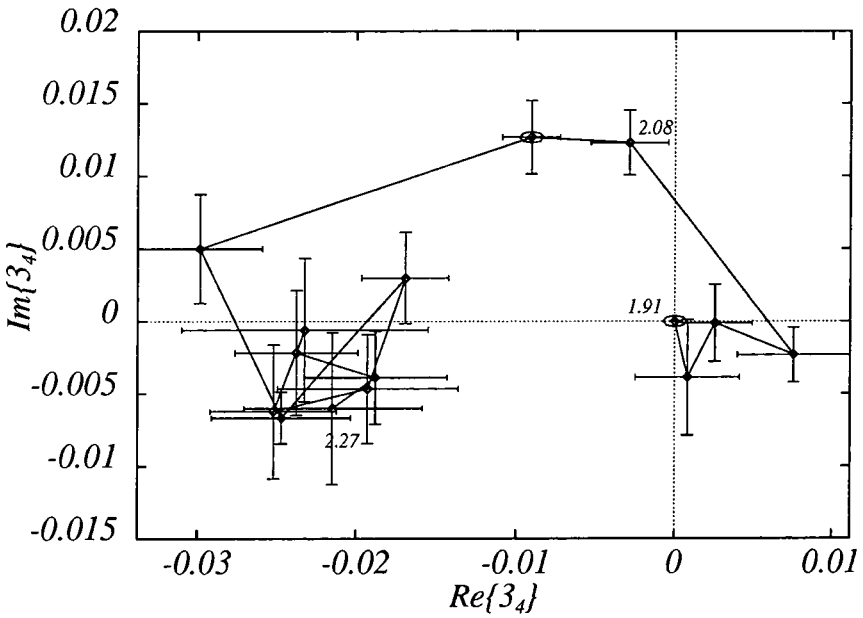

Figure 4.18: The solution $\mathcal{A}$ $J_L = 3_4$ amplitude in the Argand plane.

Both of the $L = 4$ amplitudes, Figs. 4.18 and 4.19 appear to begin to loop anti-clockwise, and the 5_4 in particular may be resonant. The confirmation of this, and any determination of its parameters would, however, require the extension of this analysis above the PS172 energy range [38] and is hence beyond the scope of this thesis.

The $L = 5$ amplitudes are exhibited in Figs. 4.20 and 4.21 but are both rather small

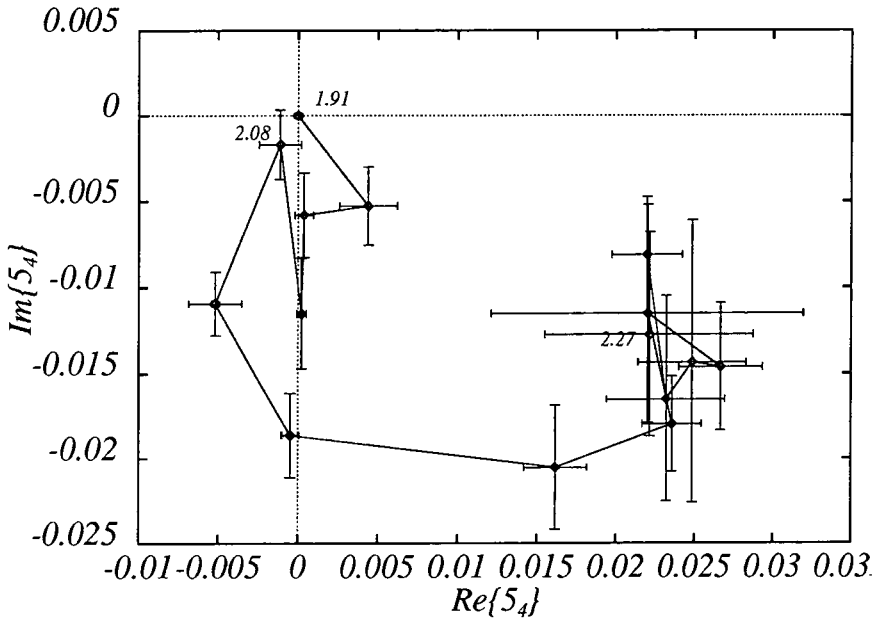

Figure 4.19: The solution $\mathcal{A}$ $J_L = 5_4$ amplitude in the Argand plane.

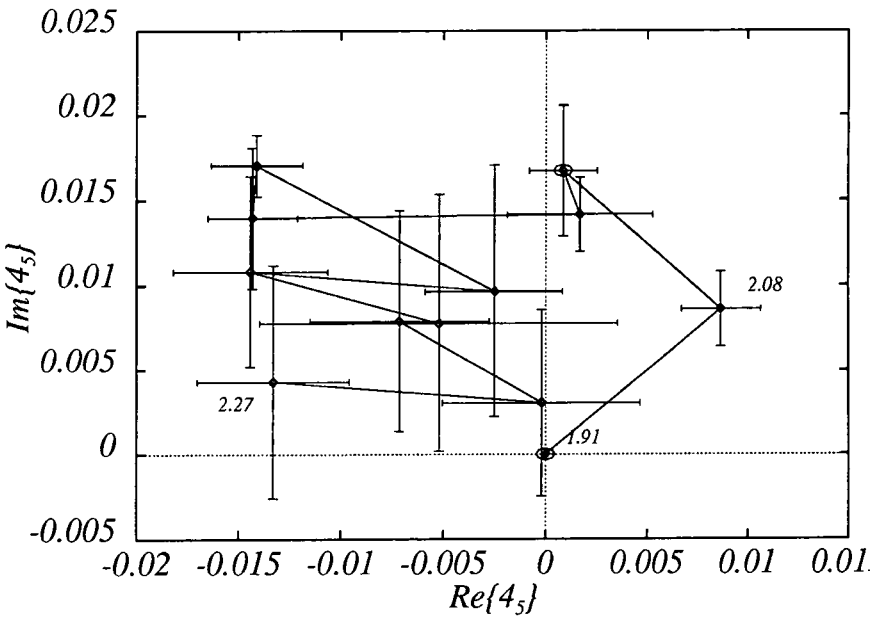

Figure 4.20: The solution $\mathcal{A}$ $J_L = 4_5$ amplitude in the Argand plane.

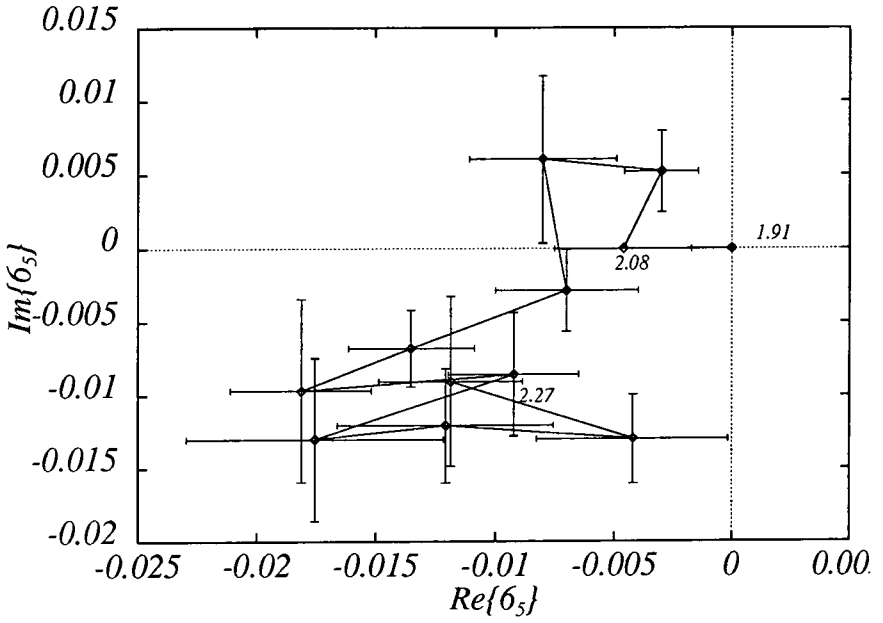

Figure 4.21: The solution $\mathcal{A}$ $J_L = 6_5$ amplitude in the Argand plane.

and show little, if any, structure which could be interpreted as anything more than statistical noise. This is just as well since if these waves were larger and did show structure it would call into question the validity of truncating the expansion at $L = 5$.

To summarise, then, the choice of overall phase described above, motivated by the posited resonant behaviour of the dominant structures appearing in the 0_1 and 2_1 waves, does indeed lead to reasonable behaviour in the Argand plane for the other amplitudes. There are candidate resonances with spins 0,2, and 3 and a possible signal for the spin-4 $f_4(2050)$ although the background in the 4_3 wave is a little too large to be certain of this. In addition, may be a state of spin-5 which is just beginning to resonate at the top end of the energy range here studied.

4.1.2 The Solution $\mathcal{B}$ Partial Wave Amplitudes.

Analogously to the treatment of solution $\mathcal{A}$ just described, one may also choose the overall phase in solution $\mathcal{B}$ so that the dominant waves 0_1 and 2_1 (Fig. 4.4), which ap-

pear resonant, have Breit-Wigner type phase variation. The 2_1 state has the same parameters as in solution $\mathcal{A}$, the two solutions being identical in the region $\sqrt{s} > 2.1$ GeV . The 0_1 has similar mass, $m_{01} = 2.05$ but is somewhat narrower in solution $\mathcal{B}$, its width being approximately $\Gamma_{01} = 0.09$ GeV .

Again, proceeding to examine the Argand diagrams in order of increasing L, it is apparent that solution $\mathcal{B}$ is somewhat richer in resonance candidates than solution $\mathcal{A}$.

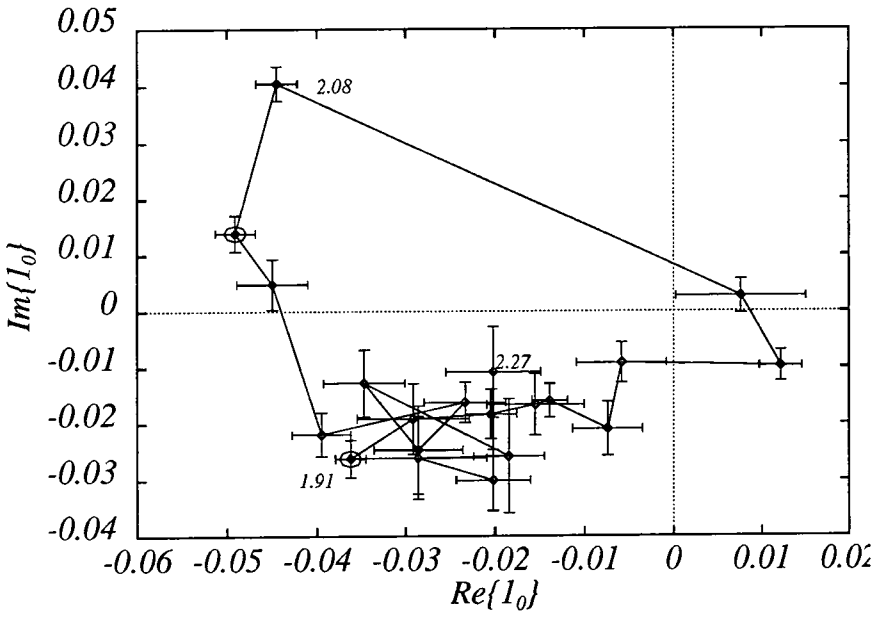

Figure 4.22: The solution $\mathcal{B}$ $J_L = 1_0$ amplitude in the Argand plane.

Examining the 1_0 wave, exhibited in Fig. 4.22, there is a possible loop although the phase variation looks a little odd. This may, of course, be due to slight inaccuracies in the estimation of the 0_1 parameters which determine the phase in this energy region. Also, there are three points in the loop which have modulae close to zero and which hence have phases which are rather ill-determined since movement of these points within their errors will lead to disproportionately large phase variations. The relative phase between the 1_2 and 1_0 waves is shown in Fig. 4.23 and shows a drop between $\sqrt{s} = 2.05$ and $\sqrt{s} = 2.1$ GeV as would be expected for a resonance in the 1_0 wave.

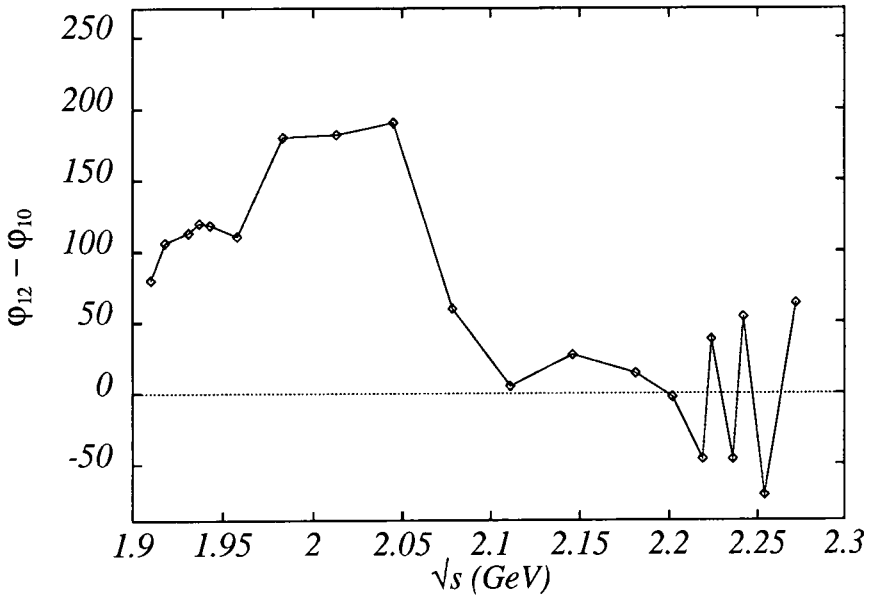

Figure 4.23: The phase difference between the 1_2 and 1_0 partial waves in solution $\mathcal{B}$.

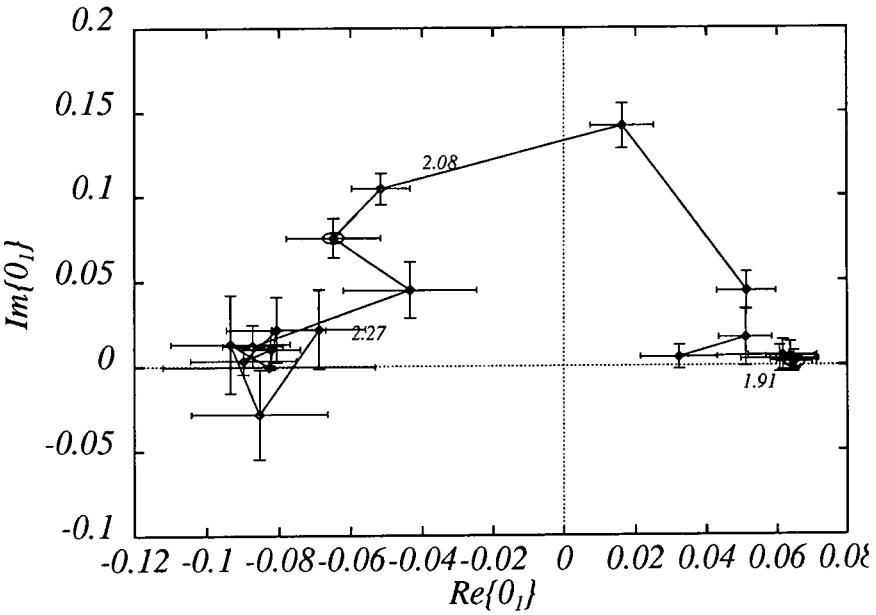

Figure 4.24: The solution $\mathcal{B}$ $J_L = 0_1$ amplitude in the Argand plane.

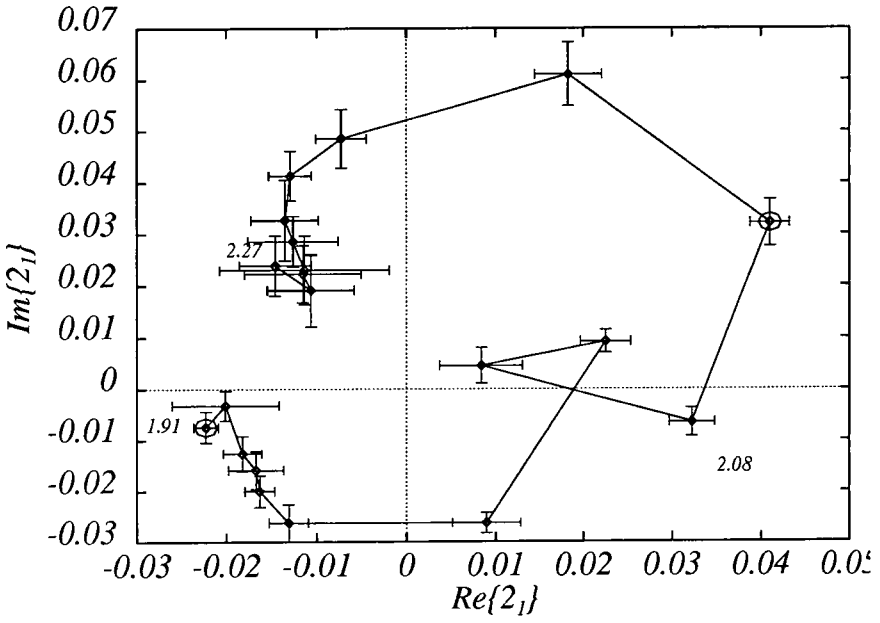

Figure 4.25: The solution $\mathcal{B}$ $J_L = 2_1$ amplitude in the Argand plane.

The 0_1 wave (Fig. 4.24), although narrower, behaves similarly to it'+s counterpart in solution $\mathcal{A}$ in that, above 2.1 GeV , where its phase is determined by the structure in the 2_1 wave, it holds almost constant within its errors. The 2_1 wave is , however, quite different in the two solutions. The loop in the region $\sqrt{s} > 2.1$ GeV is, by construction, identical to the 2_1 loop in solution $\mathcal{A}$ but in addition to this, there is a second loop, appearing in the region $\sqrt{s} < 2.1$ GeV . That this is a genuine loop and not an artifact of the assumed narrow state in the 0_1 wave , to which the phase in this region has been fixed, dragging the other amplitudes around anticlockwise is evidenced by the phase difference between the 0_1 and 2_1 waves, Fig. 4.26. In the region below ~ 2 GeV , $\phi_1^0 - \phi_1^2$ decreases, consistent with the phase increase in the 2_1 wave that would be expected here if the loop in the 2_1 in this region is, in fact, resonant. The phase difference then increases, consistent with the assumed structure in the 0_1 and finally the phase difference again decreases as the structure above $\sqrt{s} = 2.1$ GeV is reached, again consistent with the assumption that this is a resonant structure. As was

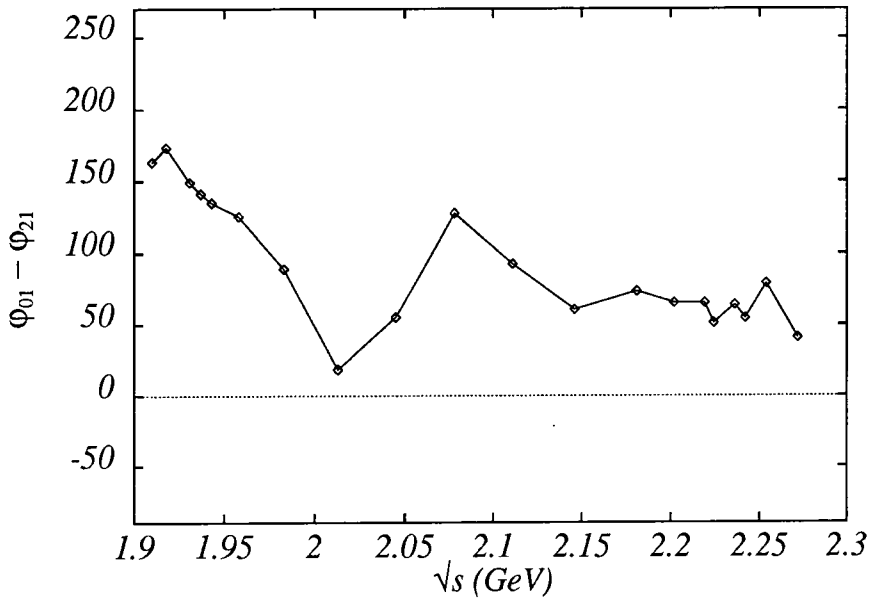

Figure 4.26: The phase difference between the 0_1 and 2_1 partial waves in solution $\mathcal{B}$.

seen in the description of solution $\mathcal{A}$ above, the consideration of both the measured phase difference $\phi_1^0 - \phi_1^2$ and the 0_1 and 2_1 amplitudes in the Argand plane with the overall phase choice determined by the apparent dominant resonant states in these waves, suggest that this phase choice is indeed reasonable. Furthermore, in solution $\mathcal{B}$, a second candidate resonance is seen in the 2_1 wave below 2.1 GeV .

The $L = 2$ waves 1_2 and 3_2 are pictured in Figs. 4.27 and 4.28. Examining first the 3_2 wave, it is apparent that there is again a loop at roughly the same mass as was seen in solution $\mathcal{A}$, although the phase variation is perhaps slower, indicating that the state is less narrow in solution $\mathcal{B}$. The phase difference $\phi_1^0 - \phi_2^3$, Fig. 4.29, does indeed drop around $\sqrt{s} = 2.08$ GeV as would be expected for a resonance in the 3_2 of around this mass, although the expected rise in $\phi_1^0 - \phi_2^3$ associated with the 0_1 state is not seen. It is unclear why this should be since the corresponding rise is seen in other phase differences e.g. $\phi_1^0 - \phi_1^2$ (Fig. 4.26) and $\phi_1^0 - \phi_2^1$ (Fig. 4.30), although perhaps the phase rise in the 0_1 is being cancelled by a similar rise in the ϕ_2^3 leading to the almost flat

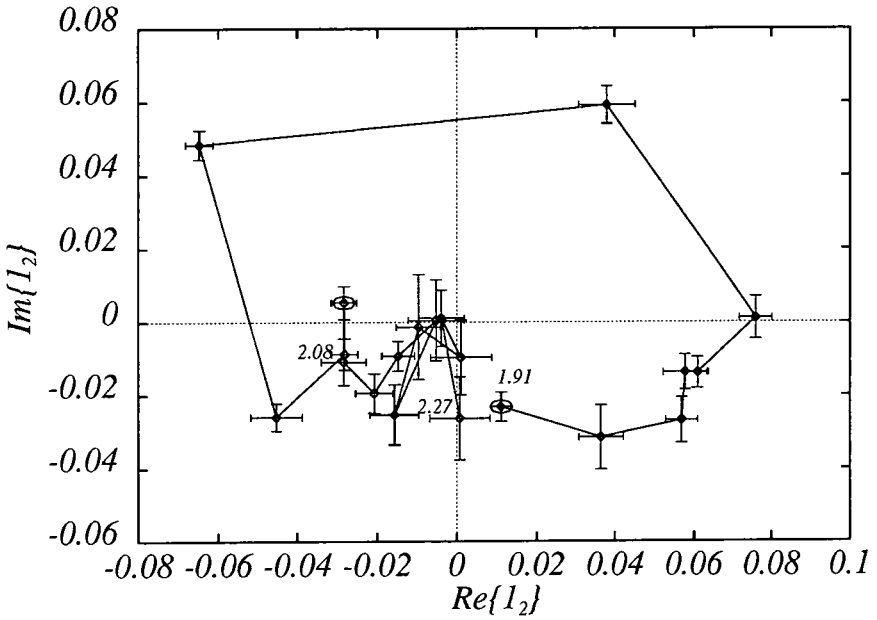

Figure 4.27: The solution $\mathcal{B}$ $J_L = 1_2$ amplitude in the Argand plane.

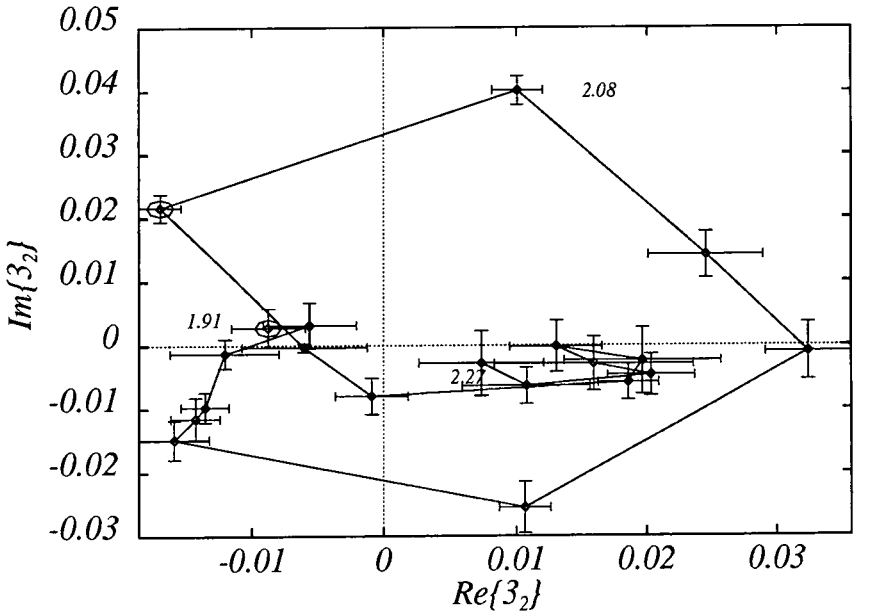

Figure 4.28: The solution $\mathcal{B}$ $J_L = 3_2$ amplitude in the Argand plane.

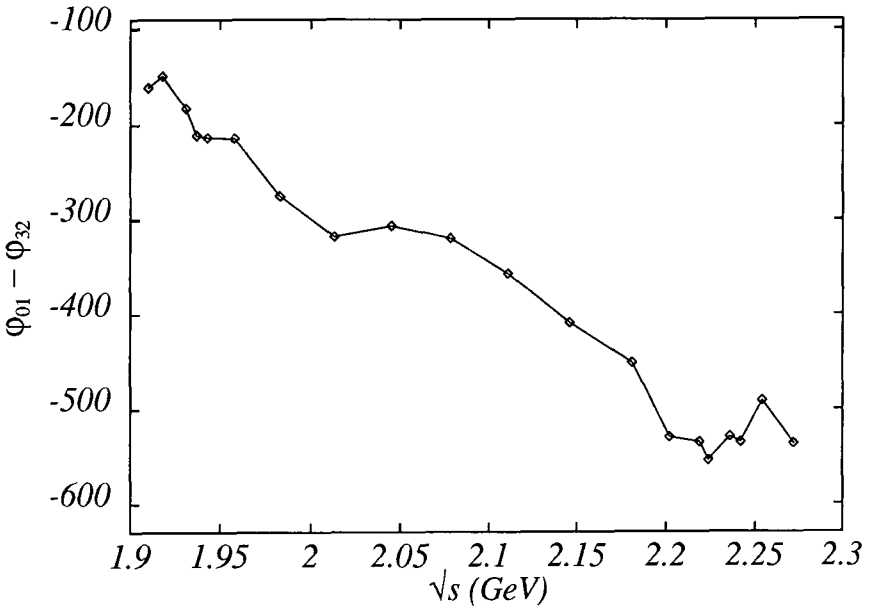

Figure 4.29: The phase difference between the 0_1 and 3_2 partial waves in solution $\mathcal{B}$.

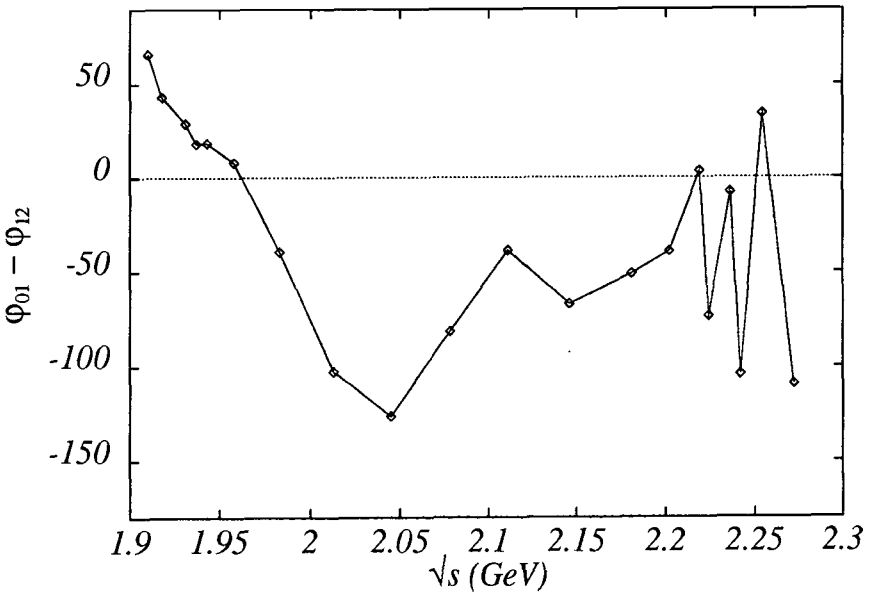

Figure 4.30: The phase difference between the 0_1 and 1_2 partial waves in solution $\mathcal{B}$.

region from $\sqrt{s} = 1.95$ to $\sqrt{s} = 2.05$ GeV in Fig. 4.29. This could occur if, for example, the 3_2 loop were caused by two (or more!) overlapping resonances, although confirmation of this would require data with even higher statistics than those of PS172. The 1_2 wave in solution $\mathcal{B}$, Fig. 4.27, is very different from its solution $\mathcal{A}$ counterpart, exhibiting a striking loop at around $\sqrt{s} = 1.97$ GeV . the resonant character of this loop is further suggested by the rapid drop in $\phi_1^0 - \phi_2^1$, Fig. 4.30 and the rise in $\phi_2^1 - \phi_0^1$, Fig. 4.23, in this region.

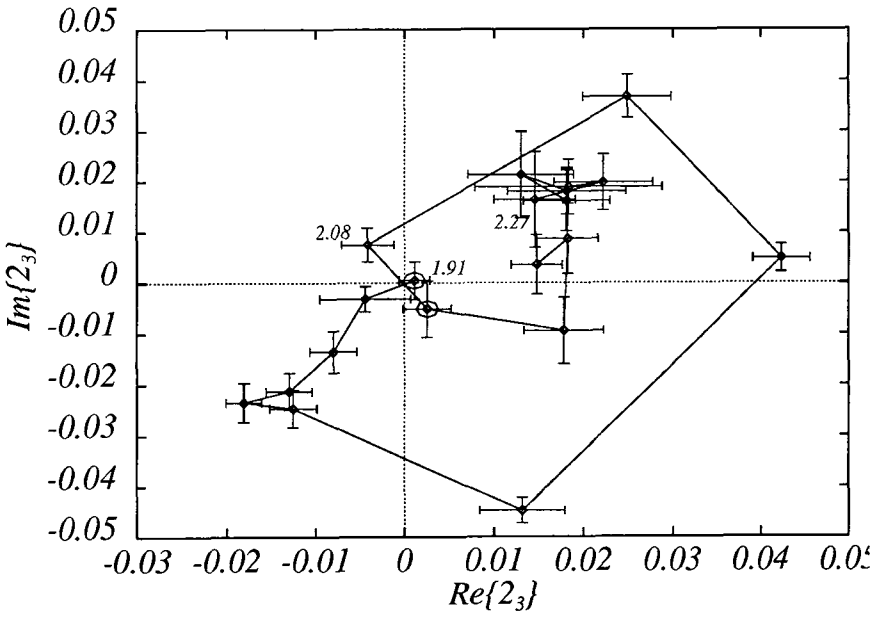

Figure 4.31: The solution $\mathcal{B}$ $J_L = 2_3$ amplitude in the Argand plane.

In Figs. 4.31 and 4.32 the $L = 3$ waves are displayed. The 4_3 wave, Fig. 4.32, behaves rather similarly to the corresponding wave in solution $\mathcal{A}$, with a possible f_4 signal in the lower part of the energy range. The 2_3 wave, Fig. 4.31, behaves rather differently in the two solutions. In solution $\mathcal{B}$ there is a loop below $\sqrt{s} = 2.1$ GeV , with similar parameters to the extra state seen in the 2_1 wave in this solution. This is suggests that these may, in fact, both be signals for the same spin-2 state.

Comparing Figs. 4.33 and 4.34 with the corresponding solution $\mathcal{A}$ waves (Figs. 4.18

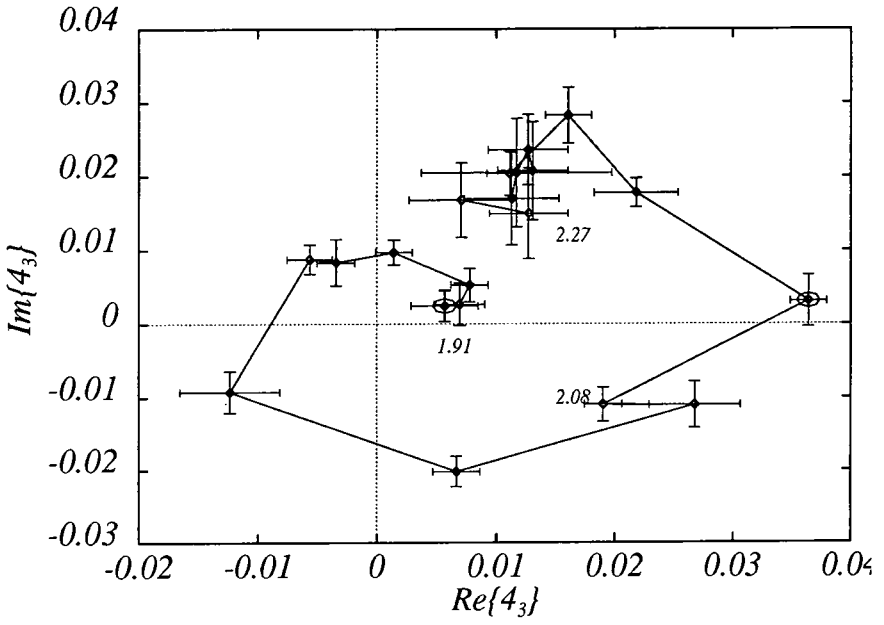

Figure 4.32: The solution $\mathcal{B}$ $J_L = 4_3$ amplitude in the Argand plane.

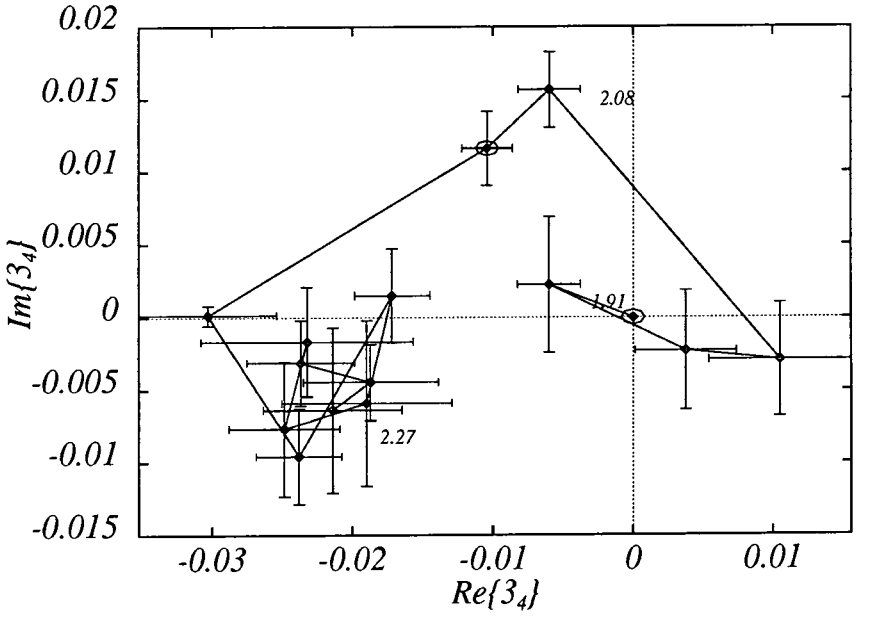

Figure 4.33: The solution $\mathcal{B}$ $J_L = 3_4$ amplitude in the Argand plane.

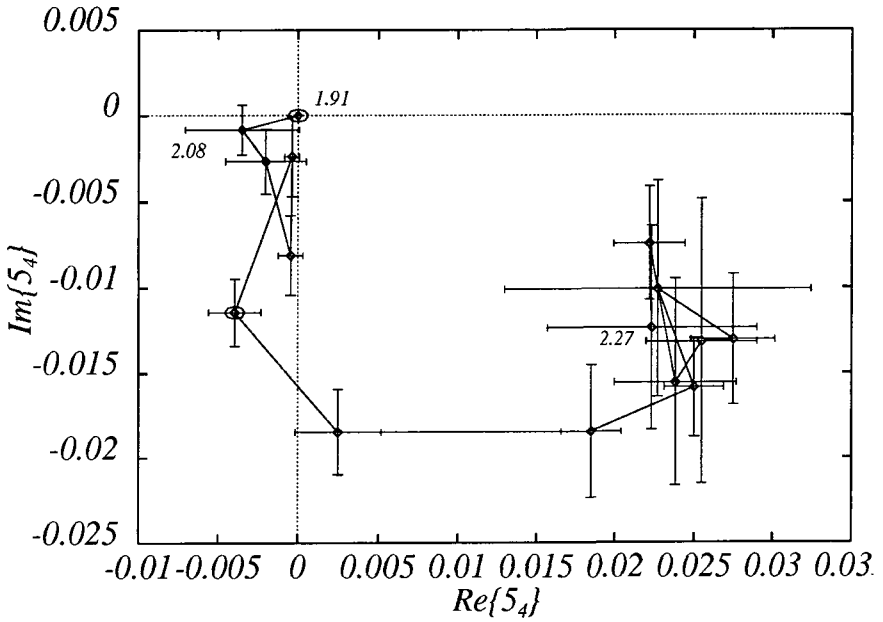

Figure 4.34: The solution $\mathcal{B}$ $J_L = 5_4$ amplitude in the Argand plane.

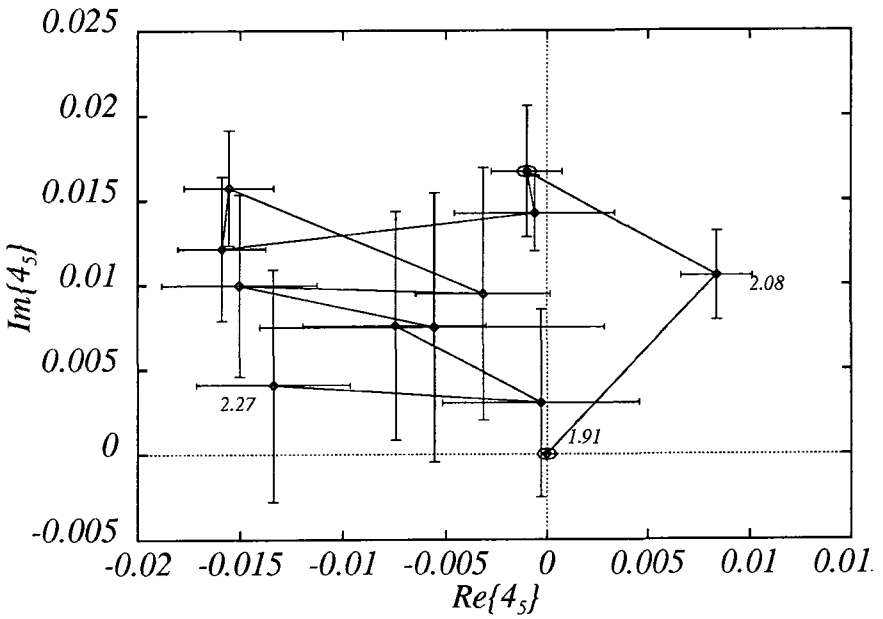

Figure 4.35: The solution $\mathcal{B}$ $J_L = 4_5$ amplitude in the Argand plane.

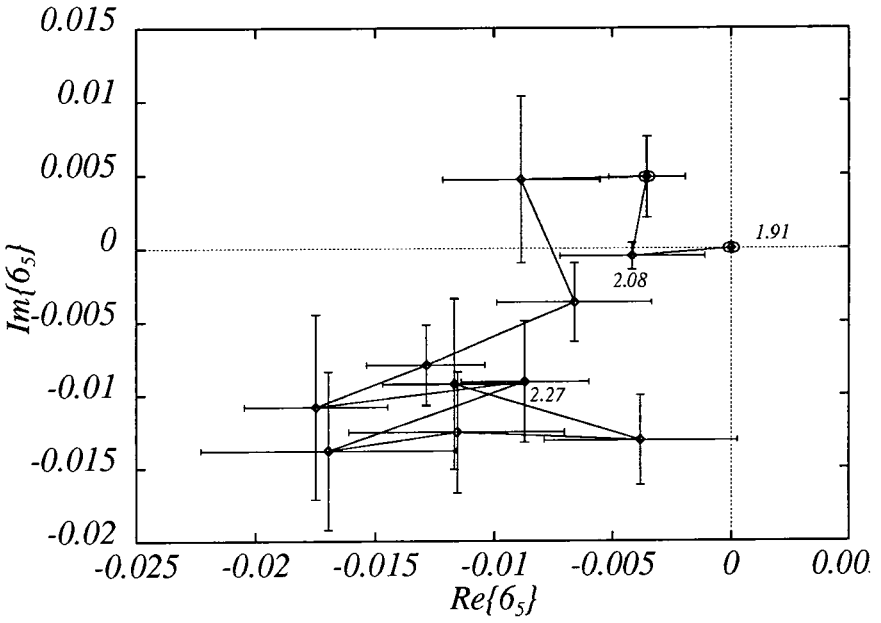

Figure 4.36: The solution $\mathcal{B}$ $J_L = 6_5$ amplitude in the Argand plane.

and 4.19) it is clear that the $L = 4$ solution $\mathcal{B}$ waves are almost identical within errors to the solution $\mathcal{A}$ waves. Similarly, the $L = 5$ waves in solution $\mathcal{B}$ are the same as those in solution $\mathcal{A}$, these waves being zero below $\sqrt{s} = 2.08$ GeV where the first threshold pair of zeros is taken to disappear.

In summary then, solution $\mathcal{B}$ has a far richer spectrum of resonance candidates than has solution $\mathcal{A}$. These include structures in the 0_1 and 2_1 waves analogous to the solution $\mathcal{A}$ structures as well as an additional spin-2 state which appears in both the 2_1 and 2_3 waves. As in solution $\mathcal{A}$, the 3_2 wave shows resonant behaviour at around $\sqrt{s} = 2.08$ GeV although with a larger width than in solution $\mathcal{A}$. The f_4 perhaps appears in the 4_3 wave, but as with solution $\mathcal{A}$ this is clouded by the background above $\sqrt{s} = 2.08$ GeV . The higher L waves are almost identical in both solutions owing to the fact that they are zero over most of the energy range in which the solutions differ since only six/eight zeros are used there.

4.2 The Effect of the Minami Transform on the Partial Waves

So far in this chapter, the partial wave content of solutions $\mathcal{A}$ and $\mathcal{B}$ have been examined at length. Up till now, however, two *a priori* equally likely candidates for the $\overline{p}p \to \pi\pi$ amplitude, the Minami transforms of solutions $\mathcal{A}$ and $\mathcal{B}$, have been ignored. in this section, the effect of the Minami transform on the partial wave amplitudes will be examined. Recall that the Minami transform is effected by simultaneously transforming *all* of the Barrelet zeros $\{\omega_i\}$ to their reflections in the unit circle, $\{\omega_i\} \mapsto \{1/\omega_i^*\}$. In the J-truncation scheme, this is equivalent to taking the complex conjugate of the amplitude. In the L-truncation scheme, this is not the case. Indeed, the complex conjugate of an L-truncation Barrelet amplitude is not itself a valid L-truncation amplitude. The amplitude in terms of the Barrelet zeros is

$$T(\omega) = \frac{|C|e^{i\phi}}{\omega^m} \prod_{i=1}^{2N} \frac{\omega - \omega_i}{1 - \omega_i}, \tag{4.17}$$

where $m = N + 1$ ($m = N$) when truncating in L (J). Its complex conjugate is then

$$\begin{aligned} T(\omega)^* &= |C|e^{i\phi}\omega^m \prod_{i=1}^{2N} \frac{1/\omega - \omega_i^*}{1 - \omega_i^*} \\ &= \frac{|C|e^{i\phi}}{\omega^{2N-m}} \prod_{i=1}^{2N} \frac{\omega - 1/\omega_i^*}{1 - 1/\omega_i^*} \end{aligned} \tag{4.18}$$

and hence this is only of the same form as Eq. (4.17) if $2N - m = m$ i.e. in the J-truncation scheme. The Minami transform $\tilde{T}(\omega)$ of the amplitude $T(\omega)$ (Eq. (4.17)) is

$$\tilde{T}(\omega) = \frac{|C|e^{i\phi}}{\omega^m} \prod_{i=1}^{2N} \frac{\omega - 1/\omega_i^*}{1 - 1/\omega_i^*}, \tag{4.19}$$

i.e. the Minami transform is not equivalent to the complex conjugate in the L-truncation scheme.

In order to ascertain what effect the Minami transform has upon the partial waves,

it is useful to first evaluate its effect on the coefficients $c_i^{(2N)}$. Examining the ten zero case, recall that the coefficient $c_0^{(10)}$ is given by,

$$c_0^{(10)} = D^{(10)} \prod_{i=1}^{10} \omega_i, \tag{4.20}$$

ad its Minami transform, denoted $\tilde{c}_0^{(10)}$ is thus

$$\tilde{c}_0^{(10)} = \tilde{D}^{(10)} \prod_{i=1}^{10} \frac{1}{\omega_i^*}, \tag{4.21}$$

where

$$\begin{aligned} \tilde{D}^{(10)} &= \sqrt{2}p|C(s)|e^{i\phi(s)} \prod_{i=1}^{10} \frac{1}{1-1/\omega_i^*} \\ &= \sqrt{2}\,p|C(s)|e^{i\phi(s)} \prod_{i=1}^{10} \frac{-\omega_i^*}{1-\omega_i^*} \\ &= \sqrt{2}\,p|C(s)|e^{i\phi(s)} \left(\prod_{j=1}^{10} \omega_i^* \right) \left(\prod_{i=1}^{10} \frac{1}{1-\omega_i^*} \right). \end{aligned} \tag{4.22}$$

Now, since the overall phase of the amplitude, $\phi(s)$, is arbitrary and can have no effect on observable quantities, such as the modulae and relative phases of the partial wave amplitudes, it will, for the purposes of this section, be ignored. Then,

$$\begin{aligned} \tilde{c}_0^{(10)} &= \sqrt{2}\,p|C(s)| \prod_{i=1}^{10} \frac{1}{1-\omega_i^*} \\ &= D^{(10)*} = c_{10}^{(10)*}. \end{aligned} \tag{4.23}$$

Examining next the transformation of $c_{10}^{(10)} = D^{(10)}$, a similar relation is found—

$$\begin{aligned} \tilde{c}_{10}^{(10)} &= \tilde{D}^{(10)} \\ &= D^{(10)*} \prod_{i=1}^{2N} \omega_i^* = c_0^{(10)*}. \end{aligned} \tag{4.24}$$

In fact, this pattern holds in general and thus

$$\tilde{c}_i^{(10)} = c_{10-i}^{(10)*}. \tag{4.25}$$

This simple transformation behaviour of the $c_i^{(2N)}$ does not, however, translate into a simple transformation of the f_L^J (or indeed the helicity amplitudes n_J and f_J) except for the $L = 0$ amplitude, f_0^1. This amplitude is given by

$$\begin{aligned} f_0^1 &= \frac{1}{3}\sqrt{\frac{2}{3}}(2f_1 + n_1) \\ &= \frac{1}{3}\sqrt{\frac{2}{3}}\left[-\frac{2}{35}c_1^{(10)} - \frac{2}{5}\left(c_3^{(10)} - c_9^{(10)}\right) + 2c_5^{(10)} - 2c_7^{(10)}\right. \\ &\quad \left. -\frac{1}{7}c_1^{(10)} - \frac{3}{5}\left(c_3^{(10)} + c_9^{(10)}\right) + c_5^{(10)} + c_7^{(10)}\right] \\ &= \frac{1}{3}\sqrt{\frac{2}{3}}\left[-\frac{1}{5}\left(c_1^{(10)} + c_9^{(10)}\right) - \left(c_7^{(10)} + c_3^{(10)}\right) + 3c_5^{(10)}\right] \end{aligned} \tag{4.26}$$

and so, substituting the transformed values of the $c_i^{(10)}$, Eq. (4.25) gives,

$$\tilde{f}_0^1 = \frac{1}{3}\sqrt{\frac{2}{3}}\left[-\frac{1}{5}\left(c_9^{(10)*} + c_1^{(10)*}\right) - \left(c_3^{(10)*} + c_7^{(10)*}\right) + 3c_5^{(10)*}\right], \tag{4.27}$$

i.e. $\tilde{f}_0^1 = f_0^{1*}$ and so $|\tilde{f}_0^1|^2 = |f_0^1|^2$.

In Figs. 4.37–4.39 the contributions to $p^2\sigma$, $(2J+1)|f_{J\pm1}^J|^2$ are shown for the Minami transform of solution $\mathcal{A}$. Comparing with the corresponding figures for the untransformed case, Figs. 4.1–4.3, at first glance it appears that the squared modulae of all the amplitudes are unchanged (as has been shown above to be the case for the f_0^1 amplitude), however, this is *not* in fact the case. Closer examination of Figs. 4.37–4.39 and Figs. 4.1–4.3 reveals that in fact the contributions with equal L are swapped over by the Minami transformation. Actually, if the figures are examined more closely still, it is noticable that even this conclusion is slightly incorrect, the swapping over being not quite exact. It should be noted that it is not the modulae squared which get swapped

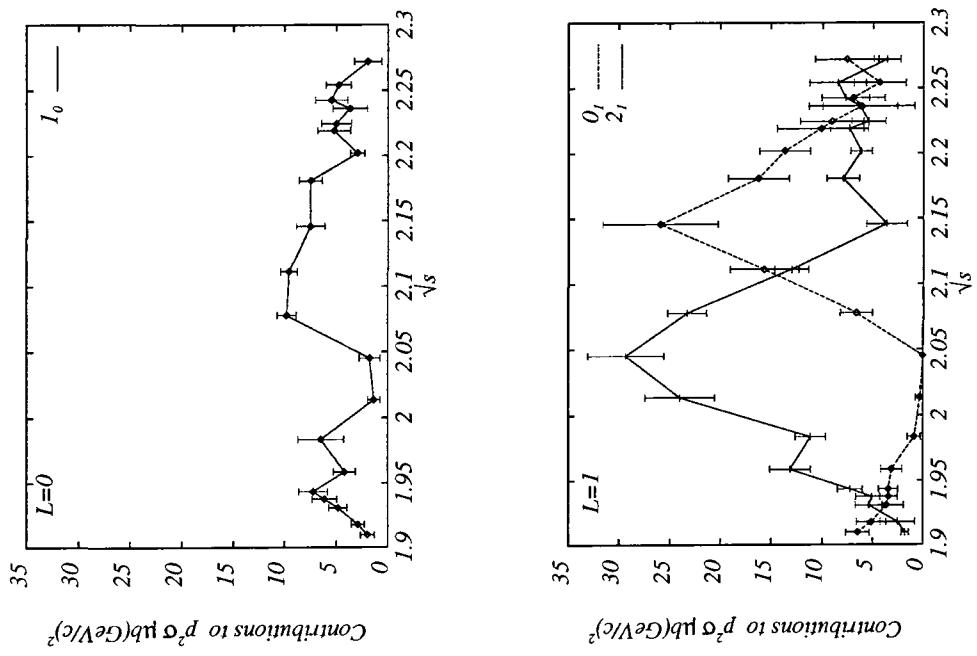

Figure 4.37: Contributions to $p^2\sigma(s)$ of the $L = 0$ and $L = 1$ partial waves of solution $\mathcal{A}$ Minami transformed.

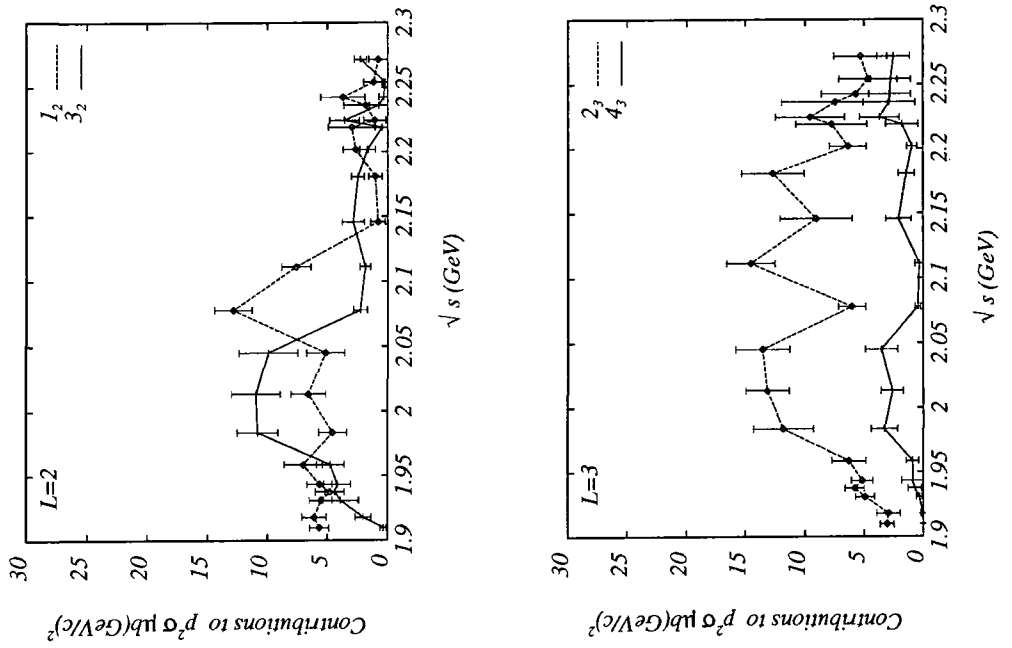

Figure 4.38: Contributions to $p^2\sigma(s)$ of the $L = 2$ and $L = 3$ partial waves of solution $\mathcal{A}$ Minami transformed.

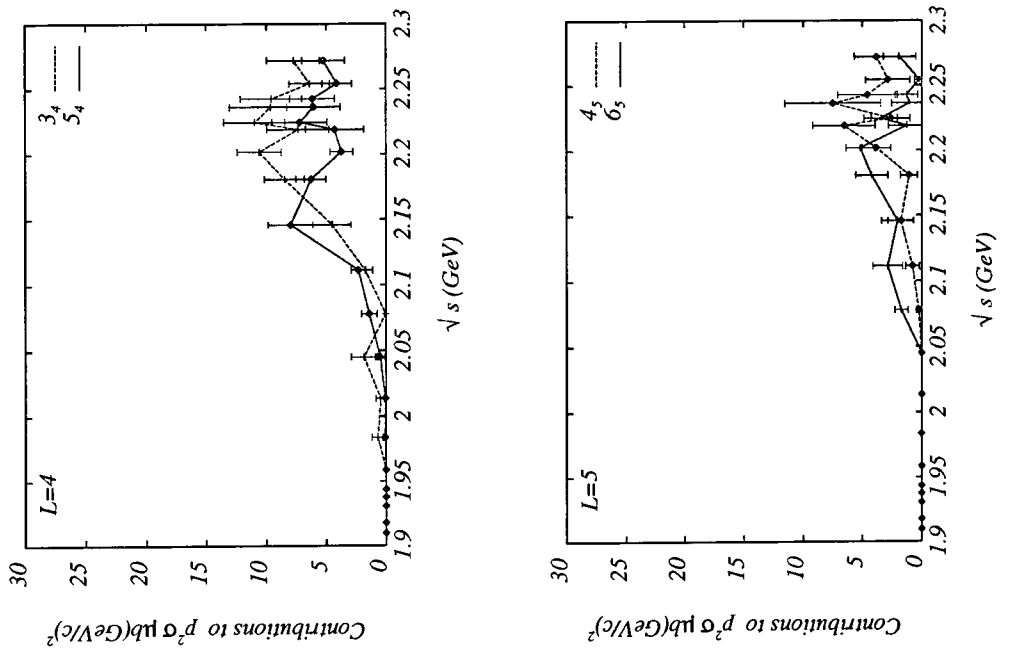

Figure 4.39: Contributions to $p^2\sigma(s)$ of the $L = 4$ and $L = 5$ partial waves of solution $\mathcal{A}$ Minami transformed.

over but $2J + 1$ times the modulae squared, i.e.

$$(2(L \pm 1) + 1)\left|\tilde{f}_L^{J=L\pm1}\right|^2 \simeq (2(L \mp 1) + 1)\left|f_L^{J=L\mp1}\right|^2 . \tag{4.28}$$

The transformations of the phase differences are also of interest, as these will, as will be argued later, allow us to disregard the Minami transformed solutions in favour of the untransformed ones. Under the Minami transformation, the relative phases of amplitudes are approximately preserved. This transformation is, however, less exact than the approximate swapping over of the contributions to the cross-section noted above. The phase differences between the equal L partial wave amplitudes at one momenta, $P_{lab} = 1.089$ GeV/c , are given for both solution $\mathcal{A}$ and its Minami transform in Table 4.1.

The above described approximate swapping over of the equal L amplitudes contributions to $p^2\sigma$ will imply certain relationships between the partial waves since the

	$\phi_1^0 - \phi_1^2$	$\phi_2^1 - \phi_2^2$	$\phi_3^2 - \phi_3^4$	$\phi_4^3 - \phi_4^5$	$\phi_5^4 - \phi_5^6$
Untransformed	93°	41°	292°	241°	327°
Transformed	98°	50°	228°	242°	331°

Table 4.1: Phase differences between equal L amplitudes at $P_{lab} = 1.089$ GeV/c for solution $\mathcal{A}$ and its Minami transform.

observables must remain unchanged. In order hopefully to understand this further it is instructive to examine the much simpler case of 2 zeros, in which there are only three non-zero L–S basis amplitudes. In the L-truncation scheme, these are f_0^1, f_1^0 and f_1^2, and are given by

$$\begin{aligned} f_0^1 &= \frac{1}{3}\sqrt{\frac{2}{3}}(2f_1 + n_1) \\ f_1^0 &= -\sqrt{2}\,n_0 \\ f_1^2 &= \frac{4}{5\sqrt{5}}(3f_2 + n_2) \end{aligned} \tag{4.29}$$

where $n_2 = 2f_2$ and $n_1 = f_1$. Now, the expansion in terms of the n_J and f_J of the transversity amplitudes is,

$$\sqrt{2}\,pT^{\pm} = n_0P_0 + n_1P_1 + n_2P_2 \pm i\left(f_1P_1^1 + f_2P_2^1\right) \tag{4.30}$$

where the P_i and P_i^1 are the Legendre functions. Hence,

$$\begin{aligned} \sqrt{2}\,pT^{\pm} &= -\frac{1}{\sqrt{2}}f_1^0P_0 + \sqrt{\frac{3}{2}}f_0^1P_1 + \sqrt{5}f_1^2P_2 \\ &\quad \pm i\left(\sqrt{\frac{3}{2}}f_0^1P_1^1 + \frac{\sqrt{5}}{2}f_1^2P_2^1\right). \end{aligned} \tag{4.31}$$

The observables $d\sigma/d\Omega$ and $Pd\sigma/d\Omega$ will then be given by

$$2p^2\frac{d\sigma}{d\Omega} = \frac{1}{2}(2p^2|T^+|^2 + 2p^2|T^-|^2)$$

$$
\begin{aligned}
&= \frac{1}{2}|f_1^0|^2(P_0)^2 - \frac{\sqrt{3}}{2}(f_1^0 f_0^{1*} + f_1^{0*} f_0^1)P_0P_1 - \sqrt{\frac{5}{2}}(f_1^0 f_1^{2*} + f_1^{0*} f_1^2)P_0P_2 \\
&\quad + \frac{3}{2}|f_0^1|^2(P_1)^2 + \sqrt{\frac{15}{2}}(f_0^1 f_1^{2*} + f_0^{1*} f_1^2)P_1P_2 + 5|f_1^2|^2(P_2)^2 \\
&\quad + \frac{3}{2}|f_0^1|^2(P_1^1)^2 + \frac{1}{2}\sqrt{\frac{15}{2}}(f_0^1 f_1^{2*} + f_0^{1*} f_1^2)P_1^1P_2^1 + \frac{5}{4}|f_1^2|^2(P_2^1)^2 \qquad (4.32)
\end{aligned}
$$

and

$$
\begin{aligned}
2p^2P\frac{d\sigma}{d\Omega} &= \frac{1}{2}(2p^2|T^+|^2 - 2p^2|T^-|^2) \\
&= \frac{i\sqrt{3}}{2}(f_1^0 f_0^{1*} - f_1^{0*} f_0^1)P_0P_1^1 + \frac{i}{2}\sqrt{\frac{5}{2}}(f_1^0 f_1^{2*} - f_1^{0*} f_1^2)P_0P_2^1 \\
&\quad - \frac{i}{2}\sqrt{\frac{15}{2}}(f_0^1 f_1^{2*} - f_0^{1*} f_1^2)P_1P_2^1 \\
&\quad - i\sqrt{\frac{15}{2}}(f_0^{1*} f_1^2 - f_0^1 f_1^{2*})P_2P_1^1. \qquad (4.33)
\end{aligned}
$$

These may then be re-expressed as a sum over Legendre functions by substituting for the products of Legendre functions in terms of sums of Legendre functions (given in Table. 4.2 for reference) thus Eqs. (4.32) and (4.33) become

$$
\begin{aligned}
2p^2\frac{d\sigma}{d\Omega} &= P_0\left(\frac{1}{2}|f_1^0|^2 + \frac{3}{2}|f_0^1|^2 + \frac{5}{2}|f_1^2|^2\right) \\
&\quad + P_1\left(-\frac{\sqrt{3}}{2}(f_1^0 f_0^{1*} + f_1^{0*} f_0^1) + \sqrt{\frac{15}{2}}(f_0^1 f_1^{2*} + f_0^{1*} f_1^2)\right) \\
&\quad + P_2\left(-\sqrt{\frac{5}{2}}(f_1^0 f_1^{2*} + f_1^{0*} f_1^2) + \frac{5}{2}|f_1^2|^2\right) \qquad (4.34)
\end{aligned}
$$

and

$$
\begin{aligned}
2p^2P\frac{d\sigma}{d\Omega} &= P_1^1\left(-\frac{\sqrt{3}}{2i}(f_1^0 f_0^{1*} - f_1^{0*} f_0^1) - \frac{1}{2i}\sqrt{\frac{15}{2}}(f_1^2 f_0^{1*} - f_1^{2*} f_0^1)\right) \\
&\quad + P_2^1\left(-\frac{1}{2i}\sqrt{\frac{5}{2}}(f_1^0 f_1^{2*} - f_1^{0*} f_1^2)\right). \qquad (4.35)
\end{aligned}
$$

Turning first to the differential cross-section equation, Eq. (4.34), and substituting for

	P_1	P_2	P_1^1	P_2^1
P_1	$\frac{2}{3}P_2 + \frac{1}{3}P_0$	$\frac{3}{5}P_3 + \frac{2}{5}P_1$	$\frac{1}{3}P_2^1$	$\frac{2}{5}P_3^1 + \frac{3}{5}P_1^1$
P_2		$\frac{18}{35}P_4 + \frac{2}{7}P_2 + \frac{1}{5}P_0$	$\frac{1}{5}P_3^1 - \frac{1}{5}P_1^1$	$\frac{9}{35}P_4^1 + \frac{1}{7}P_2^1$
P_1^1			$-\frac{2}{3}P_2 + \frac{2}{3}P_0$	$-\frac{6}{5}P_3 + \frac{6}{5}P_1$
P_2^1				$-\frac{72}{35}P_4 + \frac{6}{7}P_2 + \frac{6}{5}P_0$

Table 4.2: Products of the first few Legendre functions expressed as sums over Legendre functions. Products involving P_0 have been omitted as these are trivial.

the amplitudes the forms

$$f_0^1 = A \qquad f_1^0 = Be^{i\beta} \qquad f_1^2 = Ce^{i\gamma} \tag{4.36}$$

where A, B, C, β and γ are real and the freedom in the choice of the overall phase has been used to make the amplitude f_0^1 real Eq. (4.34) becomes

$$\begin{aligned} 2p^2\frac{d\sigma}{d\Omega} &= P_0\left(\frac{1}{2}B^2 + \frac{3}{2}A^2 + \frac{5}{2}C^2\right) \\ &\quad + P_1\left(-\sqrt{3}AB\cos\beta + \sqrt{30}AC\cos\gamma\right) \\ &\quad + P_2\left(-\sqrt{10}BC\cos(\beta-\gamma) + \frac{5}{2}C^2\right). \end{aligned} \tag{4.37}$$

Now, if the swapping over of the equal L contributions to $p^2\sigma$ is assumed to be exact, i.e. $|\tilde{f}_1^0|^2 = 5|f_1^2|^2$ and $5|\tilde{f}_1^2|^2 = |f_1^0|^2$, the transformed amplitudes will have the form

$$\tilde{f}_0^1 = A \qquad \tilde{f}_1^0 = \sqrt{5}Ce^{i\delta} \qquad \tilde{f}_1^2 = \frac{1}{\sqrt{5}}Be^{i\epsilon} \tag{4.38}$$

which leads to the expression

$$\begin{aligned} 2p^2\frac{d\sigma}{d\Omega} &= P_0\left(\frac{5}{2}C^2 + \frac{3}{2}A^2 + \frac{1}{2}B^2\right) \\ &\quad + P_1\left(-\sqrt{15}AC\cos\delta + \sqrt{6}AB\cos\epsilon\right) \end{aligned}$$

$$+ P_2\left(-\sqrt{10}BC\cos(\delta-\epsilon)+\frac{1}{2}B^2\right) \tag{4.39}$$

for the transformed differential cross-section. The charged channel differential cross-section must, however, be independent of the *in/out* configuration of the zeros and hence, the coefficients of the P_i in Eqs. (4.37) and (4.39) must be equal. The coefficient of P_0, is just proportional to the integrated cross-section and these are equal by construction in the untransformed and transformed cases. Equating the remaining coefficients leads to the following relations between the partial wave amplitudes

$$\sqrt{10}C\cos\gamma - B\cos\beta = \sqrt{2}B\cos\epsilon - \sqrt{5}C\cos\delta \tag{4.40}$$

$$\frac{5}{2}C^2 - \sqrt{10}BC\cos(\beta-\gamma) = \frac{1}{2}B^2 - \sqrt{10}BC\cos(\delta-\epsilon). \tag{4.41}$$

Following the same procedure starting from Eq. (4.35) for the polarised differential cross-section leads to a further two relations:

$$\sin(\beta-\gamma) = \sin(\delta-\epsilon) \tag{4.42}$$

$$B\sin\beta + \sqrt{\frac{5}{2}}C\sin\gamma = \sqrt{5}C\sin\delta + \frac{1}{\sqrt{2}}B\sin\epsilon. \tag{4.43}$$

Immediately, it is apparent that if Eq. (4.42) is to be satisfied, the relative phases between the 0_1 and 2_1 waves before and after the transformation, $\beta-\gamma$, and $\delta-\epsilon$ respectively, must satisfy one of the conditions

$$\beta-\gamma = \delta-\epsilon \qquad \text{or} \qquad \beta-\gamma = \pi-(\delta-\epsilon) \tag{4.44}$$

which, at first sight, appears to confirm the observation that the measured phase differences transform approximately into themselves, thus satisfying the former condition, $\beta-\gamma=\delta-\epsilon$. However, this condition along with Eq. (4.41) leads to a strict relation

between the modulae of the amplitudes:—

$$\begin{aligned} \frac{5}{2}C^2 &= \frac{1}{2}B^2 \\ \Rightarrow \quad \sqrt{5}C &= B \end{aligned} \tag{4.45}$$

i.e. the contributions to $p^2\sigma$ and the relative phases of the amplitudes with equal L can transform *exactly* into each other only if the modulae of the amplitudes were such that their contributions to the integrated cross section were equal to begin with. This is patently *not* the case in Figs. 4.37–4.39 since the two lines for the $J = L \pm 1$ contributions do not lie on top of each other! What went wrong? The answer to this question lies in the assumption that the relative phases are *exactly* equal before and after the Minami transformation was applied. In fact, as Table 4.1 showed at one energy, the phase differences are only approximately equal, and this slight inequality is enough to allow the contributions to the integrated cross-section of the equal L amplitudes still to transform approximately into each other even though their modulae do not satisfy the appropriate generalisations of Eq. (4.45) to the case of more than two zeros.

4.3 The Resolution of the Minami Ambiguity

It has been noted that, to an excellent approximation, the equal L amplitudes behave under the Minami transformation, $\{\omega_i\} \mapsto \{1/\omega_i^*\}$, so as to swap over their contributions to the integrated cross-section, (Eq. (4.28)) and furthermore, the relative phases between the equal L amplitudes remain approximately unchanged. These two observations, coupled with the fortuitous appearance of two overlapping resonant states in the $L = 1$ amplitudes actually favours the untransformed amplitudes over their Minami transforms. Looking first at solution $\mathcal{B}$, for which this is most clear, the relative phases of the 0_1 and 2_1 waves are shown in Fig. 4.40 for both the solution and its transform. The phase difference $\phi_1^0 - \phi_1^2$ in both cases has the same gross features, there is a sharp rise in the phase difference around $\sqrt{s} = 2.05$ GeV , indicating a probable resonant

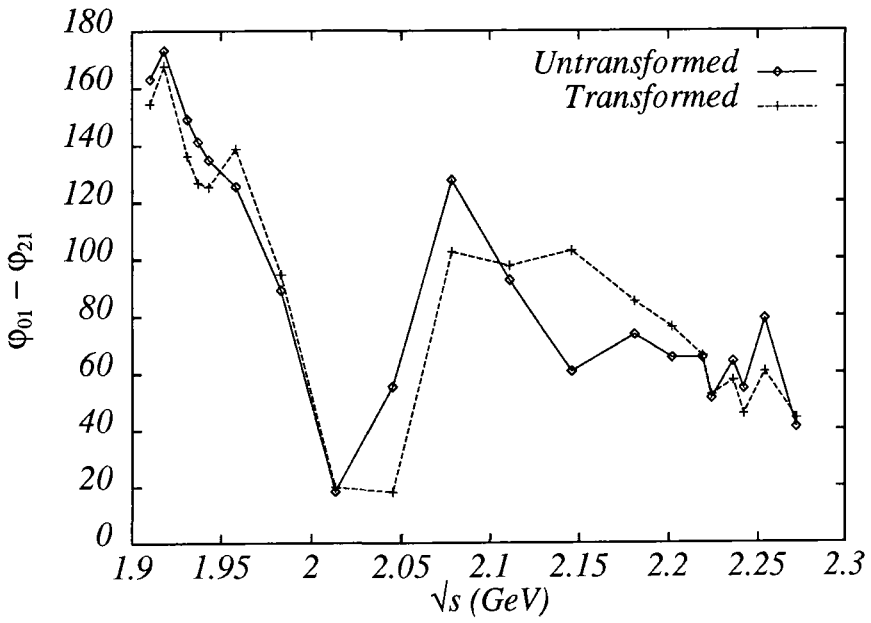

Figure 4.40: The phase difference between the 0_1 and 2_1 partial waves in solution $\mathcal{B}$ and its Minami transform.

structure in the 0_1 wave there, followed by a less sharp fall in the relative phase around $\sqrt{s} = 2.15$ GeV , suggesting a resonance appearing in the 2_1 wave at around this energy. This is completely in accord with the contributions to the cross-section of the 0_1 and 2_1 waves in solution $\mathcal{B}$, Fig. 4.4, which does indeed show just this behaviour. This is in complete contrast to the case in the Minami transform of solution $\mathcal{B}$, Fig. 4.41, in which the positions of the apparent resonant states have swapped over, even though the relative phases still indicate that they should appear in the same places and in the same waves as in the untransformed case. A similar argument applies in solution $\mathcal{A}$ but this time it is clouded slightly by the unfortunate fact that the transformed 0_1 wave, Fig. 4.37, is, within its errors, equal to zero at two energies. This leads to its phase, and hence the phase difference between it and the transformed 0_1 wave being ill-determined at these two points, these being the two points around $\sqrt{s} = 2$–2.05 GeV at which the phase difference suddenly drops. It is probable, given the fact that all other equal L phase differences seem to transform approximately into each other, that the phase difference

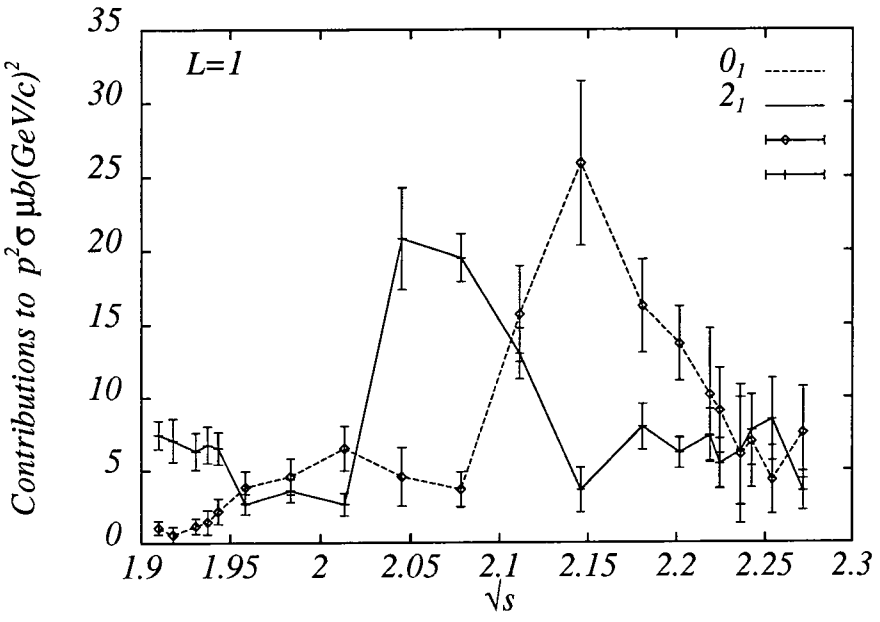

Figure 4.41: Contributions to $p^2\sigma(s)$ of the $L = 1$ partial waves of the Minami transform of solution $\mathcal{B}$.

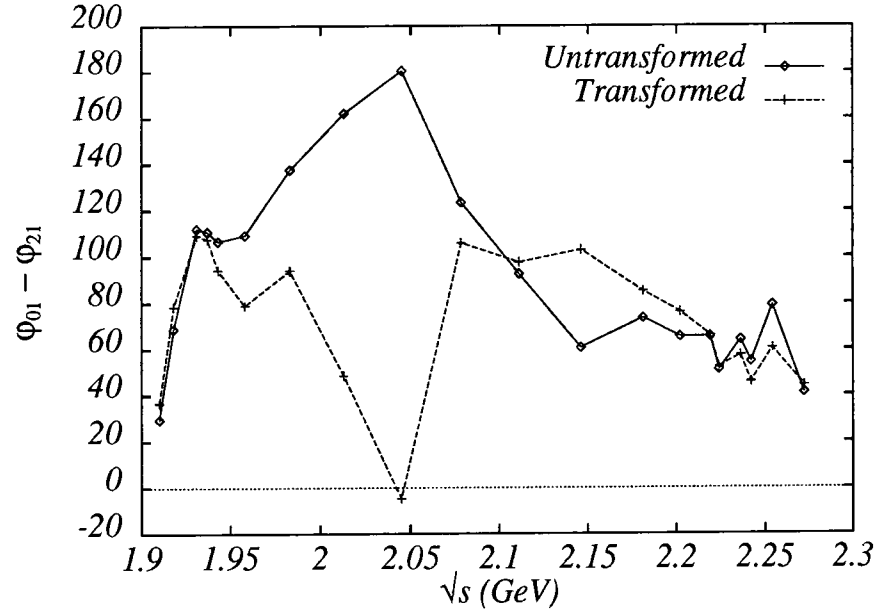

Figure 4.42: The phase difference between the 0_1 and 2_1 partial waves in solution $\mathcal{A}$ and its Minami transform.

of the transformed $L = 1$ waves at these energies is, as in the case of solution $\mathcal{B}$, approximately equal to the untransformed phase difference, the large discrepency in Fig. 4.42 being caused by the fact that moving it within its errors could lead to phase swings throughout the 360° range.

4.4 Summary

The candidates for the amplitude for $\overline{p}p \rightarrow \pi\pi$ in the energy region in which the PS172 has taken data have been narrowed to just two. The overall phase of the amplitude, although not *directly* determined by the data, has been estimated by consideration of the resonant states appearing in the partial wave decomposition of these amplitudes. Although the resonance parameters have merely been roughly guessed by examination of Figs. 4.1 and 4.4, examination of the resulting partial waves in the Argand plane confirms that these choices are probably not too far from the true values. The resulting phase $\phi(s)$ of the transversity amplitude in the forward direction is shown for reference for both solutions in Fig. 4.43. The phases for both solutions are very similar in the upper half of the energy range, as is to be expected since the zero positions and *in/out* configuration are identical there. The slight differences are due to slightly different values being estimated for the 2_1 wave in solution $\mathcal{B}$ in order to better approximate the shape in the overlap region between the 2_1 and 0_1 structures. Below about $\sqrt{s} = 2.1$ GeV , the forward phases differ, reflecting the differing widths of the structures in the 0_1 waves in the two solutions. The partial wave amplitudes with this phase choice, as shown in Figs. 4.7–4.21 and 4.22–4.36, are tabulated along with their errors in Appendix B.

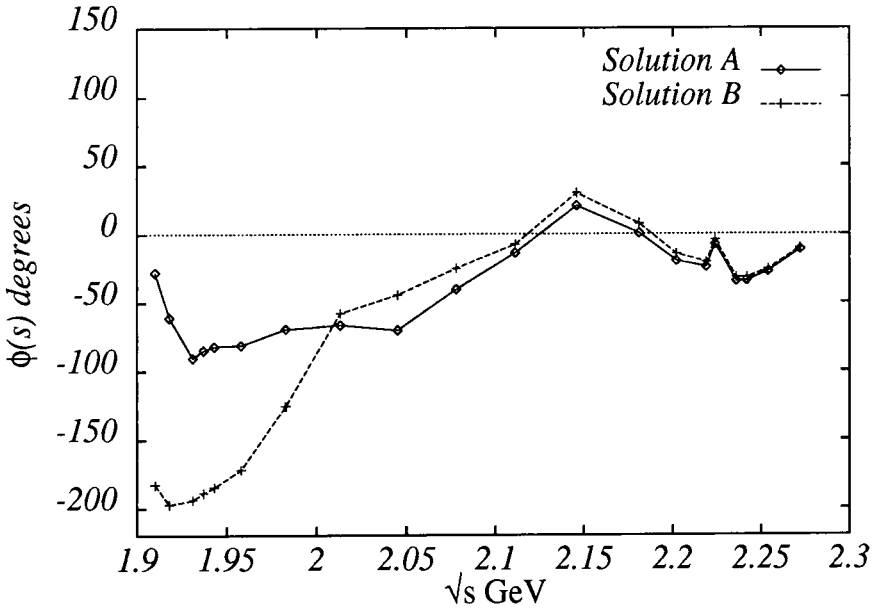

Figure 4.43: The forward phase of the amplitudes, $\phi(s)$, for solutions $\mathcal{A}$ and $\mathcal{B}$.

Chapter 5

Determination of the Resonance Parameters

In the previous chapters, the data on $\overline{p}p \rightarrow \pi^-\pi^+$ and $\overline{p}p \rightarrow \pi^0\pi^0$ taken by PS172 and Dulude *et al.* have been examined and fitted. Using the Barrelet formalism, the candidates for the $\overline{p}p \rightarrow \pi\pi$ amplitude have been narrowed from over a thousand to just four by appeal to the threshold behaviour of the Barrelet zeros and the neutral channel data and finally, to just two by a preliminary examination of the resonance content of the amplitudes. In this chapter the resonance content of these two remaining solutions will be determined by fitting suitable Breit-Wigner forms to the partial wave amplitudes in the Argand plane.

5.1 The Choice of Parametrisation

In order to determine the resonance parameters, it is necessary to perform fits to the amplitudes in the Argand plane. These, which were determined in Chapter 4 will be referred to as the "amplitude data" in this chapter. To carry out this fitting a choice of parametrisation must be made for three quantities—the energy dependence of the overall phase; the resonant amplitudes; and the non-resonant background amplitudes.

These parametrisations are examined in sections 5.1.1–5.1.3

5.1.1 The Overall Phase

The overall phase of the amplitudes was roughly determined in Chapter 4 for both solutions $\mathcal{A}$ and $\mathcal{B}$ by assuming values for the parameters of resonances in the 0_1 and 2_1 waves, estimated from the variation of the modulae squared of these waves with energy. It is clear that, when fitting resonant forms to the partial wave amplitude data, some freedom must be allowed in the overall phase, both in order not to pre-judge the parameters of the 0_1 and 2_1 waves and to allow the overall phase choice to reflect the "preferences" of all the waves being fitted. Indeed, even if the 0_1 and 2_1 waves were the only waves to be fitted, allowing for some variation in the overall phase applied to the amplitude data would be desirable in order not only to account for the inaccuracies inherent in the estimation of the 0_1 and 2_1 resonance parameters in Chapter 4 but also to allow for the effect of the background amplitudes on the overall phase, an effect which was neglected in the overall phase choice in Chapter 4, since it is expected to be small in the case of the 0_1 and 2_1 waves which exhibit only small backgrounds in the vicinity of their resonant peaks.

In the Breit-Wigner fitting of the amplitude data, the overall phase was parametrised by 19 real numbers which were used as corrections to the overall phase of the amplitude data (chosen in the previous chapter) at 19 of the 20 PS172 energies. There are, of course, only 19 such parameters since there is one overall *energy independent* phase which is completely indeterminable. Although the phase parameters are corrections to the phases of the amplitude data and should be applied as rotations of the amplitude data in the Argand plane, in the actual fitting, it is computationally more convenient to apply them as rotations of the fits in the opposite sense, since then the errorbars on the data do not need recomputing. In light of the discussion in Chapter 4 of the plausibility of the overall phase there chosen, it is expected that these corrections to the overall phase should be small and reasonably slowly varying.

5.1.2 The Resonant Amplitudes

Since the partial wave amplitudes have been determined almost right down to the $\overline{p}p$ threshold (indeed use of the proximity of the threshold was made in Chapters 3 and 4 both in the adoption of L-truncation and in the pairing property of the Barrelet zeros) it is appropriate that the threshold behaviour of the partial waves is taken into account in the choice of the Breit-Wigner form used to fit to the amplitude data. In addition, the fact that the resonant states couple to *at least* two channels, $\overline{p}p$ and $\pi\pi$, also changes slightly the appropriate form for the Breit-Wigner.

Consider the case where the resonant states couple in just three channels, these being

channel 1: $\pi\pi$,

channel 2: all channels other than $\overline{p}p$ and $\pi\pi$ with thresholds lying between $4m_\pi^2$ and $4m_p^2$, which are approximated by one two-body channel, and,

channel 3: $\overline{p}p$.

The Breit-Wigner amplitude for $3 \rightarrow 1$ is

$$T_{31} = \frac{g_3(s)g_1(s)}{m^2 - s - i\sum_{j=1}^{3} \rho_j(s)g_j^2(s)} \tag{5.1}$$

where, the phase space factors ρ_j are given by $\rho_j = 2p_j/\sqrt{s}$ with p_j the three-momentum in channel j and $g_j(s)$ is the coupling into channel j. As the threshold in channel j is approached, i.e. $p_j \rightarrow 0$, the coupling $g_j \sim p_j^{L_j}$ where L_j is the orbital angular momentum in channel j.

The denominator of Eq. 5.1 takes on a more familiar form once the identification

$$m\Gamma_{\text{tot}}(s) = \sum_{j=1}^{3} \rho_j(s)g_j^2(s) \tag{5.2}$$

is made. Now, assuming that the couplings into channel 3, $\overline{p}p$, are not dominant, and

further assuming that channel 2 has a threshold far below $2m_p^2$ (so that $\rho_2 \simeq \rho_1$), this becomes

$$m\Gamma_{\rm tot} \simeq \rho_1(s) g_{\rm eff}^2(s), \tag{5.3}$$

where g_1^2 and g_2^2 have been combined into $g_{\rm eff}^2$. Now, since $\rho_1 \sim p_1$ and $g_{\rm eff}^2 \sim p_1^{2L_1}$, Eq. (5.3) may be written,

$$m\Gamma_{\rm tot} \simeq m\Gamma_0 \left(\frac{p_1}{p_{1R}}\right)^{2L_1+1} D_{L_1}\left(\frac{p_1}{p_{1R}}\right) \tag{5.4}$$

where $\Gamma_0 = \Gamma(m)$ and $p_{1R} = p_1|_{\sqrt{s}=m}$. The function D_L is a barrier penetration factor. Then,

$$g_{\rm eff}^2(s) \simeq m\Gamma_0 \left(\frac{\sqrt{s}}{2p_{1R}}\right)\left(\frac{p_1}{p_{1R}}\right)^{2L_1} D_{L_1}\left(\frac{p_1}{p_{1R}}\right), \tag{5.5}$$

and,

$$g_j^2(s) \simeq m\Gamma_j \left(\frac{\sqrt{s}}{2p_{jR}}\right)\left(\frac{p_j}{p_{jR}}\right)^{2L_j} D_{L_j}\left(\frac{p_j}{p_{jR}}\right), \tag{5.6}$$

where Γ_j is the partial width into channel j. Thus, the resonant amplitude for $3 \to 1$ may be written as

$$T_{31} = \frac{mG_{31}(s)}{m^2 - s - im\Gamma_{\rm tot}} \tag{5.7}$$

with

$$\Gamma_{\rm tot} \simeq \Gamma_0 \left(\frac{p_1}{p_{1R}}\right)^{2J+1} D_J\left(\frac{p_1}{p_{1R}}\right) \tag{5.8}$$

and,

$$G_{31}(s) \simeq \sqrt{\Gamma_3\Gamma_1}\sqrt{\frac{s}{4p_{3R}p_{1R}}}\left(\frac{p_3}{p_{3R}}\right)^L \left(\frac{p_1}{p_{1R}}\right)^J \sqrt{D_L\left(\frac{p_3}{p_{3R}}\right) D_J\left(\frac{p_1}{p_{1R}}\right)}. \tag{5.9}$$

The factor $\sqrt{\Gamma_3\Gamma_1}$ may be re-written as Γ_0 times the square root of the product of the $\overline{p}p$ and $\pi\pi$ branching ratios of the resonant state, i.e.

$$\sqrt{\Gamma_3\Gamma_1} = N\Gamma_0 \tag{5.10}$$

where, $Br(\overline{N}N) \cdot Br(\pi\pi) \sim N^2$, and the length of the resonance vector at $s = m^2$ is

$$|T(m^2)| = N\sqrt{\frac{m^2}{4p_{3R}p_{1R}}}. \tag{5.11}$$

The functions D_{L_i} may be set equal to 1 if the threshold is very close. However, as s increases away from threshold, the threshold factors $(p_i/p_{iR})^{2L_i}$ have the undesirable property that they grow without bound. A more complete treatment of the threshold effects, within a non-relativistic potiential model [39], leads one to replace these factors with Blatt-Weisskopf factors, $B_{L_i}(z_i)$, where $z_i = p_i^2R^2$ with $R \sim 0.5$fm. The first few B_L are:-

$$\begin{aligned}
B_0 &= 1 \\
B_1 &= \frac{z}{1+z} \\
B_2 &= \frac{z^2}{9+3z+z^2} \\
B_3 &= \frac{z^3}{225+45z+6z^2+z^3} \\
B_4 &= \frac{z^4}{11025+1575z+135z^2+10z^3+z^4}
\end{aligned} \tag{5.12}$$

and these can be seen to go as p_i^{2L} as $p_i \to 0$ and to approach unity as p_i increases. The actual parametrisation of the resonant amplitudes employed in the fitting to the amplitude data of solutions $\mathcal{A}$ and $\mathcal{B}$ is obtained from Eqs. (5.7), (5.8) and (5.9) above by making the replacement

$$\left(\frac{p_i}{p_{ir}}\right)^{2L_i} D_{L_i}\left(\frac{p_i}{p_{ir}}\right) \to \frac{B_{L_i}(z_i)}{B_{L_i}(z_{iR})} \tag{5.13}$$

where z_{iR} is just z_i evaluated at $s = m^2$. The fitting parameters employed in each J_L wave being, m, Γ_0, N and a starting phase $e^{i\theta}$.

5.1.3 The Non-resonant Background

The choice of a suitable form for the background is, perhaps, the most arbitrary part of the fitting procedure. It is certainly reasonable to parametrise the background as a (complex) polynomial in $\sqrt{s}$, modified to have suitable threshold behaviour although, since each wave requires a separate background, this will, for all but the lowest order polynomials, add greatly to the number of parameters needed for the simultaneous fitting which is required in order to make use of the phase differences between waves in the amplitude data in determining the resonance parameters. For this reason, the choice adopted in this analysis is to parametrise the background by a single complex number which is then multiplied by Blatt-Weisskopf factors to give it the same threshold suppression as the resonant amplitude in the wave, i.e. the background amplitude in the J_L wave, $T^{\rm back}_{J_L}$ has the form,

$$T^{\rm back}_{J_L} = C^J_L \sqrt{B_J(s) B_L(s)}, \tag{5.14}$$

where C^J_L is the complex fitting parameter and is assumed constant over the width of the resonance. In practice this assumption is applied by fitting each wave only over the $\sqrt{s}$-range over which it appears resonant.

5.2 The Fitting Procedure

Having determined suitable forms for the parametrisation of the amplitudes, fits to the amplitude data may be performed to determine the masses, widths and couplings of resonances in the channel $\overline{p}p \to \pi\pi$. Again the CERN `MINUIT` package was used to perform this fitting. Since there are six parameters associated with each resonant wave fitted (these being the mass, the width, the normalisation, the starting phase and the real and imaginary parts of the background parameter, C^J_L) as well as 19 parameters describing the deviations from the energy dependence of the overall phase chosen in Chapter 4, it is not practicable (or, in fact, possible for solution $\mathcal{B}$ without re-compiling

the MINUIT package) to fit simultaneously to all the apparently resonant amplitudes. The approach adopted in this analysis was to perform fits to all possible subsets of 4 of the apparent resonances, with the constraint that each subset fitted to should include the two dominant structures appearing in the 0_1 and 2_1 waves. In addition, in both solution $\mathcal{A}$ and solution $\mathcal{B}$, some additional fitting runs were performed, the details of which will be given in Sections 5.2.1 and 5.2.2.

For each combination of amplitudes two fitting runs were performed, utilising two different fitting methods. These were found to be necessary since just minimising naively, with all the parameters allowed to vary at once was found, in some cases, to fail due to some parameters, most often the phase parameters, varying too wildly in the early stages of the minimisation, thus upsetting the fit. In order to prevent this, two schemes were devised, one will be referred to here as the "iterative" scheme **I** and the other as the "penalty function" scheme **P**.

In scheme **I**, the parameters are split into two classes, the phase parameters, and all other parameters, referred to in what follows as the resonance parameters (although in actual fact the background amplitude parameters are also included in this class). The fitting is then performed as follows.

1. Set all overall phase parameters to 0. (Recall that these are expected to be small, being the deviations from the phase choice adopted in Chapter 4, wherein it was argued that this phase choice was, in fact, consistent with the resonant content of the solutions, as suggested by the measured phase differences between the partial wave amplitudes). The resonance parameters' starting values are determined by examination of the amplitude Argand plots (Chapter 4).

2. Fix all the phase parameters, and minimise to "refine" the values of the resonance parameters.

3. Now fix the values of the resonance parameters and re-minimise allowing the phase parameters to vary freely.

4. Iterate steps 2 and 3 until the parameter values converge.

In this way, the rapid initial variation of parameters that can cause fitting problems are side-stepped.

In scheme **P** a (small) penalty function is added to the fit χ^2 which (loosely) constrains the phase parameters to be small and not too quickly varying.

Both schemes yield very similar fit results, and summaries of these fits are presented in Sections 5.2.1 and 5.2.2 below, along with sample fits to the amplitudes. The fit results are tabulated in full in Appendix C.

5.2.1 Solution $\mathcal{A}$

Consideration of the solution $\mathcal{A}$ partial waves in Chapter 4 uncovered five resonance candidates, appearing in the 0_1, 1_0, 2_1, 3_2 and 4_3 waves. Eight fitting runs were performed for each of the fitting schemes **I** and **P**. The states fitted in each run, along with the dominant structures appearing in the 0_1 and 2_1 waves (which are fitted in *all* runs) are summarised in Table 5.1. A "•" indicates that the given state was fitted

Run #	J_L		
	1_0	3_2	4_3
1	•	•	
2	•		•
3	•		o
4		•	•
5		•	o
6*	•	•	
7*	•		•
8*		•	•

Table 5.1: Summary of fitting runs showing which resonance candidates were included in which run. A • indicates that the wave was fitted in the run. The o's indicate runs in which the 4_3 wave was included but it's mass and width were fixed at the PDG values for the f_4 [40]. Runs marked with a * had the 2_1 waves errors reduced by a factor 1.4.

(along with the 0_1 and 2_1) and those runs with a "o" in the 4_3 column included the 4_3

state but with its mass and width fixed at the PDG f_4 values of $m = 2.05$ GeV and $\Gamma = 0.2$ GeV [40]. Runs 6, 7 and 8 were identical to runs 1, 2 and 4 respectively except that the errors on the 2_1 amplitude data were reduced by a factor of 1.4 in order to attempt to force better fitting of this wave since (subjectively) the fits for this state appeared a little worse than might have been expected from simply inspecting the amplitude data plots of Chapter 4.

The parameters determined for the 4_3 wave are, however, rather uncertain since the fitting is performed over a range which extends only 1 data point past the maximum. This range was adopted since the background becomes rather large above this energy and fitting over a larger energy range would thus require a more complicated parametrisation of the background amplitude. In the present case, this would lead to the number of fit parameters rapidly approaching the number of data degrees of freedom, thus rendering such fitting almost meaningless. In order to perform fits to this wave with more complicated parametrisations of the background it would hence be desirable to have data taken on a finer P_{lab} grid. In Figs. 5.1–5.8 typical examples of fits from various fitting runs are shown. The fits and amplitude data are shown over the P_{lab} range in which fitting to that wave was performed. The amplitude data shown in the figures have been transformed by the phase parameters determined by the relevant fitting run. The points shown along the fit curves indicate the values of the fit at the s values corresponding to the s values of the amplitude data points. The data points are shown connected by a dotted line in order to indicate their ordering in s, although this makes some of the fits appear worse than they actually are, since the fit curves "miss" the dotted lines quite badly in some cases.

Fig. 5.1 shows the fit to the 0_1 wave obtained in run 1 of the penalty function fitting scheme, denoted **P**, runs. A comparison with Fig. 4.10 reveals that the phase corrections which the fit requires are indeed small, as expected.

Fig. 5.2 shows a typical fit to the 1_0 wave in solution $\mathcal{A}$. At first glance the fit looks rather bad although closer examination reveals that most of the apparent misfitting could be removed if the data point near $(-0.020, -0.005)$ were ignored (or moved by

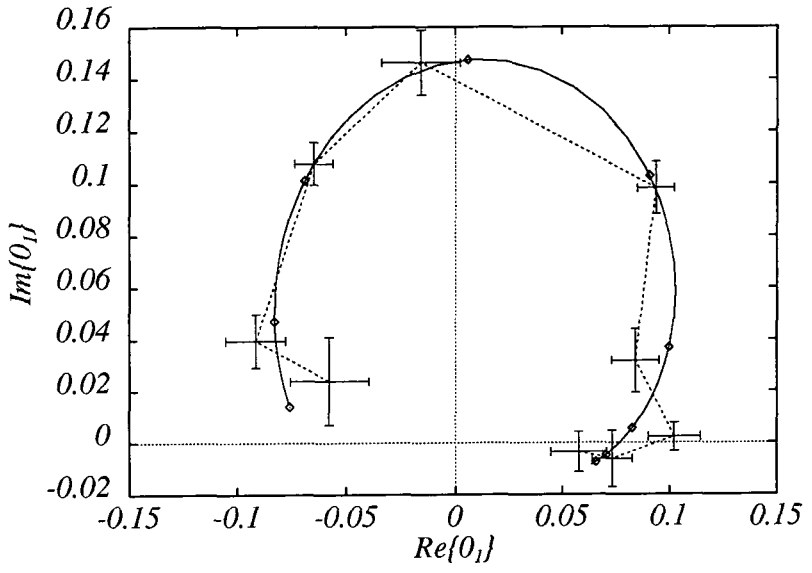

Figure 5.1: A typical fit to the solution $\mathcal{A}$ $J_L = 0_1$ amplitude data in the Argand plane. (Taken from fitting scheme **P** run 1).

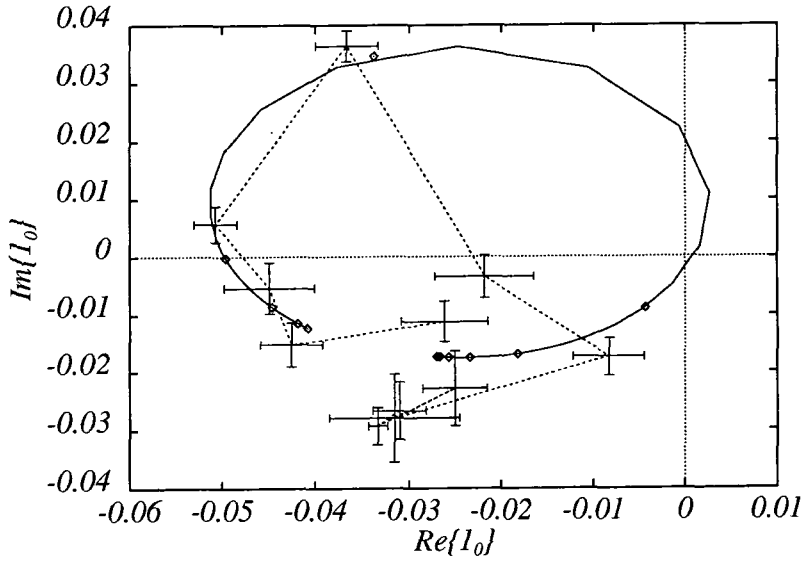

Figure 5.2: A typical fit to the solution $\mathcal{A}$ $J_L = 1_0$ amplitude data in the Argand plane. (Taken from fitting scheme **I** run 1).

a distance corresponding to 1–2 times the errorbar shown). In Figs. 5.3 and 5.4 two

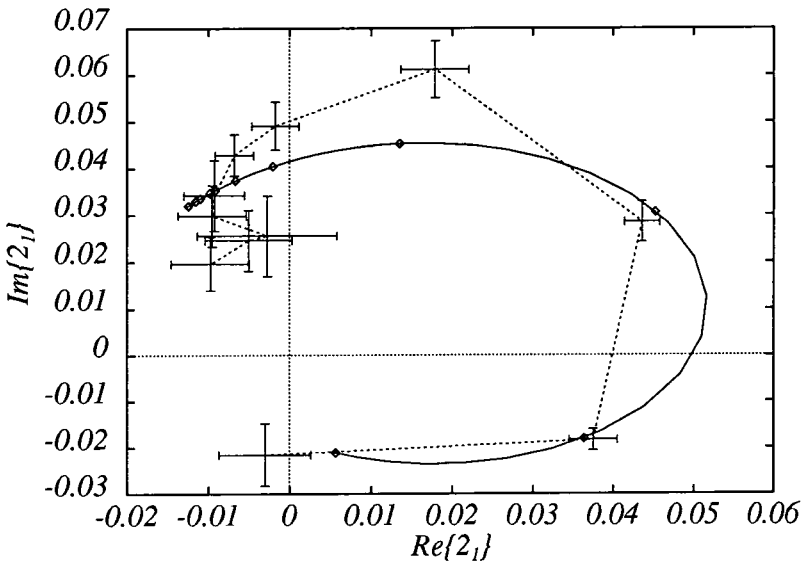

Figure 5.3: A typical fit to the solution $\mathcal{A}$ $J_L = 2_1$ amplitude data in the Argand plane. (Taken from fitting scheme **I** run 4).

fits to the 2_1 wave are shown. In each case the fits included the same states in addition to the 0_1 and 2_1 waves, the only difference between the runs being that in the fit run **I8** shown in Fig. 5.4 the contribution of the 2_1 wave to the fit χ^2 has been multiplied by a factor 2.0 in order to attempt to fit this wave better. Although the fits don't look too bad when displayed in the Argand plane, when the squared modulae of the fits and data are compared, the missing of the upper points of Figs. 5.3 and 5.4 is emphasised (Fig. 5.5). In Fig. 5.5, the solid (dotted) curve corresponds to the fit shown in Fig. 5.3 (Fig. 5.4). And it is clear that this weighting of the 2_1 contribution to the χ^2 does not have much effect in improving the 2_1 fit although the misfitting is much less striking when the fits are examined in the Argand plane.

In Fig. 5.6 a fit to the 3_2 wave is exhibited. This state appears very narrow and is hence fitted over only 5 data points. Its parameters are thus less well determined than those for other waves, e.g. the 0_1 wave in which the large number of data points fitted make one more confident in the determined resonance parameters. Data more finely

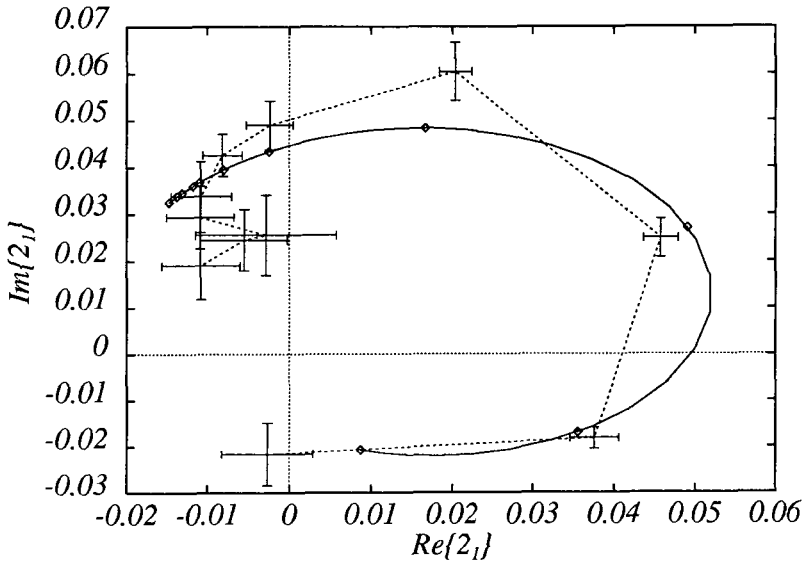

Figure 5.4: A fit to the solution $\mathcal{A}$ $J_L = 2_1$ amplitude data in the Argand plane. The contribution of this wave to fit χ^2 was multiplied by a factor 2.0 for this fit. (Taken from fitting scheme **I** run 8).

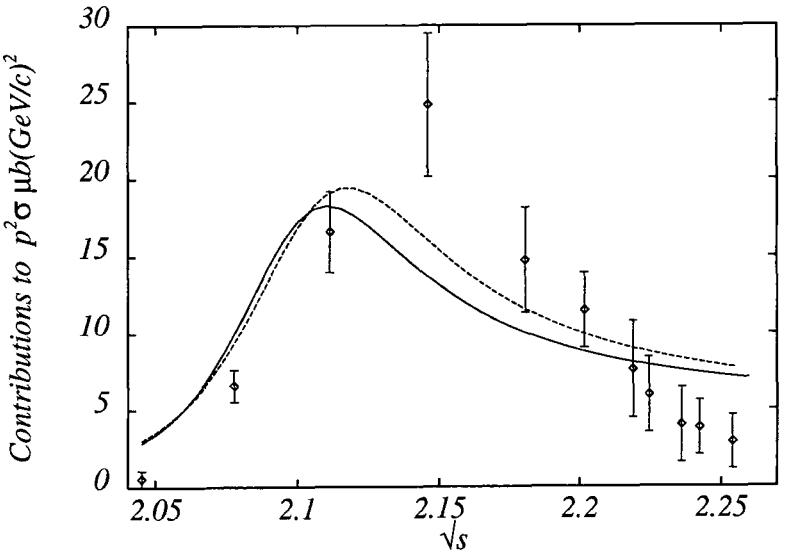

Figure 5.5: The modulae squared of the 2_1 fits displayed in Figs. 5.3 (solid line) and 5.4 (dashed line) compared with the amplitude data.

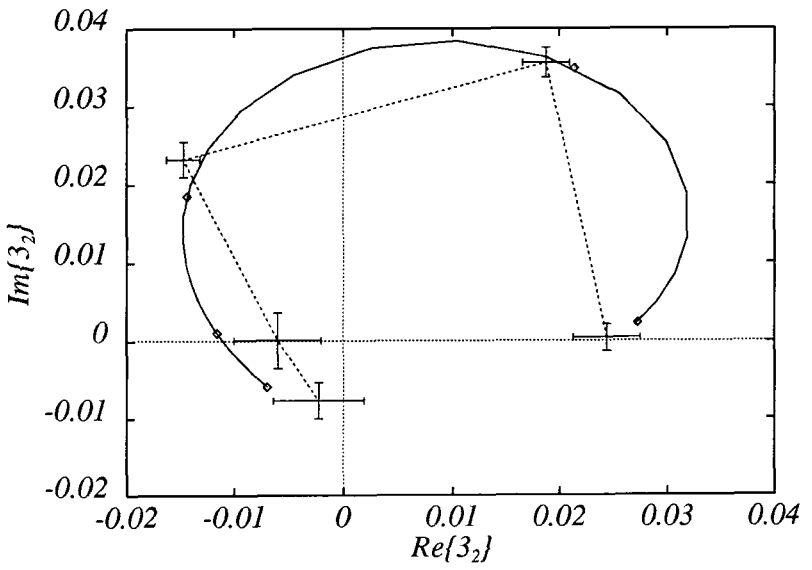

Figure 5.6: A typical fit to the solution $\mathcal{A}$ $J_L = 3_2$ amplitude data in the Argand plane. (Taken from fitting scheme **P** run 5).

spaced in P_{lab} would, of course, tie this state down more precisely.

Figs. 5.7 and 5.8 show two fits to the 4_3 wave. In each case, in order that the fits be directly comparable, the additional states fitted simultaneously were the same. The difference being that in the fit shown in Fig. 5.7 the parameters of the 4_3 state were allowed to vary freely whilst the fit shown in Fig. 5.8 had the mass and width of this state fixed at the PDG $f_4(2050)$ values. Although the free fit is, of course, better, there is very little to choose between the two. The highest energy data point included in the fitting range is, however, only two P_{lab} values above the energy of the maximum of the fit modulus, leading to fit values of the mass and width which should only be regarded as rough estimates.

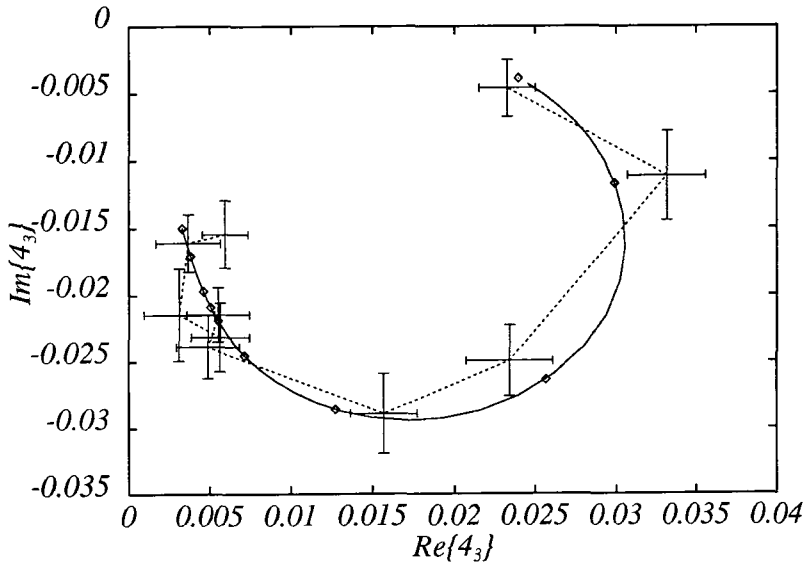

Figure 5.7: A typical fit to the solution $\mathcal{A}$ $J_L = 4_3$ amplitude data in the Argand plane. (Taken from fitting scheme **P** run 2).

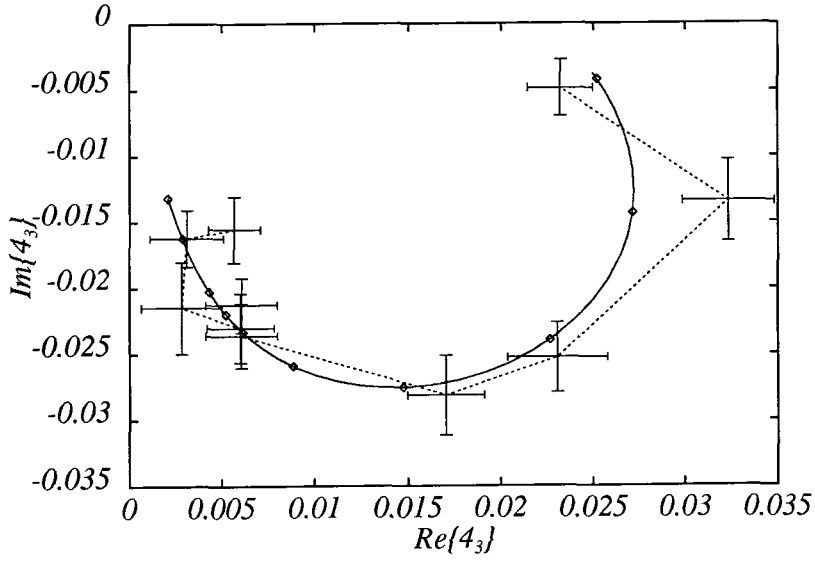

Figure 5.8: A typical fit to the solution $\mathcal{A}$ $J_L = 4_3$ amplitude data in the Argand plane in which the mass and width were fixed at the PDG $f_4(2050)$ values. (Taken from fitting scheme **P** run 3).

5.2.2 Solution $\mathcal{B}$

In Chapter 4 it was seen that the spectrum of apparently resonant states in solution $\mathcal{B}$ is quite a bit richer than that in solution $\mathcal{A}$, eight states as compared with the five solution $\mathcal{A}$ states, appearing in the 0_1, 1_0, 1_2, $2_1(\times 2)$, 2_3, 3_2 and 4_3 waves. Twenty fits were done for each of the two fitting schemes **I** and **P**, with subsets of the states being present in each fit, as was the case in the solution $\mathcal{A}$ fitting. The partial wave content of the runs are summarised in Table 5.2, with circles again indicating which states, *in addition to the dominant* 0_1 *and* 2_1 *states*, were included in each fitting run. The open circles again indicate runs in which the 4_3 wave had its mass and width fixed at the PDG f4(2050) values. Figs. 5.9–5.17 show sample fits to the solution $\mathcal{B}$ amplitude

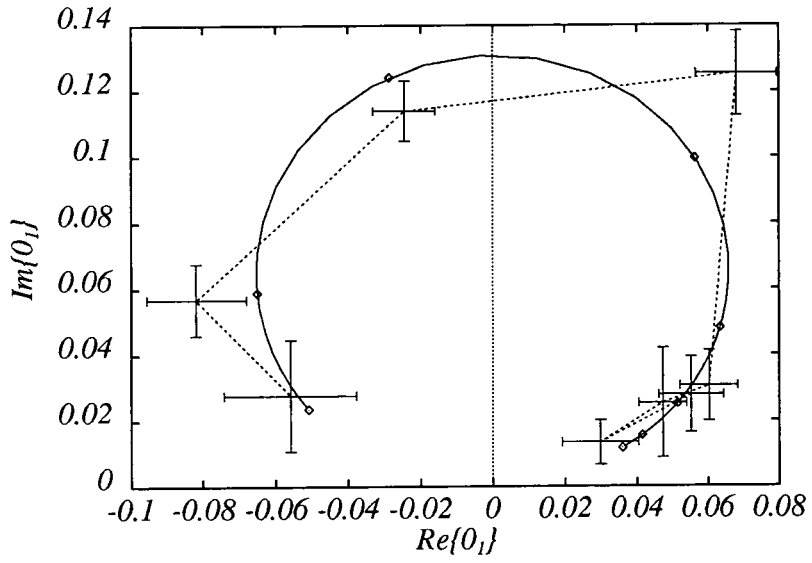

Figure 5.9: A typical fit to the solution $\mathcal{B}$ $J_L = 0_1$ amplitude data in the Argand plane. (Taken from fitting scheme **P** run 3).

data. As in Section 5.2.1, the data and fits are shown for each wave in the energy range in which the wave was fitted.

In Fig. 5.9 a sample fit to the 0_1 wave is shown and again comparison with the same wave in Chapter 4 shows that the phase corrections to the amplitude data required by

Run #	J_L					
	1_0	1_2	$2'_1$	2_3	3_2	4_3
1	•	•				
2	•		•			
3	•			•		
4	•				•	
5	•					•
6	•					o
7		•	•			
8		•		•		
9		•			•	
10		•				•
11		•				o
12			•	•		
13			•		•	
14			•			•
15			•			o
16				•	•	
17				•		•
18				•		o
19					•	•
20					•	o

Table 5.2: Summary of fitting runs showing which resonance candidates were included in which run. A • indicates that the wave was fitted in the run. The o's indicate runs in which the 4_3 wave was included but it's mass and width were fixed at the PDG values for the f_4.

the fitting are, again, small. As in solution $\mathcal{A}$, this spin 0 state is the dominant wave in terms of the size of the contributions to the integrated cross-section.

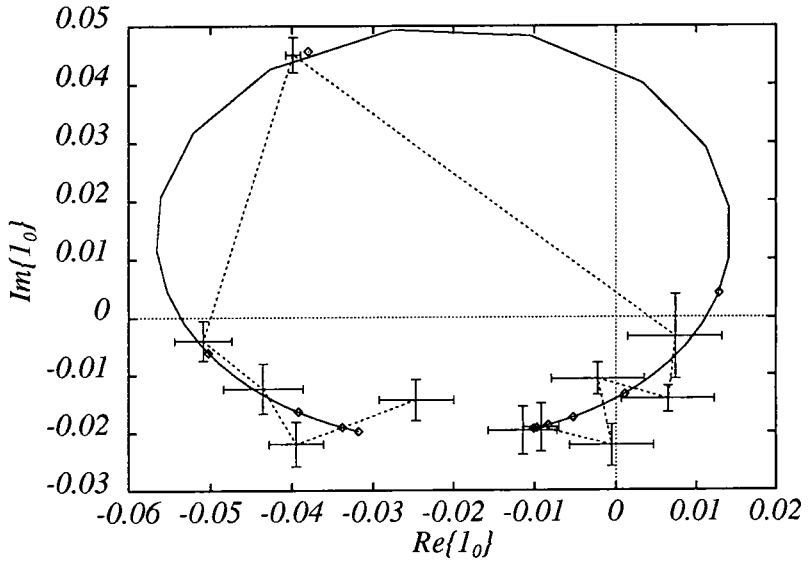

Figure 5.10: A typical fit to the solution $\mathcal{B}$ $J_L = 1_0$ amplitude data in the Argand plane. (Taken from fitting scheme **I** run 1).

FIg. 5.10 shows a sample fit to the solution $\mathcal{B}$ 1_0 wave amplitude data. The fit is somewhat better than the corresponding fit in solution $\mathcal{A}$, although the narrowness of the state means that over the main part of the resonant loop, the fit is constrained by only 3 data points, the main part of the data occurring in the tails of the resonance. Again, much more confidence in the resonance parameters would result if data more finely spaced in P_{lab} were available.

Fig. 5.11 shows a fit to the 1_2 wave, a state which does not appear in solution $\mathcal{A}$ but which is the second largest wave in solution $\mathcal{B}$. It is in fact this state which is the major difference between the two solutions' spin decompositions.

The two states appearing in the 2_1 wave are shown in Figs. 5.12 and 5.13. The more dominant of the two, corresponding to the state used to fix the approximate overall phase in Chapter 4 is shown in Fig. 5.12. The second state, which does not appear in solution $\mathcal{A}$, is shown in Fig. 5.13. Although, these ought to have been fitted together,

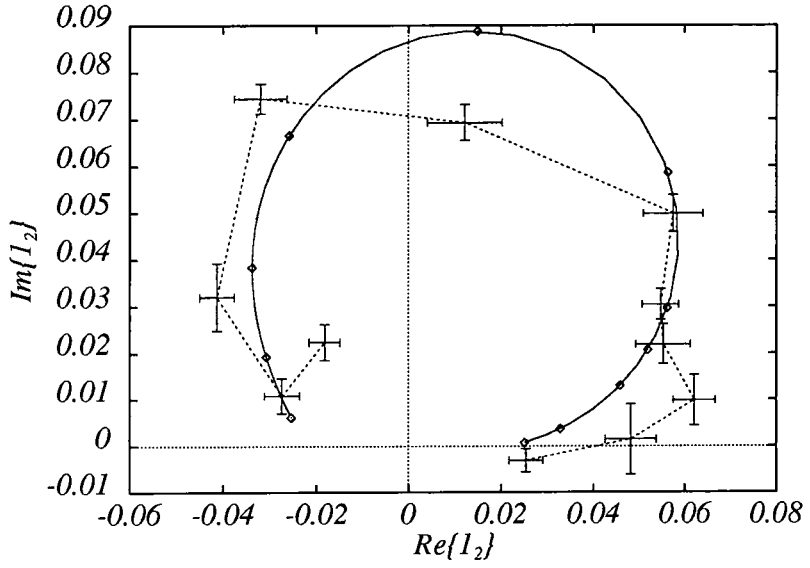

Figure 5.11: A typical fit to the solution $\mathcal{B}$ $J_L = 1_2$ amplitude data in the Argand plane. (Taken from fitting scheme **P** run 8).

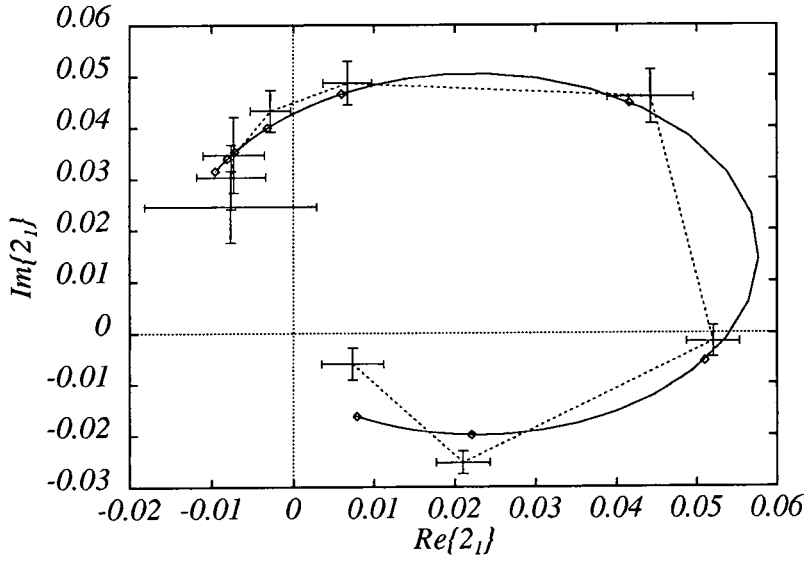

Figure 5.12: A typical fit to the solution $\mathcal{B}$ dominant $J_L = 2_1$ amplitude data in the Argand plane. (Taken from fitting scheme **P** run 8).

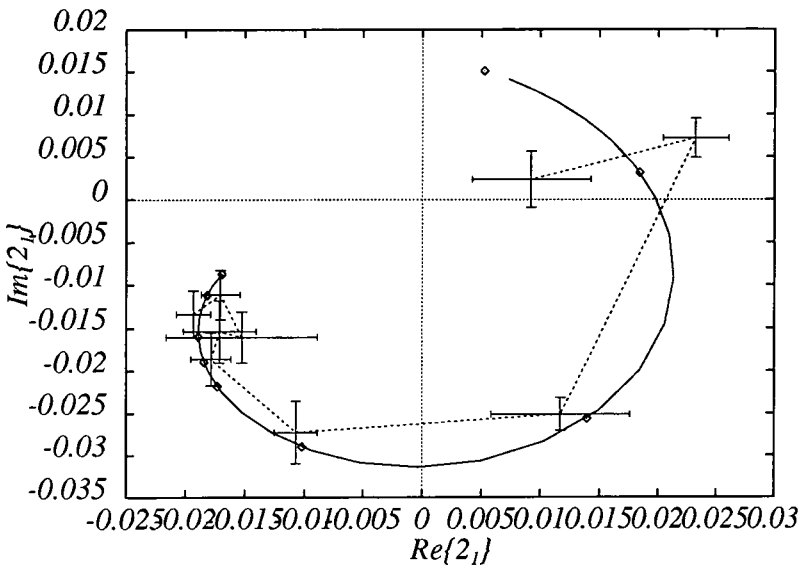

Figure 5.13: A typical fit to the extra state appearing in the solution $\mathcal{B}$ $J_L = 2_1$ amplitude data in the Argand plane. (Taken from fitting scheme **I** run 14).

allowing interference between the two resonant waves, and using a common background amplitude for both, in the fitting runs performed, these states were fitted independently (i.e. as if they occurred in separate J_L waves). There were three main reasons for adopting this approach. Firstly, there are only $\sim$1–3 P_{lab} values at which both resonant waves are simultaneously non-negligible and hence the interference effects are small (and easily absorbed into the other wave's background term). Secondly, although the parametrisation of the background in terms of a single complex constant with appropriate threshold factors is expected to be reasonable when fitting over the small energy ranges involved in fitting individual states over their widths, over energy ranges much greater than this, a more complicated (e.g. complex polynomial) form for the background would be required since the background could change considerably over the fit region. In the independent approach adopted this variation in the background (and to some extent the inteference between the tails of the two resonances) is taken into account by allowing independent background parameters in each of the waves' fit energy ranges. Thirdly, from a purely computational point of view, it is far simpler to

perform the large number of fitting runs necessary (here 40 runs) if all the waves are treated in the same manner.

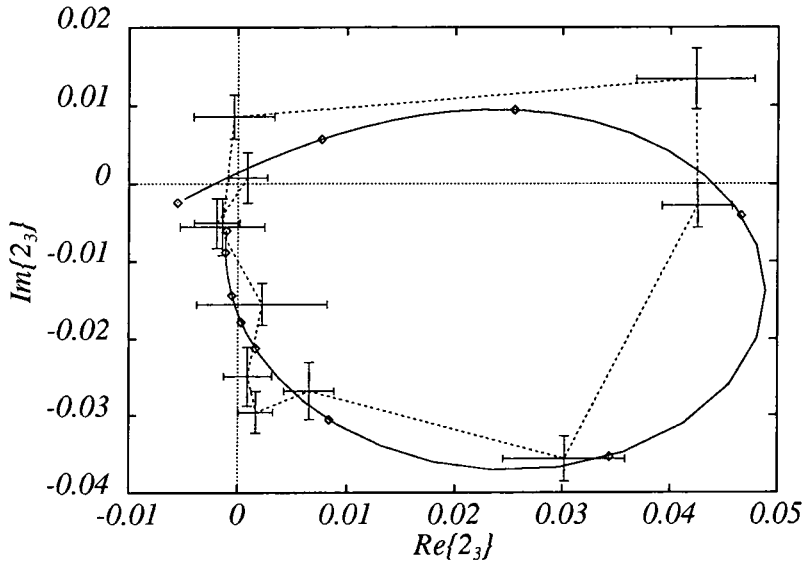

Figure 5.14: A typical fit to the solution $\mathcal{B}$ $J_L = 2_3$ amplitude data in the Argand plane. (Taken from fitting scheme **P** run 17).

In Fig. 5.14 a fit to the 2_3 wave is shown. The parameters determined for this state are so similar to those of the lower mass of the two 2_1 states fitted that it seems natural to interpret these as being signals for the same $J = 2$ state.

A typical fit to the $J_L = 3_2$ wave is shown in Fig. 5.15. This state is less narrow than the corresponding state in solution $\mathcal{A}$ and hence the fit is performed over many more P_{lab} points.

Figs. 5.16 and 5.17 show two fits to the 4_3 wave. In Fig. 5.16, the mass and width parameters were allowed to vary freely whilst in Fig. 5.17, these parameters were held fixed at the PDG $f_4(2050)$ values. In solution $\mathcal{B}$ this makes a larger difference to the fit than in solution $\mathcal{A}$, although the same remarks regarding the P_{lab} range over which the fitting was performed and the effect of this on the uncertainty of the resonance parameters also apply here.

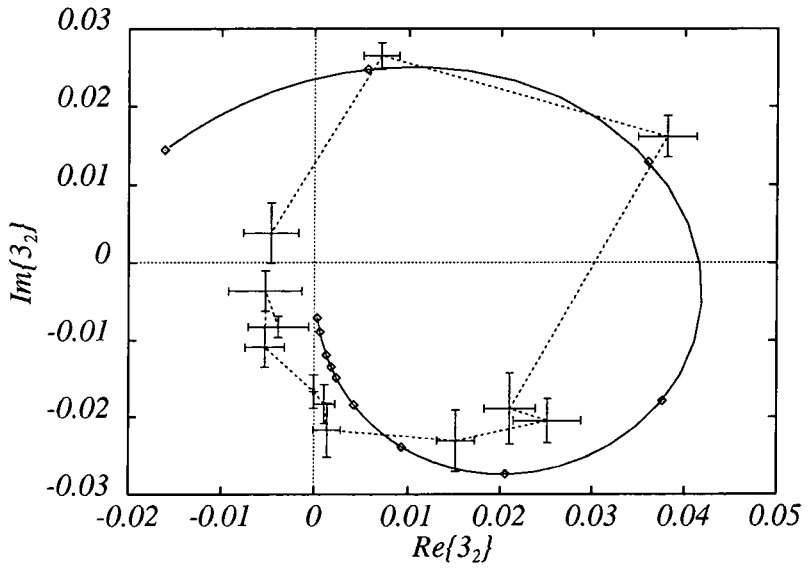

Figure 5.15: A typical fit to the solution $\mathcal{B}$ $J_L = 3_2$ amplitude data in the Argand plane. (Taken from fitting scheme **P** run 9).

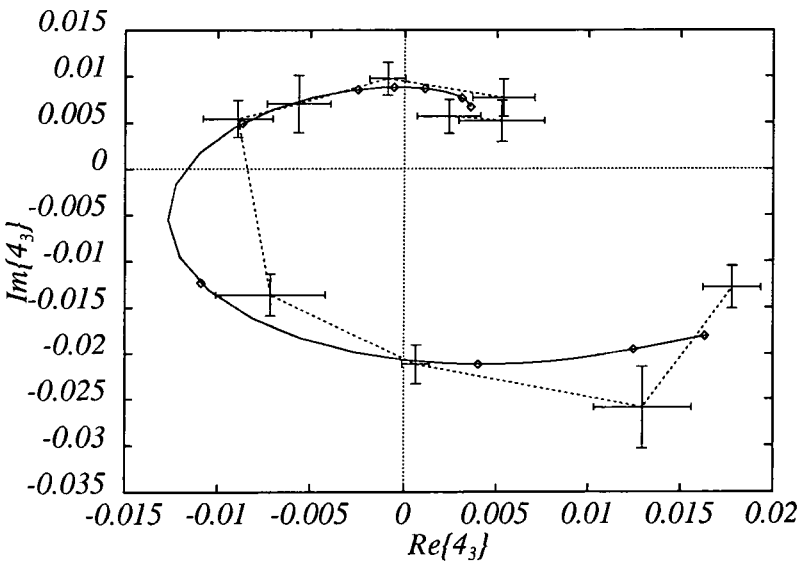

Figure 5.16: A typical fit to the solution $\mathcal{B}$ $J_L = 4_3$ amplitude data in the Argand plane. (Taken from fitting scheme **I** run 10).

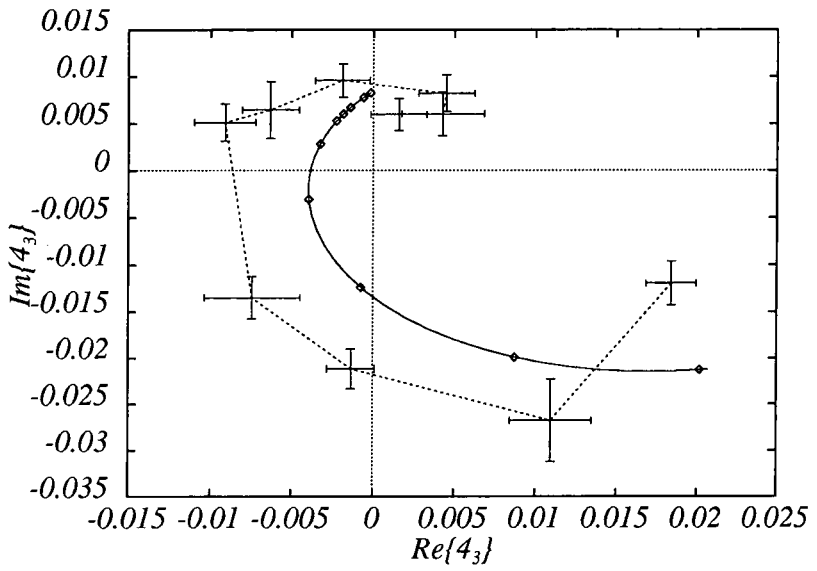

Figure 5.17: A typical fit to the solution $\mathcal{B}$ $J_L = 4_3$ amplitude data in the Argand plane in which the mass and width were fixed at the PDG $f_4(2050)$ values. (Taken from fitting scheme **I** run 11).

5.3 Summary of results of Breit-Wigner Fitting

The parameter values obtained in each of the solution $\mathcal{A}$ and $\mathcal{B}$ fitting runs are tabulated in Appendix C. Table 5.3 shows the mean values of these parameters for each state fitted. The errors quoted in the table are to be regarded as no more than a rough estimate of the actual uncertainties on the parameters, being merely averages over the different fitting runs of the individual errors returned by `MINUIT`. No account has been taken of the scatter in the central values of the parameters over different fitting runs.

The final column in the table gives the product of branching ratios, $\mathrm{Br}(\overline{N}N) \cdot \mathrm{Br}(\pi\pi)$, expressed in $(\%)^2$. These are given in terms of the normalisation parameter N, (Eq. (5.10)) by

$$\mathrm{Br}(\overline{N}N) \cdot \mathrm{Br}(\pi\pi) = C_I N^2 \times 10^4, \tag{5.15}$$

where C_I is a combined isospin/spin factor, equal to 3 for $I = 0$ (even J) waves and equal to 2 for $I = 1$ (odd J) waves. N may be estimated from the lengths of

Solution $\mathcal{A}$					
I	J^{PC}	J_L	Mass (GeV)	Width (GeV)	$\mathrm{Br}(\overline{N}N) \cdot \mathrm{Br}(\pi\pi)$ (%^{2})
0	0^{++}	0_1	2.05 ± 0.02	0.12 ± 0.04	318 ± 99
1	1^{--}	1_0	2.07 ± 0.01	0.04 ± 0.02	20 ± 8
0	2^{++}	2_1	2.09 ± 0.01	0.07 ± 0.02	58 ± 13
1	3^{--}	3_2	2.09 ± 0.01	0.06 ± 0.04	20 ± 5
0	4^{++}	4_3	2.04 ± 0.03	0.06 ± 0.04	4.3 ± 3.6
Solution $\mathcal{B}$					
I	J^{PC}	J_L	Mass (GeV)	Width (GeV)	$\mathrm{Br}(\overline{N}N) \cdot \mathrm{Br}(\pi\pi)$ (%^{2})
0	0^{++}	0_1	2.06 ± 0.01	0.05 ± 0.02	238 ± 112
1	1^{--}	1_0	2.07 ± 0.01	0.04 ± 0.01	44 ± 11
		1_2	1.97 ± 0.01	0.09 ± 0.02	72 ± 17
0	2^{++}	2_1	1.99 ± 0.02	0.10 ± 0.04	19 ± 8
		2_3	1.99 ± 0.01	0.08 ± 0.02	35 ± 10
		2_1	2.12 ± 0.01	0.07 ± 0.02	53 ± 15
1	3^{--}	3_2	2.06 ± 0.01	0.09 ± 0.02	39 ± 7
0	4^{++}	4_3	1.99 ± 0.02	0.08 ± 0.02	8.7 ± 3.1

Table 5.3: Mean parameter values for fits to solution $\mathcal{A}$ and $\mathcal{B}$ amplitude data.

the resonance vectors, V, on the Argand plots in the sections 5.2.1 and 5.2.2 using Eq. (5.11) and noting that for m, the mass of the resonance, in the energy region of study, the factor $\sqrt{m^2/4p_{3R}p_{1R}}$ may be approximated by 2/3, thus $N = 2V/3$ and,

$$\mathrm{Br}(\overline{N}N) \cdot \mathrm{Br}(\pi\pi) \simeq \frac{4}{9} C_I V^2 \times 10^4. \tag{5.16}$$

In both solutions there is evidence for states with spins 0–4, and the parameters of these states have been estimated by fitting. These states are exhibited in the Chew-Frautschi plots, Figs. 5.18 and 5.19. The states in each solution are shown along with a horizontal error bar of length $m\Gamma$. The states along the leading meson trajectory are also shown. The dashed curve is the so called peripherality curve and is the highest value of J that may contribute to the reaction, given by $J = pR + 1$, where R is the range of the interaction (assumed in Figs. 5.18 and 5.19 to be equal to 1.5 fm).

In addition to these fitted states, the 5_4 wave may be beginning to resonate at the upper end of the PS172 energy range. Confirmation of this state and an estimate of its parameters would, however, require the extension of this analysis to the Eisenhandler *et al.* and Carter *et al.* $\overline{p}p \to \pi^-\pi^+$ data.

In solutions $\mathcal{A}$ and $\mathcal{B}$, the 4_3 wave shows resonant behaviour, and performing fitting runs with the parameters of this state fixed at the PDG $f_4(2050)$ values (Figs. 5.8 and 5.17) shows it to be consistent with the f_4, although less so in solution $\mathcal{B}$ than solution $\mathcal{A}$. Assuming that this spin-4 state *is* the f_4, its branching ratio to $\overline{N}N$ may be determined since the branching ratio of the f_4 to $\pi\pi$ is known to be 17%. In solutions $\mathcal{A}$ and $\mathcal{B}$ the branching ratio products $\mathrm{Br}(\overline{N}N) \cdot \mathrm{Br}(\pi\pi)$ are determined to be $(4.3 \pm 3.6)\%^2$ and $(8.7 \pm 3.1)\%^2$ respectively, leading to values for for $\mathrm{Br}(\overline{N}N)$ of 0.25–0.5%. These values are of order expected for conventional $\overline{q}q$ states.

Both solutions also exhibit resonant behaviour in the 3_2 wave. The branching ratio products are determined to be (20 ± 5) and $(39 \pm 7)\%^2$ in solutions $\mathcal{A}$ and $\mathcal{B}$ respectively. Assuming that $\pi\pi$ branching ratios of 10–20% are typical of $\overline{q}q$ states in this mass region then the 3_2 state has $\overline{N}N$ branching ratios of 1–2% (solution $\mathcal{A}$) and

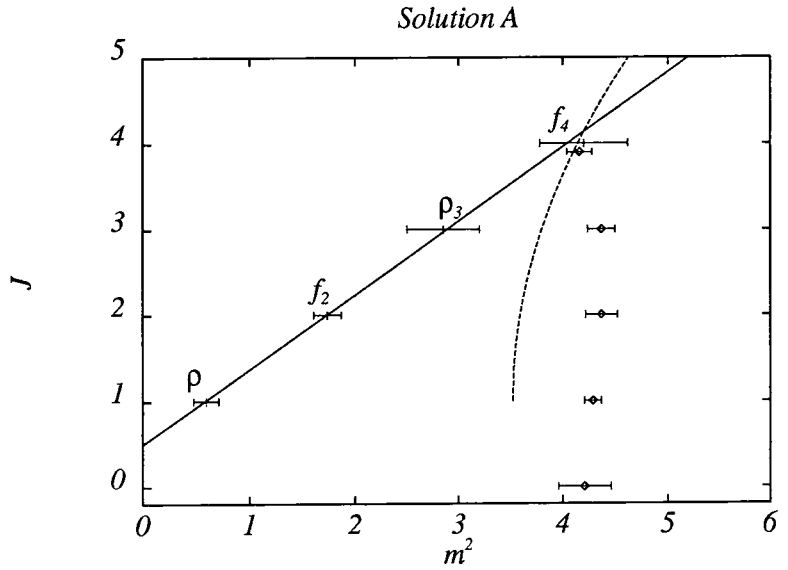

Figure 5.18: Chew-Frautschi plot showing the states found in solution $\mathcal{A}$ of this analysis (open points), along with the states along the leading Regge trajectory (crosses). The error bars correspond to the intervals $[m^2 - m\Gamma, m^2 + m\Gamma]$ for each state shown. The dashed curve is the peripherality curve $J = pR + 1$ with $R = 1.5\ fm$. (The solution $\mathcal{A}$ spin-4 state has been displaced to slightly below $J = 4$ for clarity).

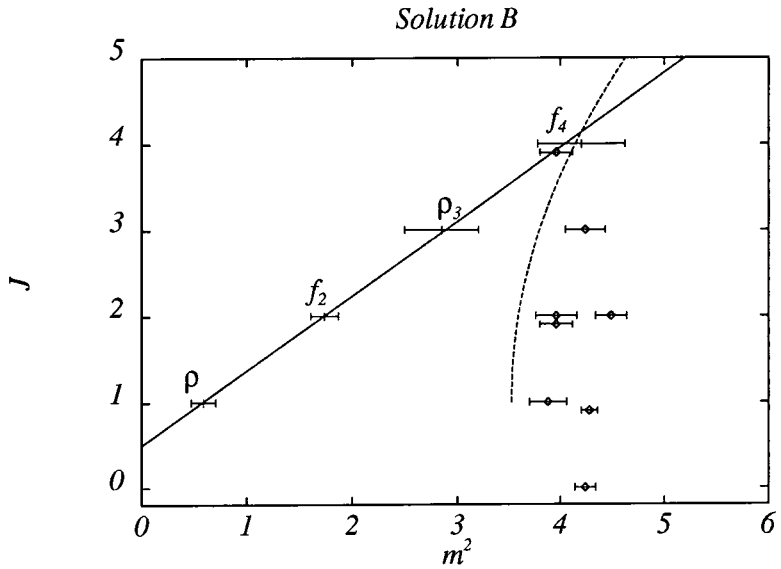

Figure 5.19: Chew-Frautschi plot showing the states found in solution $\mathcal{B}$ of this analysis (open points), along with the states along the leading Regge trajectory (crosses). The error bars correspond to the intervals $[m^2 - m\Gamma, m^2 + m\Gamma]$ for each state shown. The dashed curve is the peripherality curve $J = pR + 1$ with $R = 1.5\ fm$. (Some states have been displaced slightly from exact integer values of J for clarity).

2–4% (solution $\mathcal{B}$). These values are again consistent with the structure being a $\overline{q}q$ state.

It is in the spin-2 waves that the solutions differ the most in their resonance spectrum. Both solutions have a dominant state appearing in the 2_1 wave. In solution $\mathcal{B}$, however, there are two additional states, appearing in the 2_1 and 2_3 waves with masses somewhat lower than the dominant 2_1 state. Turning first to the dominant state appearing in the 2_1 wave of both solutions, its branching ratio to $\overline{N}N$ is, again assuming $\mathrm{Br}(\pi\pi) \simeq$ 10–20%, between 3% and 6% in both solutions, again of the order expected for $\overline{q}q$ resonances, although perhaps a little high. The two extra states appearing in solution $\mathcal{B}$, in the 2_1 and 2_3 waves have such similar masses and widths that it is tempting to interpret these as signals for the same $J = 2$ state, in which case its total branching ratio to $\overline{N}N$ is again in the range 3–6%. Of course, if these are distinct states their $\overline{N}N$ branching ratios will be proportionately smaller.

Again, in the spin-1 contributions to the process $\overline{p}p \to \pi\pi$, the two solutions differ. In both solutions the 1_0 wave appears to resonate, although this state is more marked in solution $\mathcal{B}$ than solution $\mathcal{A}$, the branching ratio product being around twice as high in solution $\mathcal{B}$, $(44 \pm 11)\%^2$ as compared to $(20 \pm 8)\%^2$ in solution $\mathcal{A}$. These values correspond, if the $\mathrm{Br}(\pi\pi) \simeq$ 10–20%, to $\overline{N}N$ branching ratios of 1–2% and 2–4% for solutions $\mathcal{A}$ and $\mathcal{B}$ respectively. The 1_2 wave resonates only in solution $\mathcal{B}$, with a comparatively large branching ratio product of $(72 \pm 17)\%^2$. With the same $\pi\pi$ branching ratio as assumed for the other states so far examined this state is determined to have a branching ratio to $\overline{N}N$ of 4–7%. Again compatible with a $\overline{q}q$ configuration although again perhaps a little high when the $\pi\pi$ branching ratio assumes its lowest value.

The spin-0 state appearing in the 0_1 wave in both solutions is, however, rather different. Its branching ratio product is so high, $318\%^2$ in solution $\mathcal{A}$ and $238\%^2$ in solution $\mathcal{B}$ that it is unlikely to be a simple $\overline{q}q$ state. Even assuming a $\pi\pi$ branching ratio as high as 30% leads to $\overline{N}N$ branching ratios of 11% and 8% for the two solutions, extremely high values, especially considering that the $\pi\pi$ branching ratio is unlikely to

be as high as this. A multiquark $\overline{q}\overline{q}qq$ state, as mentioned in Chapters 1 and 2, would be expected to couple more strongly to $\overline{N}N$ than a conventional, naive quark model $\overline{q}q$ state. Furthermore, in the MIT bag model, a $J^{PC} = 0^{++}$ $\overline{q}\overline{q}qq$ state is expected in this mass region [41].

5.4 Comparison with Other Analyses

There have been several analyses of the channel $\overline{p}p \to \pi\pi$ performed since the Eisenhandler *et al.* data became available in 1975, although, of course, the earliest analyses, based on the charged channel differential cross section data alone, could not address the numerous ambiguities in the amplitude. As was noted in Chapter 3, even with the addition of data on the charged channel polarisation asymmetry, P, there is still a large discrete ambiguity in the amplitude, showing up in the formalism adopted here as the Barrelet ambiguity $\omega_i \mapsto 1/\omega_i^*$. Only by including the data on $\overline{p}p \to \pi^0\pi^0$ can these ambiguities be properly resolved and the amplitude determined. "Amplitude analyses" performed prior to the appearance of $\overline{p}p \to \pi^-\pi^+$ polarisation and $\overline{p}p \to \pi^0\pi^0$ differential cross section data can thus only be considered as being tests of the consistency of the available data with particular resonance hypotheses. Table 5.4 summarises the spin content implied by several resonance plus background analyses.

Donnachie and Thomas analysed the results of Eisenhandler *et al.* on the two channels $\overline{p}p \to \pi^-\pi^+$ and $\overline{p}p \to K^-K^+$ using a resonance plus background model. They found evidence for resonances with masses 2.11, 2.30 and 2.48 GeV with spins 3,4, and 5 respectively along with less clear evidence for a spin-2 state near threshold lying along a granddaughter trajectory (that is to say a Regge trajectory with spin 2 units below the leading trajectory).

A related analysis, although not strictly an analysis of $\overline{p}p \to \pi\pi$, is that of Rozanska *et al.* [44]. They analysed data on $\pi^-p \to n\pi^+\pi^-$, which is related to $\overline{p}p \to \pi\pi$ if one pion exchange is assumed to be dominant. They performed a resonance plus background analysis, allowing for one resonance in each spin wave as well as an extra state in the

Ref.	J	m GeV	Γ GeV	Remarks
[42]	2	1.98	0.14	Spin-2 state ill-determined.
	3	2.11	0.21	
	4	2.30	0.29	
	5	2.48	0.26	
[43]	3	2.15	0.20	
	4	2.31	0.21	
	5	2.48	0.26	
[44]	2	2.18	0.27	
	3	2.11	0.19	
	4	2.04	0.14	Identified with f_4.
	4	2.38	0.38	
	5	2.45	0.28	
	6	2.71	0.17	
[45]	2	2.15	0.25	
	4	2.33	0.30	Consistent with analysis but not required.

Table 5.4: Summary of resonance content suggested by resonance plus background analyses.

spin-4 wave to allow for the $f_4(2050)$ and found evidence for states with spins 2–6 and masses as shown in Table 5.4. As is the case in the analyses of $\overline{p}p \to \pi^-\pi^+$ alone, no treatment of the ambiguities in the amplitude was possible in this analysis, although the spin-2 and spin-3 states in their analysis could correspond to those in the present analysis. The states in the Rozanska *et al.* analysis are, however, somewhat wider than the corresponding states found here.

As more complete data became available, with the release of the polarisation measurements of Carter *et al.* , potentially less model dependent analyses became possible and the first such analysis, performed by Carter *et al.* [43], provided some confirmation of the states reported by Donnachie and Thomas. The Carter *et al.* analysis, based on the assumption that only one partial wave was important at any one energy, found a simple progression of states with spins 3, 4 and 5 and masses 2.15, 2.31 and 2.48 GeV , in keeping with the Donnachie and Thomas values.

These analyses, although performed without the aid of data on $\overline{p}p \to \pi^0\pi^0$, will

have specific implications for the neutral channel differential cross-section. The neutral channel measurements of Dulude *et al.* , allowed analyses to be performed which *could* address the ambiguities and hence check the earlier findings. In fact, an initial analysis by Dulude *et al.* [45] found that the Donnachie–Thomas and the Carter *et al.* analyses were not in agreement with the $\overline{p}p \to \pi^0\pi^0$ differential cross-section. Dulude *et al.* found evidence for a spin-2 resonance with mass around 2.15 GeV and found that a spin-4 resonance of mass around 2.33 was consistent with their analysis but not required by it. They found no evidence for the spin-3 state reported by Donnachie and Thomas and Carter *et al.* .

Two distinct amplitude analyses of the channel $\overline{p}p \to \pi\pi$ were performed by (B.R.) Martin and Morgan, based on different methods. The first of these, referred to here as MM1 [46], employed a dispersion relation method [47] to extract partial wave amplitudes from the data on $\overline{p}p \to \pi\pi$ along with constraints from the crossed channel $\pi N \to \pi N$. In their analysis they find evidence for resonances with spins 0–5 with masses as given in Table 5.5. Their spin-0 ($m \simeq 2.07$) and spin-2 ($m \simeq 2.11$ GeV) states could correspond to states seen in this analysis, although they note in their later analysis, described below, that the angular complexity of the amplitudes emerging from the dispersion relation analysis is hard to control. Recently, an analysis based on this method, utilising more up to date πN scattering amplitudes and with some refinements in the technique, has been performed by (B.R.) Martin and Oades [48], although they present results only for the πN invariant amplitudes (linearly related to the $\overline{p}p \to \pi\pi$ transversity amplitudes) and do not discuss the spin content and possible resonances, preferring to leave such more subjective analysis for a future publication.

The Barrelet formalism, as adopted in this analysis, allows a very natural treatment of the ambiguities in the amplitude and three analyses of the combined Eisenhandler *et al.* , Carter *et al.* and Dulude *et al.* datasets utilising this formalism were performed in 1979–80, two analyses by (A.D.) Martin and Pennington, MP1 [35] and MP2 [34], and one by (B.R.) Martin and Morgan, MM2 [36]. It is these analyses which are most directly comparable with the analysis presented here, the second of the two Martin-

Pennington analyses, MP2, particularly so since they also adopted the L-truncation scheme which has been used here. Comparisons between the present analysis and the J-truncation analyses MP1 and MM2 can only be superficial. The resonance content found in these analyses is summarised in Table 5.5.

MP1				
	Sol I		Sol II	
$J_\pm$	m GeV	Γ GeV	m GeV	Γ GeV
1_+			2.10	0.20
2_+	2.15	0.25	2.15	0.30
5_-	2.45	0.30	2.45	0.30

MP2				
	Sol A		Sol B	
J_L	m GeV	Γ GeV	m GeV	Γ GeV
1_0	2.30	0.25		
1_2	2.10	0.15	2.10	0.20
2_3	2.15	0.25	2.15	0.25
3_4	2.30	0.20	2.30	0.20
4_5	2.30	0.20	2.30	0.20
5_4	2.25	0.30	2.25	0.30

MM1		
J	m GeV	Γ GeV
0	2.07	0.23
0	2.46	0.40
1	2.31	0.20
2	2.11	0.24
2	2.44	0.40
3	2.28	0.16
4	2.04 (f_4)	0.18
4	2.45	0.41
5	2.37	0.22

MM2	
All solutions	
$J_\pm$	m GeV
1_+	2.17
2_+	2.17
3_-	2.25
4_+	2.30
5_-	2.30

Table 5.5: Summary of states found in the Barrelet zero analyses MP1, MP2, and MM2 and the dispersion relation analysis MM1.

In MP1, Martin and Pennington identified 2 solutions, in the range $1.1 \leq P_{lab} \leq 2.0$ GeV , finding sizeable contributions from all spins 1–5 although not all of these waves showed unequivocal resonant character. They performed their spin decomposition in the helicity basis, with waves denoted here as $J_\pm$ where the plus (minus) sign corresponds to spin nonflip (flip) contributions. Their spin-5 wave 5_- is consistent with a $J^{PC} = 5^{--}$ resonance of mass ~ 2.45 and width ~ 0.3 GeV . In both of their solutions the resonant character of the 4_+ wave is unclear whilst the spin 3 waves show no resonant behaviour. Both of their solutions have a resonance with spin 2, with mass

~ 2.15 GeV in both solutions and width 0.25 and 0.3 GeV . Additionally, in one of their solutions, they find evidence for a $J^{PC} = 1^{--}$ state of mass around 2.1 GeV and width around 0.2 GeV .

In MM2, Martin and Morgan found nine alternative solutions which agreed with the data on both the charged and neutral channels, although they note that three of their solutions agree rather less well with the $\overline{p}p \to \pi^0\pi^0$ channel data than the remaining six. In all their solutions, they find evidence for resonances with spins 1–5, if plausible assumptions for the overall phase are made. They also address the Minami ambiguity (which in the J-truncation scheme simply corresponds to an ambiguity between the amplitude and its complex comjugate) in a manner similar to this analysis, noting that the resonance hypotheses which seem most plausible also single out one or other of the complex conjugate alternatives for the amplitude. In all solutions, they find resonant behaviour in the 1_+ and 2_+ waves at around $m = 2.17$ GeV , in the 3_- at $m \simeq 2.25$ GeV and in the 4_+ and 5_- waves at $m \simeq 2.3$ GeV , above the upper energy limit of the present analysis. It is possible that their spin 2 state corresponds to the structure seen in solutions $\mathcal{A}$ and $\mathcal{B}$ of this analysis, although it must be borne in mind that the analyses are based on different truncation schemes. The structures appearing in the spin-1 waves in the present analysis, however, appear at somewhat lower masses than the MM2 1_+ state. The possible resonance in the 5_4 wave of the present analysis could correspond to the resonance that Martin and Morgan find in their 5_- wave although, as noted earlier in the chapter, this analysis would have to be extended to include the Eisenhandler *et al.* data before this state could be confirmed.

As was previously noted, by far the most comparable analysis to the present one is MP2. They followed essentially the same procedure as has been adopted here, truncating in L rather tahn J and applying threshold constraints in the selection of the *in/out* configuration of the Barrelet zeros. It is in the threshold pair identification that the MP2 analysis differs from this analysis. Whereas in this analysis, the threshold paired zeros are actually seen to disappear within the energy range covered by the PS172 data, in MP2, the threshold paired zeros were identified as follows. Four zeros

which appeared to remain close to the unit circle throughout the energy range that they studied were assumed to be the first four to appear as energy increased away from threshold. The remaining six zeros were then taken to be in three threshold pairs, although the actual allocation of the pairs is left unknown by this, the Barrelet zero threshold constraint is imposed by allowing only in/out configurations in which exactly three of these zeros lie on one side of the unit circle. Unfortunately, as is revealed by the PS172 data, it appears that one of the zeros that they assumed to be in the last four to disappear (labelled as E in Fig. 3.13) actually disappears at around 0.36 GeV/c , leaving a different set of four zeros. As far as can be ascertained, given the ambiguities in identifying zeros in the MP2 analysis with those in the present analysis (caused both by their use of an extra zero and by the fact that zeros in the upper half of the unit circle are not so well determined since the polarisation is close to 1 over large ranges of the angular region), the in/out configuration preferred in the present analysis is one that was considered to have unacceptable threshold behaviour in the MP2 analysis. Although the two solutions found by Martin and Pennington are distinct from the nine found in MM, both analyses find states with all spins 1–5. Although most of the structures found in MP2 lie outside the energy range of the present analysis, the states common to both of their solutions in the 1_2 and 2_3 waves do lie within the PS172 P_{lab} range. Certainly, the 1_0 state in the present analysis occurs with a similar mass to the MP2 state, but the MP2 state is considerably broader than that seen here. In both of their solutions, they find a state in the 2_3 wave with mass around $m = 2.15$ GeV . In the present analysis, only solution $\mathcal{B}$ shows structure in the 2_3 wave, and then at much lower mass than the MP2 2_3 state. The spin-2 2_1 wave, however, does resonate in both solution $\mathcal{A}$ and solution $\mathcal{B}$ with mass very near to the MP2 spin-2 state although again, the state is narrower in the present analysis.

5.5 Concluding Remarks

$\overline{p}p \to \pi\pi$ has long been regarded as a promising channel in which to look for states off the leading Regge trajectory. Several analyses of this channel have suggested rich structure with states of all spins 0–6. The PS172 experiment, has extended the region in which such states may be sought almost right down to the $\overline{p}p$ threshold, and, together with the added constraints supplied by the $\overline{p}p \to \pi^0\pi^0$ data of Dulude *et al.* , the PS172 data have been analysed here, showing that the spin structure of the channel is also quite rich below lab momenta of ~ 1 GeV/c . Perhaps the most striking feature of the present analysis is the 0^{++} state at 2.05 GeV which, in both of the solutions found here, couples so strongly to both $\overline{N}N$ and $\pi\pi$ that it is unlikely to be a $\overline{q}q$ state. As has been noted, strong couplings to $\overline{N}N$ are an expected characteristic of $\overline{q}\overline{q}qq$ states, although whether or not this state has anything to do with the rich spectrum of such states predicted by the MIT bag model will have to await further measurements. The spin-2 states seen in this analysis have masses which may suggest that one of them is an excitation of the quark model to partner the $K_2^*(1978)$ of LASS [49] and, in the case of solution $\mathcal{B}$, one is possibly the $f_2(g_T(2010))$ of the BNL-CCNY group [50] (but now in the $\overline{p}p$ channel). However, in the present analysis, they each have such rapid phase variation and hence small widths that one of these tensors might be identified with the $\xi(2.2)$ first observed by Mark III [51] in $J/\psi \to \gamma\overline{K}K$ and now seen by BES [52] in not just the K^+K^- and K_sK_s channels of Mark III, but also $\eta\eta$ and $\overline{p}p$. This state BES find to have a mass of 2.16–2.22 GeV and a width of less than 50 MeV and a preliminary $J^{PC} = 2^{++}$ [52]. The relative normalization of the different BES channels would be a useful guide to the product of the $f_2(\xi)$'s $\overline{N}N$ and di-meson branching ratios to compare with the rather large values coming out of this analysis.

A particularly useful measurement, at least from the point of view of this analysis, would be the $\overline{p}p \to \pi^0\pi^0$ differential cross section at lab momenta lower than 1 GeV/c since these would allow confirmation of either solution $\mathcal{A}$ or solution $\mathcal{B}$ which have quite different predictions for the neutral channel differential cross section. Indeed,

Crystal Barrel [53] have taken measurements of $d\sigma^n/d\Omega$ at 600 MeV/c, but these data are not yet finalised. Further measurements of the charged channel differential cross section and polarisation, on a finer mesh of P_{lab} values would also be of great value in firming up estimates of the resonance parameters, particularly in the case of the 1_0 and to a lesser extent 3_2 states resonant in the middle of the PS172 lab momentum range.

Owing to the quality and P_{lab} range of the PS172 data, there are several features of this analysis that are of note. Firstly, the PS172 data have high statistics, in particular, the polarised $\overline{p}p \to \pi^-\pi^+$ cross-section is much more well determined than in previous experiments. This ties down the zero positions more tightly than previous Barrelet analyses, particularly in the upper half of the ω-plane where the zeros are less well known. Secondly, the PS172 experiment took data on both the unpolarised and polarised cross-sections *at common momenta* which has allowed this analysis to stay much closer to the data than the Martin-Pennington Barrelet analyses, MP1 and MP2, mentioned above, which used interpolations of the Legendre moments of the data in order to fit simultaneously the various observables at common momenta. Thirdly, and perhaps most importantly, the PS172 data extend far closer to the $\overline{p}p$ threshold than the previously available data of Eisenhandler *et al.* and Carter *et al.* . This has allowed the application of L-truncation threshold conditions in a way not before possible, as here the threshold paired zeros can actually be determined whereas in the previous L-truncation analysis, MP2, these pairings had to be inferred much more indirectly, leading to a choice of threshold paired zeros which is ruled out by the data near to threshold. Excitingly, the low spin states uncovered here, the 0_1 states in both solutions and possibly the 1_2 state in solution $\mathcal{B}$, have extremely large couplings to $\overline{N}N$, suggesting that these could be $\overline{q}\overline{q}qq$ states. Confirmation of the nature of these resonances is eagerly awaited.

Appendix A

The Eight and Six Zero Helicity Basis Partial Waves

Defining, as in Chapter 4, the quantities $\{c_i^{(2N)}\}$ as the coefficients in the monomial expansion (i.e. Laurent expansion) of $T(\omega)$,

$$T(\omega) = \sum_{i=0}^{2N} c_i^{(2N)} \omega^{i-m}, \tag{A.1}$$

where, in the L-truncation scheme, $m = N + 1$, and the quantity $D^{(2N)}$,

$$D^{(2N)} = \sqrt{2}\, p |C(s)| e^{i\phi(s)} \prod_{i=1}^{2N}, \frac{1}{1-\omega_i} \tag{A.2}$$

the eight and six zero formulae for the $\{n_J, f_J\}$ (as defined in Chapter 4) are easily obtained by the substitution in Eq. (4.7) for the $\{c_i\}$ in terms of the $\{c_i^{(8)}\}$ and $\{c_i^{(6)}\}$ as indicated in Chapter 4. The same formulae also result from repeating the equating of coefficients method used in Chapter 4 to derive the ten zero formulae, Eq. (4.7), using $2N = 8$ and $2N = 6$.

A.1 Eight Zero Formulae

Substituting $c_0 = c_{10} = 0$ and $c_i = c_{i-1}^{(8)}$, $1 \leq i \leq 9$ into Eq. (4.7) leads to the following eight zero formulae.

$$
\begin{aligned}
n_0 &= -\frac{1}{15}c_1^{(8)} - \frac{1}{3}(c_3^{(8)} + c_7^{(8)}) + c_5^{(8)} \\
n_1 &= -\frac{1}{7}c_0^{(8)}\ \frac{3}{5}(c_2^{(8)} + c_8^{(8)}) + c_4^{(8)} + c_6^{(8)} \\
n_2 &= -\frac{16}{21}c_1^{(8)} + \frac{4}{3}(c_3^{(8)} + c_7^{(8)}) \\
n_3 &= -\frac{8}{45}c_0^{(8)} + \frac{8}{5}(c_2^{(8)} + c_8^{(8)}) \\
n_4 &= \frac{64}{35}c_1^{(8)} \\
n_5 &= \frac{128}{63}c_0^{(8)} \\
f_1 &= -\frac{1}{35}c_0^{(8)} - \frac{1}{5}(c_2^{(8)} - c_8^{(8)}) + c_4^{(8)} - c_6^{(8)} \\
f_2 &= -\frac{4}{21}c_1^{(8)} + \frac{2}{3}(c_3^{(8)} - c_7^{(8)}) \\
f_3 &= -\frac{8}{45}c_0^{(8)} + \frac{8}{15}(c_2^{(8)} - c_8^{(8)}) \\
f_4 &= \frac{16}{35}c_1^{(8)} \\
f_5 &= \frac{128}{315}c_0^{(8)}
\end{aligned}
\tag{A.3}
$$

A.2 Six Zero Formulae

Substituting $c_0 = c_1 = c_9 = c_{10} = 0$ and $c_i = c_{i-2}^{(6)}$, $2 \leq i \leq 8$ into Eq. (4.7) leads to the following six zero formulae.

$$
\begin{aligned}
n_0 &= -\frac{1}{15}c_0^{(6)} - \frac{1}{3}(c_2^{(6)} + c_6^{(6)}) + c_4^{(6)} \\
n_1 &= -\frac{3}{5}c_1^{(6)} + c_3^{(6)} + c_5^{(6)} \\
n_2 &= -\frac{16}{21}c_0^{(6)} + \frac{4}{3}(c_2^{(6)} + c_6^{(6)}) \\
n_3 &= \frac{8}{5}c_1^{(6)} \\
n_4 &= \frac{64}{35}c_0^{(6)} \\
f_1 &= -\frac{1}{5}c_1^{(6)} + c_3^{(6)} - c_5^{(6)} \\
f_2 &= -\frac{4}{21}c_0^{(6)} + \frac{2}{3}(c_2^{(6)} - c_6^{(6)}) \\
f_3 &= \frac{8}{15}c_1^{(6)} \\
f_4 &= \frac{16}{35}c_0^{(6)}
\end{aligned}
\tag{A.4}
$$

Appendix B

The Partial Wave Amplitudes in the Argand Plane

The values of the amplitude data for solutions $\mathcal{A}$ and $\mathcal{B}$ are given in Tables B.1–B.12. For details of the overall phase chosen see Chapter 4.

P_{lab} GeV/c	$\sqrt{s}$ GeV	$\Re\{1_0\}$	$\Im\{1_0\}$
.360	1.910	$.002 \pm .002$	$-.023 \pm .002$
.404	1.918	$-.005 \pm .003$	$-.028 \pm .003$
.467	1.931	$-.019 \pm .003$	$-.031 \pm .004$
.497	1.937	$-.019 \pm .002$	$-.036 \pm .004$
.523	1.943	$-.019 \pm .004$	$-.040 \pm .005$
.585	1.958	$-.015 \pm .004$	$-.030 \pm .004$
.679	1.983	$-.026 \pm .007$	$-.033 \pm .008$
.783	2.013	$-.006 \pm .004$	$-.018 \pm .003$
.886	2.045	$-.022 \pm .005$	$.001 \pm .005$
.988	2.078	$-.038 \pm .003$	$.035 \pm .003$
1.089	2.111	$-.047 \pm .002$	$.019 \pm .003$
1.190	2.146	$-.044 \pm .001$	$.012 \pm .005$
1.291	2.181	$-.042 \pm .003$	$-.017 \pm .004$
1.351	2.202	$-.025 \pm .005$	$-.014 \pm .004$
1.400	2.219	$-.030 \pm .005$	$-.023 \pm .008$
1.416	2.224	$-.035 \pm .004$	$-.011 \pm .006$
1.449	2.236	$-.020 \pm .005$	$-.025 \pm .010$
1.467	2.242	$-.030 \pm .007$	$-.025 \pm .007$
1.500	2.254	$-.021 \pm .004$	$-.029 \pm .005$
1.550	2.272	$-.020 \pm .005$	$-.010 \pm .008$

Table B.1: The real and imaginary parts of the $L = 0$ amplitudes for solution $\mathcal{A}$ at the twenty PS172 momenta.

P_{lab} GeV/c	$\sqrt{s}$ GeV	$\Re\{0_1\}$	$\Im\{0_1\}$	$\Re\{2_1\}$	$\Im\{2_1\}$
.360	1.910	$.057 \pm .006$	$.010 \pm .006$	$.025 \pm .002$	$-.009 \pm .002$
.404	1.918	$.051 \pm .014$	$.011 \pm .014$	$.015 \pm .003$	$-.022 \pm .004$
.467	1.931	$.057 \pm .009$	$.016 \pm .011$	$-.003 \pm .002$	$-.028 \pm .004$
.497	1.937	$.055 \pm .011$	$.017 \pm .009$	$-.002 \pm .002$	$-.027 \pm .003$
.523	1.943	$.070 \pm .009$	$.023 \pm .010$	$.001 \pm .002$	$-.026 \pm .002$
.585	1.958	$.094 \pm .011$	$.040 \pm .008$	$.002 \pm .002$	$-.024 \pm .002$
.679	1.983	$.076 \pm .012$	$.048 \pm .012$	$-.005 \pm .004$	$-.018 \pm .002$
.783	2.013	$.088 \pm .009$	$.103 \pm .010$	$-.007 \pm .003$	$-.016 \pm .003$
.886	2.045	$.038 \pm .014$	$.142 \pm .014$	$-.006 \pm .006$	$-.021 \pm .007$
.988	2.078	$-.029 \pm .009$	$.122 \pm .008$	$.039 \pm .003$	$-.014 \pm .002$
1.089	2.111	$-.056 \pm .013$	$.082 \pm .012$	$.044 \pm .002$	$.027 \pm .004$
1.190	2.146	$-.036 \pm .018$	$.051 \pm .016$	$.028 \pm .006$	$.057 \pm .006$
1.291	2.181	$-.085 \pm .008$	$.022 \pm .012$	$-.001 \pm .003$	$.049 \pm .005$
1.351	2.202	$-.081 \pm .008$	$.017 \pm .011$	$-.009 \pm .002$	$.042 \pm .005$
1.400	2.219	$-.089 \pm .015$	$.009 \pm .022$	$-.011 \pm .004$	$.034 \pm .008$
1.416	2.224	$-.079 \pm .014$	$.026 \pm .019$	$-.011 \pm .004$	$.029 \pm .007$
1.449	2.236	$-.083 \pm .030$	$.003 \pm .008$	$-.010 \pm .011$	$.024 \pm .007$
1.467	2.242	$-.093 \pm .017$	$.017 \pm .028$	$-.011 \pm .008$	$.023 \pm .006$
1.500	2.254	$-.086 \pm .019$	$-.026 \pm .027$	$-.010 \pm .005$	$.019 \pm .006$
1.550	2.272	$-.069 \pm .013$	$.023 \pm .023$	$-.014 \pm .004$	$.024 \pm .006$

Table B.2: The real and imaginary parts of the $L = 1$ amplitudes for solution $\mathcal{A}$ at the twenty PS172 momenta.

P_{lab} GeV/c	$\sqrt{s}$ GeV	$\Re\{1_2\}$	$\Im\{1_2\}$	$\Re\{3_2\}$	$\Im\{3_2\}$
.360	1.910	$.004 \pm .003$	$-.011 \pm .003$	$.025 \pm .002$	$-.005 \pm .002$
.404	1.918	$.002 \pm .004$	$-.029 \pm .003$	$.017 \pm .005$	$-.017 \pm .004$
.467	1.931	$-.001 \pm .004$	$-.039 \pm .005$	$.009 \pm .002$	$-.019 \pm .002$
.497	1.937	$-.001 \pm .003$	$-.040 \pm .005$	$.011 \pm .003$	$-.016 \pm .004$
.523	1.943	$-.008 \pm .005$	$-.037 \pm .005$	$.017 \pm .002$	$-.016 \pm .003$
.585	1.958	$-.019 \pm .005$	$-.033 \pm .006$	$.020 \pm .002$	$-.019 \pm .003$
.679	1.983	$-.027 \pm .007$	$-.048 \pm .007$	$.018 \pm .003$	$-.012 \pm .004$
.783	2.013	$-.025 \pm .006$	$-.046 \pm .004$	$.029 \pm .002$	$-.007 \pm .002$
.886	2.045	$-.005 \pm .005$	$-.052 \pm .005$	$.024 \pm .003$	$-.001 \pm .002$
.988	2.078	$-.019 \pm .004$	$.002 \pm .004$	$.016 \pm .002$	$.037 \pm .002$
1.089	2.111	$-.028 \pm .003$	$.008 \pm .005$	$-.014 \pm .002$	$.023 \pm .002$
1.190	2.146	$-.030 \pm .002$	$-.006 \pm .006$	$-.006 \pm .003$	$.001 \pm .003$
1.291	2.181	$-.023 \pm .005$	$-.017 \pm .005$	$-.002 \pm .005$	$-.008 \pm .002$
1.351	2.202	$-.015 \pm .004$	$-.008 \pm .004$	$.018 \pm .002$	$-.007 \pm .003$
1.400	2.219	$-.005 \pm .007$	$.001 \pm .011$	$.019 \pm .006$	$-.004 \pm .004$
1.416	2.224	$-.017 \pm .006$	$-.024 \pm .008$	$.013 \pm .004$	$-.001 \pm .004$
1.449	2.236	$-.010 \pm .007$	$-.001 \pm .014$	$.016 \pm .008$	$-.004 \pm .005$
1.467	2.242	$.001 \pm .007$	$-.010 \pm .010$	$.020 \pm .003$	$-.006 \pm .004$
1.500	2.254	$-.004 \pm .006$	$.001 \pm .008$	$.011 \pm .004$	$-.007 \pm .003$
1.550	2.272	$.000 \pm .007$	$-.026 \pm .011$	$.007 \pm .006$	$-.003 \pm .005$

Table B.3: The real and imaginary parts of the $L = 2$ amplitudes for solution $\mathcal{A}$ at the twenty PS172 momenta.

P_{lab} GeV/c	$\sqrt{s}$ GeV	$\Re\{2_3\}$	$\Im\{2_3\}$	$\Re\{4_3\}$	$\Im\{4_3\}$
.360	1.910	$.003 \pm .002$	$-.001 \pm .002$	$.015 \pm .002$	$-.008 \pm .002$
.404	1.918	$.000 \pm .003$	$-.001 \pm .004$	$.010 \pm .002$	$-.013 \pm .002$
.467	1.931	$-.004 \pm .002$	$.002 \pm .004$	$.006 \pm .002$	$-.021 \pm .003$
.497	1.937	$.001 \pm .002$	$.007 \pm .004$	$.012 \pm .003$	$-.021 \pm .003$
.523	1.943	$.007 \pm .003$	$.008 \pm .002$	$.012 \pm .002$	$-.019 \pm .002$
.585	1.958	$.008 \pm .003$	$.006 \pm .003$	$.011 \pm .002$	$-.022 \pm .003$
.679	1.983	$.017 \pm .004$	$.016 \pm .003$	$.023 \pm .002$	$-.023 \pm .003$
.783	2.013	$.019 \pm .003$	$.011 \pm .003$	$.025 \pm .003$	$-.023 \pm .003$
.886	2.045	$.015 \pm .008$	$.020 \pm .006$	$.031 \pm .003$	$-.017 \pm .003$
.988	2.078	$.004 \pm .003$	$.006 \pm .003$	$.019 \pm .002$	$-.014 \pm .002$
1.089	2.111	$.002 \pm .003$	$-.005 \pm .005$	$.037 \pm .001$	$-.001 \pm .003$
1.190	2.146	$.016 \pm .006$	$-.012 \pm .007$	$.024 \pm .003$	$.014 \pm .002$
1.291	2.181	$.019 \pm .004$	$.006 \pm .006$	$.019 \pm .002$	$.026 \pm .004$
1.351	2.202	$.015 \pm .003$	$.002 \pm .006$	$.013 \pm .002$	$.019 \pm .002$
1.400	2.219	$.016 \pm .005$	$.015 \pm .009$	$.014 \pm .003$	$.020 \pm .007$
1.416	2.224	$.023 \pm .005$	$.018 \pm .008$	$.014 \pm .003$	$.023 \pm .005$
1.449	2.236	$.019 \pm .012$	$.018 \pm .006$	$.013 \pm .008$	$.020 \pm .007$
1.467	2.242	$.019 \pm .008$	$.017 \pm .005$	$.012 \pm .004$	$.016 \pm .006$
1.500	2.254	$.014 \pm .006$	$.021 \pm .008$	$.008 \pm .004$	$.017 \pm .005$
1.550	2.272	$.018 \pm .005$	$.016 \pm .007$	$.013 \pm .003$	$.015 \pm .006$

Table B.4: The real and imaginary parts of the $L = 3$ amplitudes for solution $\mathcal{A}$ at the twenty PS172 momenta.

P_{lab} GeV/c	$\sqrt{s}$ GeV	$\Re\{3_4\}$	$\Im\{3_4\}$	$\Re\{5_4\}$	$\Im\{5_4\}$
.679	1.983	$.001 \pm .003$	$-.004 \pm .004$	$.004 \pm .002$	$-.005 \pm .002$
.783	2.013	$.003 \pm .002$	$.000 \pm .003$	$.000 \pm .001$	$-.006 \pm .002$
.886	2.045	$.008 \pm .004$	$-.002 \pm .002$	$.000 \pm .000$	$-.012 \pm .003$
.988	2.078	$-.003 \pm .002$	$.012 \pm .002$	$-.001 \pm .001$	$-.002 \pm .002$
1.089	2.111	$-.009 \pm .002$	$.013 \pm .003$	$-.005 \pm .002$	$-.011 \pm .002$
1.190	2.146	$-.030 \pm .004$	$.005 \pm .004$	$.000 \pm .001$	$-.019 \pm .002$
1.291	2.181	$-.025 \pm .004$	$-.007 \pm .002$	$.016 \pm .002$	$-.021 \pm .004$
1.351	2.202	$-.017 \pm .003$	$.003 \pm .003$	$.024 \pm .002$	$-.018 \pm .003$
1.400	2.219	$-.019 \pm .006$	$-.005 \pm .004$	$.022 \pm .010$	$-.012 \pm .006$
1.416	2.224	$-.025 \pm .004$	$-.006 \pm .005$	$.027 \pm .003$	$-.015 \pm .004$
1.449	2.236	$-.023 \pm .008$	$-.001 \pm .005$	$.025 \pm .003$	$-.014 \pm .008$
1.467	2.242	$-.024 \pm .004$	$-.002 \pm .004$	$.023 \pm .004$	$-.017 \pm .006$
1.500	2.254	$-.019 \pm .005$	$-.004 \pm .003$	$.022 \pm .002$	$-.008 \pm .003$
1.550	2.272	$-.021 \pm .006$	$-.006 \pm .005$	$.022 \pm .007$	$-.013 \pm .006$

Table B.5: The real and imaginary parts of the $L = 4$ amplitudes for solution $\mathcal{A}$ at fourteen of the twenty PS172 momenta. Note that the $L = 4$ amplitudes are zero below 0.679 GeV/c , since only 6 zeros are used there.

P_{lab} GeV/c	$\sqrt{s}$ GeV	$\Re\{4_5\}$	$\Im\{4_5\}$	$\Re\{6_5\}$	$\Im\{6_5\}$
.988	2.078	$.009 \pm .002$	$.009 \pm .002$	$-.005 \pm .003$	$.000 \pm .000$
1.089	2.111	$.001 \pm .002$	$.017 \pm .004$	$-.003 \pm .002$	$.005 \pm .003$
1.190	2.146	$.002 \pm .004$	$.014 \pm .002$	$-.008 \pm .003$	$.006 \pm .006$
1.291	2.181	$-.014 \pm .002$	$.014 \pm .004$	$-.007 \pm .003$	$-.003 \pm .003$
1.351	2.202	$-.014 \pm .002$	$.017 \pm .002$	$-.014 \pm .003$	$-.007 \pm .003$
1.400	2.219	$-.003 \pm .003$	$.010 \pm .007$	$-.018 \pm .003$	$-.010 \pm .006$
1.416	2.224	$-.014 \pm .004$	$.011 \pm .006$	$-.009 \pm .003$	$-.009 \pm .004$
1.449	2.236	$-.005 \pm .009$	$.008 \pm .008$	$-.018 \pm .005$	$-.013 \pm .006$
1.467	2.242	$-.007 \pm .004$	$.008 \pm .007$	$-.012 \pm .005$	$-.012 \pm .004$
1.500	2.254	$.000 \pm .005$	$.003 \pm .006$	$-.004 \pm .004$	$-.013 \pm .003$
1.550	2.272	$-.013 \pm .004$	$.004 \pm .007$	$-.012 \pm .003$	$-.009 \pm .006$

Table B.6: The real and imaginary parts of the $L = 5$ amplitudes for solution $\mathcal{A}$ at eleven of the twenty PS172 momenta. Note that the $L = 5$ amplitudes are zero below 0.988 GeV/c , since only 8 zeros are used there.

P_{lab} GeV/c	$\sqrt{s}$ GeV	$\Re\{1_0\}$	$\Im\{1_0\}$
.360	1.382	$-.036 \pm .002$	$-.026 \pm .003$
.404	1.385	$-.029 \pm .006$	$-.019 \pm .006$
.467	1.389	$-.020 \pm .003$	$-.018 \pm .004$
.497	1.392	$-.015 \pm .005$	$-.017 \pm .005$
.523	1.394	$-.014 \pm .002$	$-.016 \pm .003$
.585	1.399	$-.007 \pm .004$	$-.021 \pm .005$
.679	1.408	$-.006 \pm .005$	$-.009 \pm .004$
.783	1.419	$.012 \pm .002$	$-.010 \pm .003$
.886	1.430	$.008 \pm .007$	$.003 \pm .003$
.988	1.441	$-.044 \pm .002$	$.040 \pm .003$
1.089	1.453	$-.049 \pm .002$	$.014 \pm .003$
1.190	1.465	$-.045 \pm .004$	$.005 \pm .004$
1.291	1.477	$-.039 \pm .003$	$-.022 \pm .004$
1.351	1.484	$-.023 \pm .005$	$-.016 \pm .004$
1.400	1.490	$-.029 \pm .005$	$-.025 \pm .008$
1.416	1.491	$-.035 \pm .005$	$-.013 \pm .006$
1.449	1.495	$-.018 \pm .004$	$-.026 \pm .010$
1.467	1.497	$-.029 \pm .008$	$-.026 \pm .007$
1.500	1.501	$-.020 \pm .004$	$-.030 \pm .005$
1.550	1.507	$-.020 \pm .005$	$-.011 \pm .008$

Table B.7: The real and imaginary parts of the $L = 0$ amplitudes for solution $\mathcal{B}$ at the twenty PS172 momenta.

P_{lab} GeV/c	$\sqrt{s}$ GeV	$\Re\{0_1\}$	$\Im\{0_1\}$	$\Re\{2_1\}$	$\Im\{2_1\}$
.360	1.382	$.065 \pm .005$	$.002 \pm .004$	$-.022 \pm .001$	$-.007 \pm .003$
.404	1.385	$.065 \pm .007$	$.003 \pm .006$	$-.020 \pm .006$	$-.003 \pm .003$
.467	1.389	$.061 \pm .011$	$.004 \pm .008$	$-.018 \pm .002$	$-.013 \pm .003$
.497	1.392	$.064 \pm .007$	$.005 \pm .009$	$-.017 \pm .003$	$-.016 \pm .004$
.523	1.394	$.062 \pm .010$	$.006 \pm .009$	$-.016 \pm .002$	$-.020 \pm .003$
.585	1.399	$.032 \pm .011$	$.005 \pm .007$	$-.013 \pm .002$	$-.026 \pm .004$
.679	1.408	$.051 \pm .008$	$.017 \pm .017$	$.009 \pm .004$	$-.026 \pm .002$
.783	1.419	$.051 \pm .008$	$.044 \pm .011$	$.023 \pm .003$	$.009 \pm .002$
.886	1.430	$.016 \pm .009$	$.142 \pm .013$	$.008 \pm .005$	$.005 \pm .003$
.988	1.441	$-.052 \pm .008$	$.104 \pm .009$	$.032 \pm .003$	$-.007 \pm .003$
1.089	1.453	$-.065 \pm .013$	$.076 \pm .011$	$.041 \pm .002$	$.032 \pm .005$
1.190	1.465	$-.043 \pm .019$	$.045 \pm .016$	$.018 \pm .004$	$.061 \pm .006$
1.291	1.477	$-.087 \pm .008$	$.012 \pm .013$	$-.007 \pm .003$	$.049 \pm .006$
1.351	1.484	$-.082 \pm .008$	$.010 \pm .011$	$-.013 \pm .002$	$.041 \pm .005$
1.400	1.490	$-.090 \pm .015$	$.003 \pm .008$	$-.014 \pm .004$	$.033 \pm .008$
1.416	1.491	$-.081 \pm .014$	$.022 \pm .019$	$-.013 \pm .005$	$.029 \pm .005$
1.449	1.495	$-.083 \pm .029$	$-.001 \pm .001$	$-.011 \pm .009$	$.023 \pm .007$
1.467	1.497	$-.093 \pm .016$	$.013 \pm .029$	$-.012 \pm .006$	$.022 \pm .006$
1.500	1.501	$-.085 \pm .019$	$-.028 \pm .026$	$-.011 \pm .005$	$.019 \pm .007$
1.550	1.507	$-.069 \pm .013$	$.022 \pm .023$	$-.015 \pm .004$	$.024 \pm .006$

Table B.8: The real and imaginary parts of the $L = 1$ amplitudes for solution $\mathcal{B}$ at the twenty PS172 momenta.

P_{lab} GeV/c	$\sqrt{s}$ GeV	$\Re\{1_2\}$	$\Im\{1_2\}$	$\Re\{3_2\}$	$\Im\{3_2\}$
.360	1.382	$.011 \pm .002$	$-.023 \pm .004$	$-.009 \pm .003$	$.003 \pm .003$
.404	1.385	$.036 \pm .006$	$-.031 \pm .009$	$-.006 \pm .004$	$.003 \pm .004$
.467	1.389	$.057 \pm .004$	$-.027 \pm .006$	$-.012 \pm .004$	$-.001 \pm .002$
.497	1.392	$.058 \pm .006$	$-.014 \pm .005$	$-.014 \pm .002$	$-.010 \pm .002$
.523	1.394	$.061 \pm .003$	$-.014 \pm .004$	$-.014 \pm .002$	$-.012 \pm .003$
.585	1.399	$.076 \pm .004$	$.001 \pm .006$	$-.016 \pm .003$	$-.015 \pm .003$
.679	1.408	$.038 \pm .007$	$.059 \pm .005$	$.011 \pm .002$	$-.025 \pm .004$
.783	1.419	$-.065 \pm .003$	$.048 \pm .004$	$.032 \pm .003$	$-.001 \pm .005$
.886	1.430	$-.045 \pm .007$	$-.026 \pm .004$	$.025 \pm .004$	$.014 \pm .004$
.988	1.441	$-.028 \pm .003$	$-.009 \pm .004$	$.010 \pm .002$	$.040 \pm .002$
1.089	1.453	$-.028 \pm .003$	$.005 \pm .005$	$-.017 \pm .002$	$.022 \pm .002$
1.190	1.465	$-.028 \pm .006$	$-.011 \pm .006$	$-.006 \pm .005$	$.000 \pm .001$
1.291	1.477	$-.021 \pm .005$	$-.019 \pm .005$	$-.001 \pm .003$	$-.008 \pm .003$
1.351	1.484	$-.015 \pm .004$	$-.009 \pm .004$	$.019 \pm .002$	$-.006 \pm .003$
1.400	1.490	$-.005 \pm .007$	$.000 \pm .011$	$.020 \pm .006$	$-.002 \pm .005$
1.416	1.491	$-.016 \pm .006$	$-.025 \pm .008$	$.013 \pm .004$	$.000 \pm .004$
1.449	1.495	$-.010 \pm .006$	$-.001 \pm .014$	$.016 \pm .008$	$-.003 \pm .004$
1.467	1.497	$.001 \pm .008$	$-.010 \pm .010$	$.020 \pm .003$	$-.005 \pm .003$
1.500	1.501	$-.004 \pm .006$	$.001 \pm .008$	$.011 \pm .005$	$-.006 \pm .003$
1.550	1.507	$.001 \pm .007$	$-.026 \pm .011$	$.007 \pm .005$	$-.003 \pm .005$

Table B.9: The real and imaginary parts of the $L = 2$ amplitudes for solution $\mathcal{B}$ at the twenty PS172 momenta.

P_{lab} GeV/c	$\sqrt{s}$ GeV	$\Re\{2_3\}$	$\Im\{2_3\}$	$\Re\{4_3\}$	$\Im\{4_3\}$
.360	1.382	$.001 \pm .002$	$.000 \pm .004$	$.006 \pm .003$	$.002 \pm .002$
.404	1.385	$-.004 \pm .005$	$-.003 \pm .002$	$.007 \pm .002$	$.003 \pm .003$
.467	1.389	$-.008 \pm .003$	$-.014 \pm .004$	$.008 \pm .002$	$.005 \pm .002$
.497	1.392	$-.013 \pm .003$	$-.021 \pm .004$	$.001 \pm .002$	$.010 \pm .002$
.523	1.394	$-.018 \pm .002$	$-.023 \pm .004$	$-.003 \pm .002$	$.008 \pm .003$
.585	1.399	$-.012 \pm .003$	$-.025 \pm .004$	$-.006 \pm .002$	$.009 \pm .002$
.679	1.408	$.013 \pm .005$	$-.045 \pm .003$	$-.012 \pm .004$	$-.009 \pm .003$
.783	1.419	$.042 \pm .003$	$.005 \pm .003$	$.007 \pm .002$	$-.020 \pm .002$
.886	1.430	$.025 \pm .005$	$.037 \pm .004$	$.027 \pm .004$	$-.011 \pm .003$
.988	1.441	$-.004 \pm .003$	$.008 \pm .003$	$.019 \pm .002$	$-.011 \pm .002$
1.089	1.453	$.003 \pm .003$	$-.005 \pm .006$	$.036 \pm .002$	$.003 \pm .003$
1.190	1.465	$.018 \pm .004$	$-.009 \pm .007$	$.022 \pm .004$	$.018 \pm .002$
1.291	1.477	$.018 \pm .003$	$.009 \pm .007$	$.016 \pm .002$	$.028 \pm .004$
1.351	1.484	$.015 \pm .003$	$.004 \pm .006$	$.011 \pm .002$	$.020 \pm .003$
1.400	1.490	$.015 \pm .005$	$.016 \pm .009$	$.013 \pm .003$	$.021 \pm .007$
1.416	1.491	$.022 \pm .006$	$.020 \pm .006$	$.013 \pm .003$	$.024 \pm .005$
1.449	1.495	$.018 \pm .010$	$.019 \pm .005$	$.012 \pm .008$	$.020 \pm .007$
1.467	1.497	$.018 \pm .007$	$.018 \pm .005$	$.011 \pm .004$	$.017 \pm .006$
1.500	1.501	$.013 \pm .006$	$.021 \pm .009$	$.007 \pm .004$	$.017 \pm .005$
1.550	1.507	$.018 \pm .005$	$.016 \pm .006$	$.013 \pm .003$	$.015 \pm .006$

Table B.10: The real and imaginary parts of the $L = 3$ amplitudes for solution $\mathcal{B}$ at the twenty PS172 momenta.

P_{lab} GeV/c	$\sqrt{s}$ GeV	$\Re\{3_4\}$	$\Im\{3_4\}$	$\Re\{5_4\}$	$\Im\{5_4\}$
.679	1.408	$-.006 \pm .002$	$.002 \pm .005$	$-.004 \pm .004$	$-.001 \pm .001$
.783	1.419	$.004 \pm .004$	$-.002 \pm .004$	$-.002 \pm .003$	$-.003 \pm .002$
.886	1.430	$.011 \pm .005$	$-.003 \pm .004$	$.000 \pm .001$	$-.008 \pm .002$
.988	1.441	$-.006 \pm .002$	$.016 \pm .003$	$.000 \pm .000$	$-.002 \pm .002$
1.089	1.453	$-.010 \pm .002$	$.012 \pm .003$	$-.004 \pm .002$	$-.011 \pm .002$
1.190	1.465	$-.030 \pm .005$	$.000 \pm .001$	$.003 \pm .003$	$-.018 \pm .003$
1.291	1.477	$-.024 \pm .003$	$-.010 \pm .003$	$.019 \pm .002$	$-.018 \pm .004$
1.351	1.484	$-.017 \pm .003$	$.002 \pm .003$	$.025 \pm .002$	$-.016 \pm .003$
1.400	1.490	$-.019 \pm .006$	$-.006 \pm .006$	$.023 \pm .010$	$-.010 \pm .006$
1.416	1.491	$-.025 \pm .004$	$-.008 \pm .005$	$.027 \pm .003$	$-.013 \pm .004$
1.449	1.495	$-.023 \pm .008$	$-.002 \pm .004$	$.025 \pm .004$	$-.013 \pm .008$
1.467	1.497	$-.024 \pm .004$	$-.003 \pm .003$	$.024 \pm .004$	$-.016 \pm .006$
1.500	1.501	$-.019 \pm .005$	$-.004 \pm .003$	$.022 \pm .002$	$-.007 \pm .003$
1.550	1.507	$-.021 \pm .005$	$-.006 \pm .006$	$.022 \pm .007$	$-.012 \pm .006$

Table B.11: The real and imaginary parts of the $L = 4$ amplitudes for solution $\mathcal{B}$ at fourteen of the twenty PS172 momenta. Note that the $L = 4$ amplitudes are zero below 0.679 GeV/c , since only 6 zeros are used there.

P_{lab} GeV/c	$\sqrt{s}$ GeV	$\Re\{4_5\}$	$\Im\{4_5\}$	$\Re\{6_5\}$	$\Im\{6_5\}$
.988	1.441	$.008 \pm .002$	$.011 \pm .003$	$-.004 \pm .003$	$-.001 \pm .001$
1.089	1.453	$-.001 \pm .002$	$.017 \pm .004$	$-.004 \pm .002$	$.005 \pm .003$
1.190	1.465	$-.001 \pm .004$	$.014 \pm .002$	$-.009 \pm .003$	$.005 \pm .006$
1.291	1.477	$-.016 \pm .002$	$.012 \pm .004$	$-.007 \pm .003$	$-.004 \pm .003$
1.351	1.484	$-.016 \pm .002$	$.016 \pm .003$	$-.013 \pm .002$	$-.008 \pm .003$
1.400	1.490	$-.003 \pm .003$	$.009 \pm .007$	$-.017 \pm .003$	$-.011 \pm .006$
1.416	1.491	$-.015 \pm .004$	$.010 \pm .005$	$-.009 \pm .003$	$-.009 \pm .004$
1.449	1.495	$-.006 \pm .008$	$.008 \pm .008$	$-.017 \pm .005$	$-.014 \pm .005$
1.467	1.497	$-.007 \pm .004$	$.008 \pm .007$	$-.012 \pm .005$	$-.013 \pm .004$
1.500	1.501	$.000 \pm .005$	$.003 \pm .006$	$-.004 \pm .004$	$-.013 \pm .003$
1.550	1.507	$-.013 \pm .004$	$.004 \pm .007$	$-.012 \pm .003$	$-.009 \pm .006$

Table B.12: The real and imaginary parts of the $L = 5$ amplitudes for solution $\mathcal{B}$ at eleven of the the twenty PS172 momenta. Note that the $L = 5$ amplitudes are zero below 0.988 GeV/c , since only 8 zeros are used there.

Appendix C

Resonance Parameters

In solution $\mathcal{A}$, eight runs were performed for each of the two fitting methods described in Chapter 5. In each of these runs, fitting was performed to (subsets of) assumed structures in the 0_1, 1_0, 2_1, 3_2, and 4_3 waves. The particular states included in each run are summarised in Tables 5.1 in Chapter 5. The details of the iterative and penalty function fitting schemes are also presented in Chapter 5. The scheme **I** results are given in Tables C.1–C.5 and the scheme **P** results are shown in Tables C.6–C.10.

In solution $\mathcal{B}$, twenty runs were performed for each of the fitting schemes, fitting to subsets of assumed structures in the 0_1, 1_0, 1_2, $2_1(\times 2)$, 2_3, 3_2, and 4_3 waves. The particular states included in each run are summarised in Tables 5.2 in Chapter 5. The scheme **I** results are given in Tables C.11–C.18 and the scheme **P** results are shown in Tables C.19–C.26.

Run	m	δm	Γ	$\delta\Gamma$	N	δN
1	2.0364	.0179	.1298	.0356	.1079	.0162
2	2.0547	.0064	.1215	.0316	.1100	.0129
3	2.0564	.0065	.1214	.0267	.1101	.0128
4	2.0529	.0090	.1286	.0280	.0912	.0122
5	2.0543	.0139	.1314	.0231	.0937	.0106
6	2.0350	.0202	.1300	.0395	.1069	.0167
7	2.0529	.0061	.1214	.0285	.1086	.0130
8	2.0497	.0072	.1265	.0260	.0885	.0109

Table C.1: Fit parameters for the 0_1 wave in solution $\mathcal{A}$ using the iterative fitting procedure described in Chapter 5.

Run	m	δm	Γ	$\delta\Gamma$	N	δN
1	2.0887	.0039	.0618	.0158	.0435	.0032
2	2.0878	.0049	.0609	.0135	.0428	.0034
3	2.0877	.0058	.0611	.0156	.0425	.0035
4	2.0971	.0050	.0788	.0121	.0452	.0031
5	2.0960	.0083	.0779	.0206	.0446	.0041
6	2.0893	.0074	.0651	.0191	.0446	.0047
7	2.0885	.0071	.0643	.0146	.0436	.0037
8	2.1037	.0039	.0871	.0089	.0466	.0029

Table C.2: Fit parameters for the 2_1 wave in solution $\mathcal{A}$ using the iterative fitting procedure described in Chapter 5.

Run	m	δm	Γ	$\delta\Gamma$	N	δN
1	2.0712	.0038	.0357	.0128	.0349	.0062
2	2.0690	.0065	.0461	.0132	.0335	.0044
3	2.0679	.0071	.0485	.0138	.0332	.0042
6	2.0709	.0053	.0361	.0130	.0349	.0065
7	2.0682	.0060	.0476	.0131	.0332	.0045

Table C.3: Fit parameters for the 1_0 wave in solution $\mathcal{A}$ using the iterative fitting procedure described in Chapter 5.

Run	m	δm	Γ	$\delta\Gamma$	N	δN
1	2.0868	.0044	.0499	.0083	.0323	.0027
4	2.0856	.0065	.0561	.0082	.0318	.0026
5	2.0818	.0028	.0530	.0071	.0320	.0026
6	2.0868	.0070	.0510	.0124	.0322	.0038
8	2.0855	.0076	.0594	.0104	.0315	.0028

Table C.4: Fit parameters for the 3_2 wave in solution $\mathcal{A}$ using the iterative fitting procedure described in Chapter 5.

Run	m	δm	Γ	$\delta\Gamma$	N	δN
2	2.0313	.0380	.0844	.0530	.0108	.0045
3	2.0500	(fixed)	.2000	(fixed)	.0137	.0041
4	2.0441	.0099	.0336	.0267	.0112	.0039
5	2.0500	(fixed)	.2000	(fixed)	.0122	.0028
7	2.0303	.0399	.0853	.0559	.0108	.0045
8	2.0439	.0090	.0327	.0254	.0114	.0038

Table C.5: Fit parameters for the 4_3 wave in solution $\mathcal{A}$ using the iterative fitting procedure described in Chapter 5.

Run	m	δm	Γ	$\delta\Gamma$	N	δN
1	2.0366	.0213	.1133	.0354	.1171	.0178
2	2.0464	.0194	.1056	.0343	.1218	.0176
3	2.0495	.0179	.1052	.0338	.1218	.0181
4	2.0499	.0201	.1347	.0627	.0743	.0287
5	2.0562	.0172	.1340	.0308	.0868	.0180
6	2.0361	.0164	.1132	.0354	.1167	.0167
7	2.0457	.0182	.1057	.0342	.1213	.0180
8	2.0398	.0238	.1244	.0684	.0635	.0272

Table C.6: Fit parameters for the 0_1 wave in solution $\mathcal{A}$ using the penalty function fitting procedure described in Chapter 5.

Run	m	δm	Γ	$\delta\Gamma$	N	δN
1	2.0867	.0078	.0609	.0246	.0413	.0060
2	2.0857	.0096	.0588	.0217	.0409	.0065
3	2.0857	.0096	.0578	.0246	.0411	.0067
4	2.1080	.0246	.0915	.0305	.0464	.0068
5	2.0968	.0138	.0807	.0281	.0440	.0065
6	2.0867	.0088	.0632	.0233	.0422	.0051
7	2.0860	.0087	.0610	.0203	.0416	.0064
8	2.1297	.0274	.0965	.0239	.0505	.0074

Table C.7: Fit parameters for the 2_1 wave in solution $\mathcal{A}$ using the penalty function fitting procedure described in Chapter 5.

Run	m	δm	Γ	$\delta\Gamma$	N	δN
1	2.0711	.0066	.0319	.0139	.0307	.0083
2	2.0709	.0108	.0352	.0169	.0288	.0079
3	2.0708	.0113	.0362	.0179	.0290	.0081
6	2.0707	.0074	.0322	.0138	.0307	.0077
7	2.0703	.0105	.0357	.0171	.0286	.0083

Table C.8: Fit parameters for the 1_0 wave in solution $\mathcal{A}$ using the penalty function fitting procedure described in Chapter 5.

Run	m	δm	Γ	$\delta\Gamma$	N	δN
1	2.0819	.0095	.0478	.0142	.0321	.0039
4	2.0888	.0116	.0648	.0194	.0311	.0032
5	2.0825	.0089	.0550	.0149	.0317	.0038
6	2.0816	.0068	.0484	.0123	.0321	.0039
8	2.0914	.0135	.0752	.0235	.0305	.0036

Table C.9: Fit parameters for the 3_2 wave in solution $\mathcal{A}$ using the penalty function fitting procedure described in Chapter 5.

Run	m	δm	Γ	$\delta\Gamma$	N	δN
2	2.0253	.0383	.0968	.0530	.0152	.0056
3	2.0500	(fixed)	.2000	(fixed)	.0192	.0048
4	2.0527	.0174	.0271	.0291	.0117	.0063
5	2.0500	(fixed)	.2000	(fixed)	.0124	.0088
7	2.0248	.0325	.0970	.0521	.0152	.0058
8	2.0544	.0183	.0245	.0237	.0130	.0079

Table C.10: Fit parameters for the 4_3 wave in solution $\mathcal{A}$ using the penalty function fitting procedure described in Chapter 5.

Run	m	δm	Γ	$\delta\Gamma$	N	δN
1	2.0625	.0060	.0465	.0132	.0987	.0170
2	2.0535	.0128	.0832	.0282	.0883	.0140
3	2.0662	.0195	.0792	.0312	.0862	.0169
4	2.0546	.0049	.0552	.0151	.0844	.0164
5	2.0592	.0100	.0853	.0240	.0902	.0135
6	2.0593	.0146	.0741	.0292	.0917	.0154
7	2.0598	.0065	.0377	.0149	.1081	.0232
8	2.0599	.0060	.0342	.0118	.1071	.0215
9	2.0584	.0049	.0288	.0092	.1160	.0263
10	2.0611	.0074	.0446	.0143	.0945	.0164
11	2.0598	.0067	.0358	.0116	.1041	.0193
12	2.0564	.0105	.0599	.0251	.0884	.0162
13	2.0530	.0046	.0452	.0147	.0978	.0169
14	2.0536	.0061	.0814	.0313	.0848	.0100
15	2.0544	.0048	.0666	.0252	.0881	.0109
16	2.0549	.0066	.0401	.0165	.0858	.0204
17	2.0579	.0059	.0570	.0198	.0827	.0130
18	2.0571	.0053	.0453	.0180	.0889	.0164
19	2.0540	.0058	.0429	.0114	.0879	.0169
20	2.0535	.0074	.0399	.0150	.0880	.0195

Table C.11: Fit parameters for the 0_1 wave in solution $\mathcal{B}$ using the iterative fitting procedure described in Chapter 5.

Run	m	δm	Γ	$\delta\Gamma$	N	δN
1	2.0934	.0033	.0511	.0088	.0392	.0043
2	2.0952	.0069	.0542	.0153	.0374	.0051
3	2.0943	.0065	.0497	.0190	.0397	.0065
4	2.1017	.0138	.0757	.0292	.0368	.0035
5	2.0954	.0068	.0545	.0150	.0379	.0050
6	2.0955	.0076	.0552	.0212	.0380	.0058
7	2.1005	.0105	.0729	.0253	.0382	.0046
8	2.0986	.0046	.0688	.0118	.0386	.0041
9	2.1069	.0130	.0936	.0181	.0377	.0033
10	2.0997	.0060	.0678	.0131	.0391	.0041
11	2.1007	.0053	.0718	.0116	.0389	.0033
12	2.1145	.0138	.0800	.0204	.0401	.0044
13	2.1281	.0063	.0997	.0242	.0387	.0041
14	2.1187	.0070	.0792	.0185	.0404	.0038
15	2.1190	.0054	.0803	.0130	.0407	.0034
16	2.1249	.0059	.0916	.0139	.0402	.0036
17	2.1164	.0057	.0797	.0122	.0409	.0037
18	2.1188	.0071	.0812	.0122	.0411	.0041
19	2.1262	.0060	.0941	.0168	.0394	.0035
20	2.1242	.0061	.0916	.0157	.0400	.0037

Table C.12: Fit parameters for the 2_1 wave in solution $\mathcal{B}$ using the iterative fitting procedure described in Chapter 5.

Run	m	δm	Γ	$\delta\Gamma$	N	δN
1	2.0730	.0036	.0407	.0070	.0461	.0049
2	2.0682	.0030	.0411	.0078	.0471	.0056
3	2.0720	.0041	.0431	.0096	.0477	.0061
4	2.0703	.0028	.0446	.0094	.0472	.0052
5	2.0694	.0032	.0418	.0080	.0468	.0060
6	2.0700	.0041	.0413	.0097	.0468	.0066

Table C.13: Fit parameters for the 1_0 wave in solution $\mathcal{B}$ using the iterative fitting procedure described in Chapter 5.

Run	m	δm	Γ	$\delta\Gamma$	N	δN
1	1.9769	.0062	.0714	.0088	.0661	.0060
7	1.9758	.0066	.0675	.0085	.0660	.0065
8	1.9755	.0050	.0738	.0091	.0642	.0052
9	1.9791	.0071	.1019	.0122	.0618	.0056
10	1.9747	.0054	.0675	.0083	.0650	.0059
11	1.9760	.0068	.0751	.0095	.0642	.0063

Table C.14: Fit parameters for the 1_2 wave in solution $\mathcal{B}$ using the iterative fitting procedure described in Chapter 5.

Run	m	δm	Γ	$\delta\Gamma$	N	δN
2	1.9776	.0051	.1011	.0143	.0266	.0023
7	1.9732	.0173	.0992	.0342	.0242	.0041
12	1.9725	.0168	.1018	.0343	.0256	.0042
13	2.0120	.0211	.1051	.0506	.0250	.0060
14	1.9840	.0100	.0781	.0122	.0270	.0032
15	1.9879	.0137	.0855	.0259	.0265	.0039

Table C.15: Fit parameters for the $2_1'$ wave in solution $\mathcal{B}$ using the iterative fitting procedure described in Chapter 5.

Run	m	δm	Γ	$\delta\Gamma$	N	δN
3	1.9852	.0095	.0656	.0138	.0328	.0043
8	1.9856	.0091	.0756	.0096	.0305	.0035
12	1.9853	.0098	.0625	.0125	.0322	.0042
16	2.0036	.0099	.0837	.0137	.0350	.0049
17	1.9889	.0083	.0619	.0104	.0334	.0042
18	1.9931	.0088	.0662	.0133	.0333	.0041

Table C.16: Fit parameters for the 2_3 wave in solution $\mathcal{B}$ using the iterative fitting procedure described in Chapter 5.

Run	m	δm	Γ	$\delta\Gamma$	N	δN
4	2.0598	.0067	.0776	.0082	.0452	.0032
9	2.0602	.0059	.0704	.0078	.0439	.0032
13	2.0522	.0063	.0706	.0082	.0437	.0020
16	2.0587	.0071	.0869	.0113	.0431	.0027
19	2.0563	.0068	.0840	.0165	.0433	.0033
20	2.0602	.0067	.0866	.0179	.0432	.0024

Table C.17: Fit parameters for the 3_2 wave in solution $\mathcal{B}$ using the iterative fitting procedure described in Chapter 5.

Run	m	δm	Γ	$\delta\Gamma$	N	δN
5	1.9944	.0110	.0693	.0133	.0173	.0022
6	2.0500	(fixed)	.2000	(fixed)	.0201	.0040
10	1.9807	.0147	.0738	.0189	.0152	.0020
11	2.0500	(fixed)	.2000	(fixed)	.0197	.0026
14	1.9850	.0065	.0590	.0121	.0167	.0022
15	2.0500	(fixed)	.2000	(fixed)	.0187	.0029
17	1.9825	.0061	.0703	.0121	.0159	.0023
18	2.0500	(fixed)	.2000	(fixed)	.0201	.0021
19	2.0092	.0068	.0949	.0272	.0170	.0027
20	2.0500	(fixed)	.2000	(fixed)	.0209	.0025

Table C.18: Fit parameters for the 4_3 wave in solution $\mathcal{B}$ using the iterative fitting procedure described in Chapter 5.

Run	m	δm	Γ	$\delta\Gamma$	N	δN
1	2.0621	.0100	.0405	.0286	.1057	.0361
2	2.0562	.0087	.0785	.0356	.0921	.0193
3	2.0704	.0216	.0830	.0363	.0863	.0178
4	2.0590	.0165	.0580	.0324	.0834	.0245
5	2.0606	.0200	.0847	.0407	.0915	.0158
6	2.0627	.0078	.0736	.0311	.0936	.0162
7	2.0560	.0064	.0234	.0154	.1062	.0500
8	2.0548	.0075	.0266	.0150	.0900	.0337
9	2.0513	.0070	.0301	.0172	.0769	.0286
10	2.0553	.0069	.0266	.0153	.0924	.0325
11	2.0562	.0060	.0232	.0128	.1090	.0390
12	2.0521	.0131	.0437	.0264	.0681	.0270
13	2.0455	.0153	.0433	.0211	.0673	.0229
14	2.0544	.0090	.0554	.0273	.0765	.0195
15	2.0545	.0091	.0390	.0216	.0847	.0264
16	2.0453	.0145	.0411	.0226	.0609	.0226
17	2.0530	.0102	.0404	.0229	.0672	.0253
18	2.0546	.0092	.0366	.0188	.0788	.0159
19	2.0504	.0130	.0433	.0227	.0695	.0238
20	2.0506	.0099	.0417	.0187	.0749	.0226

Table C.19: Fit parameters for the 0_1 wave in solution $\mathcal{B}$ using the penalty function fitting procedure described in Chapter 5.

Run	m	δm	Γ	$\delta\Gamma$	N	δN
1	2.0956	.0099	.0565	.0314	.0409	.0066
2	2.0954	.0107	.0550	.0265	.0377	.0059
3	2.0952	.0092	.0501	.0230	.0408	.0062
4	2.1005	.0196	.0678	.0415	.0392	.0059
5	2.0959	.0111	.0552	.0290	.0385	.0068
6	2.0965	.0103	.0559	.0276	.0395	.0063
7	2.1286	.0142	.0816	.0240	.0474	.0072
8	2.1311	.0138	.0799	.0234	.0481	.0065
9	2.1361	.0184	.0784	.0213	.0498	.0076
10	2.1294	.0140	.0807	.0230	.0476	.0066
11	2.1278	.0145	.0816	.0235	.0473	.0070
12	2.1350	.0192	.0756	.0241	.0468	.0114
13	2.1427	.0196	.0801	.0251	.0469	.0084
14	2.1311	.0185	.0784	.0240	.0451	.0098
15	2.1343	.0168	.0780	.0239	.0474	.0090
16	2.1435	.0146	.0786	.0243	.0471	.0084
17	2.1351	.0175	.0760	.0234	.0468	.0111
18	2.1357	.0186	.0770	.0231	.0472	.0094
19	2.1435	.0225	.0821	.0276	.0466	.0120
20	2.1406	.0094	.0816	.0231	.0475	.0072

Table C.20: Fit parameters for the 2_1 wave in solution $\mathcal{B}$ using the penalty function fitting procedure described in Chapter 5.

Run	m	δm	Γ	$\delta\Gamma$	N	δN
1	2.0750	.0052	.0388	.0109	.0462	.0066
2	2.0693	.0065	.0402	.0091	.0464	.0063
3	2.0735	.0057	.0431	.0106	.0481	.0061
4	2.0732	.0053	.0452	.0124	.0474	.0063
5	2.0703	.0062	.0415	.0092	.0466	.0065
6	2.0722	.0050	.0408	.0092	.0467	.0060

Table C.21: Fit parameters for the 1_0 wave in solution $\mathcal{B}$ using the penalty function fitting procedure described in Chapter 5.

Run	m	δm	Γ	$\delta\Gamma$	N	δN
1	1.9799	.0096	.0804	.0178	.0662	.0076
7	1.9707	.0104	.0958	.0249	.0542	.0087
8	1.9691	.0095	.0874	.0202	.0534	.0078
9	1.9723	.0103	.1163	.0292	.0500	.0070
10	1.9697	.0077	.0882	.0222	.0540	.0071
11	1.9722	.0076	.1051	.0274	.0544	.0066

Table C.22: Fit parameters for the 1_2 wave in solution $\mathcal{B}$ using the penalty function fitting procedure described in Chapter 5.

Run	m	δm	Γ	$\delta\Gamma$	N	δN
2	1.9836	.0202	.0984	.0248	.0267	.0038
7	1.9859	.0368	.1208	.0558	.0216	.0063
12	1.9768	.0472	.1180	.0564	.0239	.0057
13	2.0166	.0260	.0992	.0619	.0228	.0067
14	1.9903	.0239	.0944	.0371	.0256	.0049
15	2.0093	.0207	.0960	.0498	.0235	.0057

Table C.23: Fit parameters for the $2_1'$ wave in solution $\mathcal{B}$ using the penalty function fitting procedure described in Chapter 5.

Run	m	δm	Γ	$\delta\Gamma$	N	δN
3	1.9875	.0097	.0638	.0154	.0334	.0047
8	1.9965	.0183	.1017	.0328	.0320	.0065
12	1.9942	.0153	.0807	.0265	.0330	.0056
16	2.0104	.0163	.0989	.0287	.0379	.0068
17	1.9923	.0131	.0794	.0256	.0327	.0051
18	1.9994	.0150	.0845	.0253	.0342	.0057

Table C.24: Fit parameters for the 2_3 wave in solution $\mathcal{B}$ using the penalty function fitting procedure described in Chapter 5.

Run	m	δm	Γ	$\delta\Gamma$	N	δN
4	2.0648	.0086	.0705	.0212	.0457	.0048
9	2.0767	.0145	.1132	.0299	.0431	.0045
13	2.0598	.0168	.1109	.0317	.0420	.0045
16	2.0616	.0114	.1191	.0311	.0411	.0046
19	2.0572	.0181	.1073	.0316	.0420	.0050
20	2.0618	.0097	.1011	.0258	.0426	.0043

Table C.25: Fit parameters for the 3_2 wave in solution $\mathcal{B}$ using the penalty function fitting procedure described in Chapter 5.

Run	m	δm	Γ	$\delta\Gamma$	N	δN
5	1.9921	.0185	.0670	.0238	.0172	.0037
6	2.0500	(fixed)	.2000	(fixed)	.0199	.0031
10	1.9684	.0191	.0893	.0327	.0125	.0031
11	2.0500	(fixed)	.2000	(fixed)	.0195	.0030
14	1.9869	.0184	.0733	.0253	.0154	.0031
15	2.0500	(fixed)	.2000	(fixed)	.0199	.0028
17	1.9681	.0158	.0742	.0247	.0131	.0032
18	2.0500	(fixed)	.2000	(fixed)	.0191	.0031
19	1.9892	.0263	.0981	.0432	.0140	.0041
20	2.0500	(fixed)	.2000	(fixed)	.0192	.0029

Table C.26: Fit parameters for the 4_3 wave in solution $\mathcal{B}$ using the penalty function fitting procedure described in Chapter 5.

References

[1] G. Goldhaber, "From the Neutron to Three Light Neutrino Species: Some Highlights from Sixty Years of Particle Physics", The Proceedings of the Dalitz Conference (1990), Ed. I.J.R. Aitchison, C.H. Llewellyn Smith and J.E. Paton, (World Scientific 1990).

[2] M.R. Pennington, "In Search of Hadrons Beyond the Quark Model", The Proceedings of the Dalitz Conference (1990), Ed. I.J.R. Aitchison, C.H. Llewellyn Smith and J.E. Paton, (World Scientific 1990).

[3] J. Chadwick, Nature, **129** (1932) 312.

[4] C.D. Anderson, Science, **76** (1932) 238.

[5] H. Yukawa, Proc. Phys. Math. Soc. Japan, **17** (1935) 48.

[6] S. Neddermeyer and C.D. Anderson, Phys. Rev. **51** (1937) 884.

[7] M. Conversi, E. Pancini, and O. Piccioni, Phys. Rev. **71** (1947) 3.

[8] D.H. Perkins, Nature, **159** (1947) 126.

[9] C.M.G. Lattes *et al.* , Nature **159** (1947) 694.

[10] G.D. Rochester and C.C. Butler, Nature, **160** (1947) 855.

[11] W. Heisenberg, Z. Phys. **77** (1932) 1.

[12] F. Halzen and A.D. Martin, Quarks and Leptons, Wiley, New York, (1984) Chap. 2.

[13] P. Carruthers, Introduction to Unitary Symmetry, Interscience, New York, (1966) Chap. 1.

[14] N. Kemmer, Proc. Cambridge Phil. Soc. **34** (1938) 354.

[15] A.G. Carlson *et al.* , Phil. Mag. **41** (1950); R. Bjorkland *et al.* , Phys. Rev.**77** (1950) 213.

[16] M. Gell-Mann, "The Eightfold Way: A Theory of Strong Interaction Symmetry", Caltech Synchrotron Lab. Report CTSL-70 (1961) unpublished; Y. Ne'eman, Nucl. Phys. **76** (1961) 222.

[17] V.E. Barnes *et al.* , Phys. Rev. Lett. **12** (1964) 204.

[18] M. Gell-Mann, Phys. Lett. **8** (1964) 214; G. Zweig, CERN Reports TH401 (1964) and TH412 (1964).

[19] *See for example* R.H. Dalitz, "Fundamentals of Quark Models", Proc. 17^{th} Scottish Universities Summer School in Physics, 1976, Eds. I.M. Barbour and A.T. Davies, (SUSSP, Edinburgh) p. 151.

[20] O.W. Greenberg, Phys. Rev. Lett. **13** (1964) 598.

[21] M. Gell-Mann, Acta Phys. Austriaca Suppl. **9** (1972) 733.

[22] H. Pilkuhn, The Interactions of Hadrons, North Holland, Amsterdam, (1967).

[23] D. Gross and F. Wilcek, Phys. Rev. Lett. **30** (1973) 1343; S. Weinberg, Phys. Rev. Lett. **31** (1973) 494; H. Fritzsch, M. Gell-Mann and H. Leutwyler, Phys. Lett. **47B** (1973) 365.

[24] *See for example* C. Michael, "Quarks, Gluons and Lattices", The Proceedings of the Dalitz Conference (1990), Ed. I.J.R. Aitchison, C.H. Llewellyn Smith and J.E. Paton, (World Scientific 1990).

[25] *See for example* N. Brown and M.R. Pennington, Phys. Rev. **D39** (1989) 2723.

[26] E. Barrelet, Nuovo Cimento **84** (1972) 331.

[27] A. Hasan *et al.* , Nucl. Phys. **B378** (1992) 3.

[28] M.R. Pennington, "Two Body Annihilation Processes in $\overline{N}N$ Interactions", Invited Talk at 5^{th} European Symp. on Nucleon-Anti Nucleon Interactions, Bressanone, Italy (1980).

[29] P.D. Barnes *et al.* , Nucl. Phys. **A526** (1991) 575.

[30] E. Eisenhandler *et al.* , Nucl. Phys. **B96** (1975) 109.

[31] A.A. Carter *et al.* , Nucl. Phys. **B127** (1977) 202.

[32] R.S. Dulude *et al.* , Phys. Lett. **B79** (1978) 329.

[33] T. Tanimori *et al.* , Phys. Rev. **D41** (1990) 744.

[34] A.D. Martin and M.R. Pennington, Nucl. Phys. **B169** (1980) 216.

[35] A.D. Martin and M.R. Pennington, Phys. Lett. **86B** (1979) 93.

[36] B.R. Martin and D. Morgan, Nucl. Phys. **B176** (1980) 355.

[37] F. James and M. Roos, Computer Phys. Commun. **10** (1975) 343.

[38] M.N. Oakden and M.R. Pennington, work in progess.

[39] J.M. Blatt and V.F. Weisskopf, Theoretical Nuclear Physics, Wiley, (1952).

[40] K. Hikasa *et al.* (Particle Data Group), Phys. Rev. **D45** (1992) S1.

[41] R.L. Jaffe, Phys. Rev. **D17** (1978) 1444.

[42] A. Donnachie and P.R. Thomas, Nuovo Cimento **26A** (1975) 117.

[43] A.A. Carter *et al.* , Phys. Lett. **67B** (1977) 117.

[44] M. Rozanska *et al.* , Nucl. Phys. **B162** (1980) 505.

[45] R.S. Dulude *et al.* , Phys. Lett. **79B** (1978) 335.

[46] B.R. Martin and D. Morgan, Proc. IVth European Antiproton Symposium, Barr (1978), Vol. 2 p. 101; Proc. Vth European Symposium on Nucleon-Antinucleon Interactions, Bressanone (1980), p. 397.

[47] G.E. Hite, R.J. Jacob and F. Steiner, Phys. Rev. **D6** (1972) 3333.

[48] B.R. Martin and G.C. Oades, Nucl. Phys. **A483** (1988) 669.

[49] D. Aston *et al.* , Nucl. Phys. **B292** (1987) 693.

[50] A. Etkin *et al.* , Phys. Lett. **165B** (1985) 217.

[51] R.M. Baltrusaitis *et al.* , Phys. Rev. Lett. **56** (1986) 107.

[52] Xiaoling Fan, contribution to *Hadron '93*, Como (June 1993), to be published in the Proceedings.

[53] C. Amsler *et al.* , Z. Phys. **C58** (1993) 175.